2017

Sol-Gel Chemistry: An Advanced Technique to Produce Macroscopic Nanostructures of Metal and Semiconductor Colloids

Lamia Nahar
VCU

Sol-Gel Chemistry: An Advanced Technique to Produce Macroscopic Nanostructures of Metal and Semiconductor Colloids

A dissertation submitted in partial fulfillment of the requirements for the degree of Doctor of Philosophy at Virginia Commonwealth University

by

Lamia Nahar

Advisor: Indika U. Arachchige

Assistant Professor, Department of Chemistry

Virginia Commonwealth University

Richmond, Virginia, 23284-2006

United States

Acknowledgements

I would like to thank my parents and my sisters, without whose constant inspiration and encouragement it would have been difficult to successfully complete this Doctoral degree. I am grateful that my parents believed in my potentials and decided to let me come here to achieve this precious degree. I cannot thank enough to my beloved husband who was always there to keep me in sanity. I am truly blessed to have him in my life, his presence itself made differences in every spare of the ongoing journey. He is not only the person who I have shared my life with, but he is the best friend of mine who always stood beside me when everyone was left behind.

I would like to convey my deepest gratitude to my advisor Dr. Indika U. Arachchige. It is an honor to work under such a helpful and knowledgeable person. His insurmountable amount of guidance throughout this time period has helped me to successfully complete my degree. Without his assistance this stressful journey would have been much more difficult. Organizing the work and prioritizing them according to their importance is the key to your success - this is the most significant lesson I have learned from my advisor. Besides his enormous work load as a tenure track professor, he was always there not only for my research guidance, but also for my career goals.

Being a third world country's people, most importantly being a girl, I showed that courage to come to United States for higher education. I would like to thank my three sisters Dr. Lutfun Nahar, Samia Nahar, and Sadia Nahar who always stand up with my decision, specially my elder sister who helped me in every way to make this difficult choice possible. My endless love to the new member of my family- Umair Islam Faizan.

Graduate studies are always challenging, on top of that being an international student, I was battling with so many complications when I first arrive in United States. During that time period I came to know some of the wonderful people, one of them is Tasnim Rahman. It's not only the help they provided me, but the time they offered me from their busy schedule was a wonderful gesture. I would like to thank all my friends in Richmond, without those gatherings we had every week I could not have get together my head for the upcoming challenges.

I specially thank to my three childhood friends Tanima Dey, Ivey Rashid, and Naima Khalek Chowdhuri. I still remember that day when Tanima finally convinced me to apply here for graduate studies. I appreciate her help during the application processes.

I believe during this stressful graduate study, a friendly environment in the lab and good lab mates always play a crucial part to handle this pressure. I feel lucky to have such a wonderful lab mates. I am especially grateful to Dr. Richard Esteves, Dr. Xiaonan Gao, and Minh Ho, whom I have started my journey with. One of the newest members Venkatesham Tallapally, who is not only a very a good lab mate but is like a brother to me. I wish all the luck to the new lab members.

Finally, I would like to thank Dr. Pradip Kumar Bakshi, my undergraduate and M. S. advisor. It is an honor to meet a person with such immense knowledge. He is the person who taught me it is not only the knowledge that will make you accountable; it is the good nature of yours that will be remembered too.

I would like to thank God for providing me this honor to achieve my goals in my life. I truly believe he was always there to show me path not only during last five years, but in every spare of my life.

TABLE OF CONTENTS

LIST OF FIGURES

LIST OF SCHEMES

LIST OF TABLES

Abstract

Sol-Gel Chemistry: An Advanced Technique to Produce Macroscopic Nanostructures of Metal and Semiconductor Colloids

by

Lamia Nahar

A dissertation submitted in partial fulfillment of the requirements for the degree of

Doctor of Philosophy at Virginia Commonwealth University

Advisor: Dr. Indika U. Arachchige

Assistant Professor, Department of Chemistry

The fascinating physical properties that arise in materials limited to dimensions of 1-100 nm have gained noteworthy interest from the scientific community. Accordingly, there has been a lot of attention paid to the synthesis of discrete nanoparticles (NPs) and they are being investigated for a range of advanced technologies. Nonetheless, efficient use of nanomaterials in device applications require them to be assembled into solid state macro-structures while retaining their unique, nanoparticulate properties. To date, most commonly investigated assembling techniques include: covalent coupling of NPs surface groups, control evaporation of the solvent to produce ordered supercrystals or non-ordered glassy films, and polymer or bimolecular mediated self-assembly. However, in each of these cases, the interactions among discrete NPs are mediated by

intervening ligands, the presence of which are detrimental for efficient electronic transport and interparticle coupling that limit performance in optoelectronic, electro-catalytic, and chemical sensor studies. Thus, novel and efficient strategies that can be predictably manipulated for direct, self-supported assembly of NPs are of critical need.

A method that has proved useful to construct direct interfacial linkages of colloidal NPs is the sol-gel technique.[1-5] Oxidative removal of surfactant ligands has been shown to produce self-supported NP monoliths that in most cases retain the physical properties of primary NPs. The ability to create direct interfacial bonds contributes to enhanced electrical and thermal transport as well as tunable interparticle interactions, expanding the potential range of NP technologies. During oxidation, low coordinated active sites are produced on the NP surface that interacts with a nearby NP to reduce the surface energy. The formed active sites are highly reactive allowing the NPs to establish direct interfacial linkages, polymerize into low dimensional clusters, and consequently highly porous superstructures that augment the unique, nanoparticulate properties. An added advantage of this chemistry is the ability to couple chemically similar or dissimilar systems with the potential to achieve novel/tunable physical properties. In this dissertation, application of sol-gel chemistry in efficient integration of similar and dissimilar nanoscale materials will be discussed with an aim of achieving improved optoelectronic and electro-catalytic properties.

Hybrid nanomaterials composed of metal-semiconductor components exhibit unique properties in comparison to their individual counterparts, making them of great interest for optoelectronic technologies. The direct cross-linking of NPs via sol-gel chemistry provides a versatile route to tune interfacial interactions in a manner that has not been

thoroughly investigated. Thus, the first part of the dissertation will illustrate the synthesis of CdSe/Ag hetero-nanostructures (aerogels) via oxidation induced self-assembly of thiol-coated NPs and investigate the evolution of optical properties as a function of Ag composition. Two hybrid systems were investigated, where the first and second excitonic energies of CdSe were matched with plasmonic energy of Au and Ag NPs. The optical properties of the CdSe/Ag hybrids were systematically examined through UV-visible, photoluminescence, and time resolved photoluminescence spectroscopy. A new emission (640 nm) from CdSe/Ag aerogels was emerged at Ag loading as low as 0.27 % whereas absorption band tailing and PL quenching effects were observed at higher Ag and Au loading, respectively. The TRPL decay time of the new emission (~600 ns) is markedly different from those of the band-edge (1.83 ± 0.03 ns) and trap state (1190 ± 120 ns) emission maxima of phase pure CdSe, supporting the existence of alternate radiative relaxation pathways in sol-gel derived CdSe/Ag hybrids.

An added benefit of newly developed sol-gel chemistry is the potential to produce porous, conducting nanoarchitectures that provide a facile pathway for efficient transfer of charge carriers and small molecules. Thus, aerogels composed entirely of noble metal NPs are expected to exhibit high electrical conductivity making them promising for electrocatalysis. Thus, the second part of the dissertation will describe the extension of NP condensation strategy for the fabrication of ternary noble metal (Au/Ag/Pd, Au/Ag/Pt) aerogels for electro-oxidation of alcohols. The precursor alloy NPs were produced via stepwise galvanic replacement of thiol-coated Ag NPs. The resultant alloy NPs were self-assembled into large, free-standing aerogels that exhibit direct interparticle connectivity, high surface area (282 – 98 m^2/g) and mesoporosity (2 – 50

nm) via controlled oxidation of the surfactant ligands. The gelation kinetics has been controlled by varying the oxidant/surfactant molar ratio that governs the dealloying of Ag from ternary superstructures with in-situ generated HNO_3. The monolithic Au/Ag/Pd alloy aerogels exhibit higher catalytic activity and durability compared to the discrete alloy NPs (~ 20-30 times) and commercial Pd/C catalyst (2-3 times). On the other hand, Au/Ag/Pt alloy aerogels showed excellent stability at higher concentration of methanol (12 M) during electro-oxidation studies, suggesting its superior electro-catalytic activity. The synergistic effect of tri-metallic alloy mitigates the catalyst poisoning and increases the stability and durability whereas the self-supported superstructure with direct interparticle connectivity, high surface area and porosity offers a facile conduit for molecular and electronic transport, enabling the ternary aerogels an efficient electro-catalyst.

Chapter 1

Introduction

In the last few decades research in nanoscience and nanotechnology has been the center of interest among the scientists all over the world. The unique/tunable physical and optical properties of nanomaterials, with size confined in the regime of 1-100 nm in one or more directions, hold out the promise for many advanced technologies, including information storage, sensing, energy conversion, catalysis, and biomedical applications. The strong size dependence properties of nanoparticles (NPs) offer uncountable opportunities for surprising discoveries which led the scientist to work instantaneously on developing unique synthetic procedure with tunable sizes and physical properties. Although considerable progress has been made on the synthesis of desecrate NPs, methodologies for bottom-up assembly of NPs into solid state structures are limited.

This thesis will focus on the use of traditional sol-gel assembly as a versatile approach for the assembly of chemically dissimilar and similar nanoscale components into high surface area, highly porous, conducting aerogel superstructures. This chapter will offer an introduction to nanoscale materials, semiconductors, plasmonic metals, metal-semiconductor hybrid nanomaterials, and their size dependent physical and optical properties. In addition, the importance of sol-gel chemistry for the assembly of NPs will also be discussed with an aim of developing functional nanostructures for optoelectronic and electrocatalytic applications.

1.1 Nanomaterials

From the perspective of length, a nanometer (nm) is one billionth of a meter (m) or one millionth of a millimeter (mm) and roughly equals to the length of ten hydrogen atoms in a row. Accordingly, nanomaterials are defined as a class of materials possessing structural units in the range of 1-100 nm at least in one dimension.[2] When the material size is reduced to nanoscale, the surface-to-volume ratio increases allowing higher performance and significantly different optical, electrical, magnetic, and mechanical properties compared to traditional bulk materials.

Although an increasing attention was given towards nanomaterials in the past two decades, the use of nanomaterials has been known for centuries. In ancient Rome, Romans first empirically developed methods to stain glass with small inclusions of gold or silver.[2] In 1857, Michael Faraday reported the colloidal synthesis of gold nanoparticles which is considered as the first scientific report in nanoscience.[3] Since then, many reports have been published in scientific journals even before the age of nanoscience and technology began. To date, the nanotechnology and its revolutionary developments in science and engineering are evolving rapidly. This necessity is driven by the desire to fabricate materials with novel and improved physiochemical properties that are likely to impact virtually all area of (physical, chemical, biological, engineering, and health) sciences.

1.2 Semiconductors

Depending on the electronic structure and conductivity, materials are generally classified into three different categories namely insulators, semiconductors, and conductors. Among these three different classes, semiconductors are interesting because of their intermediate conduction property. On a macroscopic scale, semiconductor materials are composed of a large network of ordered atoms that form a set of similar-energy molecular orbitals, resulting in the formation of a continuous band.[4] At 0 K, all electrons are occupied in the lower energy level (valence band, VB), leaving the higher energy level (conduction band, CB) empty. One characteristic feature of a semiconductor is the energy difference between the VB and CB (bandgap (Eg)), and its magnitude is normally in the range of 0.3–3.8 eV[4] which is distinct for specific material. This band energy concept in semiconductors can be understood similarly to the molecular orbital theory for an individual molecule and Eg can be defined as the minimum energy required to excite an electron from HOMO to LUMO. The difference in conductivity between insulators, semiconductors and conductors is illustrated with respect to the Eg value (Figure 1.1). The larger the bandgap energy, the harder it is for electrons to travel from VB to CB, resulting lower probability for electrons to conduct.

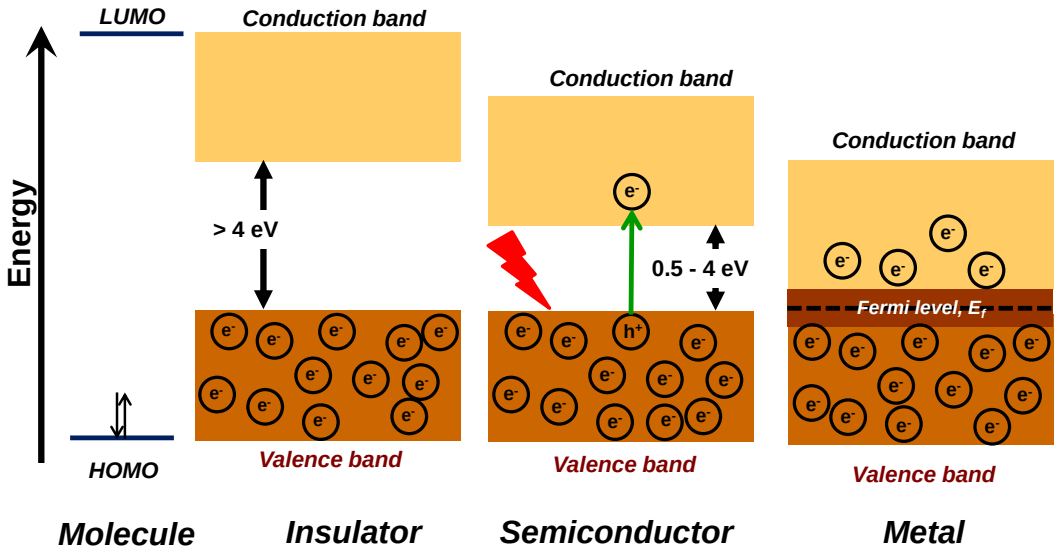

Figure 1.1 A schematic illustration showing the band energy difference between an insulator, semiconductor and a conductor along with HOMO-LUMO levels of an individual molecule.

In semiconductor materials, when sufficient thermal or electrical energy is provided, electrons in the VB can absorb photon energy and can overcome the energy gap to reach in the CB, leaving a positive hole in VB. This free electron and positive hole as a pair of opposite charges experiences a columbic attraction, which causes the electron to orbit around the hole in a certain radius similar to hydrogen atom. This electron-hole pair is known as the exciton and the certain radius they orbit around is known as Bhor radius (R_b) with the value described in the following equation 1.1.[5]

$$R_b = \frac{\hbar^2 \in}{e^2}\left[\frac{1}{m_e^*} + \frac{1}{m_h^*}\right] \ldots\ldots\ldots\ldots\ldots\ldots\ldots\ldots\ldots (1.1)$$

Where Є is the dielectric coefficient, e is the elementary charge, m^*_e and m^*_h are the electron and hole effective mass, respectively. Since electron (e), m^*_e and m^*_h are

characteristics for each material, R_b can vary in a wide range of 1-150 nm.[5] Thus, the Bohr radius and crystal size have a critical control on the optical properties of a semiconductor. When the size of a crystal is smaller than the Bohr radius, the material exhibits size dependent absorption and emission properties, which has been the center of research for the last couple of decades.

While considering the optical properties of semiconductors, they can be categorized as either direct- or indirect-gap materials (Figure 1.2). The photon induced electronic transitions not only rely on the intensity of incident photon energy relative to Eg but also the wave vector k. The wave vectors (k) of electrons are conserved during excitation and relaxation processes for a direct gap semiconductor. Since the absorption coefficient is proportional to the probability of the electronic transition,[4] direct-gap semiconductors exhibit sharp absorption peaks with large absorption coefficients (e.g., CdSe, PbSe). As a consequence, in the direct gap semiconductor materials, the relaxation of the excited electron or recombination of the electron-hole pairs will emit energy in the form of a photon which is commonly known as radiative recombination photoluminescence. These useful features of semiconductors can be used in light emitting diodes and laser applications. In contrast, the VB maximum and CB minimum of an indirect-gap semiconductor material are in different momenta of space (wave vector k), resulting in forbidden electronic transitions (e.g., Si, Ge).[6] However, the electronic transitions can still be possible for indirect band structure by the interaction of phonons (quantized lattice vibrations) as shown in Figure 1.2.[6] Nonetheless, phonon-induced optical transitions are extremely rare, and reduces the probability of exciton radiative recombination in indirect-gap semiconductor materials, reducing the

absorption and emission efficiency. This prohibits the use of indirect gap semiconductors, such as Si and Ge, in many optical technologies.

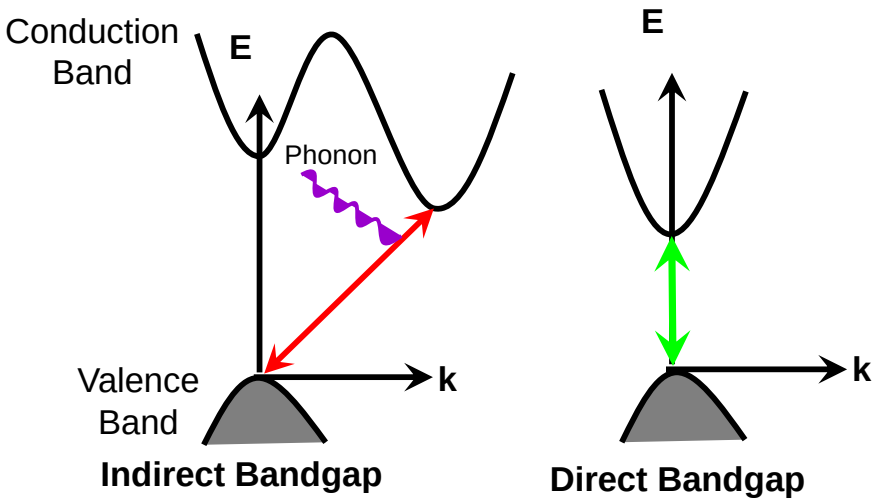

Figure 1.2 A schematic diagram showing the electronic structure of Indirect and direct bandgap semiconductors and the differences in momenta of space between the lowest point of conduction band to the highest point of valence band, E= Energy, and k= momentum vector.

1.3 Quantum Confinement

The significant changes in fundamental properties of semiconductor materials, whose sizes approach to the nanoscale, have been the most studied research topic since the emergence of nanoscience and technology. Among them, one of the remarkable property of semiconductor nanostructures is the potential tunability of optical properties as a function of size, shape, composition, allowing opportunities to exploit new photophysical properties. The quantum confinement phenomenon is quite common in nanoscale semiconductor materials when the size of the material is comparable to or

less than the bulk excitonic Bohr radius. If the size of the quantum box/dot reaches to a value smaller than Bohr radius, confinement effect lead the continuous energy bands to be separated out into discrete energy levels as depicted in Figure 1.3. This occurs due to the less overlapping between the orbitals and also because of the confined space for the excitons. These changes in energy (ΔE) in the confinement range can be modeled with equation 1.2.[4]

$$\Delta E = \frac{\hbar^2 \pi^2}{2R^2}\left[\frac{1}{m_e^*} + \frac{1}{m_h^*}\right] - \frac{1.8\, e^2}{\in R} \ldots\ldots\ldots\ldots\ldots\ldots\ldots\ldots\ldots (1.2)$$

Where R is the radius of the particle, m_e^* and m_h^* are the effective masses of an electron and hole, respectively, Є is the dielectric constants, and ħ is Planks constant and e is the elementary charge. Although this equation uses a few assumptions on charge carrier masses and dielectric constant values, it provides a decent estimation of the changes in bandgap energy with respect to particle size and confinement effects. Owing to these unique characteristics, absorption and emission properties of semiconductor NPs can be tuned as a function of particles size or shape. The size at which confinement effects are observed is highly dependent on chemical identity of the material and this typically ranges from 2-150 nm for Group II-VI, IV-VI and III-V semiconductors.

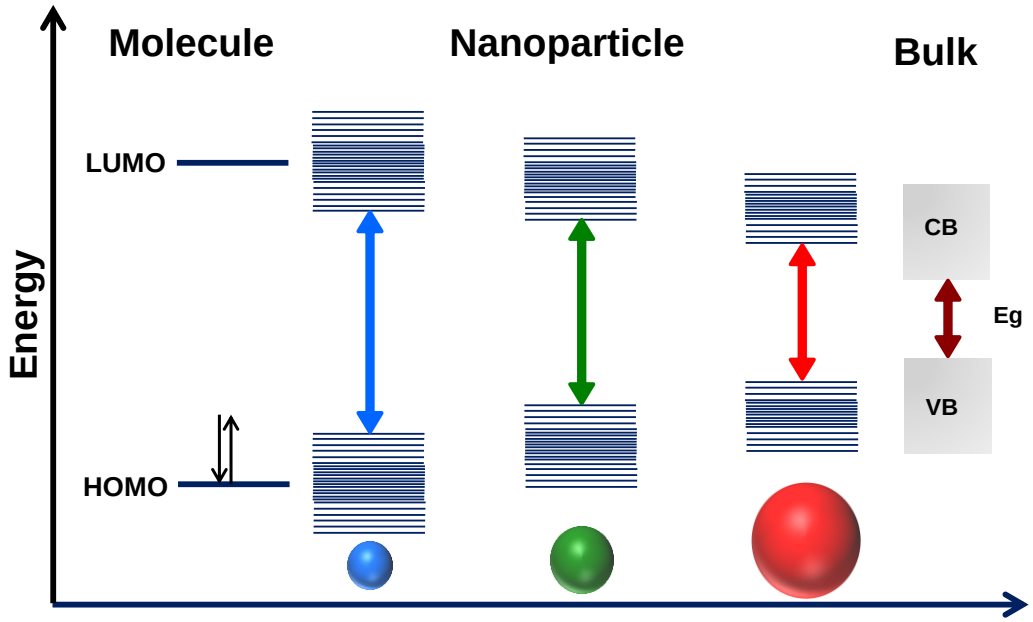

Figure 1.3 A comparative energy diagram of nanoparticles as a function of size, along with HOMO-LUMO energy gap of a single molecule and bandgap of the bulk material.

The second most observable change in the semiconductor NPs is the enhanced surface/volume ratio that has a critical control over their optical properties. As the emission energy of a semiconductor NP depends both on the core and surface atoms, this surface enlargement can affect the dynamics of electron-hole recombination. In comparison to the bulk materials, the surface atoms in NPs are highly energetic owing to incomplete bond formation, which results in higher degree of defects and dangling bonds. These surface defects collectively produce intermediate energy levels (mid-gap states) in between the VB and CB, leading to the trapping of photo-excited electrons and holes (Figure 1.4).[7] While the band-edge absorption and emission of a semiconductor NP is expected to exhibit well-defined, sharp peaks, the presence of mid-gap states can lead to much broader emission spectra specifically at longer

wavelengths. These surface effects greatly reduce the quantum efficiency of optical transitions in a semiconductor NPs, limiting their potential in optoelectronics. However, organic and inorganic passivation of the NP surface has been successfully utilized to reduce undesired non-radiative decay pathways.[7]

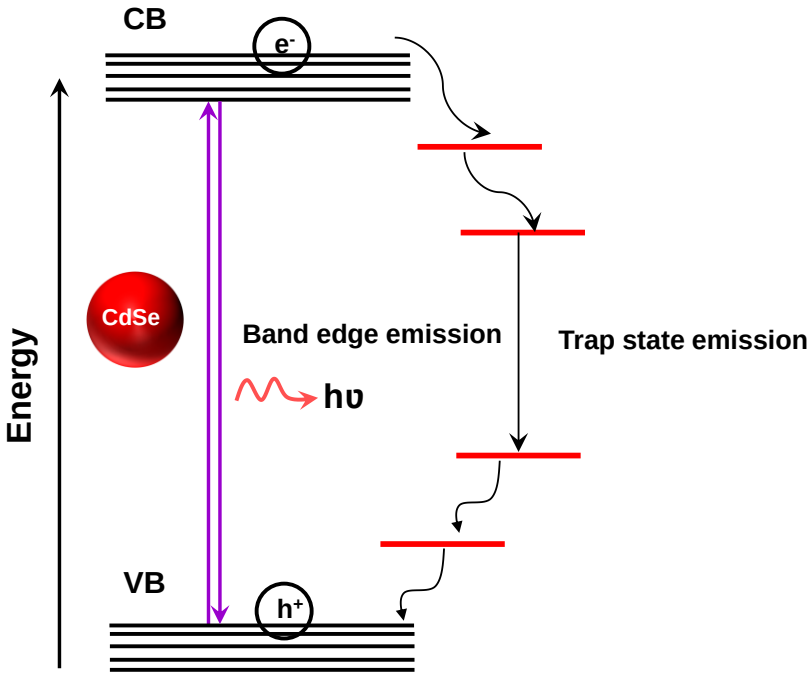

Figure 1.4 Electronic states and optical transitions of colloidal semiconductor NPs, displaying the potential radiative recombination pathways for photo-excited excitons.

Although the effects of NP size on quantum confinement has received significant attention, recent studies showed that the shape of the nanomaterials has a similar influence on the quantum confinement effects.[8] This has been attributed to the changes in excitonic properties with respect to the shape of the semiconductor material. In contrast to a macrocrystalline semiconductor, where the photo-generated exciton can move freely in all directions as a result of large size, nanocrystals (NCs) with size

reaching to bulk excitonic radius can modify the physical properties. Depending on the dimensions, three different confined nanostructures are defined; quantum wells, quantum wires, and quantum dots (Figure 1.5).[8] When the size is reduced in one direction *i.e.* in quantum well, it allows electrons to freely move in other two directions and a 2-D quantum confined nanostructure is produced. In contrast, when the size of the material is reduced in two directions, for example in quantum wires, it allows 1-D confinement effect. And if the size can be confined in all three directions, (*i.e.* in quantum dots) resultant material is expected to exhibit 0-D confinement effects.

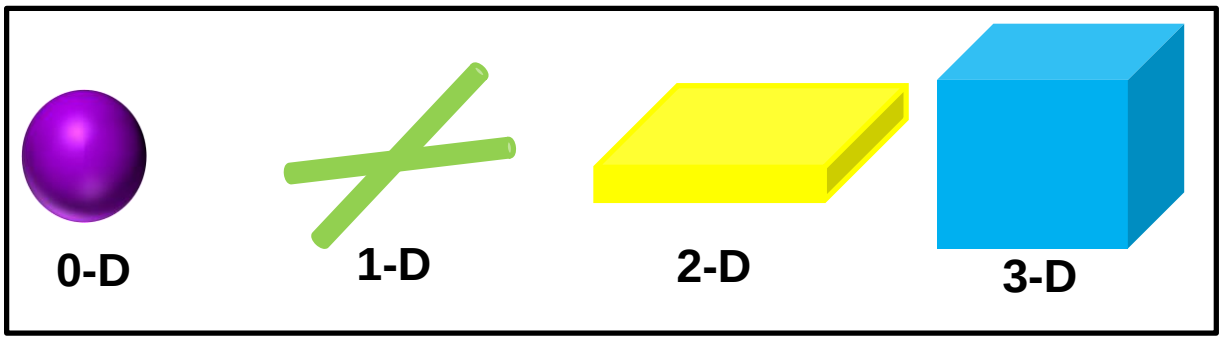

Figure 1.5 A schematic representation of the geometries of quantum dots (0-D), quantum wire (1-D), quantum well (2-D), and crystalline solid (3-D), respectively.

1.4 Plasmonic Metal NPs

Metal NPs have been used in applications long before the science of nano-sized materials have attracted much attention. The bright and fascinating colors of noble metal NPs are known since the innovation of decorative pigments in stained glasses and artworks. The intense color of metal colloids occurs due to the coherent excitation of the conduction-band electrons which is known as the surface Plasmon absorption. Precise control over shape and size can tailor the NPs physical and optical properties

that can satisfy different application requirements. In the following subsection physical properties of noble metal NPs will be discussed briefly, in light of their potential application in optoelectronic, electrocatalytic and chemical sensor technologies.

Optical Properties

The plasmonic absorption of inherent in a few of the noble metal NPs is one of the most interesting aspects that drives their potential in many technologies. When a beam of light interacts with certain metal NPs, such as Ag, Au or Cu, the free electrons in the metal can oscillate with the alternating electromagnetic field resulting in a distinct absorption known as the surface Plasmon resonance (SPR).

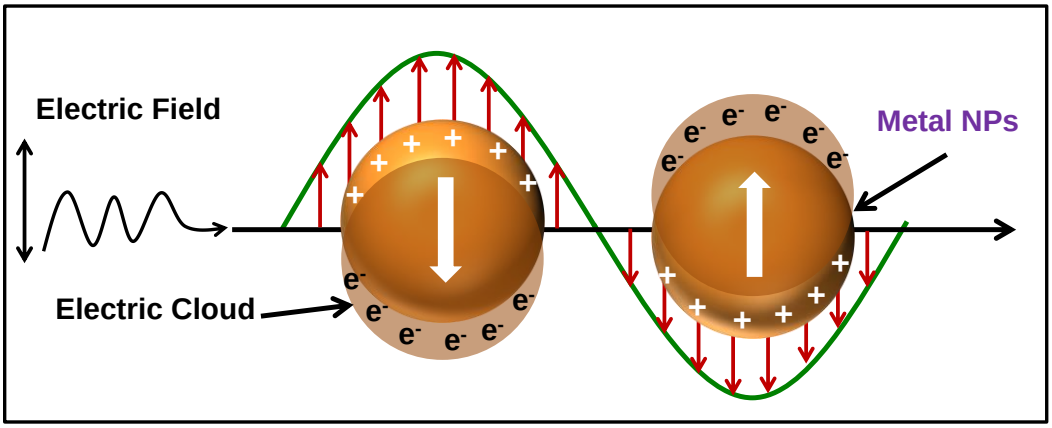

Figure 1.6 Schematic illustration of the localized surface Plasmon resonance in spherical metal NPs.

When the size of metal NPs are smaller than the wavelength of incident light, the polarization of surface charges can occur while they are excited by light. These induced charges of the metal nanoparticles cannot propagate as a wave along the flat surface, rather confine and concentrate on the particle surface. Matching the collective

oscillation frequency with incident light results in a resonance condition, which is known as localized surface plasmon resonance (LSPR, Figure 1.6).[9] The LSPR property of metal NPs is determined by several factors, such as the size, shape, and geometry,[10] and dielectric properties of the surrounding medium,[11] as well as the interparticle coupling interactions.[12] Due to the strong absorption property of LSPR and the potential to enhance the local electromagnetic field,[13] plasmonic NPs (such as Au and Ag) exhibit promising applications as surface-enhanced Raman scattering (SERS) substrates,[14] nanoscale waveguides,[15] and nanophotonics.[16]

Catalytic Properties

Recent advances in energy research focus on the rational design of catalysts with unprecedented efficiency in energy conversion reactions. Controlling the electronic structure and surface topography of nanoscale catalysts has been successfully utilized to increase the efficiency for a number of chemical reactions. Single element, binary, and ternary noble metal NPs have been widely examined as stable and durable catalysts for many reactions, including hydrogenation and oxidation of organic compounds, alcohol oxidation fuel cells, and cross coupling reactions etc.[17]

Last few decades tremendous effort has been made to find suitable catalysts for fuel cell system, where the primary goals of a perfect catalyst lie on the cost effectiveness, the high activity, and the durability. Very recently noble metals and their alloys showed promising activity as catalysts in fuel cell reactions.[18] The most common commercialized catalysts for direct alcohol fuel cell studies are the platinum (Pt) based catalyst. However, the scarcity, high cost of Pt is always a constant struggle that

motivate researchers to find low cost alternatives. Formation of poisonous CO species on the Pt electrode (anode) and the strong adsorption of OH on Pt on the cathode reduce the stability of the catalyst, which is a major problem that need to be addressed.[17a, 18b] Alloying of Au with Pt has been shown to have better catalytic activity towards alcohol oxidation due to the oxidative conversion of poisonous CO to CO_2 on Au surface.[19] Alternative to Pt NPs, Pd based catalyst showed promising catalytic efficiency toward ethanol oxidation. As ethanol is hydrogen rich, nontoxic solvent that can be conveniently produced from biomass and it has a 33 % higher energy density than methanol (eq 1.3).[20] It has been found that bimetallic or trimetallic catalysts containing Pt, Pd, and other transition metals (e.g., Fe, V, Ni, Ru, etc.)[18] exhibits better catalytic activity in electrocatalysis of methanol, ethanol, glucose, and oxygen reduction reaction compared to the single element NPs. In a conventional direct alcohol fuel cell (DAFC, Figure 1.7), in the anodic chamber flow of the alcohol with water can interact to the catalyst layer and oxidizes to CO_2, H^+ and gives away electrons (eq 1.4). On the other hand, at cathode chamber O_2 can be reduced at the catalyst layer by accepting electrons flowing from the anodic chamber (eq 1.5).[20a] During this complete process electrons are flowing through an external circuit providing electrical power.

$$CH_3CH_2OH + 12\,OH^- \rightarrow 2\,CO_2 + 9\,H_2O + 12\,e^- \ldots\ldots\ldots (1.3)$$

Anode: $$C_2H_5OH + 6H_2O \rightarrow 2CO_2 + 12\,H^+ + 12e^- \ldots\ldots (1.4)$$

Cathode: $$3\,O_2 + 12H^+ + 12e^- \rightarrow 6\,H_2O \ldots\ldots\ldots\ldots\ldots\ldots\ldots\ldots (1.5)$$

Generally in a DAFC, the catalytically active materials are supported on a porous substrate. One important factor in building a high performance fuel cell catalyst is to

obtain the well dispersity of NPs throughout the support material. However, the supported catalysts limit their efficiency due to agglomeration of NPs inside or on the surface of the support leading to pore blockage, interruption of mass transport routes as well as uneven loading.[18b] In contrast, the assembly of metal NPs via direct interfacial linkage to generate 3-D connected network will provide self-supported nanostructures with approximately uniform dispersion of NPs. Furthermore, inherently random yet continuous meso-to-macropore network will provide a facile conduit for the transportation of both electrons and small molecules and can potentially result in a better electrocatalyst.

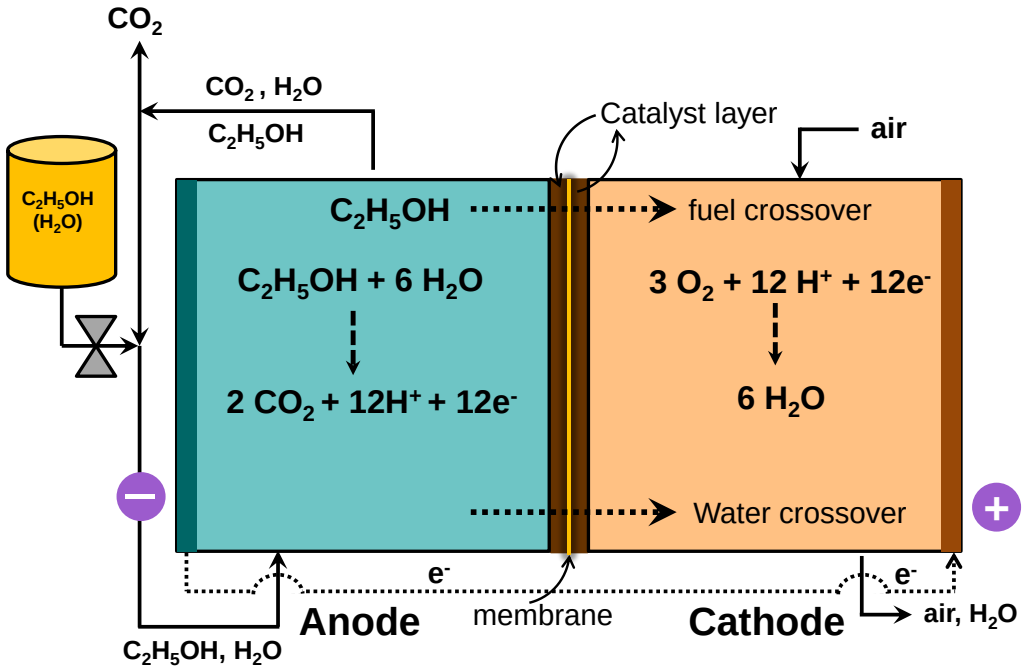

Figure 1.7 Schematic diagram of a direct ethanol fuel cell (DEFC).

Another alternative method for obtaining better or enhance catalytic and optical property is the formation of hybrid nanomaterials. Compared to single component,

hybrid nanostructures can exhibits superior properties and/or new functionalities. For instance hybrid nanostructures consist of metal/semiconductor, metal/metal, or metal/magnet has been known as high efficiency photocatalyst, catalyst, or electro-catalyst due to their improved chemical stability and bifunctional effects.[21]

1.5 Hybrid NPs and Their Significance

Easy and quick alteration of the NP properties and functionalities is one of the key requirements for device applications. One way to achieve this flexibility, is to use hybrid nanomaterials (HNMs), which exhibit different properties from those of the individual component materials. HNMs are the composites that contain two or more different compound in their structure. They can consist of semiconductor-metal, semiconductor-insulator, or semiconductor-semiconductor composites. Each composite of the hybrid structure has distinct physical properties, which when assembled together exhibits different characteristics from their individual entities. The ability to produce HNMs with novel/tunable physical properties depends on the chemical nature of the individual components and physical interactions. The interaction of two dissimilar nano-entities has been shown to governed by the interface, size, shape, and structure of both individual and two components. In the case of weak interactions, for example colloidally stable NPs, where the direct interaction between NPs is hindered by bulky organic ligands (Figure 1.8 B, C), a simple sum of the optical properties is observed. Although a number of literature showed the study of direct interactions via conducting ligands or by the use of chelating agents, most observable result is the quenching of emission properties in the HNMs. On the contrary, the strong interaction between the individual

components (Figure 1.8 A), can completely overpower the other nanomaterials physical properties. As a consequence the individual components might lose its own optical property as a result of coupling interactions. Hybrid nanomaterials with improved optical and electronic properties are gaining considerable interest in the search for the easy control of their photophysical properties and fundamental understanding of the interactions between chemically different systems as well as application in efficient light harvesting, sensing, imaging, biomedical detection and therapeutic studies.[21-22]

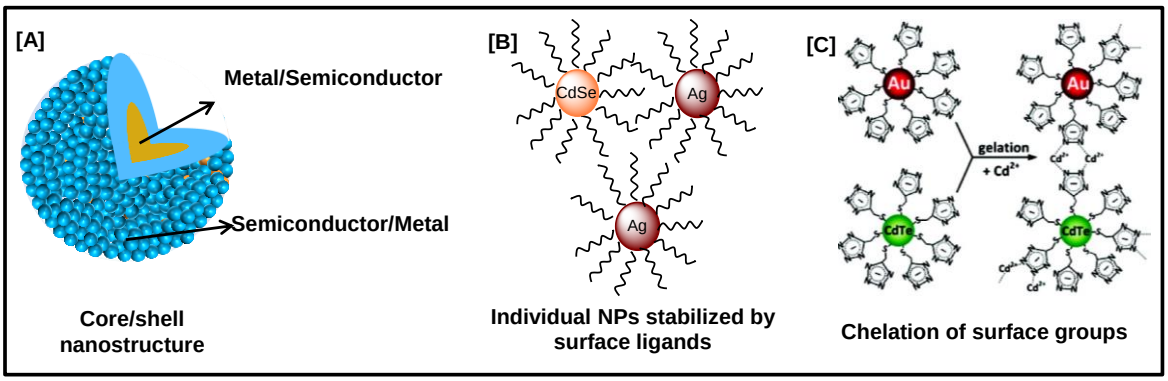

Figure 1.8 Various approaches for the production of HNMs: (A) Core/shell NPs (B) ligand stabilized metal-semiconductor hybrids, and (C) Au-CdTe hybrids resulted via chelation of colloidal NPs.

1.6 Synthesis of NPs

To date, a wide range of research efforts are focused on the synthesis of different nanoscale materials with control over morphology and physical properties, including metals,[23] semiconductors[24] and magnetic[25] materials in the form of spheres,[26] wires,[27] tubes,[28] dogbones,[29] rods,[30] cubes,[31] triangles,[32] and hollows,[33] etc. Among various synthetic approaches chemical reduction of transition metal salts, colloidal synthesis,

photochemical and sonochemical syntheses, chemical vapor decomposition, and electrochemical reduction syntheses have proved useful for fabrication of NPs.

Colloidal Synthesis

In contrast to the other synthetic routes, solution based colloidal method have shown significant control over NP size and shape, which makes it one of the most powerful technique for the preparation of high quality NPs. In general, colloidal synthesis consists of three critical steps – nucleation, seed growth, and isolation, to obtain nanomaterials. Generally, classical La-mer model is used to explain the synthesis of monodisperse NPs in solution, as shown in Figure 1.9.[34] Quick injection of the chemical reactants in a coordinating solvent solution at high temperature, creates unstable supersaturation in a confined space leading to the formation of small nuclei. While maintaining the temperature, further consumption of precursors continually facilitates the growth of the particles. As a consequence of simultaneous growth, uniform size distribution is observed over time. In contrast, a secondary growth phase can occur, known as Ostwald ripening. This particularly takes place when the high surface energy smaller nuclei starts to dissolves back into the solution and later on can be deposited on the large particles. This process is driven by the lowering the surface energy of nanocrystals. Ripening can have a number of different effects on NP morphology.[35] Alternatively, small crystals can also undergo sintering to form larger particles. If a simple coalescence occurs, all of the crystallites can connect randomly to result in a polycrystalline particle with large degree of defects. On the contrary, if the lattices of each individual crystal match up before fusing, it can give rise to a single crystal.[36] Oriented attachment can also produce nanorods and other morphologies. Hence,

different reaction conditions such as – temperature, time, and capping ligands should be adjusted to have better control over growth kinetics.

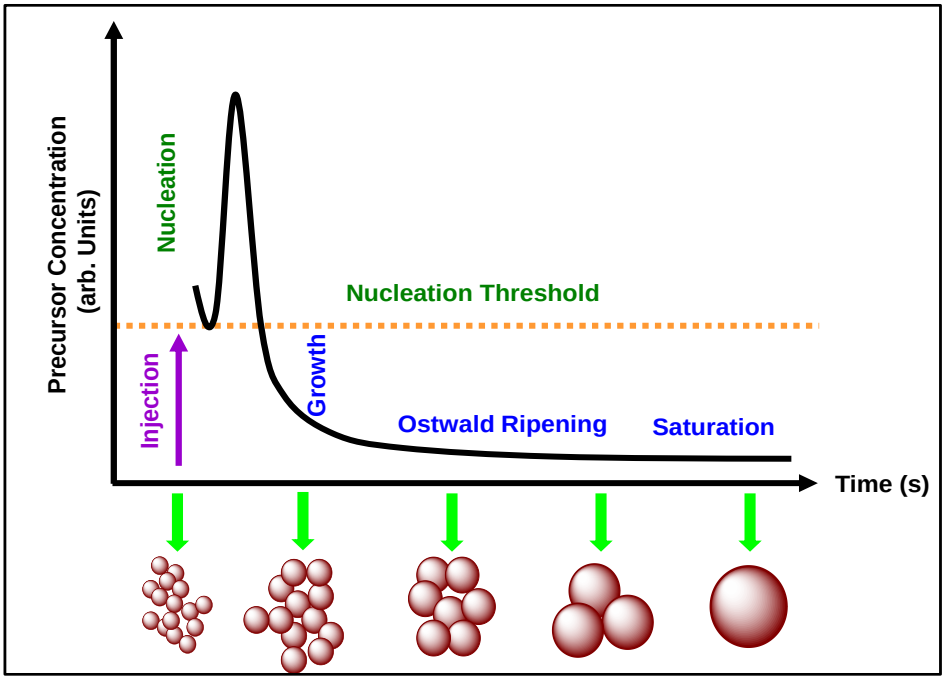

Figure 1.9 Schematic representation of La Mer nucleation and growth mechanism of colloidal synthesis of nanoparticles.

Wet Chemical Synthesis

Solution based synthesis can be classified into two main categories, aqueous and non-aqueous. Water is a versatile solvent for many NPs synthesis due to its ability to dissolve most of metal salts, oxidizing and reducing agents, surfactants, etc. Furthermore, water is the most abundant, environmental friendly solvent that provides a neutral reaction media for a number of wet-chemical reactions. Due to these mentioned factors aqueous system is one of the highly studied syatem.[37]

Galvanic Replacement Reaction (GRR)

Various properties and applications of metal NPs are determined by their size, shape, composition, crystallinity, and crystal structure. Depending on the application, the performance of metal NPs can be optimized by tuning many of these parameters. Among technique that can be used to achieve such control, GRR has gained much interest due to its simpler synthesis and ability to control the morphology and composition of the resultant nanostructures.[38] GRR is generally an irreversible reaction that occurs between colloidal NPs and metal ions in the solution. Depending on the difference in standard reduction potential between two metals, the reaction can proceeds via deposition of the metal ion with higher reduction potential. Consequently the lower reduction potential metal will be oxidized and dissolve back into the solution. For example, the reaction between $HAuCl_4$ and Ag NPs in a solution media proceeds via successive reduction and deposition of $AuCl_4^-$ on the NP surface with subsequent oxidation and dissolution of Ag^+ into the solution. Due to the significant difference in the reduction potential between Au/Au^{3+} (1.5 V) and Ag/Ag^+ (0.79 V), GRR occurs spontaneously between these two metals (Figure 1.10).[38b] Since Au and Ag both have face centered cubic structure with very similar lattice parameters (4.0786 Å for Au and 4.0862 Å for Ag), GRR can facilitate the Au/Ag alloy formation. The metals/elements with less substantial differences in reduction potential (Pt^{4+} vs. Pd^{2+}) can still undergo GRR with significantly lower reaction rate.[19, 38c] However, the presence of appropriate co-reducing agents (ascorbic acid, citric acid, etc) has been shown to enhance the rate of galvanic displacement.[38c] This simple reaction can be employed to generate a

number of metal nanostructures that is solely controlled by the favorable difference in the reduction potential between the elemental components.

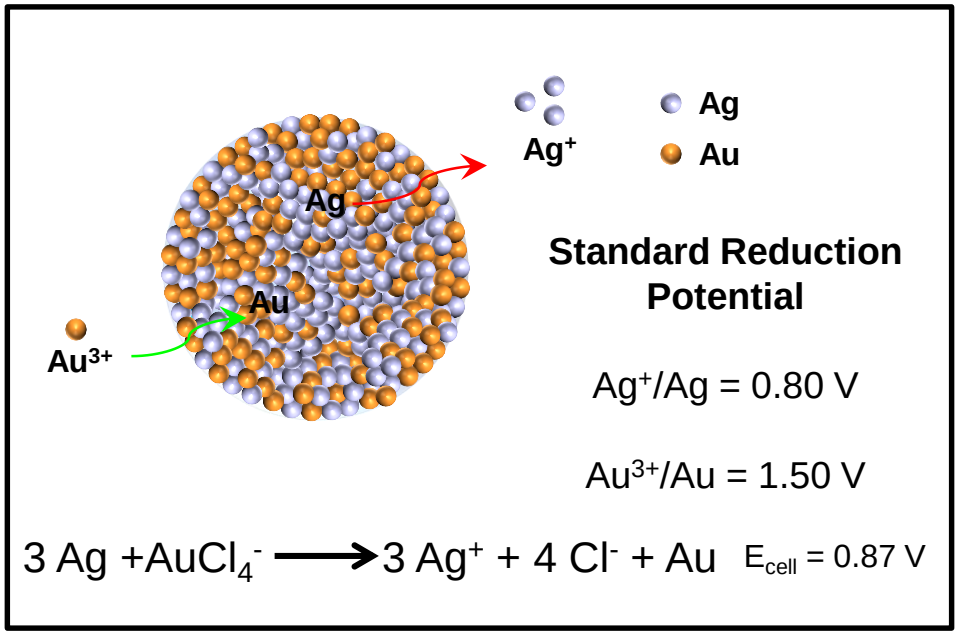

Figure 1.10 Schematic representation of GRR between Ag NPs and $HAuCl_4$ to produce Au/Ag alloy NPs.

1.7 Assembly of NPs

The ability to assemble nanoparticulate building blocks in to functional superstructures is an essential element prior to application of nanomaterials in a number of technologies. Particularly, the bottom–up assembly is an important frontier in NP research from the perspective of device applications. Over the past years, a number of different approaches for the assembly of NPs has been developed and new methods continue to appear.[39] Among those, layer by layer assembly, superlattice formation, and polymer or bimolecular mediated assembly has gained notable interest.[39b-d] In the following sub-sections these assembling techniques will be briefly discussed.

Superlattice Formation

Among the various assembly approaches, self-organization of colloidal nanocrystals into 2D or 3D architectures via electrostatic or Van der Wall forces has been extensively studied.[39b, 40] This approach can be utilized to produce long range crystalline (superlattices) architectures while maintain the size tunable physical properties (Figure 1.11).[39b, 40] The maximization of the packing density as well as the monodispersity of individual particles has been the driving force for superlattice formation.[40] However, the as-prepared superlattices are insulating with extremely low conductivity due to the large separation between NPs with bulky organic ligands. For instance, PbTe superlattices exhibit very low conductivity (10^{-13} S/cm^{-1}); however, when treated with hydrazine it showed ~ 10-12 order[39d] of magnitude increased conductivity. Hydrazine can replace the bulky surfactant ligands providing an opportunity to reduce the interparticle distance that enhances the conductivity of the self-assembled nanostructure.

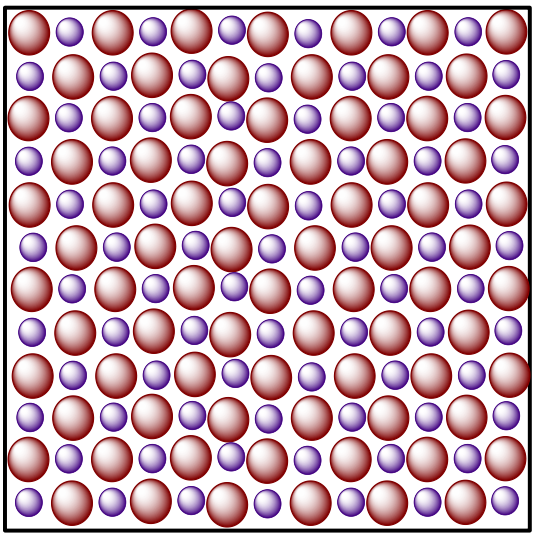

Figure 1.11 A Schematic diagram of a superlattice.

Layer-by-Layer Assembly

The layer-by-layer assembly is one of the first strategies developed for the construction of NPs thin films.[39c] Following a bottom up assembly strategy, a number of mono layers or hierarchical nanostructures can be produced via this technique. Typically, a uniform thin film functionalized with any charged molecule serve as a template, which is initially modified with oppositely charged polyelectrolytes. A monolayer of NPs is formed on the surface based on the electrostatic interaction between the polyelectrolyte charge and the surface charge of NPs (Figure 1.12). This layer formation can be repeated for definite number of time to achieve a desired thickness of the film.[39c] Varying the capping ligands and polyelectrolytes this technique can provide different superstructures with improved functional properties for multiple applications including advanced absorbents or catalyst. However, in these LbL assembled structures; the nanocrystals are physically separated by a layer of polyelectrolyte.[39c] Hence they are inefficient for applications that require direct interparticle interaction and fast conduction.

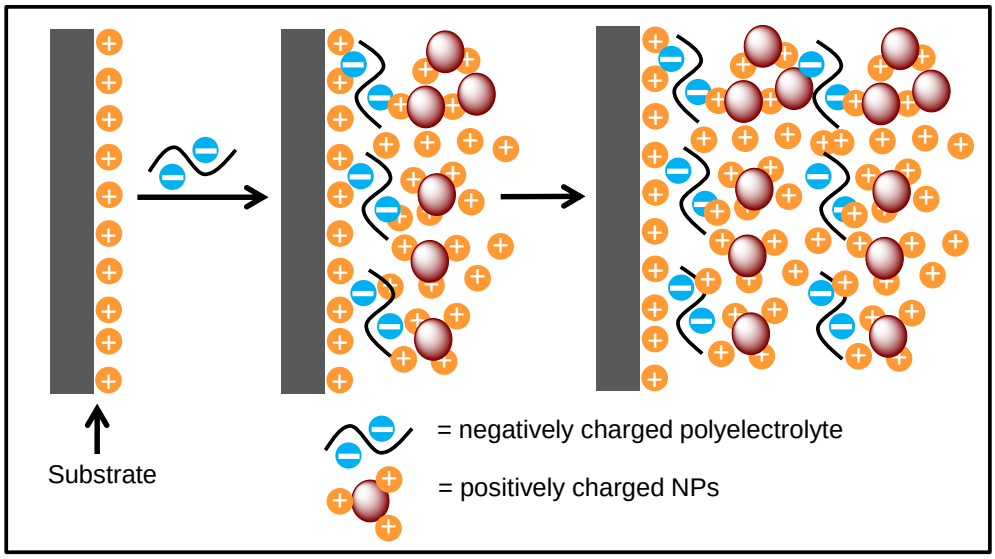

Figure 1.12 Layer-by-layer assembly of charged NPs and polyelectrolyte fabricated on a positively charged substrate.

Polymer/DNA Mediated Assembly

The formation of NP assemblies using polymer linkers or DNA strands is another strategy that has been studied extensively.[39c] The mechanism involves a specific interaction between surface modified NPs and functionalized polymer, which recognizes the NPs through H-bonding or coupling through another complementary half of DNA base pair (Figure 1.13). Due to the weak interaction between the DNA base pair via hydrogen bonding, the assembly and disassembly can be controlled via manipulation of the temperature.[39c] At high temperatures, the hydrogen bond between DNA base pairs can be stretched fully to tune the interparticle distance in the assembly.[39c] However, the interactions between nanosized units are mediated by polymers or biomolecules, presence of which are detrimental to charge transport properties and limit the interparticle coupling.

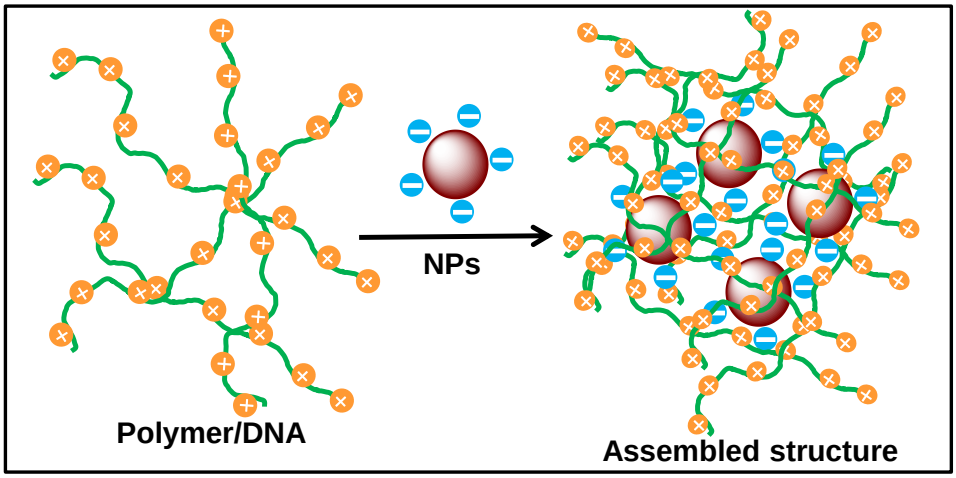

Figure 1.13 Schematic representation for the polymer/DNA mediated self-assembly.

1.8 Sol-Gel Assembly

Most common techniques available for the bottom-up assembly of NPs into functional architecture utilize intervening organic ligands or layers of polyelectrolytes for the NP assembly.[39b, 39c] However, the use of organic linkers or polyelectrolyte hinders the direct interparticle interaction, making them unfavorable for the applications that require efficient transport of charge carriers. Therefore, new methods for the direct self-supported assembly of NPs into functional solid-state structures are under constant investigation. A method that has proved useful to construct NP assemblies with direct interfacial linkages involves sol-gel chemistry.[41] In contrast to the previous techniques, sol-gel method provides a unique strategy for the assembly of NPs without the use of intervening linkers or substrate supports.

The sol-gel method is known since early 1930's and has been extensively studied for the synthesis of metal oxide gels (SiO_2, Al_2O_3 and TiO_2).[41-42] In a typical sol-gel

assembly, a series of hydrolysis and condensation occurs to result in the polymerization of metal alkoxides.[41-42] During the first step, metal alkoxides $M(OR)_n$ (M= Si, Al, Ti, V, Cr, W, and OR is the alkoxy groups) will hydrolyze to produce a hydroxylated metal centers and alcohols (equation 1.6), which in the next step will condensed to generate oxy-polymers (equation 1.7).[41] The nanoscale particles will be connected by the oxygenated bonds by eliminating water or alcohols in the condensation step.

(a) Hydrolysis

$$M(OR)_n + H_2O \rightarrow [M(OR)_{n-1}(OH)] + ROH \ldots\ldots\ldots\ldots\ldots\ldots\ldots\ldots (1.6)$$

(b) Condensation

$$M - OH + M - OX \rightarrow M - O - M + XOH\ (X = H\ or\ R) \ldots\ldots\ldots (1.7)$$

Typically, the hydrolysis and condensation occurs simultaneously and the kinetics of the reaction is highly pH dependent.[41] In the acid-catalyzed reaction, hydrolysis is favored and condensation is the rate determining step and monomers mostly polymerizes in a linear structures/gels consists of small degree of porosity. In contrast, in base catalyzed reactions, the condensation is favored and hydrolysis is the rate determining step.[41] Hence, the resulting gel network consists of an interconnected network of colloidal particles (pearl necklace morphology) with higher degree of porosity. The resultant hydrogels can be dried on benchtop to produce dense xerogels, or they can be supercritically dried to produce highly porous aerogels.[42b]

Aerogels

The method that is used to remove the pore liquids from the hydrogel or wet gel will determine the physical properties of the dried gel material.[42b] Evaporation of the solvent

via bench top drying or vacuum drying results in low surface area, dense xerogels. During the drying process, the strong capillary forces between solid NP surface and the solvent resulted in significant destruction and densification of the gel framework.[42b] Hence, the xerogels lose a considerable amount of porosity. In contrast, supercritical drying of the wet gels can be used to maintain the parent architecture of the wet-gels.[42b] Above the critical temperature and pressure of any substance, distinct liquid and gas phase boundary disappears to produce a supercritical fluid. Due to the absence of capillary forces at this temperature and pressure, the wet gel can be dried without rapturing the internal porous structure (Figure 1.14).[42b] As-synthesized aerogels are a unique class of micro-to-mesoporous material consisting entirely of an interconnected network of NPs known as the “classic pearl necklace” morphology of an *aerogel.*[42b]

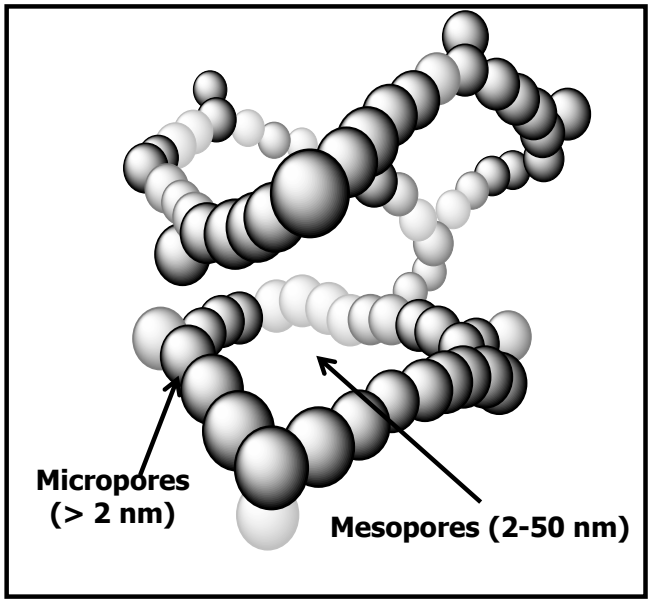

Figure 1.14 A pearl-necklace morphology of the base catalyzed silica aerogel.[42b]

To date, a great deal of research has been conducted on aerogels based on metal oxides, amongst the traditional SiO_2, Al_2O_3, and TiO_2 are the widely studied systems.[42b] Although the metal oxide based aerogels have received much attention from the scientific community, unsupported non-oxide aerogels have been largely limited to semiconducting metal chalcogenides, pnictides, and carbon aerogels for many years.[43]

1.9 Previous Studies on Metal Chalcogenide Gels

Over the last two decades, scientists have begun to extend sol-gel chemistry to non-oxide systems. This has led to the development of carbon aerogels, the first class of non-oxide aerogels prepared from pyrolysis of resorcinol-formaldehyde gel frameworks.[44] Later in 1997, Gacoin et al. first reported the synthesis of CdS wet-gels from thiolate-coated CdS nanoparticles by oxidative removal of the surface ligands.[45] This novel approach has been extended by Brock et al. for the assembly of a variety of metal chalcogenide and pnictide NPs including CdS,[46] CdSe,[1b, 47] CdTe,[1e, 48] ZnS,[1b, 47a, 49] PbS,[1b, 47a] PbTe,[50] InP,[51] Bi_2Te_3 and $Bi_{2-x}Sb_xTe_3$ particles.[52] Moreover, the synthesis of CdSe/Ag,[53] Ag/CdS,[54] and Au/CdS[55] metal-semiconductor hybrid gel frameworks by employing a similar strategy has also been reported.

In contrast to traditional metal oxide sol-gel chemistry where hydrolysis and condensation of molecular precursors are used to produce metal oxide gels, gelation in metal chalcogenide and pnictide systems has been achieved via condensation of the pre-formed NPs.[45b] In this technique, surface functionalized (preferably thiolates) colloidal NPs are synthesized by well-stablished methods (section 1.6), which then undergo oxidation to create low coordinated active sites on the NP surface. The formed

active sites are highly energetic, allowing the NPs to produce direct interfacial linkages and polymerize into low dimensional, nanostructures producing “jello” like hydrogels.[45b] The resultant hydrogels can then be supercritically dried to obtain aerogels (Figure 1.15). Even though these semiconductor NCs are assembled into three-dimensionally connected macro-structures, the aerogels are reported to exhibit the quantum confined optoelectronic properties of NP building blocks. As prepared metal-chalcogenide and pnictide aerogels exhibits extremely low density (0.07-0.35 g/cm^3), high specific surface area (~ 250 m^2/g) and porosity, and nanoparticulate physical properties making them great interest for optical and catalytic studies.[45b, 47a]

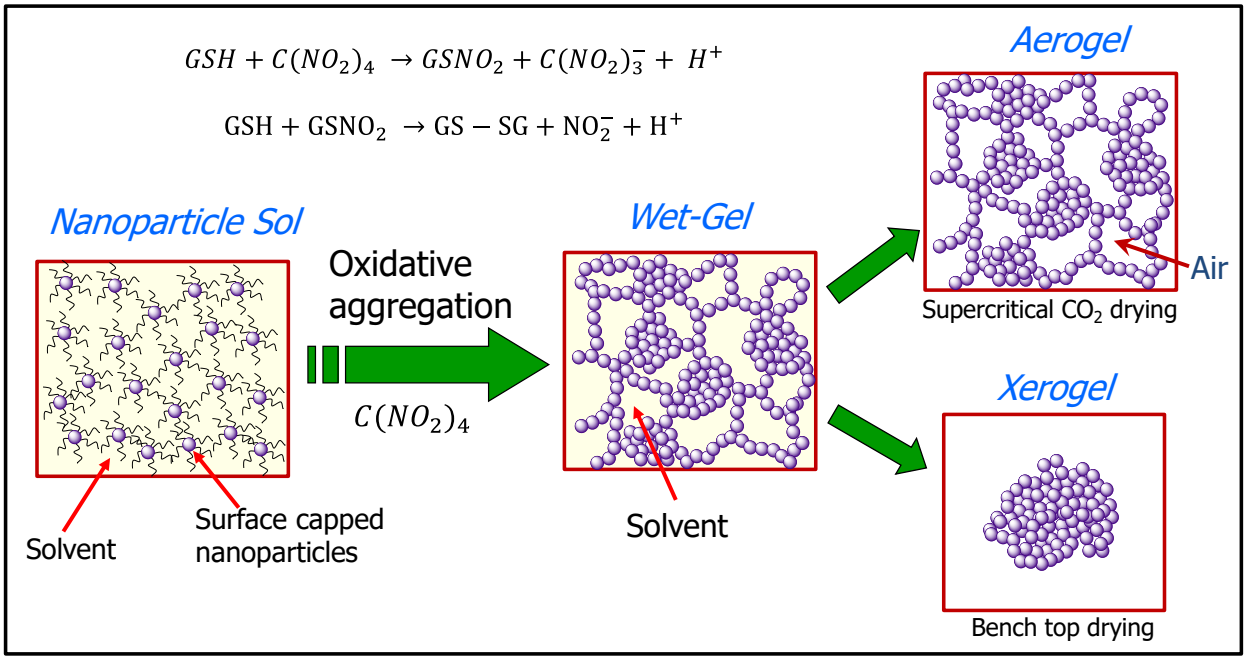

Figure 1.15 A schematic illustration of the NP condensation strategy for the production of semiconductor or metal aerogel and xerogels.

Metal Aerogels

Intriguing physical properties (large surface area, low density, and high porosity) observed in metal-chalcogenide and pinictide based aerogels led researchers to investigate the potential of sol-gel chemistry for the assembly of metal nanoparticles. However, only a handful of efforts on the oxidative self-assembly of metal NPs are reported, including transparent and opaque Ag aerogels[56] and Au−Ag and Pt−Ag heterometallic nanostructures for application in Surface enhanced Raman scattering (SERS).[1d, 57] Further, these studies have not examined the practical applications of metal aerogels in catalysis/electrocatalysis despite their controllable morphology, high surface area, and mesoporosity and ability to produce highly conducting nanostructures. Considering the unique plasmonic properties of noble metal NPs, aerogels derived from such materials may find future applications in nanophotonics, SERS, and catalysis. Very recently our group has reported the assembly of mono metallic Ag hollows and bimetallic Au/Ag[38b] alloy NPs into aerogels via chemical oxidation of surface ligands. Aerogels composed of entirely Ag hollow particles exhibits enormously high surface area (~ 160 m^2/g), extremely low density (0.037-0.041 g/cm^3) and highly porous (2-50 nm) architecture, which makes it promising candidate for SERS based sensing applications.[56] As a continuation of this study, Au/Ag[38b] alloy aerogels were produced and their application as a SERS substrate exhibits signal intensities 10-42 times higher than the precursor Au/Ag alloy NPs. The increased signal intensities for the aerogels are attributed to highly porous gel morphology and enhanced surface roughness.[38b] Although this assembly technique has been fruitfully adapted for mono- and bi-metallic NPs, construction of such superstructures composed entirely of ternary noble metal

NPs has not been reported. Thus, an extension of NP condensation strategy for the oxidative assembly of Au/Ag/Pd and Au/Ag/Pt alloy NPs into large, free-standing aerogel superstructures for electro-oxidation of alcohol is presented in this dissertation research.

1.10 Nanoporous Metal Structures

Nanoporous materials are another class of porous metals that has gained considerable interest from the scientific community.[58] Depending on the pore size distribution they are divided into macroporous (> 50 nm), mesoporous (2-50 nm), and nanoporous (<2 nm) materials.[59] The scientific and technological importance of nanoporous materials are due to their ability to adsorb or interact with atoms, molecules, and ions in their large interior surface and in their nanometer sized pores spaces. Among all porous materials, nanoporous gold (NPG) has been the focus of many electrochemical investigations.[60] A wide variety of method is available to produce NPG,[61] among which templating and dealloying process is the most popular. Dealloying refers to the selective dissolution of one or more components out of an alloy. Although dealloying has been observed in several systems including Cu-Au,[60c] Au-Zn,[62] Pt-Cu,[63] Pt-Si,[64] and so on, most attention has been paid to the dealloying of the prototypical Ag-Au system which results in the formation of NPG. Figure 1.16 shows a schematic representation for the formation of NPG. Generally starting with an Au/Ag alloy, which is treated with an acid solution to dealloy Ag from the structure to result in NPG. Depending on the immersion time of the alloy metal in acid solution, the pore size can be manipulated to generate hierarchical porous morphology. Among many

electrochemical investigations on NPG, the study of residual Ag in the alloy on electrocatalytic properties,[60b] as well as their properties in biofouling solutions[60b] are being the most common investigations.

Recently, Xu et al.[65] reported the extraordinary applicability of NPG in CO oxidation, NO reduction, and oxidation of hydrocarbons. Very recently, Collinson et al. has reported the potentiometric responses of micro-droplet redox compounds on NPG, where high accuracy with very small amount of analyte systems has been investigated.[60d] NPG with excellent thermal stability and chemical inactivity has also been exploited as an attractive substrate for surface enhanced Raman scattering (SERS) because of its large surface area and bicontinuous porous structure in three dimensions.[66]

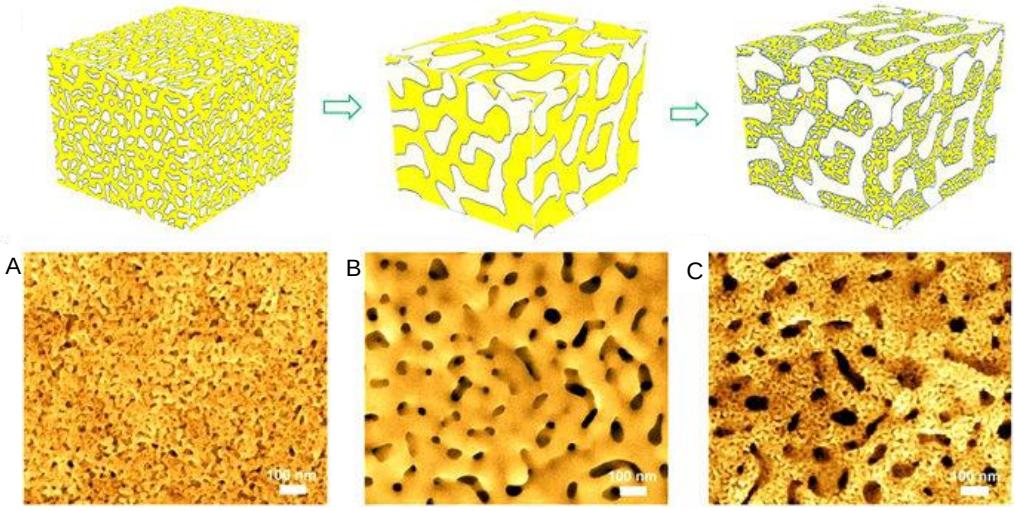

Figure 1.16 Schematic diagram of the fabrication process of three-dimensional hierarchical NPG showing the as prepared nanoporous (a) Au/Ag alloy, (b) coarsened nanoprous Au/Ag alloy, and (c) hierarchial nanoporous gold.[67]

In addition, nanoporous metal foams (NMFs) have also been investigated for biomedical applications.[68] NMFs combines the properties that is characteristic of metals, such as good electrical and thermal conductivity, catalytic activity, and ductility/malleability. The extreme materials properties are characteristic of nanoarchitectures, such as aerogels, which include high surface area, ultralow density, and high strength-to-weight ratio.[68]

1.11 Thesis Statement

Three different goals will be explored in this dissertation research in order to extend the newly developed sol-gel chemistry for efficient integration of inherently similar and dissimilar nanomaterial systems for enhanced optoelectronic and electrocatalytic applications. The first goal is to efficiently couple two chemically dissimilar nanomaterial (CdSe and Ag) systems using sol-gel chemistry to investigate the changes in optical properties of the semiconductors as a function of metal incorporation (Goal 1) and to probe novel radiative decay pathways and potentially tunable photophysical properties achieved in such complex systems. Considering the unique catalytic properties of multimetallic NPs, our second goal is to develop a general methodology for the synthesis of ternary Au/Ag/Pd alloy NPs through GRR, using Ag NPs as a sacrificial template and investigate the potential of oxidative self-assembly to produce porous, conducting gel framework for efficient electro-oxidation of ethanol (Goal 2). The third and final goal is to extend this methodology to produce Au/Ag/Pt ternary alloy aerogels to explore their electrocatalytic efficiency in methanol oxidation fuel cell reactions (Goal 3). The stepwise GRR will be employed to produce Au/Ag/Pt ternary NPs, which will be oxidatively assembled into high surface area, highly porous metallic aerogels.

The extension of NP condensation strategy for the production of hybrid aerogels consisting of metal and semiconductor NPs can lead to novel optical properties due to the potential of integration of excitonic and plasmonic properties of individual components. For instance, as discussed in section 1.3 colloidal semiconductor NPs exhibit size tunable optical properties. Likewise, noble metal NPs, such as Au and Ag NPs, exhibit strong plasmonic absorption features that can be tuned by controlling the shape of particles. The integration of semiconductors with plasmonic metals can potentially couple the high absorption cross section and size tunable optical properties of semiconductor NPs with the LSPR of metal NPs that will lead to efficient light harvesting systems. Although this hybrid system has been studied via different approaches with its limitations (as discussed in section 1.5), coupling of metal and semiconductor via sol-gel assembly has not been thoroughly investigated. A low dimensional network consisting of metal and semiconductor NPs is anticipated to provide the optimal interactions of metal and semiconductor components leading to unique hybrid energy states and potentially novel optical properties (Goal 1).

Our second goal is to develop a new general approach for the synthesis of Au/Ag/Pd alloy nanostructures through stepwise GRR on pre-formed Ag NPs and investigate their sol-gel assembly into porous, conducting gel frameworks for electro-oxidation of ethanol. Recent studies showed higher catalytic activity of Au/Pd alloy NPs toward ethanol oxidation, where the presence of Au has been proven to enhance catalytic activity by selectively oxidizing the poisonous CO to CO_2. The production of highly porous aerogel network using such highly catalytic nanoalloys will not only produce a better catalysts but also provide a facile pathway for tunneling of charge carriers and

small molecules to and from reactive surfaces. Thus, ultra-small Au/Ag/Pd alloy NPs will be produced via galvanic replacement reactions and they will be assembled into ternary alloy aerogels via newly developed sol-gel method. The in-situ generated HNO_3 (produced as a byproduct) will be utilized to dealloy the remaining Ag from the ternary alloy aerogel structure to potentially generate Au/Pd alloy aerogels, which will be the ideal catalysts for ethanol oxidation (Goal 2).

Following the synthesis of Au/Ag/Pd alloy aerogels, our third and final goal is to produce Au/Ag/Pt alloy aerogels to investigate its electrocatalytic activity towards methanol oxidation. Strong adsorption of OH^- or CO species on Pt based catalyst has been shown to reduce the catalytic activity of Pt towards methanol oxidation. This will be addressed by alloying Pt with Au and Ag metal to produce ternary Au/Ag/Pt NPs. Depending on the reduction potential, a stepwise GRR will be utilized to produce Au/Ag/Pt alloy NPs which will then be assembled into ternary alloy aerogels. Direct cross linking between the ternary NPs is expected to result in a highly crystalline gel network that can potentially enhance the electrical conductivity. Alloying effect and self-supporting nature of the ternary aerogel can mitigate the catalyst poisoning, agglomeration, or support corrosion, which will preferentially make them an efficient electrocatalyst. Thus, Au/Ag/Pt alloy aerogels will be produced and tested for electro-oxidation of methanol (Goal 3).

Chapter 2

Experimental Methods in Material Characterization

Several characterization techniques are required to obtain a full understanding about the structural, optical and physical properties of nanomaterials. In addition to these techniques, hydrogels and wet gels produced via oxidative assembly need to be dried under supercritical conditions to produce monolithic aerogels. Both metal and semiconductor NPs and aerogels produced in this dissertation research were characterized through UV visible absorption and photoluminescence spectroscopy to investigate the optical properties; powder X-ray diffraction to determine the phase purity and crystallinity; transmission electron microscopy to obtain the size distribution and morphology; scanning transmission electron microscopy and energy dispersive spectroscopy and inductively coupled plasma optical spectrometry to determine the elemental composition and distribution; X-ray photoelectron spectroscopy to evaluate the chemical states of surface atoms; surface area and porosimetry to investigate the surface area and to porous architecture. Moreover, electrocatalytic properties of resultant nanostrctures were investigated via cyclic voltammetry and Chronoamperometry. Chapter 2 of this dissertation will discuss the above mentioned experimental methods.

2.1 Aerogel Production via Supercritical Drying

Production of monolithic and crack free aerogels from wet-gels and/or hydrogels is a critical step in the processing of metal-semiconductor nanostrctures.[42b] Supercritical

drying (SCD) is a unique technique, which allows the complete removal of solvents from a wet-gel to produce a highly porous aerogel material.[42b] The supernatant around the wet-gel (acetone/water) during the sol-gel transformation process creates a heterogeneous environment that enhances the surface tension in the liquid phase and pulls against any solid structure it is in contact with. Allowing the solvent to evaporate on bench top will result in a significant collapse of the uniquely porous wet-gel architecture due to distraction enforced by capillary forces upon evaporation of the solvent. During SCD, when a liquid is heated in a closed vessel, its density decreases while the pressure and density of the vapor being formed increases.[42b] As the heating proceeds, liquid and vapor densities become closer to each other until the critical temperature and pressure (critical point) are attended, at which point densities of both phases become equivalent and the gas/liquid phase boundary disappears. Above the critical point, a single uniform phase is developed, called as a supercritical fluid (Figure 2.1). Thus, the SCD technique is known to conserve the high porosity of a wet-gel, because the pore liquid can be removed without catastrophic collapse due to capillary forces.[42b]

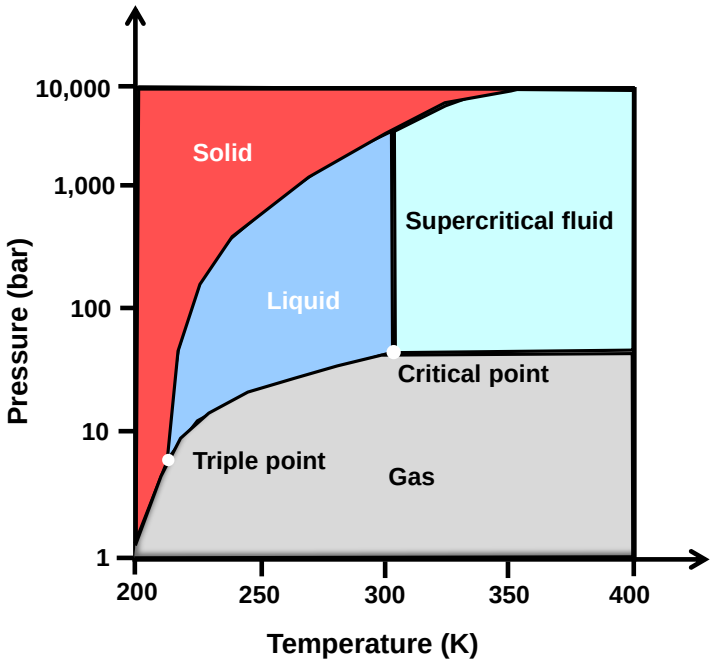

Figure 2.1 Phase diagram of CO_2 elaborating the temperature and pressure effect.

CO_2 supercritical drying (cold SCD) is a very well-known technique that has been employed to create a wide range of aerogels. In general, cold SCD involves placing wet gels in a critical point dryer which is filled with liquid carbon dioxide at near room temperature (292 K) and moderate pressure (750 – 1000 bar). Liquid CO_2 is then circulated through the vessel 3-4 times over a time period of 12-24 h for complete removal of the wet-gel solvent (acetone or methanol). The exchanged gels are slowly heated to 313 K (above the critical temperature of CO_2) to form a supercritical fluid (Figure 2.1). As the vessel is heated, the pressure of the system rises and adjusted to 1200-1400 bar to maintain a pressure slightly above the critical pressure of CO_2 (1050 bar). The system is left under these conditions for 18-30 min to assure the complete formation of a supercritical fluid. Monolithic aerogels are formed by slow removal of the supercritical fluid over a time period of 30-40 min while maintaining the temperature at

40º C. In this research, a SPI-DRY model critical pointer dryer was used to produce monolithic metal and metal-semiconductor hybrid aerogels.

2.2 Powder X-ray Diffraction

Powder X-ray diffraction is one of the basic characterization tools to identify the crystal structure, phase, and the crystallinity of a material. X-rays are the electromagnetic radiations with high penetrating power and short wavelength (0.1-100 Å), which are emitted from a target metal (Mo, Cu, Fe, Cr, Co) when it is bombarded with high energy electrons (Figure 2.2). These electrons have the capability to knock out the tightly bond electrons in the K or L electronic shell of the target (Figure 2.3). The low-energy empty levels are then filled by falling back of the electrons from higher energy levels to the inner levels and the energy will be liberated during this process in the form of X-rays. If the L electrons are falling back to fill the empty level, the generated X-ray is known as Kα, whereas electrons falling from M energy level is known as Kβ X-rays. Thus the wavelength of the emitted X-rays is dependent upon the energies of the two levels involved and is characteristics of the element. When X-ray radiation is exposed to crystalline materials having ordered arrays of atoms or molecules, diffraction takes place. The diffraction pattern of a crystalline material is unique for a specific phase of the material; hence PXRD is an excellent technique for the fingerprint characterization of crystalline materials and the determination of crystal structure.

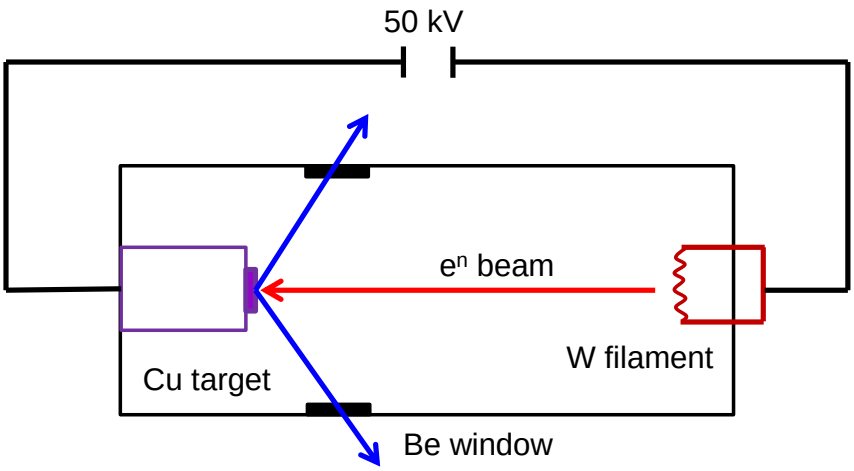

Figure 2.2 Schematic diagram of an X-ray generator tube.[69]

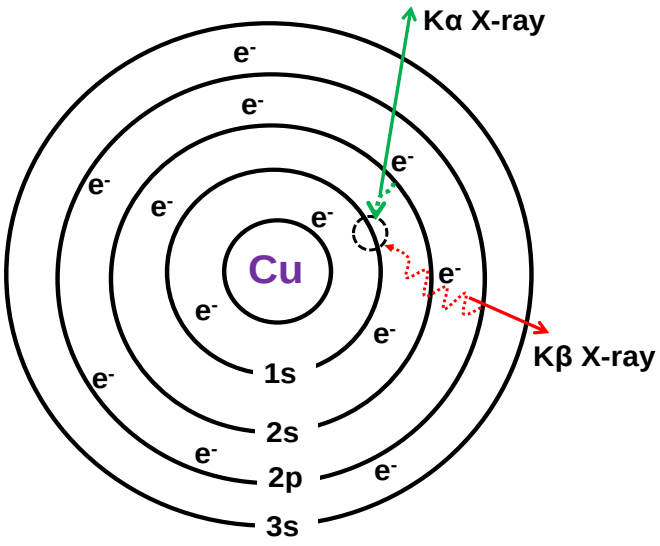

Figure 2.3 An illustration of the formation of Cu Kα radiation, which results from the ionization of 1s electron, and 2s or 2p electron is replacing the vacancy in the 1s shell releasing energy as X-rays.

The X-ray radiation used for most crystallographic studies should be as nearly monochromatic as possible and should have appropriate wavelength. The Kα line of Cu target fulfills this requirement and is the primary choice for powder diffraction analysis,

whereas the less intense Kβ radiation is filtered by the element with atomic number less than (Z-1 and Z-2) target element (most commonly by Ni in case of Cu target). When a powdered crystal sample is placed in a monochromatic X-ray beam, the X-rays are generally scattered from the lattice planes at an angle equal to the incident beam.

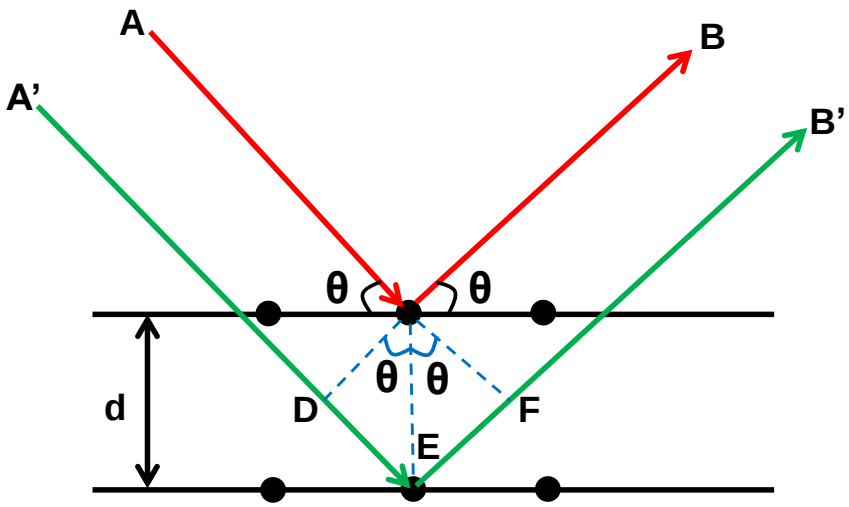

Figure 2.4 Diffraction of X-rays from parallel crystal planes.

Figure 2.4 shows a beam of X-rays falling on the crystal surface. Two successive atomic planes of the crystal are shown separated by a distance d. When the X-rays of wavelength λ strike the first plane at an angel θ, some of the X-rays will be reflected at an angle similar to incident angel from the first plane and some will penetrate and get reflected from the second plane at a same angle. If both beams reflect elastically at an angle equal to incidence it is clear that A'B' will travel further than AB. Depending on how much father A'B' travels it can end up in-phase or out of phase with AB. When the distance traveled by both X-rays is in phase, the amplitude of the wave increases. When the rays are out of phase the amplitude decreases, in some cases resulting in

complete destructive interference such as when d is equal to ¼ of the wavelength of the X-rays. Only when AB and A'B' are in phase the scattering of the X-rays is considered a diffracted beam. Knowing the conditions which lead to coherent diffraction allows to apply the Bragg Law (equation 2.1).

$$2d \sin\theta = n\lambda \quad \ldots\ldots\ldots\ldots\ldots\ldots\ldots (2.1)$$

For a crystalline powdered sample, the crystals are oriented in different directions. However, only those constructively diffracted beams will give rise to the pattern formation which will satisfy Bragg's equation. The position of the diffracted peaks (2θ) depends on the atomic composition and atomic position in a unit cell whereas the intensity of the peak depends on the size and shape of unit cell.

PXRD patterns of nanocrystalline materials are typically board in comparison to bulk single crystalline materials. This has been attributed to significantly smaller number of lattice planes present in confined nanostructures in contrast to bulk materials. As a result, the diffraction from a nanocrystalline material results in incomplete cancellation of the partially interfering waves leading to the broadening of the Bragg reflections. This broadening is indirectly proportional to the crystallite size, thus helps to estimate the crystallite radii of the material (t), as shown in Scherrer erquation[70] (Equation 2.2),

$$t = \frac{0.9\,\lambda}{\beta \cos\theta} \ldots\ldots\ldots\ldots\ldots\ldots\ldots (2.2)$$

where β is the full width at half maximum in radians, θ is the Bragg angle and 0.9 is a constant. This formula provides an average value for the crystallite size which may vary from the chromophore or primary particle size obtained from UV visible or transmission

electron microscopy studies due to the presence of surfactant or amorphous core on the NP surface.

In this study, A Philips X'Pert system equipped with a Cu Kα radiation (λ = 1.5418 Å) was used to record powder X–ray diffraction (PXRD) patterns of all samples. The crystallite sizes were estimated by employing Scherrer equation,[70] after making appropriate corrections for instrumental broadening using a Si standard. The powder samples are prepared by depositing on a low background Si holder. The X-ray diffraction patterns of powder samples were compared with International Centre for Diffraction Data (ICDD) powder diffraction file (PDF) database for identification of crystal phases.

2.3 Electron Microscopy

Electron microscopy is a very well-known technique for obtaining morphological and structural information of nanomaterials. Generally, electron microscopes use a beam of highly energetic electrons to examine materials on the micrometer to nanometer scale. When a material is bombarded with high energy electron beam, several electronic excitations occur, providing a number of different avenues to garner vital information on material's characteristics (Figure 2.5).

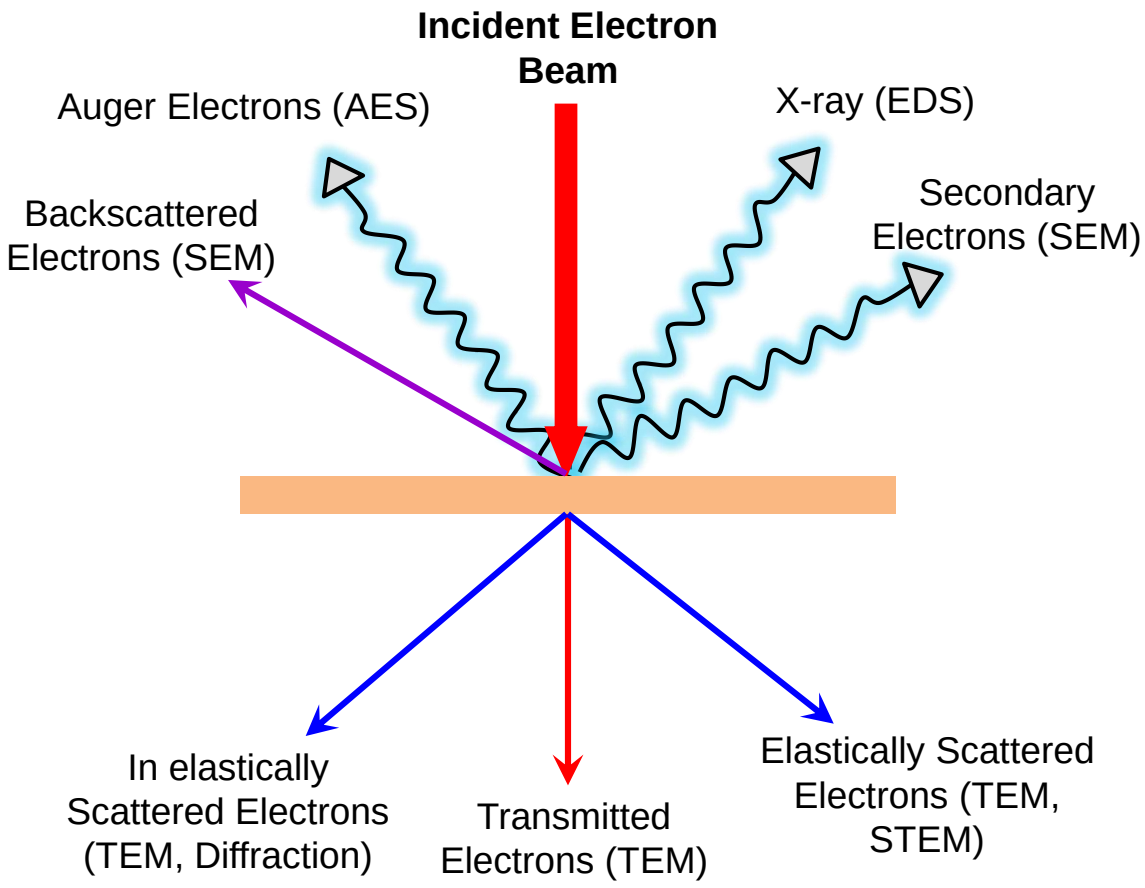

Figure 2.5 A schematic illustration of possible interactions of a highly energetic electron beam with a material.

Secondary electrons ejected from a sample are used in scanning electron microscopy (SEM) to study the texture, topology and surface features of the materials.[71] Additionally, most SEM instruments include an energy dispersive spectroscopy (EDS) unit, which provides semi-quantitattive information about the elements present in the sample. The transmitted electrons are analyzed in transmission electron microscopy (TEM) to provide information about the morphology (size and shape) of the sample as well as crystallographic information. Electron microscopy techniques were widely used in this dissertation research and are discussed in detail in the following sections.

2.4 Scanning Electron Microscopy/Energy Dispersive Spectroscopy (SEM/EDS)

SEM/EDS is one of underlying techniques to study the surface morphology and elemental composition of a material. SEM provides topographical information about a sample using the secondary electrons that are being generated while the sample is bombarded with a high energy electron beam.[71] Typically, SEM uses a tungsten filament or a LaB_6 crystal as the electron gun, and the electrons are accelerated through a voltage of 25-50 keV before striking the sample.[72] Secondary electrons are produced mainly from the inelastic interactions between the incident electron beam and weakly bound conduction band electrons in metals, or the valence electrons of insulators and semiconductors. The incident electron beam transfers a fraction of its energy to the valance electrons of a specimen, enabling some of the electrons to overcome the work function and escape. Due to the inefficient energy transfer, the secondary electrons will have low kinetic energies (2-5 eV). The slow moving secondary electrons are attracted towards a detector which is positively charged. These attractive forces allow the detector to collect secondary electrons from a wide area of the sample, including corners and edges, and provide a 3-dimensional imaging of the sample. SEM imaging requires the sample to be conductive to avoid charge build up on the surface of the specimen upon bombardment. Typically the image resolution below 0.5 μm is hard to achieve with SEM imaging, hence this technique is more suitable for studying micrometer scale surface features.

When a material is bombarded with an electron beam, X-rays are produced as the incident beam ionizes the inner shell electrons of atoms as shown in Figure 2.3. These X-rays have characteristic energies or wavelengths correspond to the elements present

in the sample.[71] Hence, identification and quantification of the elements is possible by scanning the energies of the emitted X-rays and counting the number of photons emitted corresponds to each energy or wavelength. The limitations of EDS are based on the energy of the incident electrons, range of the detectors, and spectral overlap. In this study, dried powder samples were spread on a conductive carbon tape attached to an aluminum stub and the EDS measurements were performed in a Hitachi SU-70 running at 20 keV accelerating voltage and averaged over five separate areas.

2.5 Transmission Electron Microscopy (TEM)

The electron source in a TEM is basically the same as in an X-ray tube (Figure 2.2). Typically, a tungsten filament is heated up with high voltage (80-400 kV) under vacuum to generate the flow of electrons, which then focused through a series of magnetic lenses to directly probe a sample.[73] The accelerated high energy electron beam is exposed to the sample and the transmitted portion is focused and magnified by a set of electromagnetic lenses into an image. TEM has higher resolution (0.1 – 10 nm) than SEM, and is an excellent technique to study the nanomaterials. The disadvantages to this method lay in sample thickness and attenuation coefficients of elements. To provide the best possible contrast the sample holder needs to be incredibly thin with a low electron cross section, in most cases, a thin carbon film from 3-30 nm supported by a copper mesh is sufficient for this purpose.

By changing the focus of the beam, it is possible to detect scattered and diffracted electrons that provide selected area electron diffraction (SAED) patterns and useful information of the crystal structure. Since the sample is being bombarded with high

energy electrons, some of the atoms will undergo excitations and emit X-rays in the same manner they are produced in X-ray tubes.[73] The X-rays produced are unique to each element and can be used to a determine composition using an integrated EDS detector. Some electrons are backscattered or reemitted from the sample which are typically not used in a TEM but are important for SEM. Multiple TEM instruments have been used in this study to acquire basic imaging, HRTEM, and elemental maps. A Zeiss Libra 120 and JOEL JEM-120 was utilized to acquire low resolution images at 120 kV. Elemental maps were acquired with a FEI Titan 8300 microscope equipped with a Gatan 794 multiscan camera operating at 200 kV. HRTEM was conducted on a separate FEI Titan 8300 electron microscope operating at 300 kV. All samples were prepared by dropping a dilute solution of aerogels dispersed in ethanol onto an ultra-thin carbon coated Cu TEM grid after the removal of the Formvar layer.

2.6 X-ray Photoluminescence Spectroscopy (XPS)

XPS is another powerful analytical technique to determine the surface elemental compositions of materials, and it is often called Electron Spectroscopy for Chemical Analysis (ESCA). Nanocrystalline materials are famous for their larger surface to volume ratios (40-60 % is the surface atoms). XPS is one of the most sophisticated surface characterization techniques that not only provides information on atomic composition but also determines the oxidation state of the elements, and bonding environment of a material. Although XPS is primarily a surface technique, which has a penetration depth around 5-10 nm, it can provide both the surface and bulk atoms information of smaller crystals (2-5 nm). In XPS an X-ray tube (Figure 2.1) is used as a source of X-rays to bombard the sample surface, where the X-rays interact with atomic

electrons of the sample and they can be ejected as photoelectrons. The energy required to eject an electron is equivalent to the electrons binding energy allowing for differentiation of elements, atomic orbitals, and chemical environment. A high level of vacuum is necessary for XPS to ensure accurate measurements. The stray gaseous molecules can produce interfering signal as well as can contaminate the substrate surface and more importantly attenuate the X-rays reducing the overall sensitivity of a measurement.[74] The requirement of ultra-high vacuum has driven the design of XPS instruments. Sample are loaded through a preparing chamber which pumps samples down in order to make sure any outgassing of the sample does not contaminate the analysis chamber (Figure 2.6).[74] The analysis chamber is kept under a constant level of ultra-high vacuum, however is equipped with certain extra items such as ion beams for etching and Ar flow for charge control. The X-ray source of choice is typically Al Kα due to its production of high energy and narrow line width. The high-energy nature of the photoelectrons being analyzed requires a method to adequately resolve closely spaced peaks and maintain sensitivity. The hemispherical analyzer is able to switch between the desired effects though variable voltage which will affect the path length of the electron for detection. In the following dissertation XPS measurements were performed with a Thermofisher ESCALAB 250 equipped with Al Kα source. The pass energy was 20 keV and an average of 30 scans was used. Dried nanocrystal powders were pressed onto indium foil and taped to an aluminum sample holder with conductive carbon tape. Charge correction was carried out with adventitious carbon and double checked against indium. Curve fitting was done using the Avantage XPS software for simple peaks the software database with used to determine spin coupling and peak widths. For

overlapping peaks an online database was consulted and the spin coupled peak of the overlapped peak was set at defined shape and the peak ratios used to determine the overlapping peaks. The Software uses an automated iteration process to optimize peak fits. And peak fits were performed with Themo Advantage software, utilizing a simple Gauss−Lorentz (GL) product function with smart background selection.

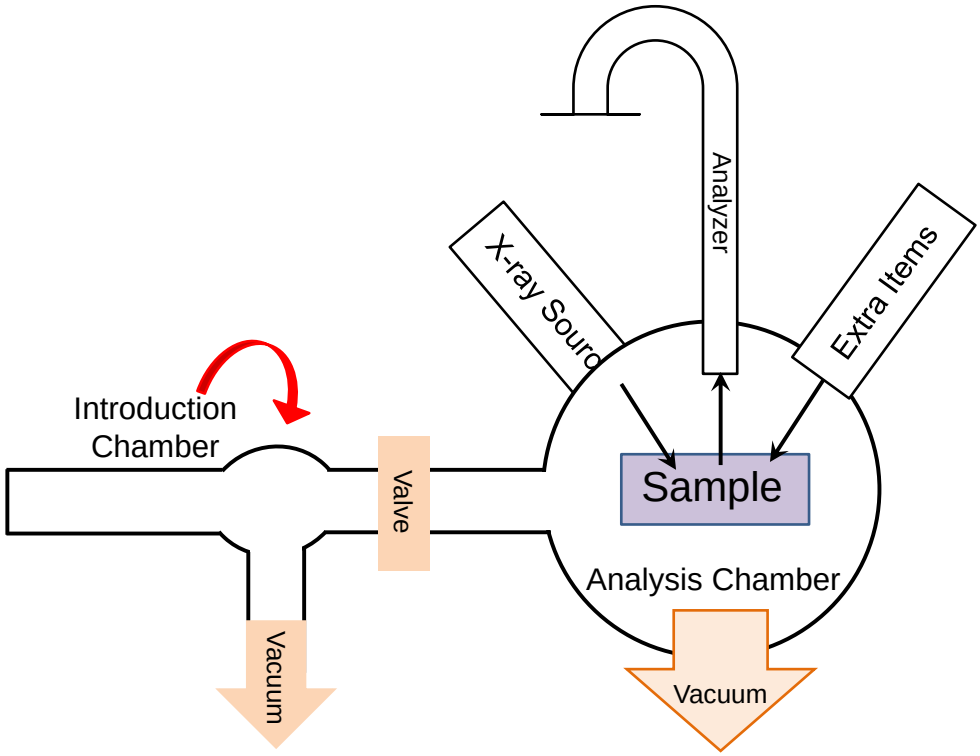

Figure 2.6 A schematic diagram of X-ray photoelectron spectrophotometer with a spherical hemisphere.

2.7 UV-visible Absorption Spectroscopy

Among all analytical techniques, UV-vis absorption spectroscopy is one of the oldest and most popular techniques used to investigate the optical properties of compounds under the influence of photon energy. For solution absorption spectroscopy, compound

molecules are dissolved in an optically transparent solution. When ultraviolet or visible light passes through these molecules, part of this energy is absorbed and part is transmitted through solution. The transmitted part can be detected and is mathematically transformed to determine the absorbance of the solution. The intensity of the absorption is directly proportional to the concentration of the analyte (c), the molar absorptivity (ε) and path length (l) of the sample holder according to Beer-Lambert law,

$$A = \in cl \ldots\ldots\ldots\ldots\ldots\ldots\ldots\ldots\ldots\ldots 2.3$$

In semiconducting materials, the absorption of light results in an electronic transition from the valence band to the conduction band, and the photon energy absorbed is equal to the band gap of the material. Quantum confined nanomaterials exhibit size and shape dependent absorption maxima and onsets that are blue shifted relative to the bulk materials. This blue shift increases with decreasing primary particle size as a result of increasing the confinement energy.

In this thesis study, UV-visible absorption spectroscopy was utilized to examine the size-dependent absorption properties of the semiconducting NCs and also the plasmonic absorption of metal NPs. Typically, the thiolate functionalized chalcogenide NCs or colloidal metal NPs were dispersed in a polar medium (H_2O) and loaded into a quartz cuvette (10 cm) prior to analyze. All solution absorption spectra were collected by a Cary 6000i UV–vis–NIR spectrophotometer (Agilent Technologies) equipped with tungsten and deuterium lamps. Instrumental parameters such as slit width and cell path length were kept constant through all experiments. Figure 2.7 illustrates a typical set up of an absorption spectrophotometer equipped with a photodiode array detector.

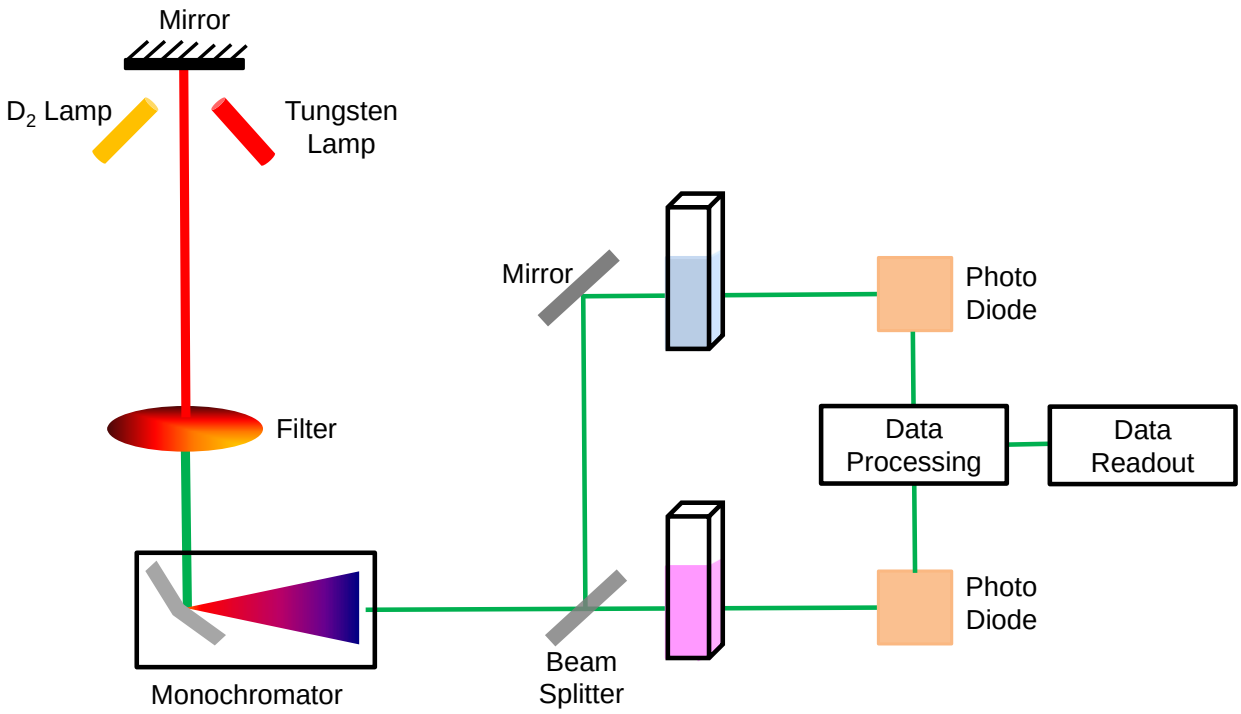

Figure 2.7 A simple schematic diagram of a typical double beam UV-Vis spectrophotometer utilizing Tungsten and Deuterium sources and a PDA detector.

2.8 Diffuse Reflectance Spectroscopy

Similar to UV-Visible absorption spectroscopy, diffuse reflectance spectroscopy analyzes the reflectance of light from a sample instead of transmittance.[75] Reflectance spectroscopy is commonly used to study the reflectance and absorption properties for the insoluble solids and nontransparent samples. When light interacts with a solid powder scattering in the form of reflectance and diffraction will occur in addition to absorption. The reflected light is recollected and can be evaluated by the Kubelka-Munk remission function (equation 2.4).[76] The percent reflectance (R) is equated to a form of

a pseudo-absorption coefficient (K/S) with this method, similar to that obtained through transmission experiments.[76b]

$$(1-R)^2/_{2R} = k/s \ldots\ldots\ldots\ldots\ldots\ldots\ldots\ldots\ldots 2.4$$

where, R is the percentage reflectance, k is the absorption coefficient and s is the scattering coefficient and the $(1\text{-}R)^2/2R$ function is defined as the Kubelka-Munk remission function.[77] In a typical reflectance measurement, the photons that are reflected are collected by a spherical mirror (integrating sphere) and focused onto the detector. This spherical mirror is coated with a 100 % reflecting material to ensure no energy loss or reflectance due to the redirection of reflected light onto the detector. In this study energy-gaps were estimated by linear extrapolation of the absorption onset to the baseline. The NCs were dispersed in a non-absorbing medium ($BaSO_4$) so that scattering is minimized. Measurements were performed with a Cary 6000i UV-Vis-NIR spectrometer (Agilent) equipped with an internal DRA 2500 integrating sphere.

2.9 Photoluminescence Spectroscopy

Photoluminescence (PL) spectroscopy is a very well-known technique for the analysis of the electronic structure and photophysical properties of semiconductor NCs. The principle of this technique is based on the emission of light from a substance due to the radiative recombination of excited electron and hole. Depending on the electronic states, PL can be further classified into fluorescence and phosphorescence.[7812] Typically, there a number of rotational and vibrational energy states are related to this electronic transitions. An excited electron can travel through these vibrational and

rotational states before falling back to the ground level. When an electron is excited from the ground state (S_0) to the first excited state (S_1), the relaxation of the electron from S_1 back to S_0 through the release of a photon is known as fluorescence (Figure 2.8). On the other hand, phosphorescence is a longer lived emission process (10^{-4} to 100 s) than fluorescence (10^{-8} to 10^{-4} s) and occurs when the excited electron undergoes intersystem crossing from the excited singlet (S_1) to an excited triplet state (T_1) before relaxing back to the electronic ground state (S_0).[78] In general, the emission band is red shifted compared to the absorption band as a result of non-radiative relaxations of the excited electrons within the vibrational levels, commonly known as the Stokes shift.[79] In this dissertation, a Cary Eclipse (Agilent) florescence spectrophotometer with 5 nm excitation and emission slits was used to investigate the emission properties of semiconductor NCs and metal-semiconductor hybrid aerogels.

To probe size and composition dependent optical properties, carrier dynamics and fine structure of energy gaps, TRPL measurements of quantum confined NCs were used.[80] A complete understanding about the energy levels and excitonic behavior is advantageous in the design of semiconducting devices. Basic steady state measurements only provide glimpse into the photoluminescence properties. Ultra-fast spectroscopy can be employed for time resolved measurements. When combined with temperature and excitation density studies it is possible to develop a comprehensive understanding of light-mater interactions in NCs. In this study, semiconductor NCs and aerogel samples were pressed between two glass slides with minimal amount of adhesive, excited with a Ti:sapphire laser at 385 nm wavelength and PL spectra were acquired with a liquid N_2 cooled charge coupled device (CCD) camera. Temperature

was controlled with liquid helium cooled cold finger and time resolved measurement were collected with a Hamamatsu streak camera with 25 ps temporal resolution.

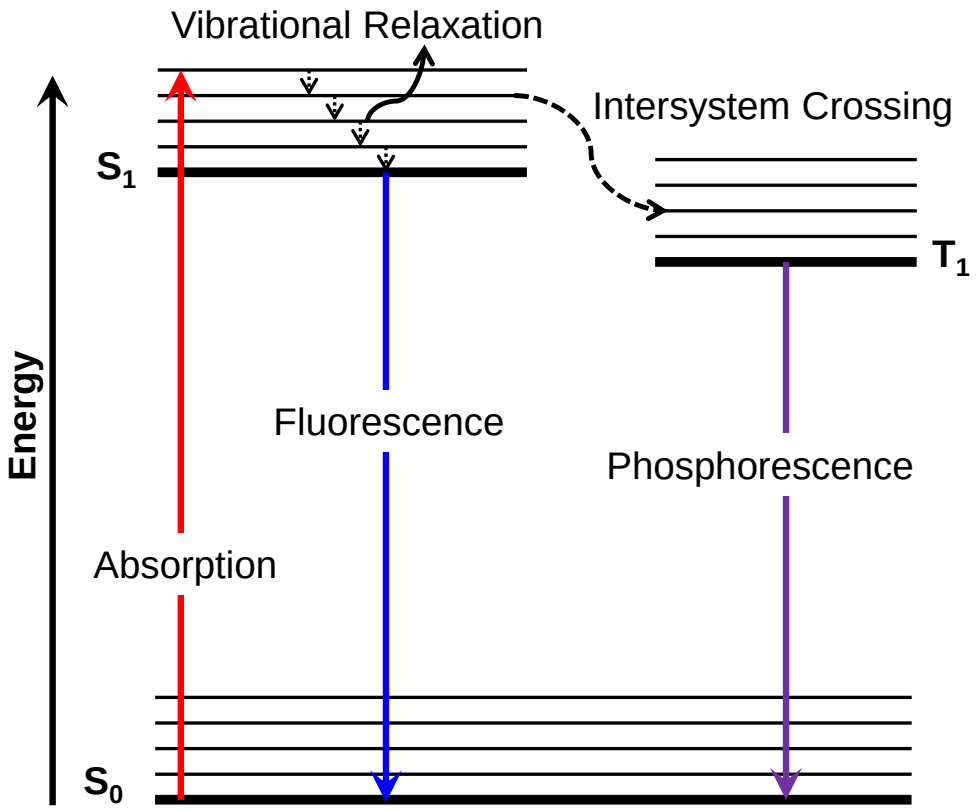

Figure 2.8 A schematic illustration of absorption followed by fluorescence and phosphorescence processes in semiconductor NPs and corresponding aerogel materials.

2.10 Inductively Coupled Plasma – Optical Emission Spectroscopy

One of the most versatile and accurate technique for determination of elemental composition is the inductively coupled plasma optical emission spectroscopy (ICP-OES). The ICP-OES has the ability to detect multiple elements accurately at very low

concentrations due to its high sensitivity.[81] This instrument usually operates based on spontaneous emission of photons from the atoms and ions in the samples.[81] Liquid and gaseous samples are introduced into ICP-OES by injection whereas, the solid samples require an acid digestion.[81] CdSe/Ag, Au/Ag/Pd, and Au/Ag/Pt aerogels were digested in 8 % nitric acid and in aqua rigia ($HCl:HNO_3$), respectively. The digestion was prepared approximately 1 ppm which was further diluted to 10 mL solution and finally introduced to the ICP-OES. The analyte solutions were converted in to aerosols when introduced to a channel of plasma. The core temperature of the inductively coupled plasma is nearly 10,000 K and the aerosols are swiftly vaporized.[81] The vaporized atoms gain energy by colliding with plasma imparts and converts them to ions. Thereafter, the ions continue to collide, and promotes their electrons to the excited states. Both excited atoms and ions relaxes down to the ground state by emitting photons.[81] The concentration of the originating element in samples are directly proportional to the total number of photons.

In this dissertation, all the standards (Au, Ag, Pd, Pt, Cd, Se) were purchased from Inorganic Ventures and was diluted accordingly to prepare different dilution to obtain the calibration curve. ICP-OES analyses were performed with a Varian VISTA-MPX instrument. The elemental composition of the aerogels was obtained by monitoring 5 wavelengths per element and the average compositions are presented.

2.11 Surface Area Analysis: Nitrogen Adsorption-Desorption Isotherm

Study of the gas sorption provides insightful information about the surface characteristics of solid samples such as surface area, porosity, and chemical reactivity.

Depending on the interaction between gas molecules (adsorbate) and the solid surface, it can be either chemical adsorption (chemisorption) or physical adsorption (physisorption). In chemisorption the adsorbate and adsorbant are attracted via valence forces (chemical bonds). On the other hand, physisorption is the adsorption process in which the forces involved are intermolecular forces (Van der Waals forces).[82] While chemisorption is known to change the electronic structure of the adsorbant and adsorbate, physisorption does not involve a change in the electronic structure.

In order to remove moisture and other volatile substance from sample surface prior to the gas sorption experiments, surface cleaning (degassing) is often carried out by placing a solid sample in a glass holder and heating it under vacuum.[82] Once degassed, the sample is brought to a constant temperature by means of an external bath (liquid N_2, 77 K). When a chemically inert gas (N_2 or He) is used as the adsorbate, the solid starts to physisorb the gas, leading to a decrease in gas pressure in the sample chamber. The amount of gas adsorbed at 77 K can be calculated by applying the gas laws considering the pressure change, volume of the tube and the mass of the adsorbant. At constant temperature, the variation of the amount of gas adsorbed with the pressure of the adsorbate is called the adsorption isotherm.[82] In general, adsorption isotherms are expressed as the volume of gas adsorbed (cm^3/g) vs. the relative pressure (P/Po), where P and Po are the equilibrium and saturation pressures of the adsorbate. Typical gas sorption isotherms consist of several distinguishable regions as shown in Figure 2.9.[82] Once the gas is introduced to the sample chamber at a very low relative pressure, micropore (< 2 nm) filling occurs (section A, Figure 2.9). With increasing relative pressure, gas molecules tend to form a monolayer of adsorbate on

the sample surface (section B, Figure 2.9). After reaching the full monolayer coverage, multilayer adsorption occurs, leading to filling of mesopores (section C, Figure 2.9) (2-50 nm) and macropores (> 50 nm). At high relative pressures, the gas condenses into a liquid due to the phenomenon of capillary condensation (section E, Figure 2.9). In general, the adsorption/desorption isotherms can be classified into 6 categories depending on the shape of the adsorption and desorption branches, namely Type I through VI (Figure 2.10).[82] Differences in rates of the pore liquid filling and emptying give rise to hysteresis loops in the adsorption/desorption isotherms. The shape of the hysteresis loops reveals information about the types of pores that are present in the material, and can be categorized into 4 types, H1-H4 as shown in Figure 2.11.[83]

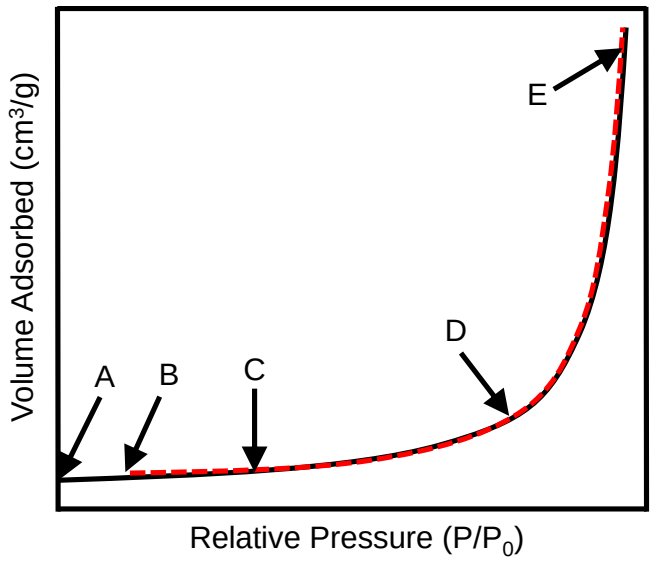

Figure 2.9 A general representation adsorption (black)/desorption (red) isotherm of a porous solid exhibiting the distinguishable areas of the adsorption branch. A-micropore filling, B-monolayer coverage, C-multilayer adsorption, D-onset of pore filling, E-capillary condensation.

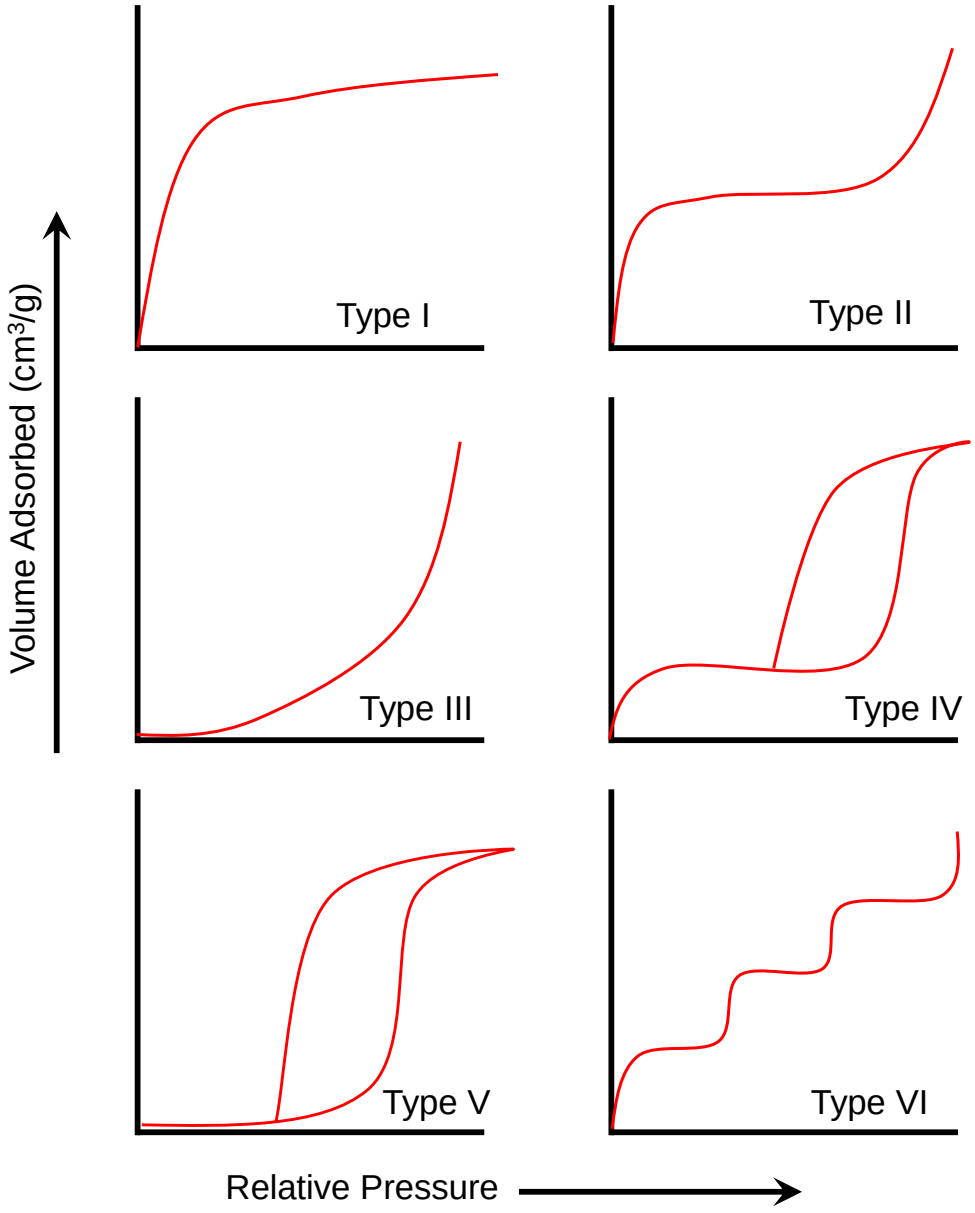

Figure 2.10 Six different types of adsorption/desorption isotherms.

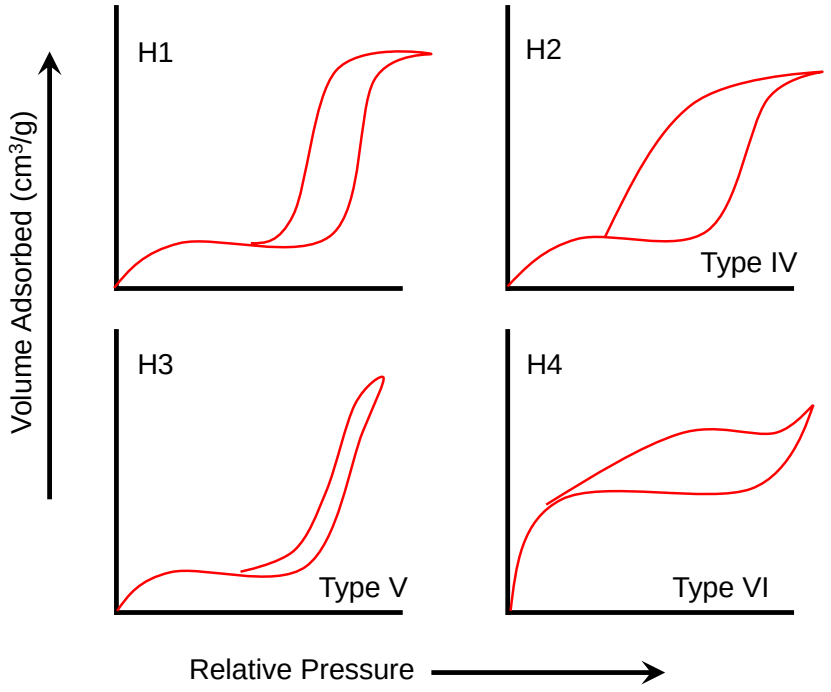

Figure 2.11 Four basic types of hysteresis loops.[83]

The surface area and pore size distributions are obtained by applying theoretical models to the adsorption/desorption isotherms. In general, chemisorption studies are modeled by Langmuir theory, assuming monolayer adsorption of the adsorbate, and this is useful for studying microporous materials.[82] Brunauer, Emmett, and Teller (BET) theory incorporates multilayer formation of adsorbate on solid samples, and useful for studying the surface characteristics of mesoporous materials.[83] BET theory collects information from the monolayer adsorption region of the adsorption isotherm to calculate the surface area of a sample using the BET equation (Equation 2.5),

$$\frac{P}{V_a(P_o - P)} = \frac{1}{V_m C} + \frac{C-1}{V_m C}\left[\frac{P}{P_o}\right] \ldots\ldots\ldots\ldots\ldots\ldots\ldots 2.5$$

where P and Po are the equilibrium and saturation pressure of the adsorbate, Va is the volume of gas adsorbed at a given relative pressure (P/Po), Vm is the volume of gas

required for monolayer coverage and C is a constant. According to Equation 2.5, a plot of P/[Va(Po–P)] vs. P/Po should be a straight line and the Vm and C values can be calculated from the slope and intercept, respectively.[82] Monolayer coverage (Vm) can be mathematically converted to number of moles or molecules of the adsorbate, and the surface area of the material can be calculated by using the molecular cross section of the adsorbate.

Average pore diameters, pore size distributions, and cumulative pore volumes are calculated by applying the Barrett, Joyner, and Halenda (BJH) model. The BJH model uses the Kelvin equation (Equation 2.6) to calculate the pore size distribution considering that the pore filling and emptying occurs in a stepwise manner. This equation describes the change of vapor pressure over a liquid curved with a radius *r* by, equation 2.10,

$$\ln\left[\frac{P^*}{P_o}\right] = -\left[\frac{2\gamma\mu\cos\theta}{R\,Tr_m}\right] \ldots\ldots\ldots\ldots\ldots\ldots\ldots 2.6$$

where P* and Po are the critical condensation and saturation pressure, γ is the surface tension of the liquid, μ is the molar volume of the condensed adsorbate, θ is the contact angle of the solid and the condensed phase, r_m is the mean radius of curvature of the liquid, R is the ideal gas constant and T is the absolute temperature.[82] The amount of gas desorbed during the step-wise desorption represents the volume of pores being emptied. THe BJH model calculates the variation in the number of layers (or thickness) of adsorbate at a given step to calculate the pore volume. Therefore, the mean radius of curvature of the liquid (r_m) can be modified by r-t, where r and t are the pore radius and thickness of the adsorbate, respectively. The thickness of the adsorbed layers

remaining on the pore walls at a particular relative pressure can be calculated from Equation 2.7,

$$t = \left[\frac{A}{B - \log_{10}(P/P_o)}\right] \ldots\ldots\ldots\ldots\ldots\ldots 2.7$$

where, A and B are the slope and intercept of the plot of $\log_{10}(P/P_o)$ vs. 1/Va.[82]

In this dissertation, The N_2 adsorption/desorption isotherms were acquired using a Micromeritics ASAP 2020 surface area and porosimetry analyzer at 77 K. All samples were degassed under vacuum at 50°C for 24 h prior to the analysis. The isotherm data were fit using the BET model to calculate the surface area values. The average pore diameters and cumulative pore volumes were obtained by applying the BJH model to desorption branches of the respective isotherms.

2.12 Cyclic Voltammetry (CV)

Cyclic voltammetry (CV) is a simple and most versatile electroanalytic technique for the study of electroactive species. It offers a promising and fast approach to determine the formal potentials of an redox species.[84] In CV, a working electrode immersed in an unstirred solution is subjected to a linear sweep of potential in a cyclic manner while measuring the resulting current. The potential of the working electrode is measured with respect to the reference electrode (such as saturated calomel electrode (SCE), silver/siver choloride (Ag/AgCl)).[85] A typical cyclic voltammogram is shown in Figure 2.12.

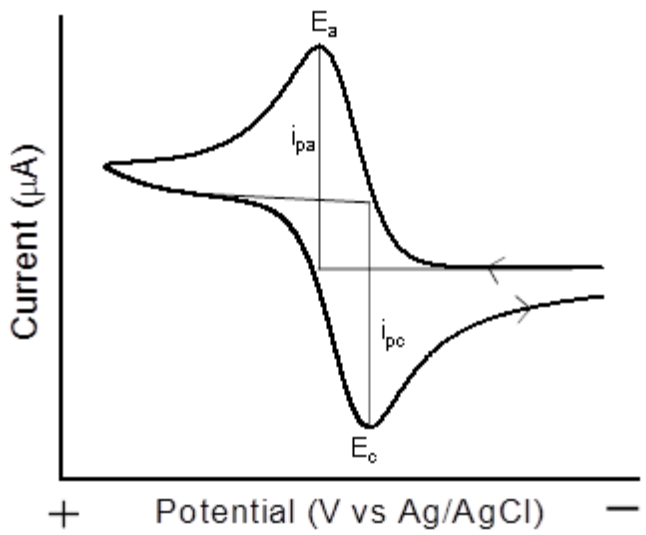

Figure 2.12 A typical cyclic voltammogram with the important parameters.[85]

The CV requires the measurement of current at the working electrode during cyclic potential scans (Figure 2.12). The arrows show the direction of the forward and backward scans. With increasing the initial potential to more positive value, the anodic current increases which results in oxidation of the material. Oxidation peak current, i_{pa} is reached when all of the materials at the surface of the electrode got oxidized and corresponding potential is known as anodic peak potential, E_a. Afterward, when the potential reaches to a predetermined switching potential, the scan direction is switched toward more negative potentials for reverse scan. The reduction current increases until the concentration of oxidized species at the electrode surface are diminished, causing the current to highest peak. The peak current is known as cathodic current i_{pc}, and corresponding potential is known as cathodic peak potential, E_c.

In this research, the ternary aerogel ink was prepared by mixing ~4 mg of the aerogels with 25 µL of nafion and 400 µL of iso-propanol followed by sonication for 30-60

seconds. The modified working electrodes were produced by drop casting the aerogel ink on the clean surface on a glassy carbon electrode (GCE, 5 mm in diameter, or 0.196 cm^2 in area). After drying the electrodes in ambient air, it was further dried at 50 °C for 12 h in an oven and stored in a desiccator prior to electrochemical measurements.

All electrochemical performance of ternary alloy aerogels for electrooxidation of ethanol/methanol was investigated using cyclic voltammetry and chronoamperometry using a CHI-401 electrochemical workstation (CH Instruments Inc.). All the electrochemical measurements were conducted in 1.0 M KOH aqueous solution containing ethanol/methanol in a conventional three-electrode test cell at room temperature. Potentials of the working electrode were recorded against Ag/AgCl (1.0 M) (CH Instruments Inc.) reference electrode and Pt wire was used as the counter electrode. Activation of the ternary alloy aerogel modified GCE was carried out by conducting CV for 100 cycles at 50 mVs^{-1} (1 M KOH) with a potential range -1.0 to 0.2 V (vs. Ag/AgCl).

Electrochemistry of Ethanol/Methanol

A representative cyclic voltammogram for the electrooxidation of alcohol using commercial Pd/C or Pt/C has been shown in Figure 2.13. Typically two current peaks (Peak I and II) are observed that is characteristics of ethanol/methanol oxidation.[20, 86] The anodic peak wave is attributed for the ethanol/methanol oxidation with the removal of the oxygenated species adsorbed on the catalyst surface. The peak potential observed for alcohol oxidation is closer to the reduction potential of oxygenated species on the catalyst surface.[20b, 86a] The reverse peak (peak II) is designated for the further oxidation of the incompletely oxidized carbonaceous intermediates (CO_{ads}, CH_3OH_{ads},

and CHO species)[20a] produced on the electrode surface produced during the forward potential sweep.

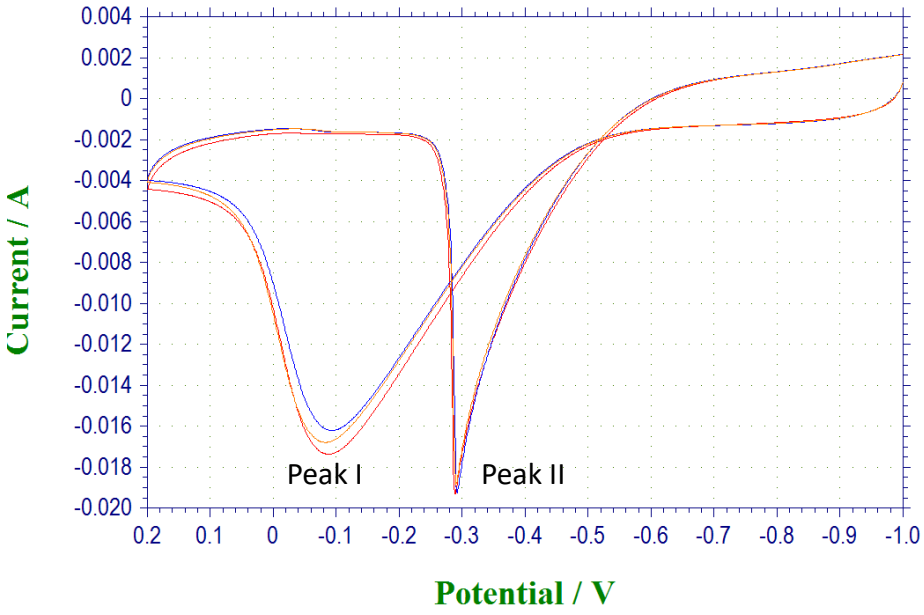

Figure 2.13 A representative CV of Pd/C catalyst for electrooxidation of ethanol in 1.0 M KOH solution.

Mechanism of Electroxidation of Ethanol

It has been proposed that the mechanism of ethanol oxidation on Pd involves the formation of Pd-(CH_3CO)ads upon C-H bond cleavage –

$$Pd + 2\ OH^- \longrightarrow Pd(OH)_2 \quad \text{Reduction Potential = 0.07 V}$$

$$Pd + CH_3CH_2OH \longrightarrow Pd\text{-}(CH_3CH_2OH)_{ads}$$

$$Pd\text{-}(CH_3CH_2OH)_{ads} + 3\ OH^- \longrightarrow Pd\text{-}(CH_3CO)_{ads} + 3\ H_2O + 3\ e^-$$

$$Pd\text{-}(CH_3O)_{ads} + Pd\text{-}OH_{ads} \longrightarrow Pd\text{-}CH_3COOH + Pd$$

$$Pd\text{-}CH_3COOH + OH^- \longrightarrow Pd + CH_3COO^- + H_2O$$

It is thus important not only to form the Pd-OH bond, but to remove easily as well.[20b]

Chronoamperometry

In chronoamperometry (CA), potential pulse is applied to the working electrode and its resulting current is measured against a reference electrode as a function of time. CA experiments are most commonly either single potential step or double potential step. In both cases, current is measured as a function of time. In this technique, initially a potential (E_1) is applied at which no electrolysis happens (Figure 2.14). The potential is then changed to a value (E_2) that leads to oxidation or reduction of particular species and is held at that potential for certain time period which is known as step time or pulse width (Figure 2.14). The single or forward potential step experiment is completed at the end of this step time. In double potential step experiment, the potential is returned to a final potential (E_2) which is identical to the initial potential (Figure 2.14). On the other hand, CA relies on recording the current (i) as a function of time (t) after setting the potential at a selected value. The resulting response is sometimes called amperometric *i-t* curve. Here, the current response is described by the Cottrell equation.[85]

$$i(t) = \frac{nFAD^{1/2}C}{\pi^{1/2}t^{1/2}} \ldots\ldots\ldots\ldots\ldots\ldots\ldots\ldots\ldots\ldots\ldots 2.8$$

Where, n= number of electrons, F = Faraday constant, A=electrode surface area, D=diffusion coefficient, C=concentration, t= time.

According to the above equation, the current is decreases as a function of $t^{-1/2}$.[85]

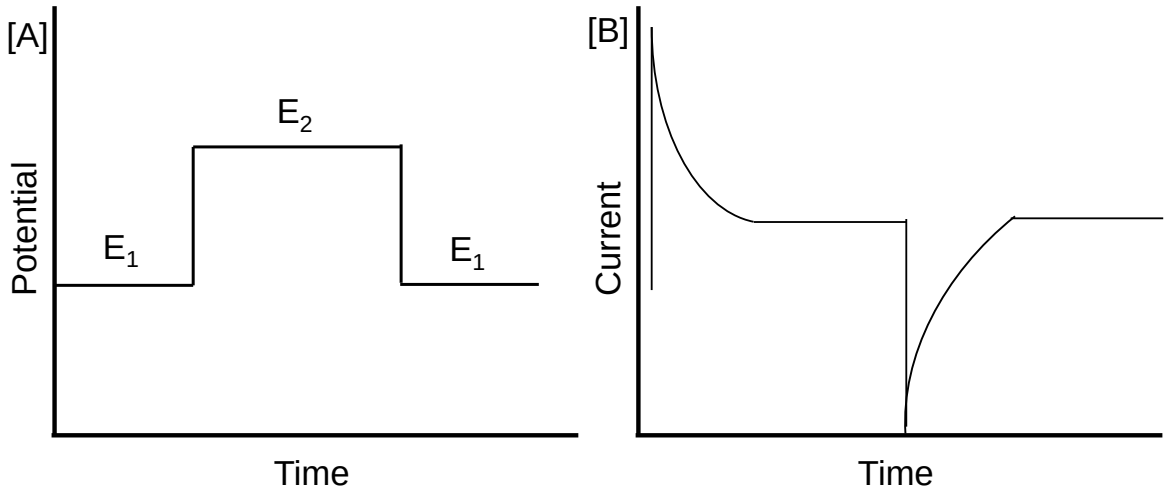

Figure 2.14 Double potential step chronoamperometry representing [A] Typical waveform, and [B] corresponding current response.[85]

Two different types of current occur at the electrode surface, faradaic and non-faradaic current. Faradaic current is the current which forms due to electron transfer across the metal–solution interface. This electron transfer cause the oxidation or reduction of redox species. On the other hand, non-faradaic or charging current arises from the charging the electrochemical double layer. The double layer forms because of the movement and arrangement of ions in solution near the electrode surface when a potential is applied. At a certain potential, there will exist a charge on the electrode surface and an equal, but opposite, charge in solution.[85]

In the following dissertation, stability and tolerance of the as-prepared ternary alloy aerogel catalysts were evaluated by chronoamperometry (1.0 M KOH + 1.0 M ethanol/methanol).

CHAPTER 3

Metal-Semiconductor Hybrid Aerogels: Evolution of Optoelectronic Properties in a Low Dimensional CdSe/Ag Nanoparticle Assembly

3.1 Introduction

Control over the optical properties of semiconductors has been an ever increasing demand to the scientific community. This ongoing thrust has led to the synthesis of nanoscale semiconductors that exhibit size, shape, and composition dependent photophysical properties.[87] However, for many semiconductor systems more sophisticated control mechanisms are desired to further improve the material properties for optimization in specific studies. As a result, diverse approaches have been utilized to improve the light-matter interactions including; doping with metals[88] and nonmetals,[89] alloying with metal and semiconductors,[90,91] and coupling semiconductor and plasmonic nanoparticles (NPs) to produce hybrid nanomaterials (HNMs).[16a, 92] HNMs are hetero-nanostructures consisting of two or more chemically different constituents, such as semiconductor-metal, semiconductor-insulator, or semiconductor-semiconductor composites.[93] Each component of the hybrid exhibits unique physical properties, which when assembled together demonstrates different characteristics.[94] The integration of

plasmonic metals with semiconductors has attracted much attention due to the potential of coupling high absorption cross section and size tunable optical properties of semiconductor NPs with the localized surface Plasmon resonance (LSPR) of metal NPs.[93b] The co-existence of similar electronic energy levels in metal and semiconductor NPs has been shown to alter the light-matter interactions with the potential to exhibit novel and tunable photophysical properties.[94-95] Hybrid interactions of metal/semiconductor systems are typically a result of long range Columbic interactions, dubbed as Förster resonance energy transfer (FRET),[96] and are less likely to occur through a direct electron tunneling effect. The FRET type interactions have been shown to produce novel absorption properties.[95b] However, in many cases, photoluminescence (PL) quenching is observed as the predominant effect.[54-55, 97] As such, metal-semiconductor hybrids with direct contact for electron tunneling have gained noteworthy interest in the search for better control over optoelectronic properties as well as the fundamental understanding of interfacial interactions among chemically different systems.[95a]

Semiconductor colloids, as synthesized, contain an organic coating which serves to provide stability in solution and offers the chemical functionality of demand. However, these organic ligands act as insulating layers that prevent the interparticle interactions needed for charge transfer.[95b] To observe electronic energy overlap direct interfacial interactions are desired. To date, direct contact between semiconductor and metal components has been studied via production of core/shell nanostructures,[95] which exhibit PL quenching. On the other hand, the metal modified semiconductor hybrids are reported to exhibit both PL quenching and enhancement when decorated with Au and

Ag NPs,[54-55] respectively. Aerogels derived from Au modified CdS NPs are reported to exhibit progressive red shifting and PL quenching effects with increasing Au content. However, the reported PL spectra exhibit no distinct band-edge features and are more consistent with trap state emission.[54-55] Conversely, with Ag modified CdS aerogels an enhancement of PL intensity has been reported, but the emission also appeared to originate from surface traps.[54-55] Further, direct contact of CdTe and Au colloids has also been achieved through photo-oxidation of surfactant ligands where concentration dependent PL quenching was reported. The PL quenching mentioned above was attributed to non-radiative relaxation of photogenerated exciton, however FRET has also been proposed as a possible pathway for depletion of emission.[97-98] In previous studies the ratio of metal to semiconductor was relatively high and no spatial separation among individual components was maintained. To minimize the FRET effects it is important to reduce the plasmonic metal concentration and increase the spatial separation.[99] It has become clear that more comprehensive studies, in the low loading ranges are needed to observe changes in optical properties without the interference of FRET quenching. A low dimensional network consisting of metal and semiconductor NPs is anticipated to provide the optimal interactions leading to hybrid energy states and potentially novel optical properties.

Recently, the synthesis of chalcogenide aerogels via oxidation-induced self-assembly of thiol coated semiconductor NPs has been reported.[1c, 47a, 48a] More recently, our group has extended this strategy for the synthesis of transparent and opaque metal aerogels composed solely of Ag NPs. The gel morphology consists of an open fractal structure with low-dimensional connectivity between the primary nanosized constituents.[47b, 47c, 47e]

The interactions between NPs in the aerogels are expected to be intermediate of those of the core/shell and ligand stabilized NP composites with the potential for optimum overlap of electronic states. Herein, we examine the oxidative assembly of CdSe and Ag or Au NPs into aerogel superstructures and monitor changes in optics as a function of composition. A new hybrid emission maxima was detected at 630–640 nm with 0.27 % Ag incorporation and minimal changes to absorption properties, whereas progressive red shifts and tailing effects in absorption onsets were noted at higher Ag loading (0.53-1.83 %). Time resolved PL (TRPL) decay time of the hybrid emission (~600 ns) is significantly different from those of the band-edge (1.83 ± 0.03 ns) and trap state (1190 ± 120 ns) emission maxima of CdSe aerogels, suggesting the generation of an alternate radiative decay pathway.

3.2 Experimental Section

Synthesis of CdSe nanocrystals

CdSe NPs were produced by following a previously reported procedure with slight modification to scale up the synthesis.[47b] In a typical reaction, 0.0514 g of CdO, 0.1116 g of TDPA, and 3.7688 g of TOPO were degassed under vacuum for 20 min at 100 °C and heated at 320 °C for 16 h under nitrogen flow to produce a homogenous colorless solution. In a separate flask, 0.0316 g of Se was dissolved in 2.4 mL of TOP inside a nitrogen glove box to produce a Se-TOP solution. The temperature of the Cd-TDPA-TOPO mixture was reduced to 270 °C and the Se-TOP precursor was swiftly injected. The resultant mixture was allowed to cool to 150 °C and the reaction temperature was slowly raised to 250 °C (10 °C/15 min). The resultant NPs were grown at 250 °C for 4 h

and isolated and purified by multistep dispersion and precipitation using toluene and methanol, respectively.

Surface functionalization of CdSe with thiolate (MUA) ligands

To facilitate more favorable gelation kinetics the TOPO capped CdSe NPs were subjected to a ligand exchange. The NPs were dispersed in 15 mL of 1.2 mM MUA in methanol after adjusting the pH to ~10 with TMAOH. The solution was stirred under nitrogen for 2 h. followed by the addition of an excess of ethyl acetate to precipitate the MUA capped CdSe NPs. The resulting NPs were dispersed in 10 mL of mili-Q filtered water to produce 0.04 M CdSe sol.

Synthesis of GSH functionalized Ag NPs and hollow particles

The solid Ag NPs and hollow NPs were produced by employing a literature method.[100] In a typical synthesis, 4 mL of 10 mM $AgNO_3$ and 300 µL of 10 mM GSH were added to 50 mL of ice cold mili-Q water. Upon adjusting the pH to ~12 with 0.1 M NaOH, the solution color changed from colorless to pale yellow indicating the formation of Ag_2O NPs. Finally, 4.8 mL of 10 mM $NaBH_4$ was slowly added at a rate of 0.5 mL/min to produce dark brown solution of Ag NPs. In contrast, the rapid injection of $NaBH_4$ resulted in an immediate color change from pale yellow to orange brown suggesting the formation of hollow NPs.[56] As prepared Ag NPs and hollows were purified and concentrated using centrifuge filtration to produce 0.004 M Ag sols. The centrifuge filters (Sartorius, Vivaspin, 20 mL, MWCO 30000) filled with 20 mL of Ag sol were centrifuged at 3500g for 7–8 min to reduce the volume to 2–3 mL. The concentrated Ag sols were then mixed with 5–10 mL of mili-Q water and centrifuged to remove the residual byproducts (Na, NO_3, OH^-, and unreacted thiolates). Centrifuge filtration was performed

multiple times to reduce the volume of the Ag sol to 10.0 mL (i.e. 0.004 M Ag) while retaining the colloidal stability of NPs.

Synthesis of GSH functionalized Au NPs

GSH-capped Au NPs were synthesized by following a literature method[101] with modification to scale up the synthesis. Briefly, 1.6 mL of 0.025 M $HAuCl_4$ and 700 µL of 0.019 M glutathione were added to 50 mL ice cold water and the pH of the mixture was adjusted to 12 using 10 mL of 0.1 M NaOH. A freshly prepared 0.05 M $NaBH_4$ solution (2.0 mL) was swiftly injected that caused a color change from colorless to ruby-red, indicating the formation of GSH-capped Au NPs. The concentrated Au sols were produced using the centrifuge filtration as discussed above.

Synthesis of CdSe/Ag hybrid hydrogels and aerogels

As-prepared CdSe sol (0.04 M) was divided into 1 mL aliquots and varying volumes (0.1–0.9 mL) of Ag sol were added (Supporting information, Table S1). The resultant mixtures were shaken vigorously to produce homogenous solutions. With increasing Ag, the CdSe/Ag sols exhibit a progression of color from orange-red to deep brown-red. The gelation is induced by the addition of 50 µL of 1% $C(NO_2)_4$ to hybrid sols, which yielded CdSe/Ag hydrogels after 2–3 h under ambient conditions.

The resulting hydrogels were aged for 1–2 days and the byproducts of the oxidation were removed by exchanging with acetone 4–6 times over 2–3 days. The CdSe/Ag aerogels were produced by CO_2 supercritical drying (SCD). Porous microcapsules (SPI Supplies Inc.) filled with acetone exchanged wet-gels were loaded into the SCD dryer and filled with liquid CO_2 at 15 °C. The acetone treated gels were then exchanged with liquid CO_2 5–6 times over 1–2 days. Finally, the wet gels were supercritically dried at 40

°C for 32 min to produce monolithic CdSe/Ag aerogels. CdSe/Au hydrogels and aerogels were produced using a similar procedure.

3.3 Results and Discussion

We have successfully developed a methodology for the synthesis of CdSe/Ag aerogels via oxidation-induced self-assembly of thiolate coated NP precursors. Luminescent CdSe NPs demonstrating the first and second excitonic transitions at 525–540 and 380–410 nm, respectively (Figure 3.1), were prepared via a literature method.[47b] These NPs were passivated with thiolate (mercaptoundecanoic acid, MUA) ligands under ambient conditions and dispersed in mili-Q filtered water to produce concentrated (0.04 M CdSe) colloidal sols. The reaction of $AgNO_3$ with NaOH in the presence of L-glutathione (GSH) was utilized to produce Ag_2O precursor seeds, which then undergo slow chemical reduction to produce solid Ag NPs. Conversely, fast addition of $NaBH_4$ resulted in larger Ag hollows via a Kirkendall type reaction.[100] For co-gelation, Ag NPs with an average diameter of 4.5 ± 1.5 nm and surface plasmon resonance (SPR) near 390–410 nm were produced to have comparable size with CdSe NPs (3.9 ± 0.8 nm, Figure 3.2A-B) and spectral overlap of plasmonic and second excitonic energies (Figure 3.1). In contrast, Ag hollow NPs with 48.0 ± 5.6 nm outer diameter and 10.4 ± 1.4 nm (Figure 3.2C) shell thickness were prepared to match the spectral overlap of Ag SPR with the first excitonic energy (Figure 3.1). The capping ligands on NP surface (CdSe with MUA and Ag with GSH) have been chosen to ensure high stability of colloids in water (0.04 M CdSe and 0.004 M Ag) and to enable efficient decomplexation when treated with a non-oxygen transfer oxidant ($C(NO_2)_4$). It has been

reported that $C(NO_2)_4$ oxidizes the thiolates to sulfenyl nitrate as an intermediate (eq. 1 and 2), which then undergoes reaction with another thiol moiety to produce disulfides,[102] creating active sites on the NP surface (Scheme 3.1). The formed active sites are highly reactive allowing the NPs to physically connect to each other yielding CdSe/Ag hydrogels (Figure 3.3). As prepared hydrogels were supercritically dried to produce CdSe/Ag aerogels (Figure 3.4).[47a, 56] The monolithic aerogels were orange to reddish brown in color and exhibit densities ($d_{CdSe} - d_{CdSe/Ag}$) as low as 0.032–0.072 g/cm^3, representing ~0.55–1.16 % of the density of corresponding CdSe/Ag bulk composites. Interestingly, with increasing Ag content the density of CdSe/Ag aerogels has progressively increased owing to slower gelation rate observed with increasing Ag NP incorporation. This can be attributed to differences in oxidation kinetics of surface thiolates (CdSe-MUA *vs.* Ag-GSH) and subsequent changes in NP aggregation that can potentially delay the co-gelation. The longer time required to produce CdSe/Ag hydrogels leads to compaction and syneresis (solvent expulsion)[47c] resulting in a systematic increase in density of corresponding CdSe/Ag hybrids.

$$RSH + C(NO_2)_4 \rightarrow RS(NO)_2 + C(NO_2)_3^- + H^+ \qquad (1)$$

$$RSH + RS(NO)_2 \rightarrow RS - SR + NO_2^- + H^+ \qquad (2)$$

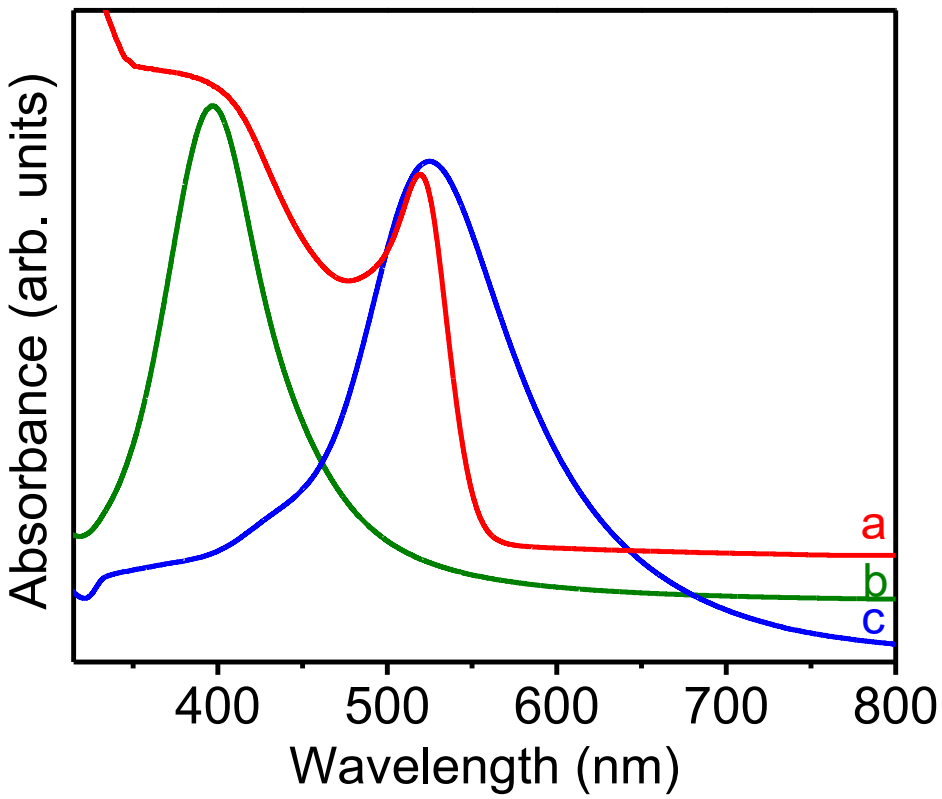

Figure 3.1 Normalized UV-visible absorption spectra of (a) CdSe and (b) Ag NPs along with (c) hollow Ag NPs demonstrating the overlap of plasmonic resonance of metal NPs with first and second excitonic absorption of CdSe NPs.

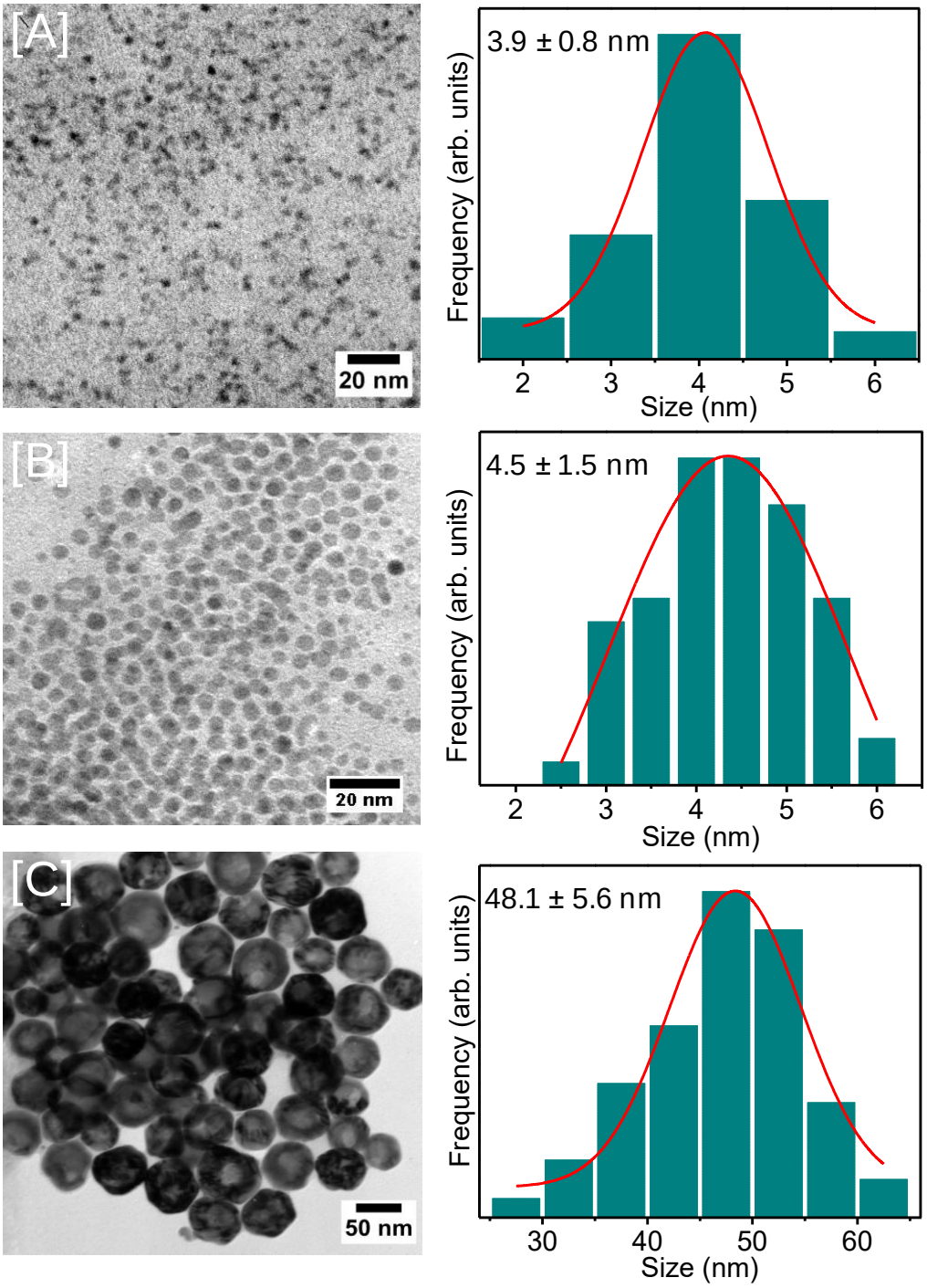

Figure 3.2 TEM images of the [A] CdSe and [B] Ag NPs along with [C] Ag hollow NPs. The size histograms of respective samples without any post-synthetic size selection are also shown.

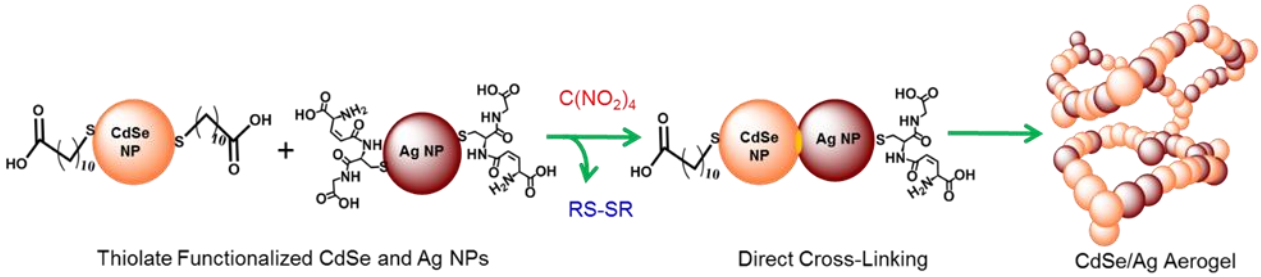

Scheme 3.1 A Schematic representation of the synthesis of CdSe/Ag aerogels. The active sites generated upon oxidative removal of surface thiolates will be directly cross-linked to produce fractal NP networks and consequently a CdSe/Ag hybrid aerogel. RS-SR = disulfide.

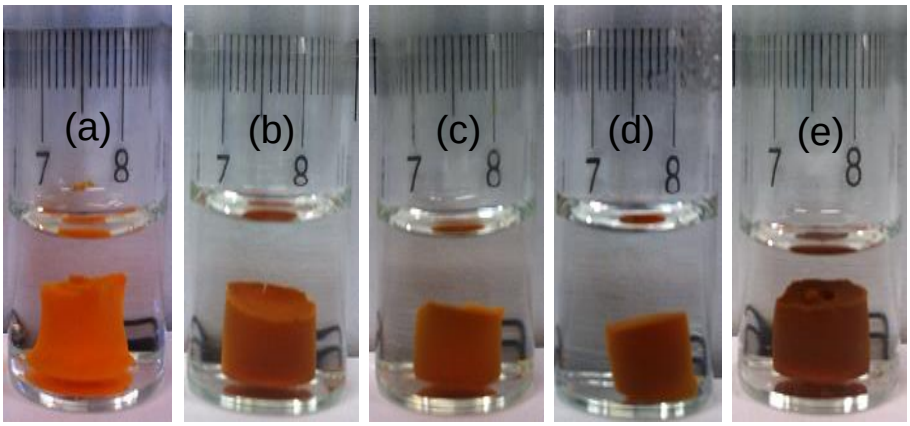

Figure 3.3 Photographs of CdSe/Ag hydrogels with varying Ag content: (a) 0, (b) 0.33, (c) 0.65, (d) 1.59, and (e) 2.01 %. The elemental compositions were obtained from inductively coupled plasma-optical emission spectroscopy (ICP-OES) analysis of corresponding CdSe/Ag aerogels. The scale bar is in centimeters.

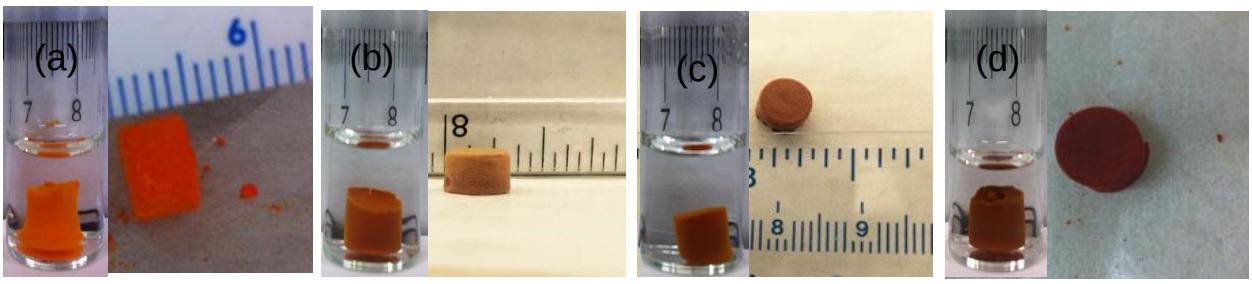

Figure 3.4 Photographs of CdSe/Ag hybrid hydrogels (on the left) and corresponding aerogels (on the right) with varying Ag content: (a) 0, (b) 0.33, (c) 0.65, and (d) 2.01 %. The elemental compositions were obtained from ICP-OES analyses of corresponding CdSe/Ag aerogels. The scale bar is in centimeters.

To probe the structure and crystallinity of hybrid aerogels powder X-ray diffraction (PXRD) was employed. Diffraction patterns of CdSe/Ag hybrids indicate the presence of hexagonal CdSe and cubic Ag, consistent with the crystal structures of NP precursors. At low Ag concentrations (0.53 % – 1.83 %, ICP-OES analysis), the Bragg reflections corresponding to Ag were not observed, whereas with increasing Ag content, typically >2 %, characteristic cubic Ag reflections were observed along with hexagonal CdSe (Figure 3.5A). Crystallite sizes of the metal and semiconductor components in the hybrids were estimated by applying the Scherrer formula[103] to (110) and (111) reflections of CdSe and Ag, respectively. A slight decrease in crystallite size of both components was noted upon co-gelation and supercritical drying, which has been previously attributed to oxidative etching of CdSe[47a, 104] NPs and dissolution of Ag[56] by in-situ generated HNO_3, respectively. The absence of Bragg reflections corresponding to metal oxides or any other elemental impurities suggests that the co-gelation has no impact on the structure and crystallinity of precursor colloids (Figure 3.5).

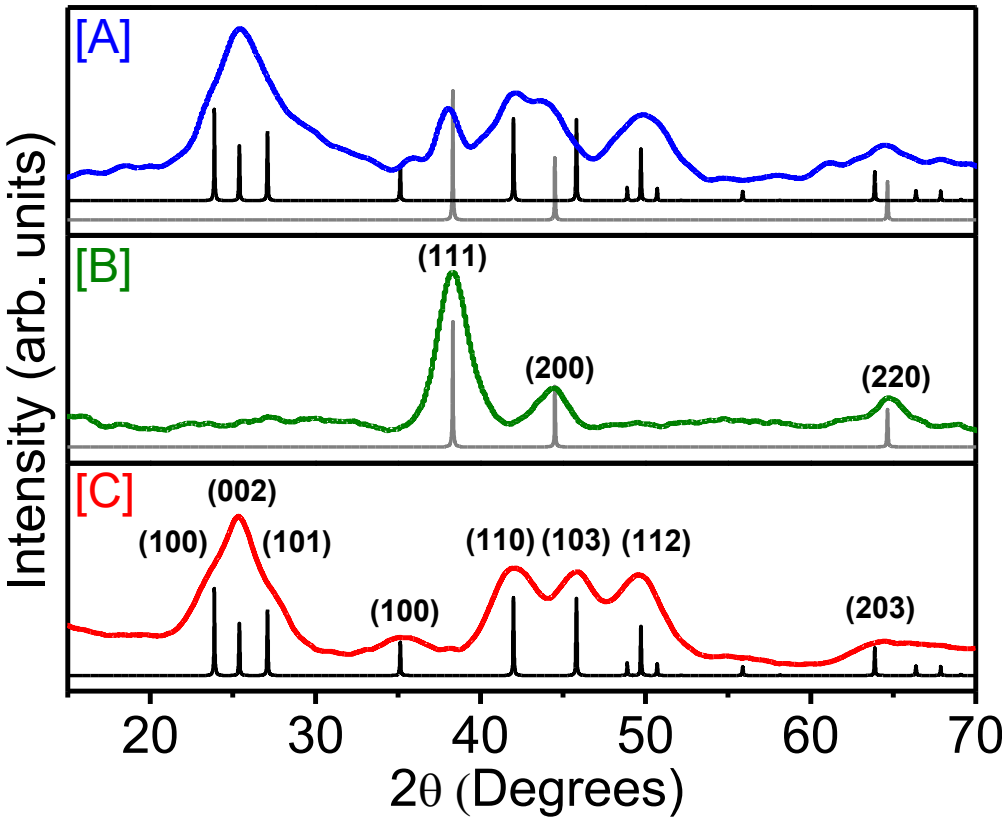

Figure 3.5 PXRD patterns of [A] CdSe/Ag aerogel (2.21% Ag by ICP-OES) along with precursor [B] Ag NPs and [C] CdSe NPs. The ICDD-PDF overlays of hexagonal CdSe (black, PDF # 08-0459) and cubic Ag (gray, PDF # 01-0870-719) are shown as vertical lines.

The binding energies of elemental components obtained from X-ray photoelectron spectroscopy (XPS) are in close agreement with those of CdSe[104] and Ag[56] aerogels reported elsewhere. At 1.83% Ag (ICP-OES analysis) loading, the CdSe/Ag hybrids exhibit binding energies of 405.1 eV (Cd $3d_{5/2}$) and 411.9 eV (Cd $3d_{3/2}$) and 54.2 eV (Se $3d_{5/2}$ and $3d_{3/2}$) (Figure 3.6), consistent with the phase pure CdSe aerogels produced by the reported method and previous studies on CdSe NPs and aerogel materials. The binding energy of Se 3d (54.2 eV) suggests the presence of reduced Se_n^{n-} surface

states that have been reported to link CdSe NPs.[104] While there is a distinct absence of CdO_x peaks ($3d_{5/2}$ 403.2 eV),[105] in few samples SeO_2 59.0 eV (Se $3d_{5/2}$) is present as a result of the oxidative gelation process. Examination of pure Ag NP aerogels specifies the presence of only metallic Ag with binding energies of 367.9 eV (Ag $3d_{5/2}$) and 373.9 eV (Ag $3d_{3/2}$) similar to a prior report.[56] Monitoring the Cd, Se, and Ag binding energies across a range of Ag concentrations (0.38–1.83%, ICP-OES analysis) indicates no significant alterations to their chemical states as shown in Figure 3.7. Further, it is well known that CdSe can undergo cation exchange with Ag to produce α-Ag_2Se.[106] However, if an exchange was occurring during the co-gelation the binding energies of both Ag and Se should shift to lower energies, which was not observed in any of the samples examined (Figure 3.6 and 3.7).[106b, 106c] The lack of binding energy shifts in the hybrids suggests a physical mixing of the two components and no chemical ion exchange, in agreement with the PXRD data (Figure 3.5A), providing further evidence that evolving optical properties are not caused by the formation of α-Ag_2Se domains. However, it is well known that metal-semiconductor interfaces can produce interface compounds[107] and with the low concentrations of Ag loading, XPS may not be able to detect the interfacial interactions between CdSe and Ag NPs. It is likely that silver–reduced selenide (Ag-Se^{n-}) linkages exist at the interface and presumably these interactions facilitate the electron transfer between metal and semiconductor components. Nonetheless, studies involving resonance Raman and NMR spectroscopy are currently underway to further elucidate the chemical nature of interparticle interactions in CdSe/Ag hybrids.

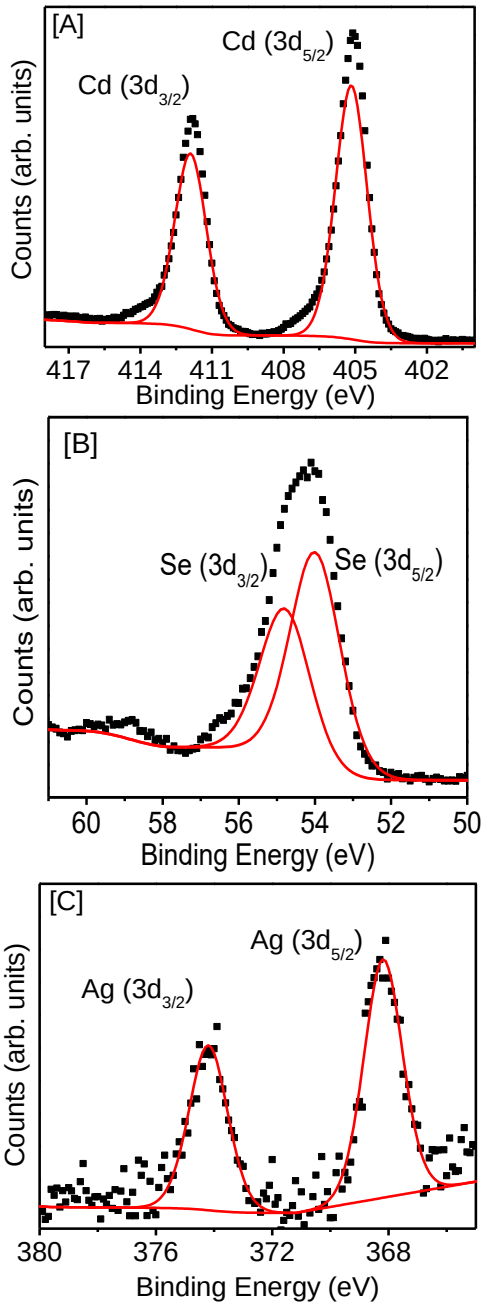

Figure 3.6 [A] Cd ($3d_{5/2}$), [B] Se ($3d_{5/2}$) and [C] Ag ($3d_{5/2}$) XPS spectra of CdSe/Ag aerogel with 1.83% Ag incorporation (ICP-OES analysis). The dotted symbols are spectral data and the red lines are fitted deconvolutions.

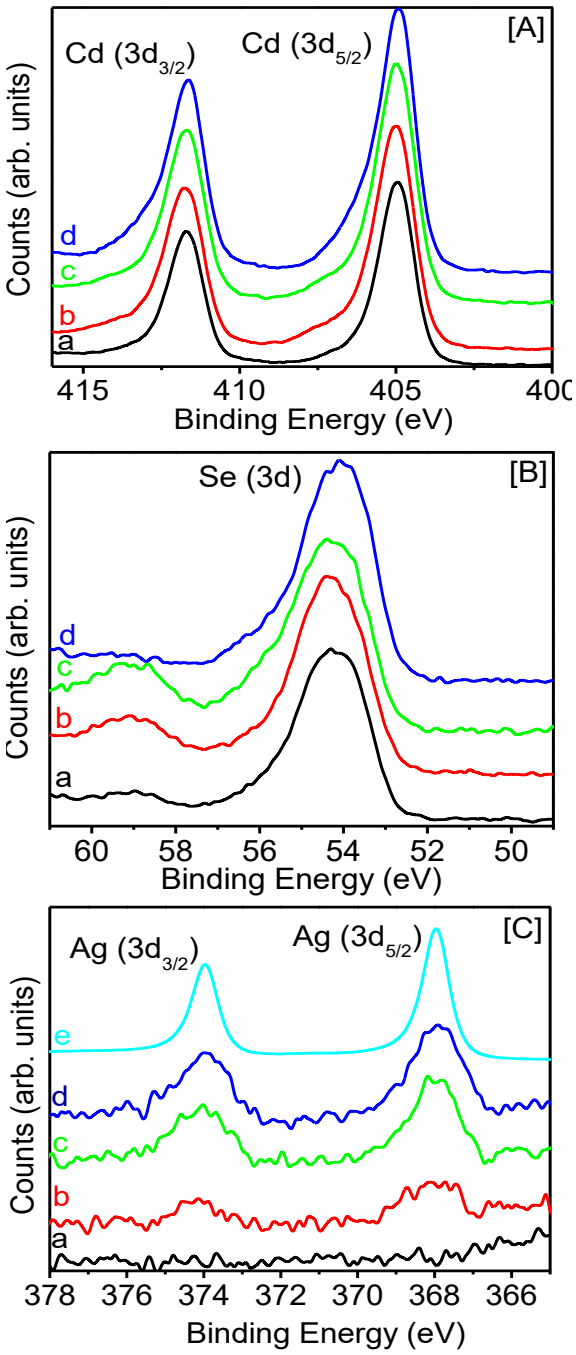

Figure 3.7 [A] Cd (3d), [B] Se (3d), and [C] Ag (3d) XPS spectra of CdSe/Ag aerogels indicating no changes in chemical states with increasing Ag loading: (a) 0.00, (b) 0.38, (c) 1.07, (d) 1.83, and (e) 100 % of Ag. Elemental compositions were obtained from ICP-OES analysis.

The elemental compositions of the precursor NPs and aerogels were investigated from scanning electron microscopy/energy dispersive spectroscopy (SEM/EDS) and ICP-OES analyses. The low Ag content in the hybrid aerogels resulted in statistically inaccurate measure of Ag composition through semi-quantitative EDS. Therefore, ICP-OES was employed to probe the Cd, Se, and Ag compositions of the hybrids. Three individually prepared samples were analyzed per each composition and the average results are presented in Table 3.1. In general, an increase in Ag content in the hybrid aerogels was noted with increasing concentration of Ag NPs in the hybrid sol. Consistent with ICP-OES, three prominent peaks were observed in the SEM/EDS spectra of hybrids, which were assigned to Cd, Se, and S (Figure 3.8). The peaks corresponding to Ag and Cd exhibit major overlap making it difficult to estimate the composition of individual metals. Nonetheless, EDS spectra indicate a significant decrease in sulfur content (19.09 % and 20.99 % in thiolate stabilized CdSe and Ag NPs, respectively to 2.81–3.82 % in CdSe/Ag aerogels), consistent with the oxidative removal of surface thiolates and direct cross-linking of metal and semiconductor components (Scheme 3.1).

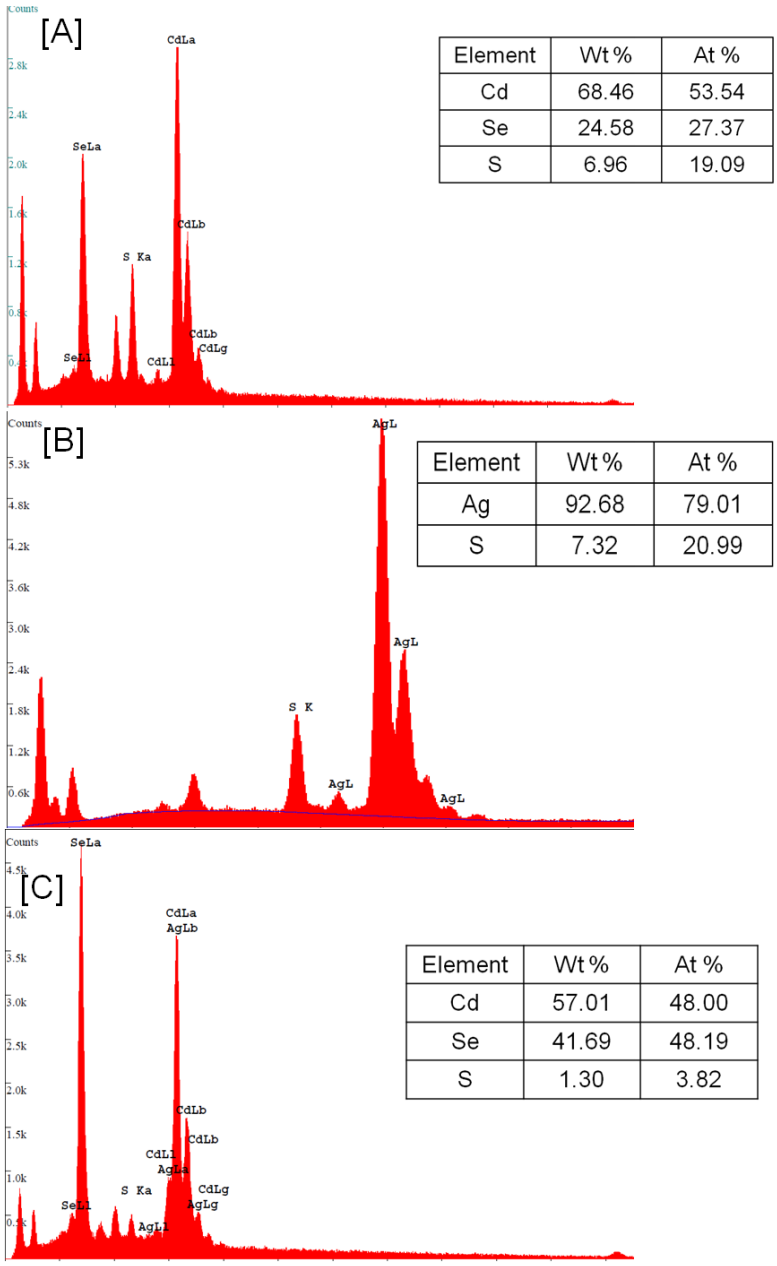

Element	Wt %	At %
Cd	68.46	53.54
Se	24.58	27.37
S	6.96	19.09

Element	Wt %	At %
Ag	92.68	79.01
S	7.32	20.99

Element	Wt %	At %
Cd	57.01	48.00
Se	41.69	48.19
S	1.30	3.82

Figure 3.8 SEM/EDS spectra of [A] CdSe NPs, [B] solid Ag NPs, and the corresponding [C] CdSe/Ag hybrid aerogel with 0.53 % Ag (ICP-OES analysis) composition.

Table 3.1 Comparison of elemental compositions, absorption band onsets, surface areas, average pore diameters, and cumulative pore volumes of the CdSe/Ag hybrid aerogels.

Sample	Elemental Composition (ICP-OES)[a]		Band gap (eV)[b]	Surface area analysis		
	CdSe	Ag		Surface area (m^2/g)[c]	Average pore diameter (nm)[d]	Cumulative pore volume (cm^3/g)[d]
1	100	0	2.21	202	15.9	0.916
2	99.73	0.27	2.20	202	15.0	1.120
3	99.49	0.51	2.18	200	15.8	1.071
4	99.47	0.53	2.18	210	18.2	0.889
5	99.37	0.63	2.08	187	16.4	0.819
6	99.19	0.81	2.07	131	18.4	0.656
7	98.70	1.30	2.04	97	18.8	0.514
8	98.54	1.46	1.97	87	17.0	0.406
9	98.27	1.73	1.93	81	16.3	0.400
10	98.17	1.83	1.82	69	19.4	0.316

[a] Weight % of Cd, Se, and Ag were calculated based on ICP-OES analysis averaging 3 individual measurements per each composition.
[b] Bandgaps were calculated by extrapolating the first absorption onset to the intersection point of the baseline.[87]
[c] BET model was applied to the nitrogen adsorption/desorption isotherms to investigate the surface area of aerogels.
[d] BJH model, which probes the pores in the size range of 1.7-300 nm, was applied to the nitrogen adsorption/desorption isotherms to investigate the porosity of aerogels.

The morphology and inner spatial distribution of CdSe and Ag NPs in the hybrid aerogels were investigated using Transmission electron microscopy (TEM). The electron micrographs of the aerogels indicate the presence of nearly spherical colloidal NPs that are physically linked together to produce CdSe/Ag hybrids (Figure 3.9). The corresponding high resolution TEM (HRTEM) images reveal the presence of CdSe and Ag NPs, as probed by the differences in (100) and (111) lattice spacings of hexagonal CdSe and cubic Ag, respectively (Figure 3.9 inset). Additional HRTEM images of the aerogels demonstrating the 3-dimensionally (3D) connected network of CdSe and Ag NPs are shown in Figure 3.10 to further support this claim. Further, SEM/EDS elemental maps indicating the random distribution of Ag NPs in the CdSe gel frameworks are shown in Figure 3.11. These data are consistent with direct cross-linking of metal and semiconductor NPs, which allows direct electron tunneling and potentially novel optical properties. Moreover, the TEM analyses of hybrids indicate the highly porous morphology of aerogels, consisting of a range of mesopores (2–50 nm) and macropores (>50 nm) throughout the gel material. Consistent with the PXRD, the size estimations of NPs using TEM images revealed a slight decrease in particle size for CdSe and Ag NPs in the hybrids (Figure 3.12) in comparison to precursor colloids (Figure 3.2 A–B).

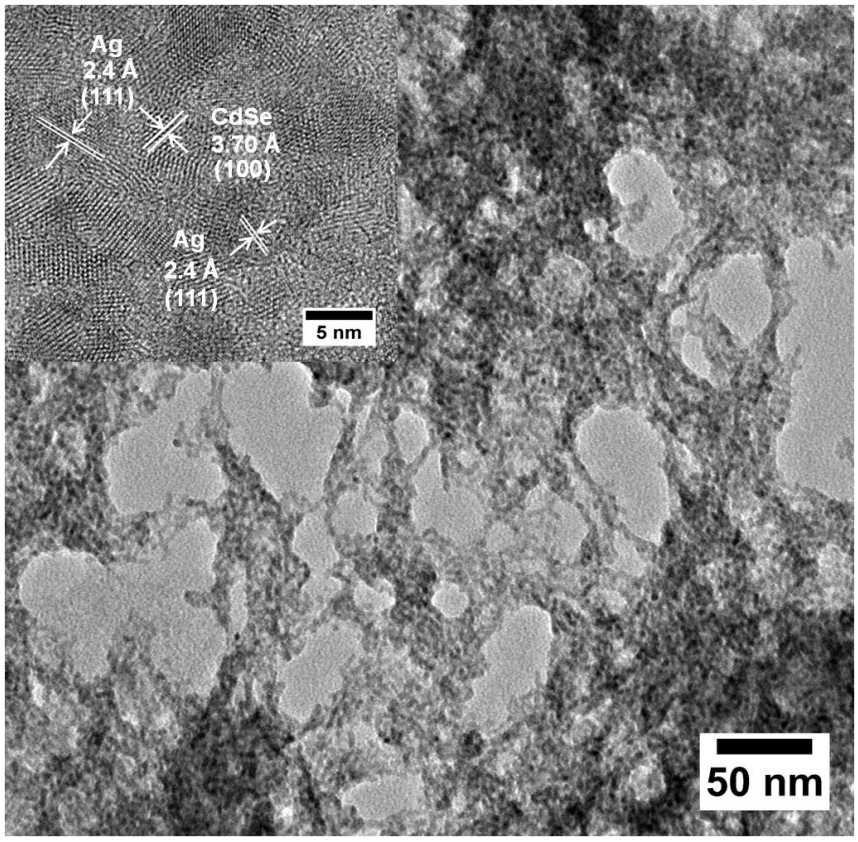

Figure 3.9 A representative low-resolution TEM image of the CdSe/Ag hybrid aerogels with 0.63 % Ag composition. Inset shows the HRTEM image of a selected area. The dark contrast areas represent the multilayers of NPs showing the 3-dimensional (3D) connectivity of NPs. The elemental composition was investigated by ICP-OES analysis.

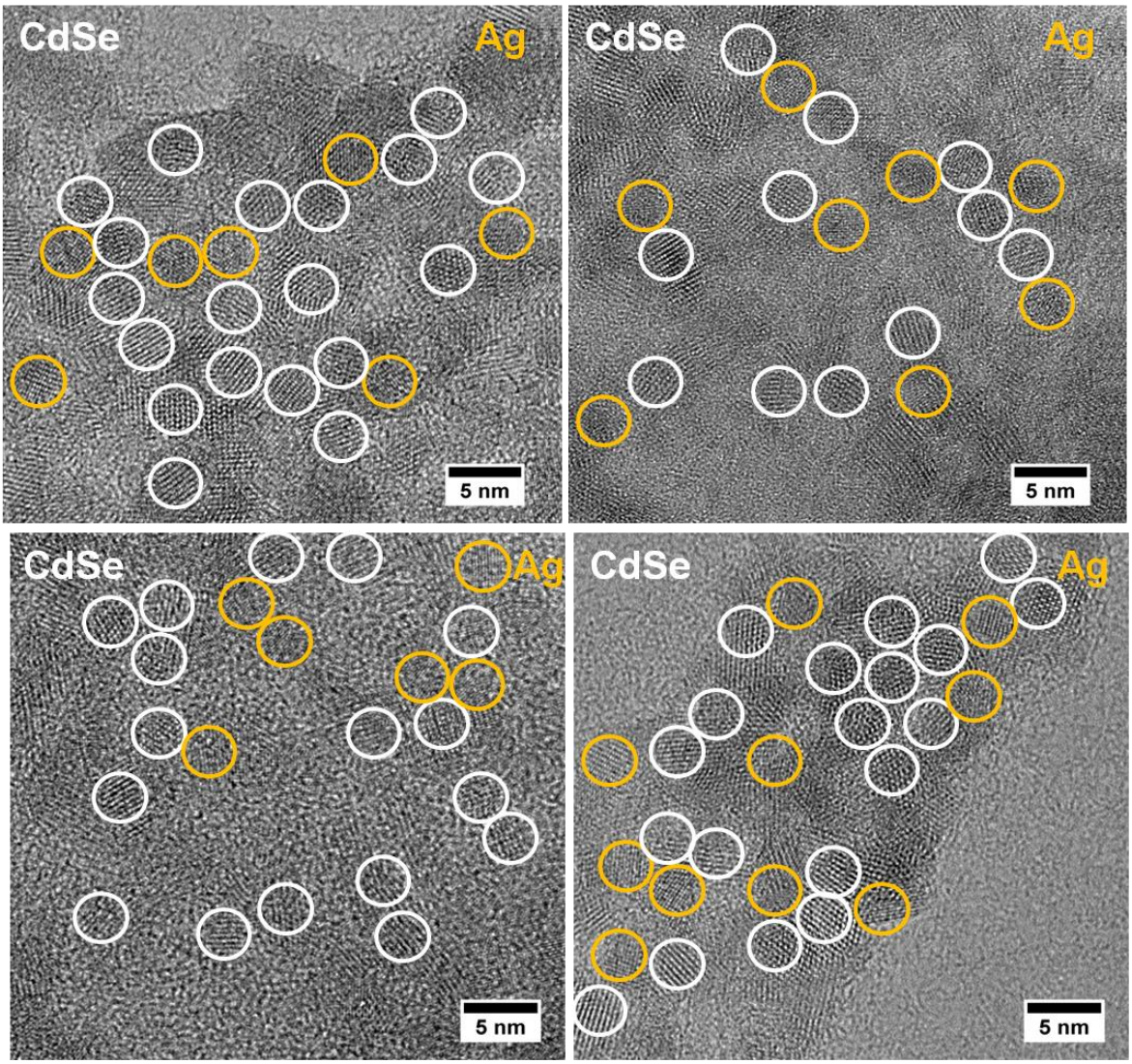

Figure 3.10 The high-resolution TEM image of the CdSe/Ag aerogel containing 2.21 % Ag (ICP-OES analysis) showing the random distribution of CdSe and Ag NPs throughout the hybrid gel framework. The white circles represent the CdSe crystallites whereas the yellow circles represent the Ag crystallites in the hybrid aerogel.

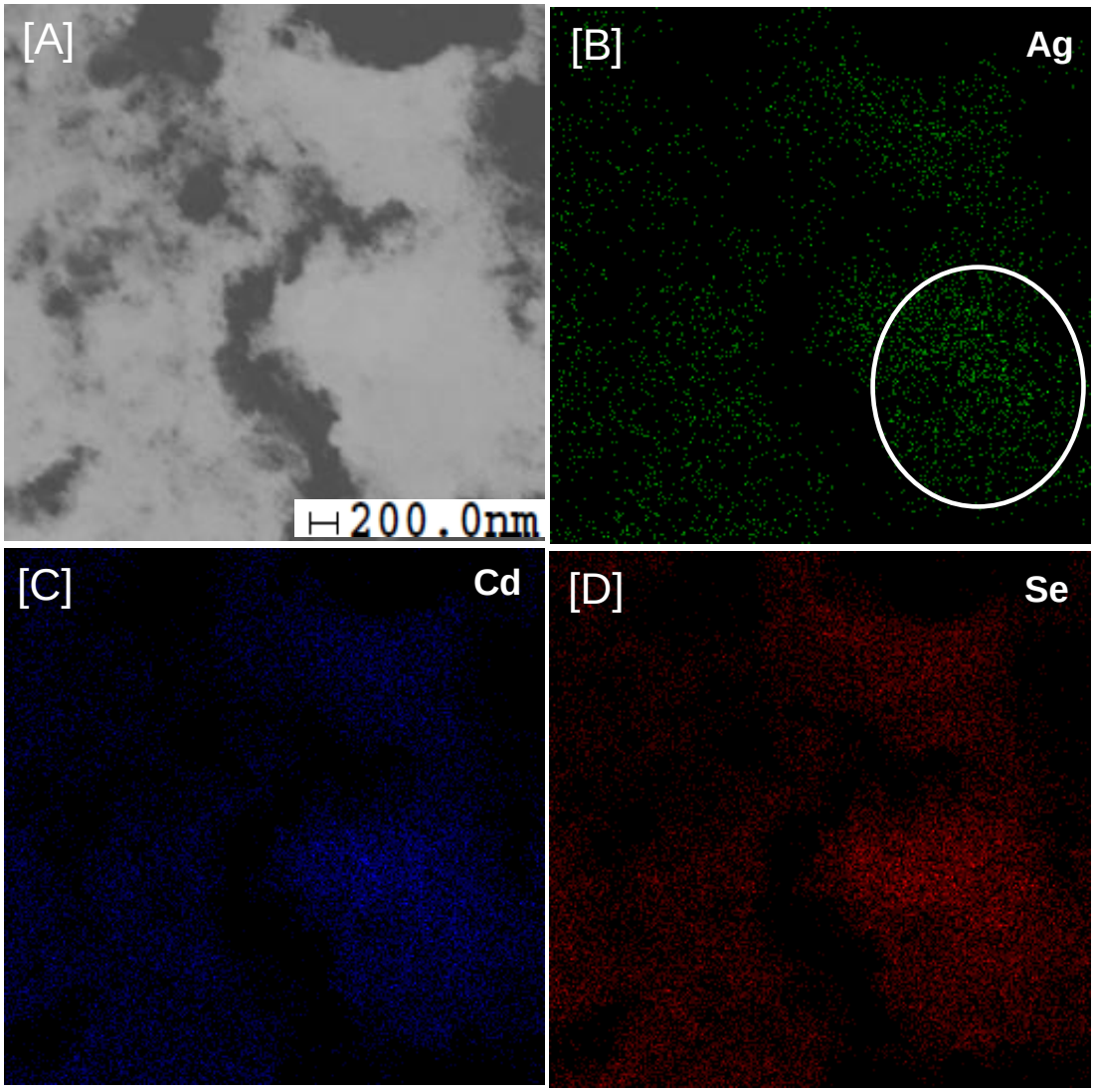

Figure 3.11 [A] High resolution SEM images of CdSe/Ag NP aerogels with 9.67 % Ag composition (obtained by ICP-OES analysis), along with corresponding SEM/EDS elemental mapping of [B] Ag, [C] Cd, and [D] Se showing the random distribution of Ag in the CdSe gel framework. Marked area in B exhibits slightly higher Ag content compared to other areas, which we referred to as regional differences in Ag content in the hybrid framework.

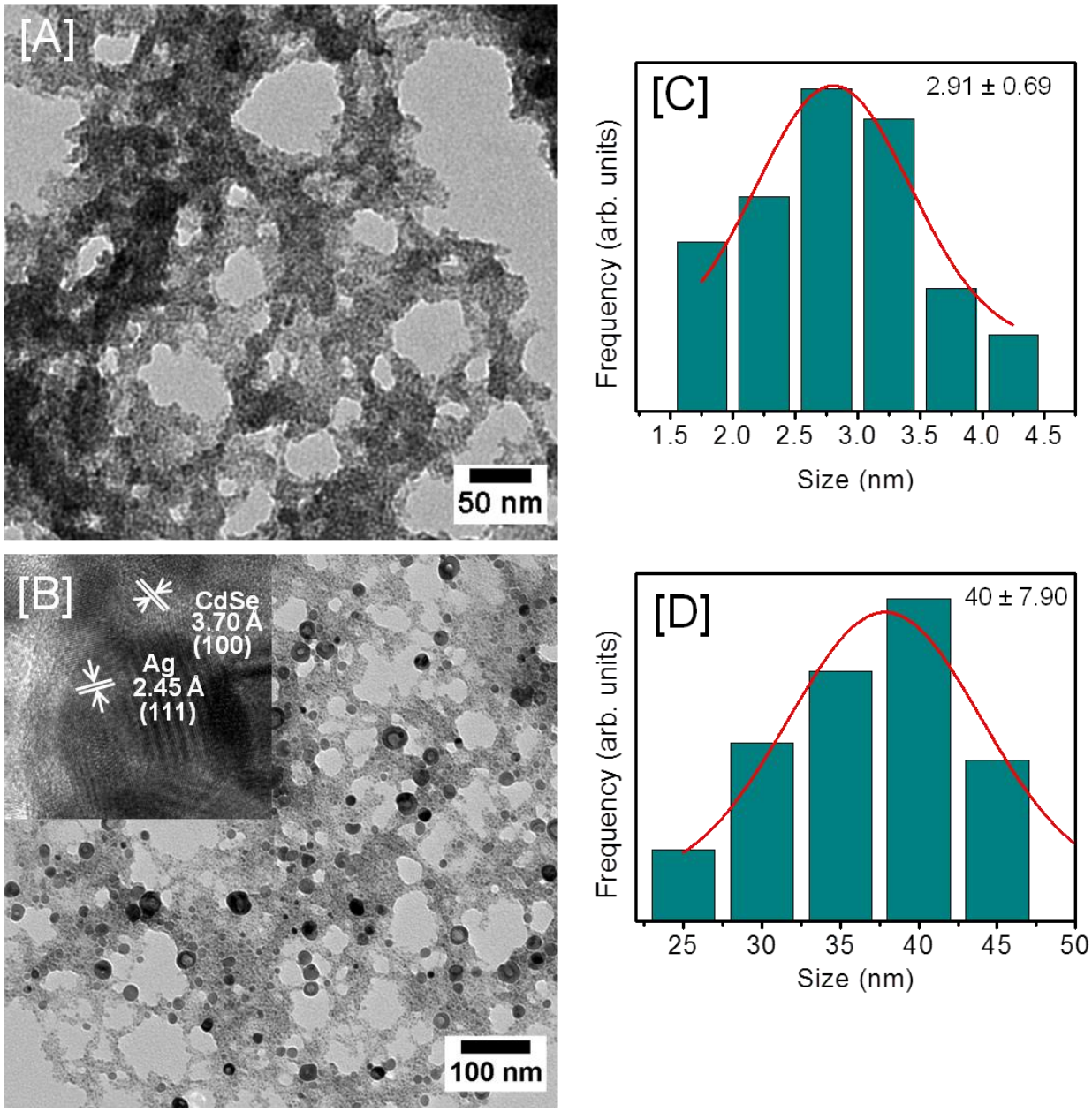

Figure 3.12 Low resolution TEM images of [A] CdSe and [B] CdSe/Ag hollow NP (8.97 %, ICP-OES analysis) aerogels. Inset in B shows the HRTEM image of the CdSe/Ag hollow NP aerogel. The size histograms of respective samples without any post synthetic size selection are shown in [C] and [D], respectively. Average particles sizes were calculating from 80-90 particles from the corresponding TEM images.

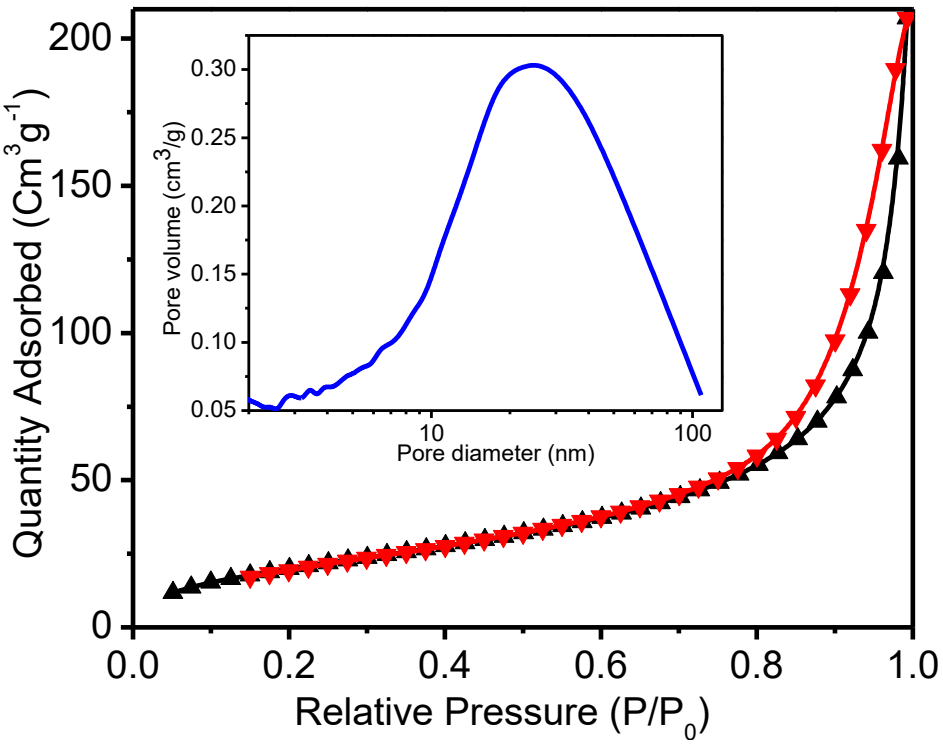

Figure 3.13 A representative nitrogen adsorption/desorption isotherm of CdSe/Ag aerogels with 0.81 % Ag composition by ICP-OES. The inset shows the corresponding BJH modeled pore size distribution plot. The aerogel samples were degassed at 50 °C for 24 h prior to analysis.

The surface areas of CdSe and CdSe/Ag hybrid aerogels were obtained by applying the Brunauer-Emmett-Teller (BET) model to nitrogen adsorption/desorption isotherms. A typical isotherm of CdSe/Ag aerogel is shown in Figure 3.13 reflecting a combination of type IV and II curves, consistent with the formation of a meso-to-macro-porous material.[56] The shape of the hysteresis loop is indicative of H1 and H3 character that corresponds to cylindrical and slit shaped pores, respectively.[47b] The BET surface area of CdSe aerogels is 201–204 m^2/g,[47a] consistent with literature reports. In contrast, CdSe/Ag hybrids exhibit surface areas in the range of 69–210 m^2/g depending on the

Ag composition (Table 1). Recent reports on Ag aerogels indicate surface areas of 43–160 m^2/g[56] while those of CdSe aerogels were 200–224 m^2/g.[47a] Therefore, the incorporation of Ag NPs in the CdSe gel framework is likely to result in a decrease in the surface area with values that are intermediate of phase pure CdSe and Ag gel materials. In addition, as discussed previously the longer gelation time required with increased Ag loading leads to compaction and syneresis (solvent expulsion) of hydrogels resulting in dense monoliths that exhibit lower surface areas (d_{CdSe} = 0.032 g/cm^3 and $d_{CdSe/Ag}$ = 0.06 – 0.072 g/cm^3 for 1.3 – 1.83% Ag incorporation). This observation is further reflected in the cumulative pore volumes of the CdSe/Ag hybrids that exhibit a systematic decrease with increasing Ag concentration (Table 3.1). However, consistent with TEM images, small variations in average pore diameters (15–19.4 nm) were observed suggesting the predominantly mesoporous nature of CdSe/Ag aerogels (Figure 3.9).

UV-visible absorption and PL spectra of hybrid aerogels were recorded to explore the influence of Ag on CdSe optical properties. Previous efforts on semiconductor-metal HNMs were mainly focused on enhancing the excitonic resonance through overlap with plasmonic energy levels to explore the optical trends.[95b, 108] In high interfacial contact systems such as core/shell hetero-nanostructures,[94-95] the formation of hybrid excitons was observed in the absence of PL whereas in low interfacial contact systems systematic PL quenching was noted with no indication of the generation of hybrid states.[108] The implementation of sol-gel strategy allows for control over NP proximity as well as the concentration of metal and semiconductor components that can potentially minimize the FRET effects while maintaining the direct electronic contacts. Such level of

controlled interfacial interactions are expected to blend the electronic energy levels of CdSe and Ag NPs without detrimental PL quenching effects. As a control study, the NPs surface passivated with thiolate ligands and mixed in solution exhibit no changes in optical properties regardless of Ag loading levels (Figure 3.14). However, interesting optical trends were obtained upon oxidative removal of the surface ligands leading to the formation of low-dimensional CdSe/Ag hybrids.

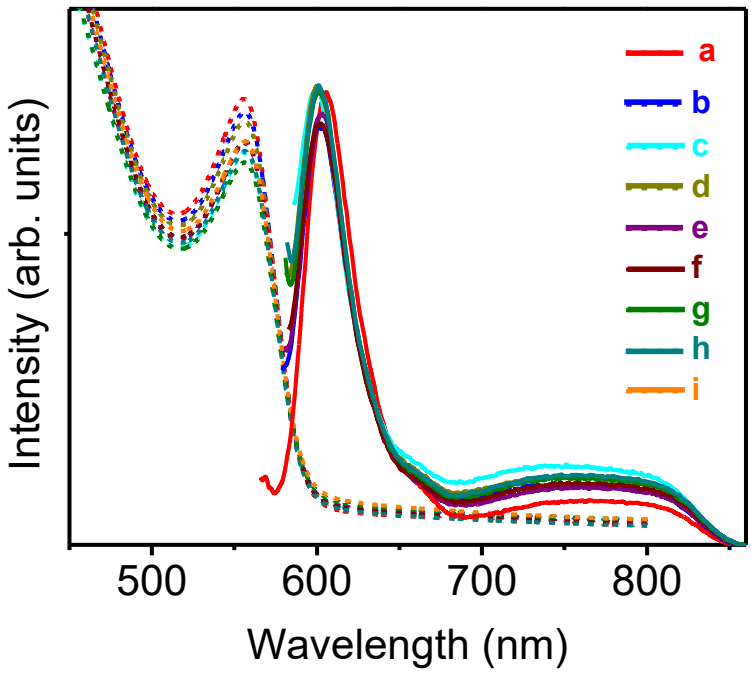

Figure 3.14 UV-visible absorption (dotted lines) and PL spectra (solid lines) of CdSe/Ag hybrid sols containing (a) 0.00, (b) 0.2, (c) 0.4, (d) 0.6, (e) 0.8, (f) 1.0, (g) 1.2, (h) 1.7, (i) 2.0 % Ag loading. Ag compositions shown here are nominal values used in the synthesis of corresponding CdSe/Ag aerogels.

The optical absorption of CdSe/Ag aerogels was investigated starting with very low Ag loading (0.13 %) and the hybrids were systematically probed up to 2.21 % Ag incorporation (Figure 3.15). All concentrations reported in the optical discussion are

experimental values obtained from ICP-OES analysis. At very low levels of Ag loading (0.13–0.51 %) no significant changes in the absorption band onsets were noted (Figure 3.15), whereas at higher Ag content (0.53–2.21 %) a systematic red shift, band tailing, and quenching effects of the absorption onsets were observed. The band tailing effect (Figure 3.16 D-F) can be attributed to slightly inhomogeneous distribution of Ag NPs in the hybrids leading to regional differences in Ag concentration (Figure 3.11). When the Ag NPs are well dispersed in the hybrids (typically < 0.81 %) there is minimal alteration to the absorption properties (Figure 3.16 A-C). Conversely, when the Ag NPs are more closely arranged in the aerogels (0.81-1.83%) overlapping electronic wave-functions result in a progressive red shift of excitonic absorption and band tailing effect. Further increasing the Ag composition (> 2.01 %) leads to significant depletion of CdSe absorption suggesting excessive loading of plasmonic NPs. The increased concentration of Ag could possibly give rise to increased dipole-dipole interactions between metal and semiconductor NPs that result in band broadening and quenching of CdSe absorption.[97, 109] In Figure 3.16 G-H, although the absorption spectra appear to be completely quenched and the bandgap features are less distinguishable, the CdSe absorption is still present. While strong quenching of absorption at 2.21 % Ag loading is unexpected, similar band tailing and quenching effects were reported for CdSe xerogels owing to lower degree of confinement effects achieved in a dense NP network.[47a] Likewise, the reduced porosity associated with the increasing Ag loading along with the effectively higher Ag concentrations achieved per unit area has the potential to rapidly quench the CdSe absorption. If the aerogels maintained the same porosity it is likely that the Ag induced changes would happen more slowly with increasing concentration.

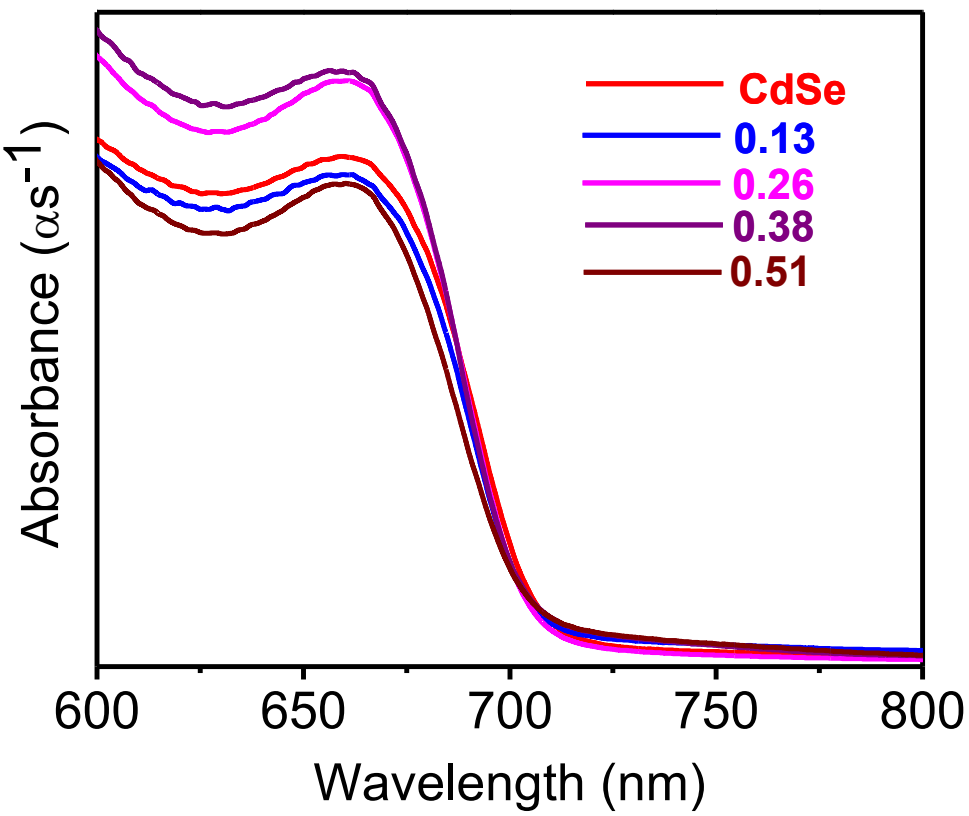

Figure 3.15 Solid state absorption spectra of CdSe/Ag hybrid aerogels containing 0.13-0.51 % of Ag. The elemental compositions of the aerogels were investigated by ICP-OES analysis and the spectra were recorded at 300 K.

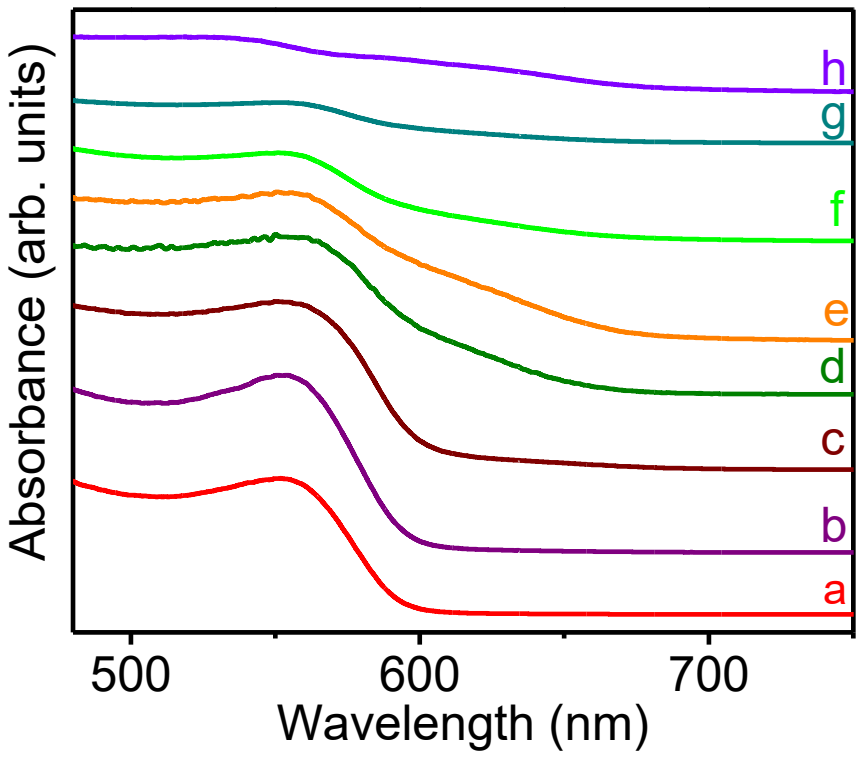

Figure 3.16 Solid state absorption spectra of CdSe/Ag aerogels with (a) 0.00, (b) 0.53, (c) 0.81, (d) 1.07, (e) 1.30, (f) 1.83, (g) 2.01, (h) 2.21 % Ag composition. The elemental compositions of the aerogels were investigated by ICP-OES analysis.

The emission spectra of pure CdSe aerogels exhibit band-edge and trap state emission maxima at 550 nm and 720 nm, respectively (Figure 3.17A).[47a, 47b, 110] With Ag loading as low as 0.13–0.53 %, the band-edge emission quenches and a new emission at 630–640 nm emerges in between the band-edge and trap state maxima of CdSe aerogels (Figure 3.17B). The temperature dependent PL measurements of CdSe/Ag hybrids with 0.27–0.53% Ag loading demonstrate the dominant nature of the 640 nm emission peak (Figure 3.17B-C and Figure 3.18). The presence of the band-edge and trap state emissions in the hybrid aerogels with 0.27–0.53% Ag loading is further

confirmed by additional time-resolved studies discussed below. The PLE spectra of the CdSe and CdSe/Ag hybrids probed at 550 nm, 720 nm, and 640 nm emission are consistent with the absorption studies and shown in Figure 3.19. The FWHM of the fitted Gaussian peak of 640 nm emission (80 ± 20 nm, 0.31 ± 0.04 eV) is distinct from those of the band-edge (25 ± 10 nm, 0.11 ± 0.06 eV) and trap state emission maxima (140 ± 30 nm, 0.42 ± 0.18 eV) of phase-pure CdSe aerogels supporting the view that the origin of new emission can be attributed to the emergence of an alternate radiative decay pathway.

To reveal the dynamics involving different relaxation pathways, TRPL spectroscopy was employed. All samples exhibit biexponential PL decays with slow and fast decaying components (Table 3.2), where the fast decays are most likely associated with surface and interfacial nonradiative recombination.[111] The CdSe aerogels exhibit PL decay times (τ_{slow}) of 1.83 ± 0.03 ns and 1190 ± 120 ns for the band-edge and trap state emission bands (Figure 3.17D), respectively, which are consistent with the literature reports.[112] The corresponding decay times of CdSe/Ag hybrids with 0.27 % Ag are 1.38 ± 0.05 ns and 944 ± 50 ns, respectively (Table 3.2). Interestingly, the main emission peak of the hybrid (640 nm) exhibits PL decay time of ~600 ns, which is significantly longer than that of the band-edge yet much shorter than that of the trap state emission. To better understand the evolution of new emission, time integrated PL spectra were recorded (Figure 3.20). For CdSe/Ag hybrids (0.27 % and 0.53 % Ag), band-edge emission (550 nm) is predominant at the initial stages of the carrier recombination (integration time 50 – 100 ns) because of its faster decay time. However, at longer time windows (integration time 200 ns–6.25 μs), band-edge emission is less predominant

and the new emission at 640 nm dominates. It is important to note that at different Ag loading (0.27–0.53 %), although the band-edge and trap state emission peaks are very weak in steady-state PL spectra (Figure 3.17A-C), their presence has been further confirmed by TRPL decay measurements (Figure 3.17E-F). Despite significant changes in absorption properties with increasing Ag composition beyond 0.53% (Figure 3.16), no change in emission properties were noted up to 1.83 % Ag incorporation. All these observations support the view that the origin of new emission peak is a result of an alternate relaxation pathway introduced by incorporation of Ag NPs in the CdSe gel framework.

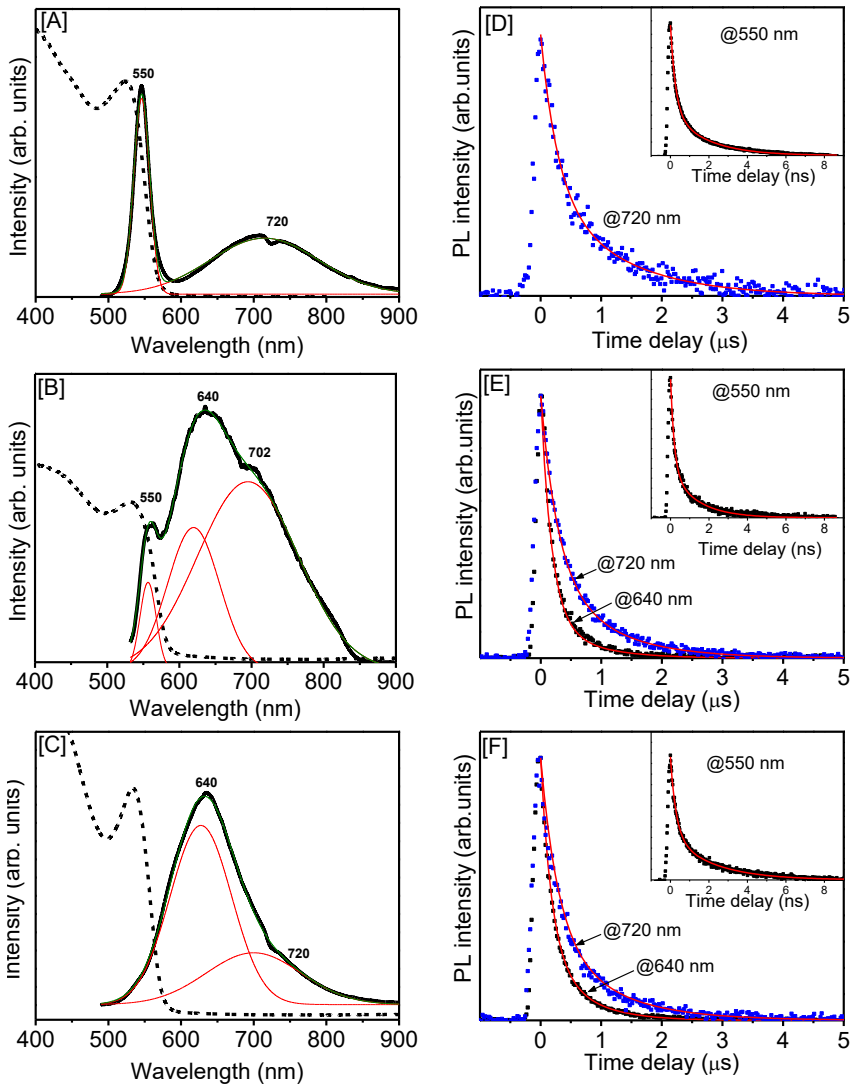

Figure 3.17 Solid state absorption and PL spectra of CdSe/Ag hybrid aerogels with [A] 0.00, [B] 0.27 and [C] 0.53 % Ag incorporation (ICP-OES analysis) along with the corresponding TRPL decay spectra probed at band edge (550 nm) and trap state (720 nm) of CdSe aerogels and at the hybrid emission maxima (640 nm). In [A–C], the black lines are spectral data, the red lines are fitted Gaussian peaks, and the green lines are the sum of all fitted peaks. The solid red lines in the TRPL decay spectra [D–F] represent the double exponential fits. The absorption spectra were recorded at 300 K whereas the PL and TRPL spectra were recorded at 15 K.

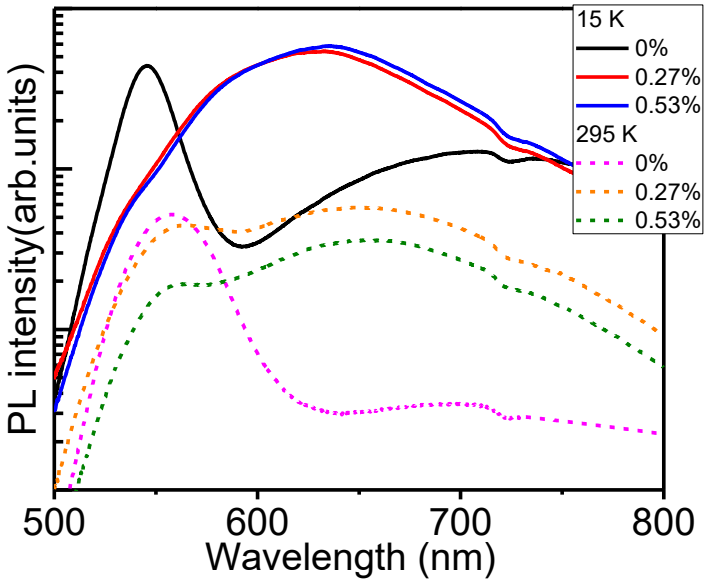

Figure 3.18 Photoluminescent spectra of CdSe and CdSe/Ag hybrids consisting 0.27% and 0.53% Ag loading at 15 K (solid lines) and 295 K (dotted lines). The emission maxima of 550 nm, 640 nm and 720 nm are visual at 295 K whereas at 15 K the 550 nm peak is not prominent but is still visible as a shoulder.

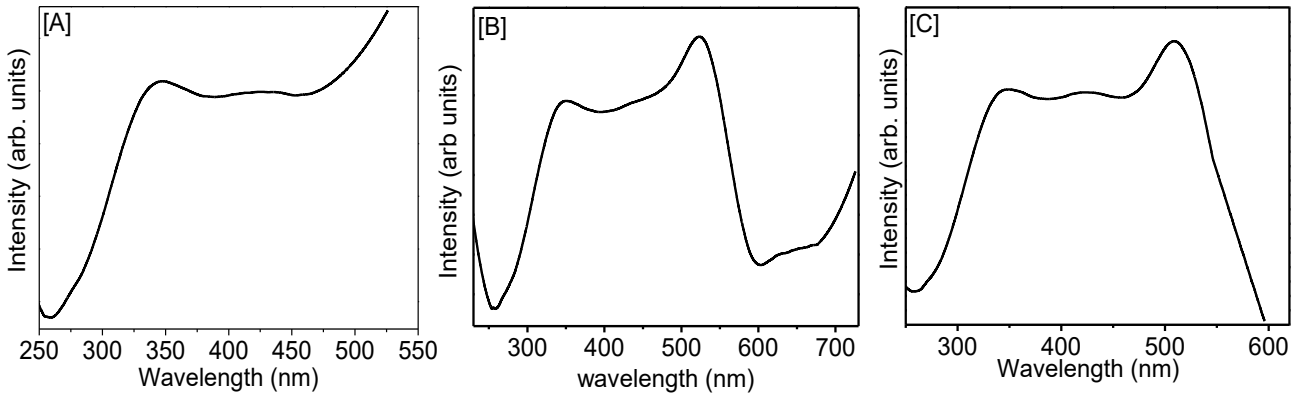

Figure 3.19 PLE spectra of [A] 550 nm, [B] 720 nm, and [C] 640 nm emission maxima of CdSe/Ag aerogels displaying 0.27% Ag composition (ICP-OES analysis).

Table 3.2 Decay times and amplitude ratios obtained from biexponential fits, $A_{fast}\exp\left(-t/\tau_{fast}\right)+A_{slow}\exp\left(-t/\tau_{slow}\right)$, to all observed emission wavelengths of CdSe/Ag aerogels with different Ag loading. The elemental compositions were obtained from ICP–OES analysis.

Band-edge emission of the CdSe/Ag hybrids[a]			
Ag composition	τ_{slow} (ns)	τ_{fast} (ns)	A_{fast}/A_{slow}
0.00 %	1.83 ± 0.03	0.26 ± 0.01	1.94
0.27 %	1.38 ± 0.05	0.2 ± 0.01	1.95
0.53 %	2.18 ± 0.06	0.3 ± 0.01	1.75
New emission peak of the CdSe/Ag hybrids[a]			
0.27 %	685 ± 76	177 ± 6	5.15
0.53 %	596 ± 17	174 ± 3	2.35
Trap state emission of the CdSe/Ag hybrids[a]			
0.00 %	1190 ± 120	280 ± 28	1.37
0.27 %	944 ± 50	277 ± 12	1.75
0.53 %	986 ± 83	285 ± 19	1.76

[a] Spectral windows used in the TRPL measurements are 500-560 nm for the band-edge emission, 600-660 nm for the hybrid emission, and 660-750 nm for trap state emission. The average decay times obtained at different spectral windows are shown with standard deviations.

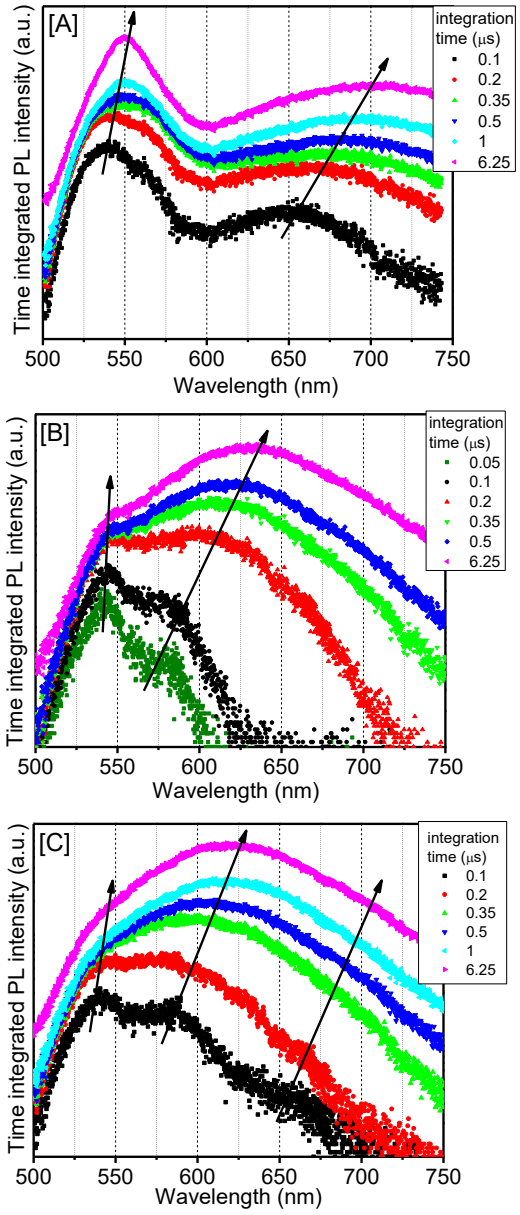

Figure 3.20 Time integrated photoluminescence (PL) spectra of CdSe/Ag aerogels with [A] 0.00, [B] 0.27, and [C] 0.53 % Ag composition probed with different integration time intervals, where the band-edge and trap state emission peaks are clearly observed along with the emission at 640 nm at earlier stages of carrier recombination. With progression of time the 640 nm peak becomes dominant over the 550 nm and 720 nm peaks.

To explore a possible reasoning behind the formation of the hybrid emission two additional studies were conducted. Since FRET has been shown to depend on the energetic overlap of the donor/acceptor pairs, the CdSe/Ag hollow NP aerogels were produced to match the plasmonic absorption with the first excitonic energy.[95b, 108] The change in plasmon energy had no discernible effects on the hybrid emission, nor did the hollow NP shape affect the gel structure. Further discussion of this study is provided in the Figure 3.21.

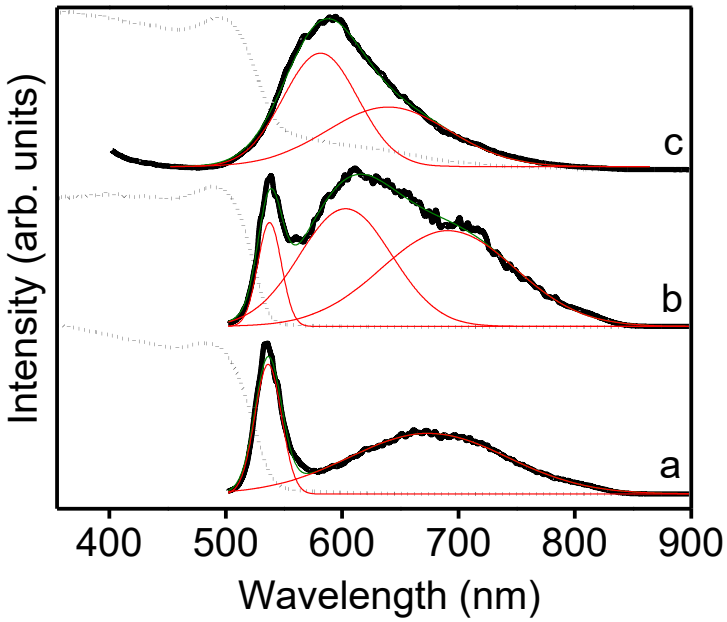

Figure 3.21 Solid state absorption (dotted lines) and PL spectra (solid lines) of (a) CdSe aerogels along with CdSe/Ag hollow NP hybrids containing (b) 0.17 % and (c) 0.65 % Ag composition (obtained through ICP-OES analysis). The red and green solid lines are the fitted Gaussian peaks and the sum of all fitted curves, respectively. The absorption and emission data were collected at 300 K and 77 K, respectively.

The lack of changes in the hybrid emission with varied plasmon energies prompted another study to explore the effects of changing the metal-semiconductor interfaces. Hybrid gels of CdSe/Au were studied at similar loading concentrations as in the case of CdSe/Ag gels. Although the plasmonic (535 nm) and excitonic energies (531 nm) were matched (Figure 3.22) as in the CdSe/Ag hollow NP aerogels and similar gelation was noted, no trends in optical properties were observed through solid state absorption and PL studies (Figure 3.23). Unlike the CdSe/Ag aerogels, the absorption spectra of the CdSe/Au aerogels show no red shifting, but systematic quenching of the emission with increasing Au content. Similar to previous studies on CdTe/Au aerogels,[97] strong PL quenching was noted even at low Au NP loadings (0.14–1.92% , Figure 3.24).

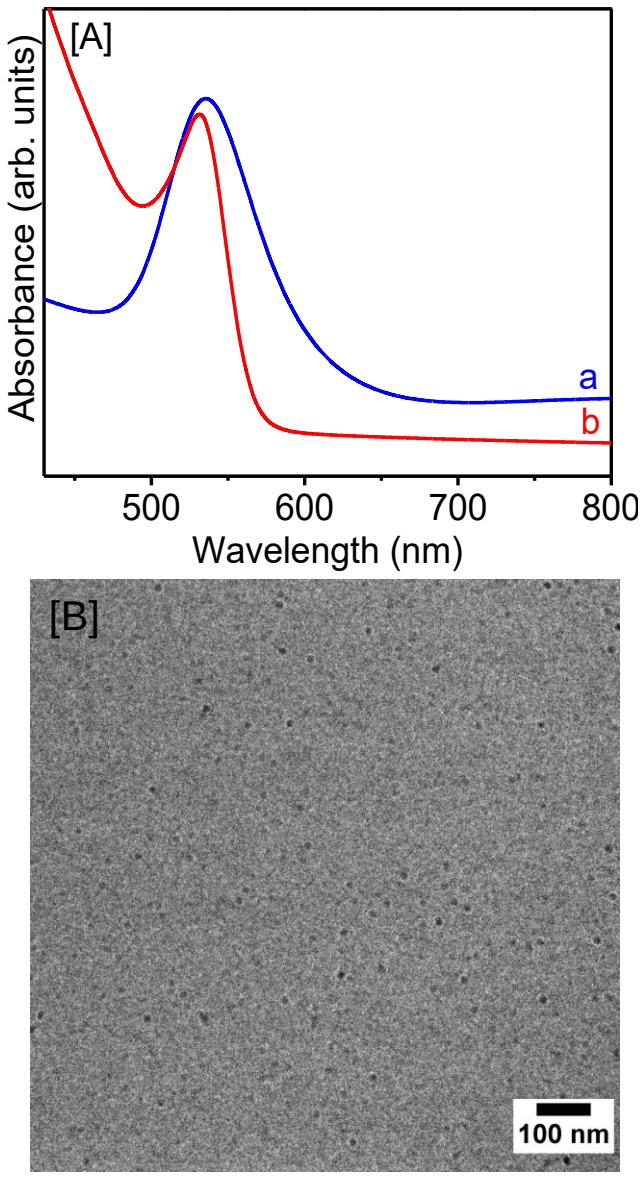

Figure 3.22 [A] Normalized UV-visible absorption spectra of (a) Au and (b) CdSe NPs representing the overlap of plasmonic resonance of (Au NPs) with first excitonic absorption of (CdSe NPs). [B] A low resolution TEM image of the thiolate-capped Au NPs.

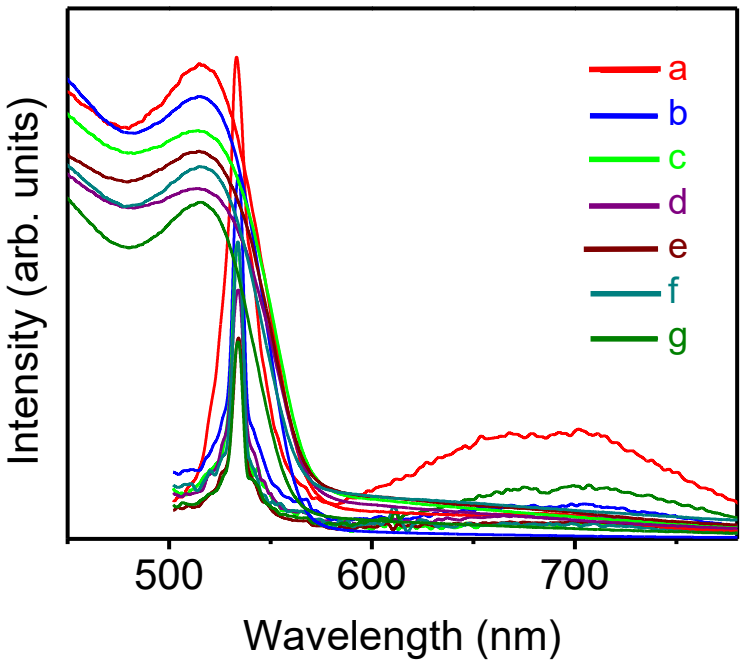

Figure 3.23 Solid state absorption and PL spectra of CdSe/Au hybrid aerogels containing (a) 0.0, (b) 0.14, (c) 0.28, (d) 0.36, (e) 0.45, (f) 0.98, and (g) 1.92 % Au composition. The compositions of the hybrids were investigated by ICP-OES analysis.

The exact reason behind the different behaviors of Ag and Au in the gel structure has not yet been fully elucidated. However, a few possible explanations can be proposed based on general semiconductor-metal interface theories. One potential reason is the difference in Fermi energy level (E_f) positions of Au *vs.* Ag with respect to the conduction band (CB) and valence band (VB) of CdSe NPs.[97] The different Schottky barrier heights formed between CdSe/Ag and CdSe/Au would lead to differences in unique interface states within CdSe's bandgap. However, ideal Schottky barrier theory is a poor model to interpret actual interfaces due to chemical interactions. It is well known that chemical reactivity also plays a role in metal-semiconductor interfaces and can result in lowering the Schottky barrier heights.[107] During the gelation process

surface ligands are oxidized off and free active sites are created. When the metal and semiconductor NPs come in contact they will link together via Cd-metal or Se_n^{n-}-metal interfacial bonds. Similar Cd-Se_n^{n-} surface states and interparticle linkages are reported to exist in phase pure CdSe aerogel superstructures.[104] From the comparison of heat of formation of AuSe (1.36 eV/metal atom) and Ag_2Se (0.52 eV/metal atom)[107] bonds, it can be anticipated that Ag will more readily bond to Se relative to Au. Furthermore, it has been shown that Au is one of the least reactive metals with respect to CdSe and while Ag is also considered unreactive it is more borderline to be reactive.[107] Previous studies on two component gel materials have shown an increased reactivity of nanosized metal domains,[113] which could allow for Ag with borderline reactivity to more easily produce Ag-Se^{n-} interfacial bonds. As such, the preferred linkage of silver-chalcogenide bonds could possibly facilitate more favorable merging of energy levels and subsequent electron transfer across the interface and potentially account for the different optical properties observed in CdSe/Ag and CdSe/Au hybrids. Further, the surface Ag-Se^{n-} linkages are likely to cause a reduction in quantum confinement due to the addition of extra atomic layers. Therefore, the emission from Ag linked CdSe NPs could possibly arise from radiative relaxation of the exciton via a lower energy CB-VB transition. In addition, if Ag linked CdSe NPs are acting as larger particles, several CB-VB energy transfers are possible, depending on the number of Ag NPs attached, causing the broad red emission. Further, it has been shown that dipole interactions between smaller and larger CdSe NPs can result in a long range energy transfer and increased PL from the larger NPs.[114] Likewise, the direct interparticle linkages present in CdSe/Ag aerogels are likely to provide an alternative direct tunneling pathway for

energy transfer. These interparticle energy transfers are likely to account for the lower energy and the increased lifetime of the hybrid emission. Further studies, which are beyond the scope of this work, are underway to more completely understand the metal-semiconductor interfaces in CdSe/Ag hybrids and their effects on optoelectronic properties.

3.4 Conclusions

We have successfully produced CdSe/Ag aerogels composed solely of nanosized constituents via co-gelation of precursor particles. Oxidative removal of surfactant ligands gives rise to close interfacial contact that has potentially generated the novel optical properties. Physical characterization on CdSe/Ag hybrids indicates, gelation has no apparent impact on the crystallinity and structure on the nanosized constituents. A systematic study on the evolution of optical properties of CdSe/Ag hybrids was performed via UV-visible, PL, and TRPL spectroscopies. PL and TRPL analyses of CdSe/Ag hybrids revealed the emergence of a new emission energy which has significantly different decay time from those of the band-edge and trap state emission of CdSe aerogels, suggesting the generation of an alternate radiative decay pathway. Gel morphology provides the opportunity to bring the NP surfaces in close contact, resulting in inter-mixing of their electronic states. Herein we introduced the co-gelation phenomena that optimizes the interfacial interactions of NP constituents to a moderate extent via the formation of fractal aggregates.

CHAPTER 4

Shape Controlled Synthesis of Au/Ag/Pd Alloy Nanoparticles and Their Oxidation-Induced Self-Assembly into Aerogel Monoliths

4.1 Introduction

Architecturally controlled noble metal nanoparticles (NPs) have gained significant interest due to their diverse applications in catalysis, electrocatalysis, chemical sensing, novel photonic devices, and drug delivery systems.[115] Despite significant efforts on the synthesis of such nanostructures, challenge remains in their self-assembly into macroscopic superstructures that exhibit unique and tunable physical properties. Among the numerous methods that have been investigated for the assembly of metal NPs, the most commonly developed strategies are covalent coupling of NP surface groups,[39a, 116] control evaporation of the solvent to produce ordered supercrystals[39b, 40] or non-ordered glassy films,[39d] and polymer or bimolecular mediated self-assembly.[39c, 117] Although each of these techniques has its advantages, the interactions between NPs are mediated by intervening ligands, the presence of which are detrimental for efficient electronic transport that limit performance in optoelectronic,[40, 118] electrocatalytic,[119] and chemical sensor studies.[120] Thus, it is of a critical need to find out a novel and efficient strategy that can conveniently manipulated for direct self-supported assembly of colloidal NPs.

Sol-gel technique provides a unique strategy to transform noble metal NPs into conducting networks, with direct interfacial connectivity, high surface area and

mesoporosity.[1] Removal of surfactant ligands during oxidation has been shown to construct self-supported NP monoliths that in most cases retain the physical properties of primary NPs.[1a-c, 40] The ability to create direct interfacial bonds contributes to enhance electrical and thermal transport[121] and tunable interparticle interactions,[53] expanding the potential range of NP technologies. Oxidative removal of surface ligands creates low coordinated active sites on the NP surface that interact with a nearby NP to reduce the surface energy. The formed active sites are highly reactive allowing the NPs to establish direct interfacial linkages, polymerize into low dimensional clusters, and consequently highly porous superstructures that augment the unique nanoparticulate properties. An added advantage of this synthesis is the production of porous nanostructures that can be tuned by manipulating the size and shape of precursor NPs.[38b] Because of inherent high surface area, mesoporosity, and high electrical conductivity,[122] aerogels composed of metal and semiconductor NPs exhibit excellent promise in catalysis,[57] sensing,[123] and light harvesting[124] applications. To date, oxidation-induced self-assembly has been investigated with metal chalcogenide, pnictide, Ag, Au–Ag, and Pt–Ag alloy or hetero-metallic nanostructures.[47b, 56, 125] However, construction of such superstructures composed entirely of ternary noble metal NPs has not been reported. In the present study, an extension of NP condensation strategy for direct cross-linking of Au/Ag/Pd alloy NPs into large, free-standing aerogel superstructures for electro-oxidation of ethanol is reported. The precursor alloy NPs (3-5 nm) with high energy facets and composition-tunable morphologies were produced by galvanic replacement reaction (GRR) of the thiolate–functionalized Ag NPs.

Over past two decades, a variety of synthetic methods have been developed for the production of nanostructured noble metal alloys.[17, 20b, 126] Higher cost and scarcity of the precious noble metals prompted the synthesis of low-cost alloy NPs, which in most cases exhibit comparable or superior physical properties to those of the single element metal NPs.[127] Despite significant advances in the synthesis of bimetallic alloy NPs, size and shape-controlled synthesis of ternary and quaternary noble metal nanostructures has not been thoroughly investigated. A few reports include Au/Pt/Ag,[17a] Au/Pt/Pd,[128] and Ag/Au/Pd[38a] alloy hollow particles and nanoboxes (20-50 nm) that exhibit enhanced catalytic performance in electro-oxidation of alcohols. Likewise, multi-metallic nanostructures composed of noble and non-noble elements have also been reported including PtPdCu,[126b] Pt-Ni-Cu[129] and Au@PdPt,[126a] Ag(Au)/CuPd,[17b] and Pd-Ni-Pt[130] alloys and core-shell nanostructures. However, to the best of our knowledge, a systematic study on the synthesis of significantly smaller (3-5 nm) ternary alloy NPs with control over morphology, composition, and tunable physical properties has not been reported.

Herein, we report the first wet-chemical synthesis of ultra-small (3-5 nm) Au/Ag/Pd alloy NPs displaying two distinct morphologies *via* step-wise galvanic replacement of the thiol-coated Ag NPs. A facile yet powerful strategy for direct cross-linking of ternary NPs into large, free-standing aerogel superstructures has been reported. The compositions of the NP monoliths were tuned by varying the oxidant/thiolate molar ratio of the sol-gel transformation reaction, which governs the acidity and dealloying effects resulting in Au and Pd rich alloy aerogels. The resultant metal aerogels exhibit extremely low density (0.02 – 0.06 g/cm^3), high surface area (282 – 80 m^2/g) and

mesoporosity (2–50 nm), and colloidal or polymeric gel morphologies that can be manipulated by varying the nanoparticulate building block. These self-supported nanostructures with direct interparticle connectivity and pristine active surface were investigated in the electro-oxidation of ethanol in alkaline medium. The alloy aerogels exhibit electrocatalytic activity that is ~20-30 times higher than those of the precursor NPs and excellent chemical and structural durability compared to commercial Pd/C catalyst, offering perspectives for a number of new technologies.

4.2 Experimental Section

Synthesis of GSH Functionalized Ag NP Templates

The glutathione coated Ag NPs were produced by employing a literature method with significant modification to scale up the synthesis.[56] In a typical reaction, 3 mL of 10 mM $AgNO_3$ and 300 µL of 10 mM GSH were added to 50 mL of ice cold milli-Q water. Then, 10 mL of 0.1 M NaOH was added to adjust the pH ~12 that resulted in a color change from colorless to pale yellow suggesting the formation of Ag_2O NPs. Finally, 3.6 mL of 10 mM $NaBH_4$ was slowly added at a rate of 0.5 mL min^{-1} to produce a yellow-brown solution of Ag NPs.

Synthesis of Au/Ag/Pd Ternary Alloy NPs Sol

To the Ag NP solution, 10 mL of 1.5 mM $PdCl_2$ and 10 mL of 10 mM AA were simultaneously injected at a rate of 1 mL min^{-1} *via* a syringe pump. The reaction color changed to dark brown suggesting the formation of Ag/Pd NPs. Finally, 10 mL of $HAuCl_4$ (0.25 mM) was added at a rate of 1 mL min^{-1} to produce Au/Ag/Pd alloy NPs. As-prepared Au/Ag/Pd NPs were purified and concentrated using centrifuge filtration to

produce 3 mM Au/Ag/Pd sol. The centrifuge filters (Sartorius, Vivaspin 20 mL MWCO 30000) filled with Au/Ag/Pd NP sol was centrifuged at 3500g for 7–8 min to reduce the volume to 2–3 mL. The concentrated sols were then mixed with 5–10 mL of milli-Q water and centrifuged to remove the residual byproducts (Na, NO_3^-, OH^-, and unreacted thiolates). This step has been performed multiple times to reduce the volume of the Au/Ag/Pd sol while retaining the colloidal stability of ternary NPs.

Synthesis of Au/Ag/Pd Alloy Hydrogels and Aerogels

The Au/Ag/Pd sol (3 mM) was divided into 2 mL aliquots and placed in glass vials. The gelation was induced by addition of 100 – 700 µL of 1% $C(NO_2)_4$ to 2 mL sols. The gradual condensation of the sol into opaque hydrogel was noted within 16-24 h. Varying amounts of the oxidant (1% $C(NO_2)_4$, 100 – 700 µL) were added to systematically study the dealloying effect.

The resulting hydrogels were aged for 2–3 days and the byproducts of the oxidation were removed by solvent exchange with acetone 4–6 times over 3–5 days. The Au/Ag/Pd aerogels were produced by CO_2 supercritical drying. Porous microcapsules (SPI Supplies Inc.) filled with acetone-exchanged hydrogels were loaded into the SCD dryer and filled with liquid CO_2 at 15 °C. The acetone treated gels were then exchanged with liquid CO_2. Finally, the CO_2-exchanged gels were dried at 40 °C for 18 min to produce monolithic Au/Ag/Pd alloy aerogels.

Electrochemical Measurements

For the electrochemical measurements, working electrodes were fabricated by depositing a thin film of nafion-impregnated alloy NPs, corresponding aerogels, or commercial Pd/C catalyst ink on glassy carbon electrodes (GCE, 5 mm in diameter or 0.196 cm^2 in area). A mixture of ~4.0 mg of the catalyst (ternary alloy NPs, aerogels, or Pd/C), 400 µL isopropanol, and 30 µL nafion were sonicated for 60 s to produce catalyst inks. Electrodes with a desired catalyst loading were fabricated by adding several coats of the catalyst ink onto GCE electrode surface. As-prepared working electrodes were dried in air after each addition of catalyst ink and further dried in a vacuum oven (50 ºC) for 12 h and stored in a desiccator.

The performance of ternary aerogels, precursor Au/Ag/Pd alloy NPs, and commercial Pd/C catalyst for electro-oxidation of ethanol was investigated by cyclic voltammetry (CV) and chronoamperometry on a CHI-401 electrochemical workstation (CH Instruments Inc.). The aqueous electrolyte solution (KOH, 1 M) was prepared with milli-Q filtered water. All test solutions were purged using high purity nitrogen for 1 h, prior to data acquisition. All electrochemical measurements were conducted in 1 M KOH containing 1 M ethanol in a conventional three-electrode cell at room temperature, under nitrogen atmosphere. The ternary alloy aerogel modified GCE and a Pt wire were used as working and counter electrodes, respectively. The potentials of the working electrodes were recorded against Ag/AgCl (1.0 M) (CH Instruments Inc.) reference. Activation of the modified GCE was performed by cycling in 1 M KOH solution from -1.0 to 0.2 V for 100 cycles at a scan rate of 50 mV s^{-1}. The effect of scan rate on the electro-oxidation of ethanol was investigated to probe the reaction mechanism. Stability and durability of alloy aerogel electrodes for oxidation of ethanol was evaluated by

chronoamperometry. The mass activities of aerogels were computed by dividing the oxidation peak current with the total mass of sample loaded onto working electrodes.

4.3 Results and Discussion

Understanding the mechanism of NP nucleation and growth is critical for the synthesis of nanostructures with desired sizes, morphologies, and physical properties. To date, only a handful reports discuss the nanoscale synthesis of ternary noble metal alloys.[38a, 38c] These studies investigate the synthesis of larger (20–50 nm) hollow NPs, cubes, or solid particles of Au/Ag/Pt,[131] Au/Ag/Pd,[38a, 132] and Au/Pd/Pt.[128] To the best of our knowledge, wet-chemical synthesis of significantly smaller (3–5 nm) Au/Ag/Pd alloy NPs with control over morphology and size dispersity has not been reported. Thus, initial efforts were focused on the synthesis of ternary alloy NPs with narrow size dispersity to understand the physical properties. Au/Ag/Pd alloy NPs were produced *via* galvanic replacement of sacrificial Ag NP templates.[56] The reaction of $AgNO_3$ with NaOH in presence of glutathione (GSH) was used to produce precursor Ag_2O seeds, which then undergo slow chemical reduction with $NaBH_4$ to produce Ag NPs (5.1 ± 1.1 nm). This conversion is accompanied by a visible color change from pale-yellow to yellow-brown and emergence of a surface plasmon resonance (SPR) maximum at ~400 nm (Figure 4.1).[53] As-prepared Ag NPs were used in the synthesis of Au/Ag/Pd alloy NPs displaying distinct elemental compositions. GRR provides a facile pathway for alloy formation among noble metals with significant difference in reduction potentials (Scheme 4.1).[38c, 133] Although Ag^+/Ag (0.80 V vs standard hydrogen electrode (SHE)) and Au^{3+}/Au (1.5 V vs SHE) exhibit a substantial difference in reduction potential that

results in spontaneous GRR, the smaller difference in reduction potential between Ag and Pd (Pd^{2+}/Pd = 0.951 V vs SHE) does not favor facile inter-diffusion. Thus, ascorbic acid (AA) was used as a co-reductant to facilitate the growth of Ag/Pd alloy NPs. This allowed the GRR to proceed in a controlled manner and provided a pathway to simultaneously manipulate the alloying and dealloying effects. It has been reported that oxidative corrosion of Ag^{+} during GRR can be minimized in the presence of AA, *via* co-deposition of Ag and Pd atoms to produce Ag/Pd alloy NPs.[38c] Thus with existing small difference in reduction potential, GRR proceeds between Ag and Pd leading to Ag/Pd alloy, which is evident from a slightly red shifted SPR maximum (Figure 4.1, 420 nm). This is further supported by the powder X-ray diffraction (PXRD), where a systematic shift in cubic Ag pattern towards higher 2θ angles is observed with increasing Pd (Figure 4.2). The introduction of $HAuCl_4$ to freshly prepared Ag/Pd NP sol further red-shifts the SPR maximum to 432 nm (Figure 4.1), suggesting the growth of Au/Ag/Pd alloy NPs. The molar ratio of elemental constituents has a significant effect on the morphology and optical properties of ternary nanoalloys. Controlled tuning of the molar ratio results in a systematic red-shifting of SPR specifically at higher Pd and Au concentrations. Conversely, a large plasmon damping effect is observed in both binary Ag/Pd and ternary Au/Ag/Pd alloy NPs at higher Pd concentrations that results in a rapid disappearance of SPR.[38c, 134]

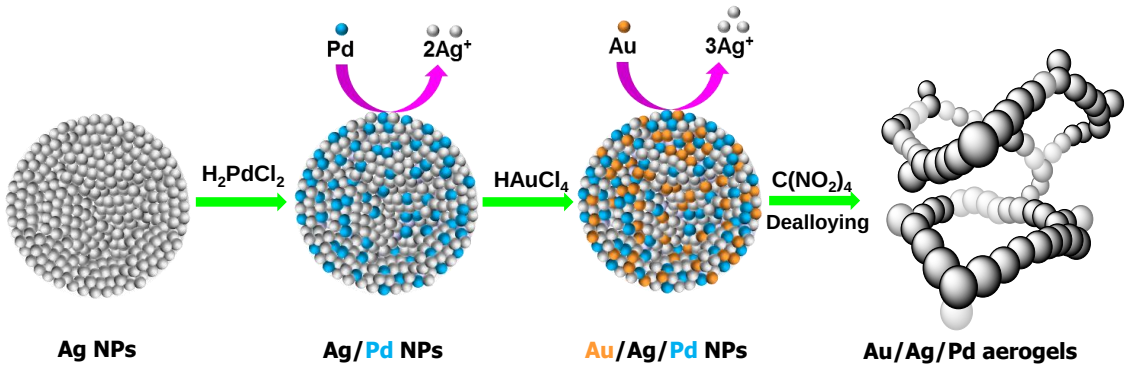

Scheme 4.1 A schematic illustration of the synthesis of Ag/Pd and Au/Ag/Pd alloy NPs *via* step-wise galvanic replacement reaction of GSH-functionalized Ag NPs, followed by oxidative self-assembly into monolithic Au/Ag/Pd alloy aerogels.

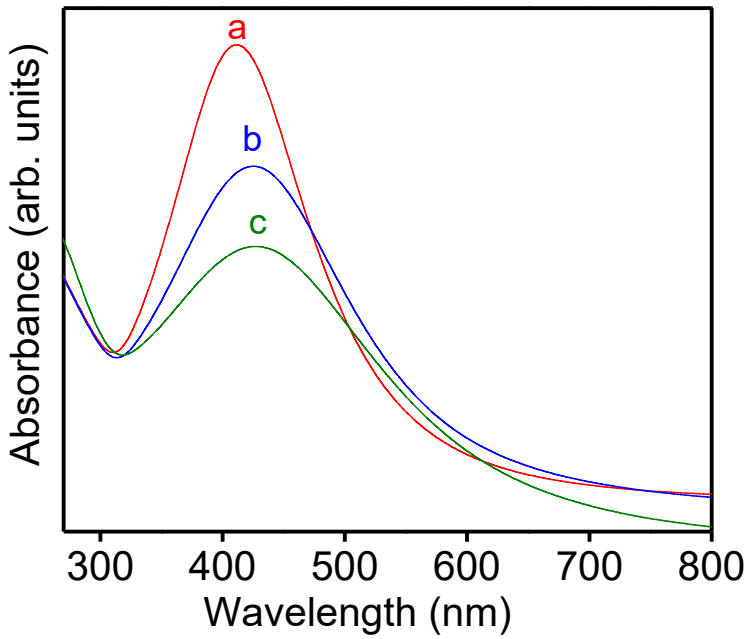

Figure 4.1 Normalized UV-visible absorption spectra of (a) Ag NPs along with (b) Ag/Pd and (c) Au/Ag/Pd alloy NPs produced *via* step-wise galvanic replacement of GSH-functionalized Ag NPs. The nominal molar ratio of Au:Ag:Pd is 0.5:3:2.

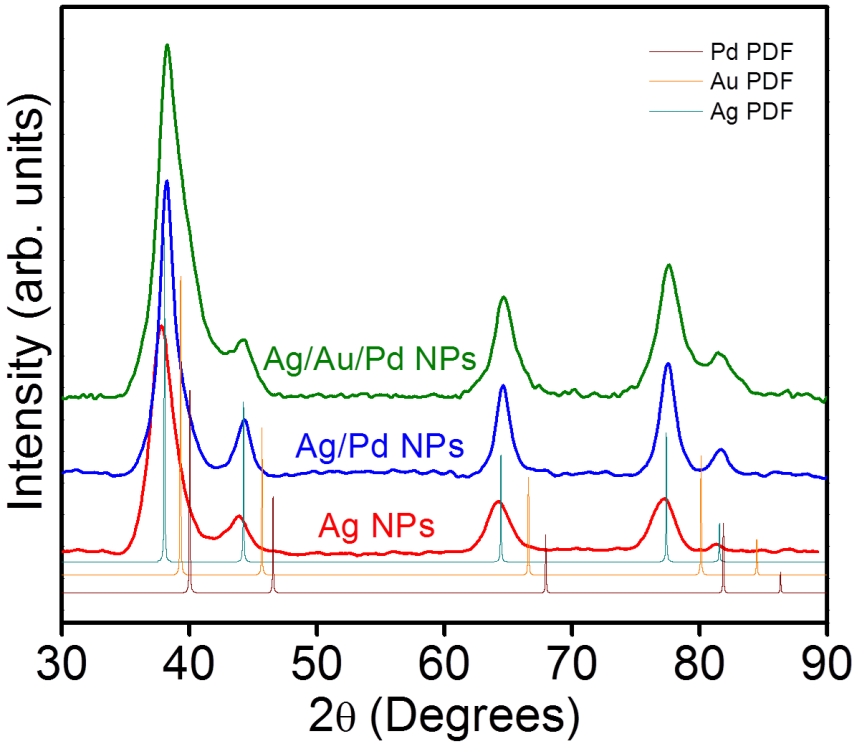

Figure 4.2 PXRD patterns of Ag NPs along with Ag/Pd and Au/Ag/Pd alloy NPs produced by galvanic replacement reactions. The ICDD-PDF overlays of cubic Ag (brown, 01-0870-719), Pd (cyan, 00-0040802) and Au (orange, 03-0658601) are shown as vertical lines.

Low resolution transmission electron microscopy (TEM) images of ternary alloy NPs exhibit a direct correlation between the morphology and composition (Figure 4.3 A). Thus, a thorough study has been conducted by varying the initial molar ratio to achieve two distinct compositions of Au/Ag/Pd alloys. While alloy NPs with higher Ag content (Au=30.9, Ag=59.8, and Pd=9.3 %) exhibit nearly spherical morphology with 4.8 ± 1.3 nm average diameter (Figure 4.3 A), alloys with lower Ag content (Au= 17.2, Ag = 23.5, and Pd=59.3 %) consistently produced anisotropic particles Figure 4.4. The alloy NPs exhibit single crystallinity with multiple facets visible *via* high resolution TEM (HRTEM)

images (Figure 2B). As evident from previous studies, GRR is a surface phenomenon that preferentially occurs at the edges resulting in highly faceted particles. It is anticipated that during GRR, inter diffusion of three elements (Ag, Pd, and Au) is highly random and spontaneous, which gives freedom to grow NPs in spherical to anisotropic shapes. High-angle annular dark-fields (HAADF) images and scanning transmission electron microscopy-energy dispersive spectroscopy (STEM-EDS) elemental maps were utilized to probe the atomic scale structure of nanoalloys. Representative data obtained from a single alloy NPs and large area of alloy NPs are shown in Figure 4.3. Overlay of the Au, Ag, and Pd maps indicate alloying and homogeneous solid solution behavior (Figure 4.3 D-F). Similar results were obtained from ternary NPs with other compositions further supporting the growth of Au/Ag/Pd nanoalloys.

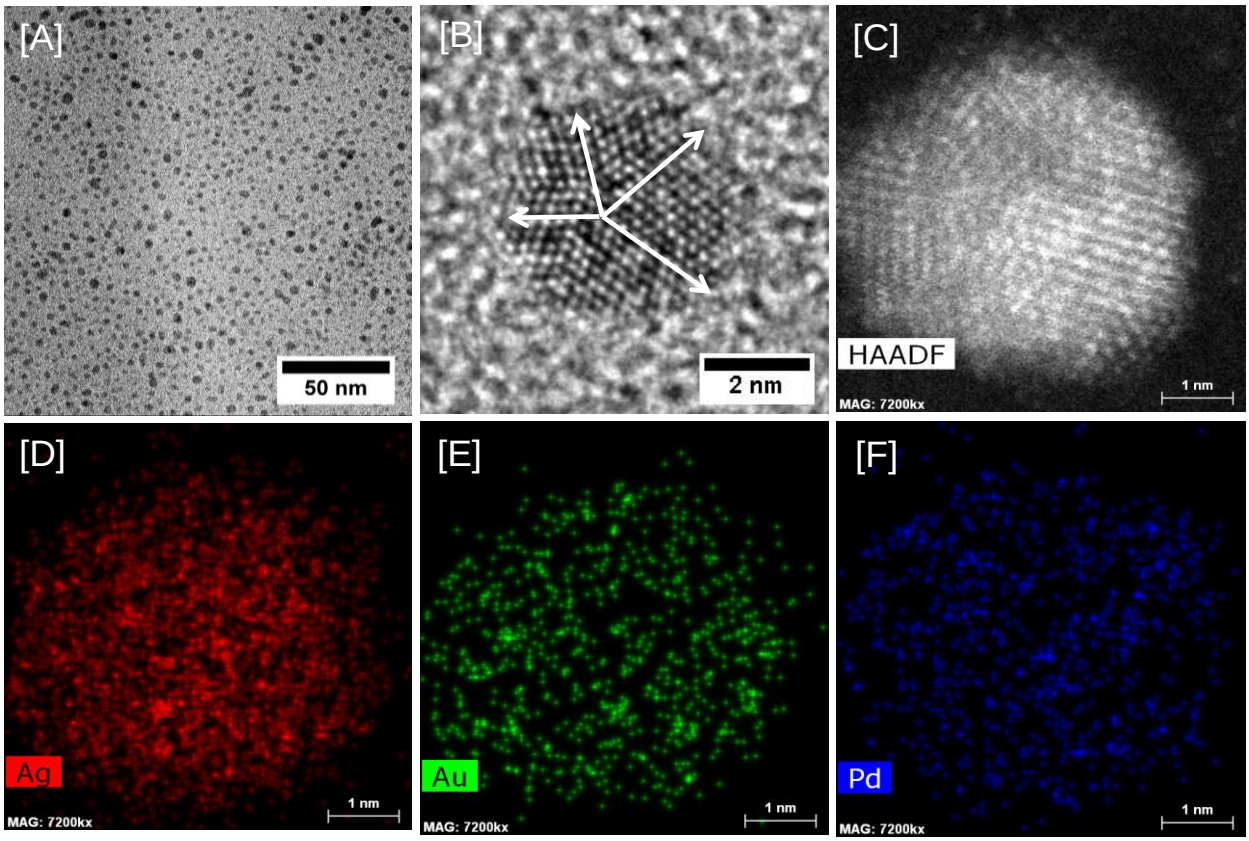

Figure 4.3 [A] Low resolution TEM image of spherical Au/Ag/Pd alloy NPs. [B] HRTEM and [C] STEM images of a single Au/Ag/Pd alloy NPs along with elemental maps of [D] Ag, [E] Au, and [F] Pd indicating the growth of homogeneous alloys.

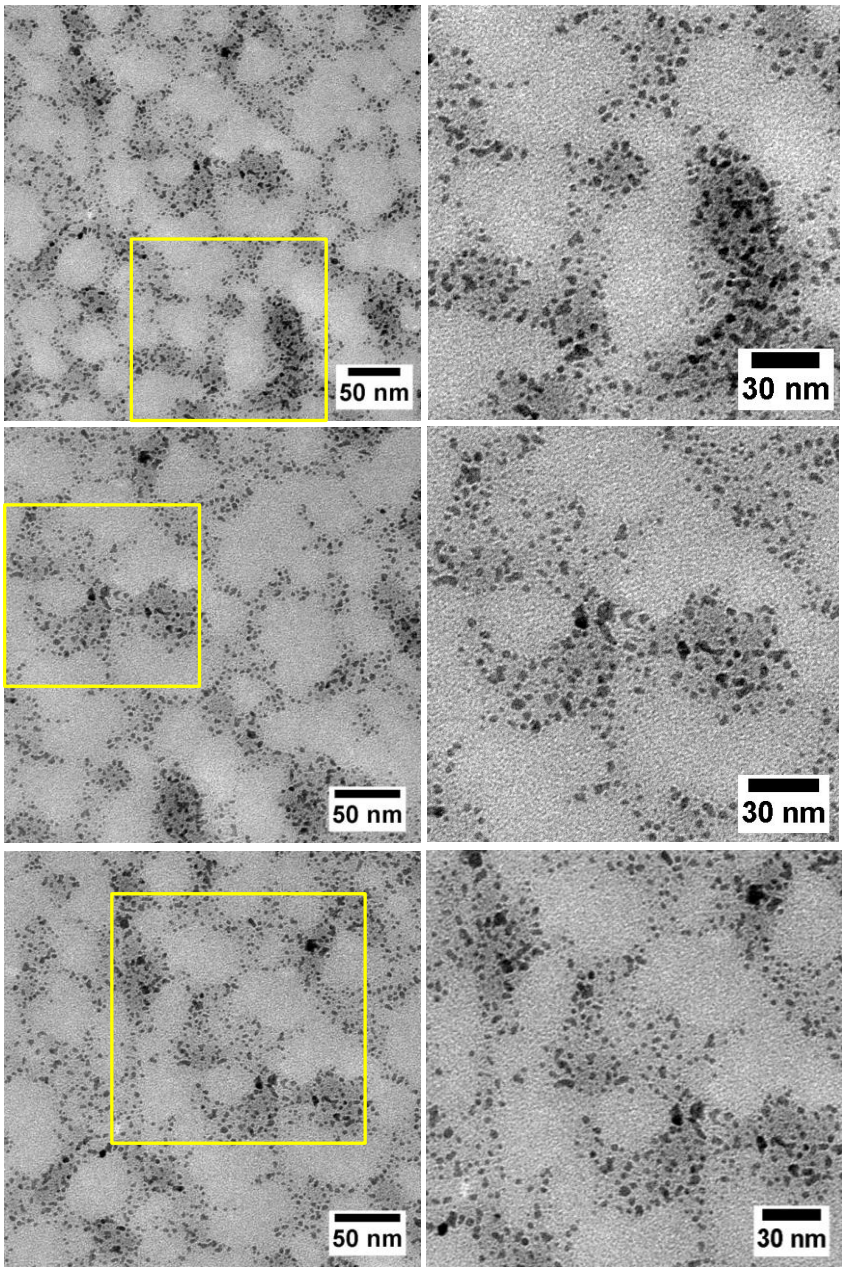

Figure 4.4 Low resolution TEM images of set II NPs produced at high concentration of Pd and low concentration of Ag (experiment compositions are Au : Ag : Pd = 17.2 : 23.5: 59.3 %) displaying the anisotropic shapes of as-synthesized NPs (average size = 4.4 ± 1.4 nm). The elemental compositions were obtained through ICP-OES analysis.

For gel formation, Au/Ag/Pd alloy NPs with two distinct elemental compositions were studied (nominal molar ratio of Au:Ag:Pd = 0.5:3:2 and 1:3:1). In all systems, molar ratio of Au, Ag, and Pd was tuned carefully to maintain the colloidal stability, which is of paramount importance for oxidative self-assembly. Concentrated colloidal sols of ternary NPs were produced by centrifuge filtration, where NP sols were purified by washing with ultrapure water to remove the ionic byproducts (Na^+, Cl^-, and BO^{2-}) of the synthesis.[56] The gelation was induced by introduction of 100–700 µL of 1% $C(NO_2)_4$. The addition of $C(NO_2)_4$ initiates the oxidation of the surface ligands (GSH) to sulfenyl nitrates ($GS\text{-}NO_2$) and disulfides (GS-SG) (equation 4.1 and 4.2).[56] The removal of surfactants creates low coordinated active sites that undergo direct interfacial linkage, producing a free-standing Au/Ag/Pd hydrogel (Figure 4.5). The use of $C(NO_2)_4$ produces HNO_3 as a secondary byproduct (equation 4.3 and 4.4) that facilitates the Ag dealloying. Thus, varying molar ratios of oxidant to surfactant (X = $C(NO_2)_4$/GSH) were employed to systematically investigate the dealloying effects. As prepared Au/Ag/Pd hydrogels were aged for 12 – 24 h under ambient conditions and exchanged with acetone to remove the byproducts of the oxidation. Finally, the acetone-exchanged wet gels were dried using supercritical CO_2 to produce monolithic Au/Ag/Pd aerogels. The ternary alloy aerogels are black color and show ~5 – 10% apparent volume loss compared to corresponding hydrogels. The densities of aerogels were 0.02 – 0.06 g/cm^3, which represent 0.32 – 1.0 % of those of the corresponding Au/Ag/Pd bulk alloys (13.25 – 15.39 g/cm^3).

$$GSH + C(NO_2)_4 \rightarrow GSNO_2 + C(NO_2)_3^- + H^+ \ldots\ldots\ldots (4.1)$$

$$GSH + GSNO_2 \rightarrow GS - SG + NO_2^- + H^+ \ldots\ldots\ldots\ldots\ldots (4.2)$$

$$3HNO_2 \rightarrow HNO_3 + 2NO + H_2O \ldots\ldots\ldots\ldots\ldots\ldots\ldots\ldots (4.3)$$

$$Ag + 2HNO_3 \rightarrow AgNO_3 + NO_2 + H_2O \ldots\ldots\ldots\ldots\ldots\ldots (4.4)$$

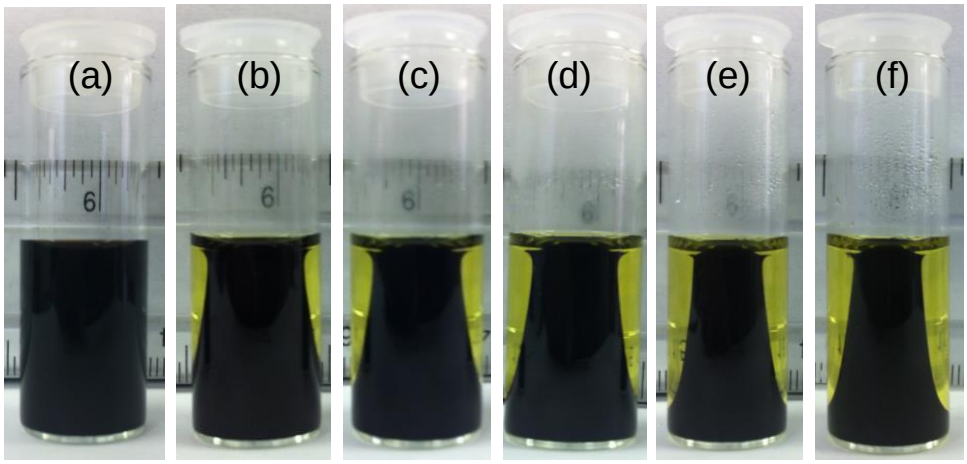

Figure 4.5 Photographs illustrating the gradual condensation of Au/Ag/Pd NP sol into free-standing hydrogels as a function of time: (a) concentrated Au/Ag/Pd NP sol, the hydrogels produced after (b) 6 h, (c) 12 h, (d) 24 h, (e) 36 h and (f) 48 h of oxidation of thiols. The oxidant/thiolate molar ratio is 1.7. Scale bar is in centimeters.

Powder X-ray diffraction was employed to probe the structure and crystallinity of Au/Ag/Pd NPs and aerogels. Characteristic peaks of face centered cubic Ag were shifted to larger 2θ angles, suggesting lattice contraction, consistent with alloying of Au and Pd. Despite the oxidation, PXRD patterns of aerogels showed no impact on crystallinity and crystal structure. No impurity peaks were detected corresponding to noble metal oxides or sulfoxides (Figure 4.6). However, significant peak broadening was noted with increasing the X value (up to X = 4.21), which led to shifting of PXRD

patterns to higher 2θ angles (Figure 4.6). Beyond X = 4.21, the diffraction patterns show poor crystallinity or amorphous-like structure. Nonetheless, HRTEM analysis of corresponding aerogels showed lattice fringes of 2.28 Å, confirming the short range crystalline order Figure 4.7. Thus, the poor crystallinity can be attributed to the dealloying of Ag from ternary alloy NPs (equation 4.4). Higher X values are expected to generate large amounts of HNO_3, promoting substantial dealloying and consequently producing significantly smaller, poorly crystalline particles.[56, 135] Continuous dealloying also results in a significant decrease in Ag content and as a consequence diffraction patterns become closer to that of binary Au/Pd. This observation has been further supported by elemental and surface analysis *via* inductively coupled plasma–optical emission spectroscopy (ICP-OES) and X-ray photoelectron spectroscopy (XPS), presented in Table 4.1.

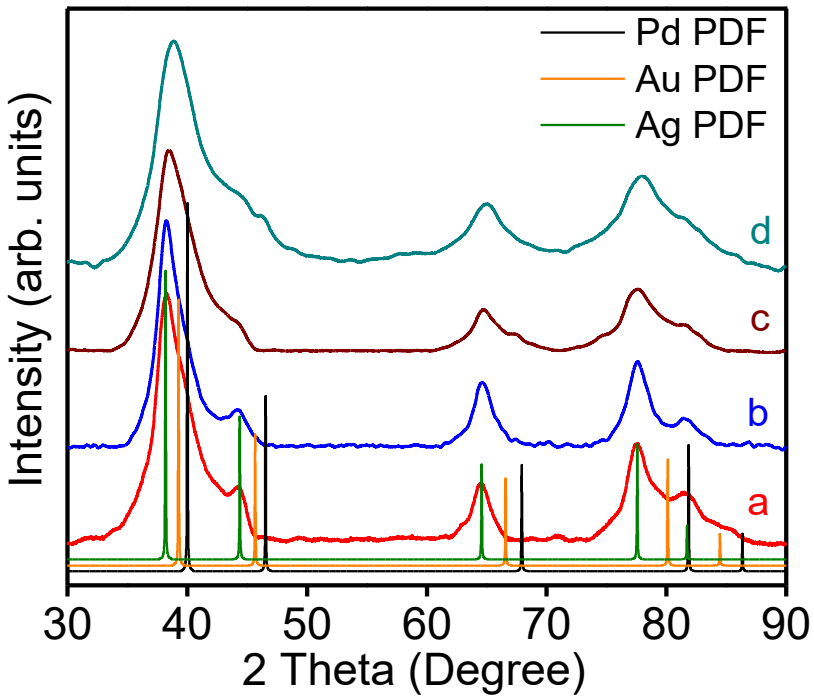

Figure 4.6 Powder X-ray diffraction patterns of (a) precursor Au/Ag/Pd alloy NPs along with Au/Ag/Pd alloy aerogels produced with X = (b) 1.05, (c) 2.14, (d) 3.15 and (d) 4.21. The ICDD-PDF overlays of cubic Ag (olive, 01-0870719), Pd (black, 00-0040802) and Au (orange, 03-0658601) are shown as vertical lines.

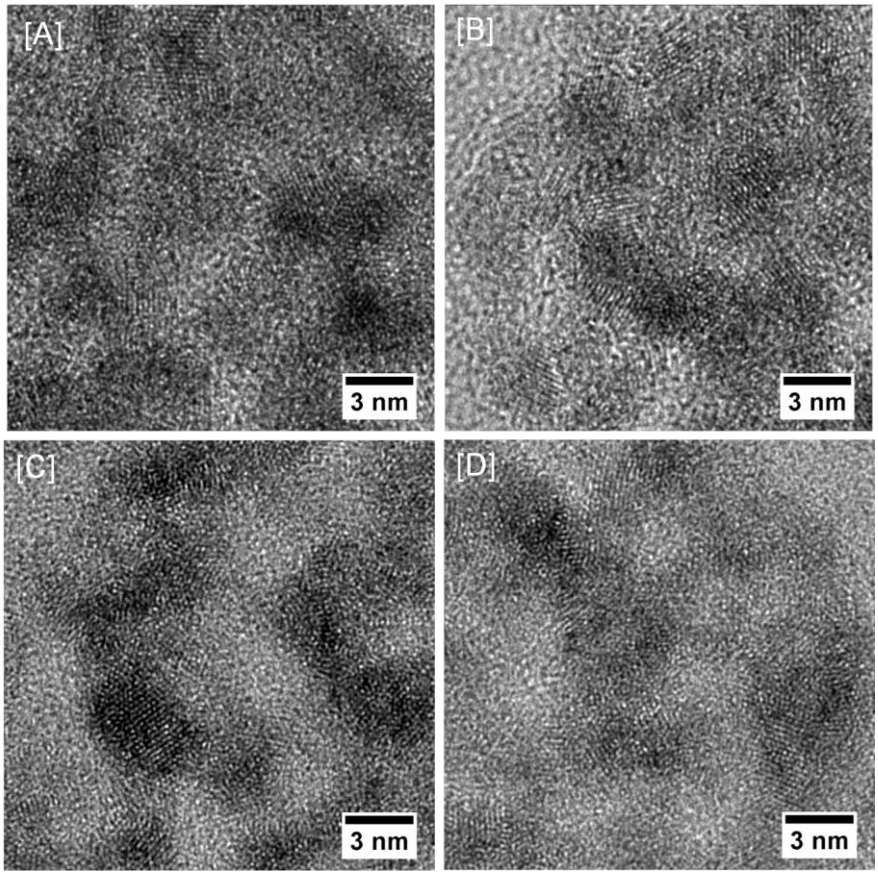

Figure 4.7 HRTEM images of Au/Ag/Pd aerogels (Ag = 26.9, Pd = 22.4, and Au = 50.7 %) produced at higher concentration of C(NO2)4 (X = 7.34) demonstrating short range crystallinity.

Table 4.1 Comparative Results of Crystallite Sizes, Average Particle Sizes, Elemental Compositions, and Wavelengths of SPR Maxima of the Au/Ag/Pd Alloy NPs and the Corresponding Aerogels along with Densities, Surface area, Average Pore Diameters, and Cumulative Pore Volumes of Ternary Alloy Aerogels.d

Sample			Au/Ag/Pd NPs	Au/Ag/Pd aerogel X = 1.05	Au/Ag/Pd aerogel X = 2.14	Au/Ag/Pd aerogel X = 3.15	Au/Ag/Pd aerogel X = 4.21
Crystallite size (nm)[a]			4.2 ± 0.2	3.8 ± 0.2	2.4 ± 0.2	2.3 ± 0.2	2.3 ± 0.2
Average particles size (nm)[b]			4.8 ± 1.3	5.6 ± 1.4	4.4 ± 1.3	4.3 ± 1.1	4.3 ± 1.2
Elemental composition (ICP-OES)[c]	Set I	Ag	59.8	58.2	52.8	29.3	24.7
		Pd	9.3	10.6	11.6	16.1	21.6
		Au	30.9	31.2	35.6	54.6	53.7
	Set II	Ag	23.5	21.4	20.3	23.7	21.5
		Pd	59.3	60.2	53.1	54.4	56.2
		Au	17.2	18.4	26.6	21.9	22.3
SPR maxima (nm)	Ag		410	N/A	N/A	N/A	N/A
	Ag/Pd		424				
	Au/Ag/Pd		430				
Density (g/cm^3)			N/A	0.02	0.05	0.06	N/A
Surface area (m^2/g)[d]			2.3	282	112	96	80
Average pore width (nm)[d]			16.7	9.3	11.8	16.1	11.3
Average pore volume (cm^3/g)[d]			0.004	0.70	0.36	0.43	0.25

[a] Crystallite sizes were calculated by applying the Scherrer formula to all diffraction peaks in the PXRD pattern.
[b] Average particle size were obtained by measuring the diameters of 120 – 150 particles from low resolution TEM image.
[c] Weight % of Ag, Pd, and Au were calculated based on ICP-OES analysis averaging 3 individually prepared samples.
[d] Brunauer–Emmett–Teller (BET) and Barrett–Joyner–Halenda (BJH) models were applied to the nitrogen adsorption/desorption isotherms to compute the surface area and porosity, respectively.

XPS was employed to study the chemical state of precursor NPs, aerogels, and to assess potential changes of surface properties during oxidative self-assembly. Supporting Information, Figure 4.8 shows the representative spectra of Au/Ag/Pd alloy NPs (Au=17.2, Ag=23.5, and Pd=59.3 %). Similar to previous studies,[56] there are two peaks present in the Ag (3d) spectrum that indicate a small amount of surface Ag^{+} (366.5 eV), bound to GSH ligands and a primary contribution from metallic Ag^{0} (367.7 eV)[56] from the core of the particles. Similarly, both surface Pd^{2+} (337.7 eV)[136] and Pd^{0} (335.2 eV)[136b] are evident suggesting that during the GRR, Pd is able to fully reduce into the core of the NP as well as deposit on the surface as Pd^{2+}, which can be passivated by GSH ligands. The Au (4f) spectrum indicates successful incorporation of Au^{0} (83.6 eV)[136] through GRR into the NPs and a minor signal from surface Au^{3+} (83.9 eV).[136] Examination of the N (1s), S (2p), and O (1s) spectra confirms the presence of the GSH ligand on the surface of the alloy NPs. Binding energies of both N (1s) 399.5 eV[137] and S (2p) 162.6[138] eV suggest amine and thiol binding to metal surface. The major peak in the O (1s) 531.4 eV[139] spectrum can be assigned to multiple C-O species typically adsorbed on the NP surface. The overlapping signal of Pd (3p) at 535.2 eV is consistent with the presence of Pd^{2+}. It is important to note that there is no indication of the metal-oxygen bonds, which would show up between 528-530 eV in the O (1s) spectrum.[139-140] This is consistent with results obtained from PXRD analysis, suggesting that Ag^{+} and Pd^{2+} are bound to GSH ligands and the absence of metal oxide impurities.

Upon gelation, a significant change in the chemical state of the alloyed metals was noted. For both Ag (3d) (368.0 eV)[56] and Au (4f) (83.8 eV)[136] there is only one species detected, which can be assigned to zero valent state (Figure 4.9 A-C). A similar effect

has been reported during the gelation of Ag NPs indicating the successful removal of surfactant ligands.[56] In contrast, the Pd (3d) spectrum indicates that Pd^{2+} (337.0 eV)[136a] is still present on the surface (Figure 4.9 B). However, the relative ratio of Pd^{2+}/Pd^{0} is greatly reduced from NPs to aerogels, suggesting that a major portion of the ligands were removed and the surface of the aerogels primarily consist of metallic Au, Ag, and Pd. This further proves the direct attachment of alloy NPs during oxidative self-assembly. However, the presence of a small amount of GSH was noted in the aerogels, which can either be bound to Pd^{2+} or even possibly trapped inside the porous network. Insignificant changes were monitored from the NPs to the aerogels in the N (1s) 400.0 eV[141] and S (2p) 162.3 eV spectra with both being consistent with the presence of residual, surface abound, or trapped GSH or GS-SG species (Figure 4.9 D-E). Similarly, the O (1s) (531.9 eV) peak did not significantly change after gelation. However, the overlapping peak of Pd (3p) is shifted to lower binding energy (532.5 eV),[140] which is consistent with a reduction in Pd^{2+} compared to Pd^{0}, as expected at 535.2 and 532.5 eV, respectively (Figure 4.9 F).[136b, 142]

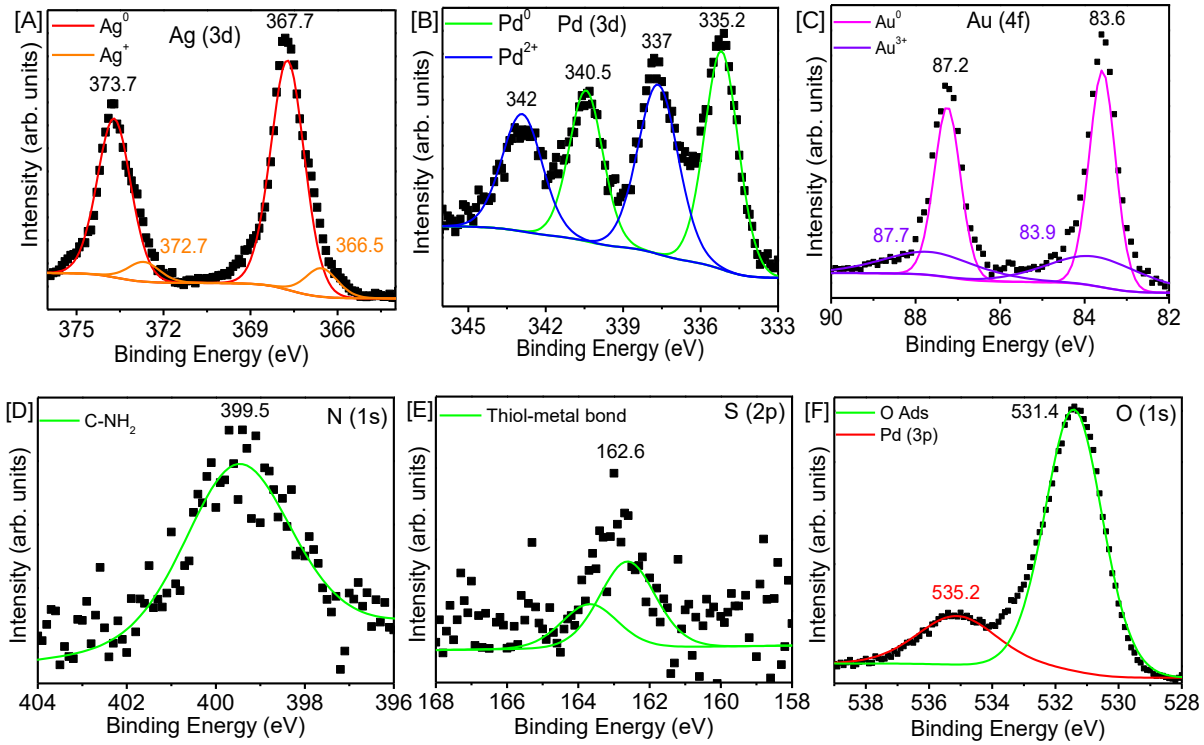

Figure 4.8 XPS spectra of set II Au/Ag/Pd alloy NPs (experimental compositions are Ag = 23.5, Pd = 59.3, and Au = 17.2 %) (A) Ag (3d), (B) Pd (3d) and (C) Au (4f) along with (D) N (1s), (E) S (2p) and (F) O (1s). The dotted symbols indicate the spectral data and the color lines are fitted deconvolutions. The elemental compositions were obtained through ICP-OES analysis.

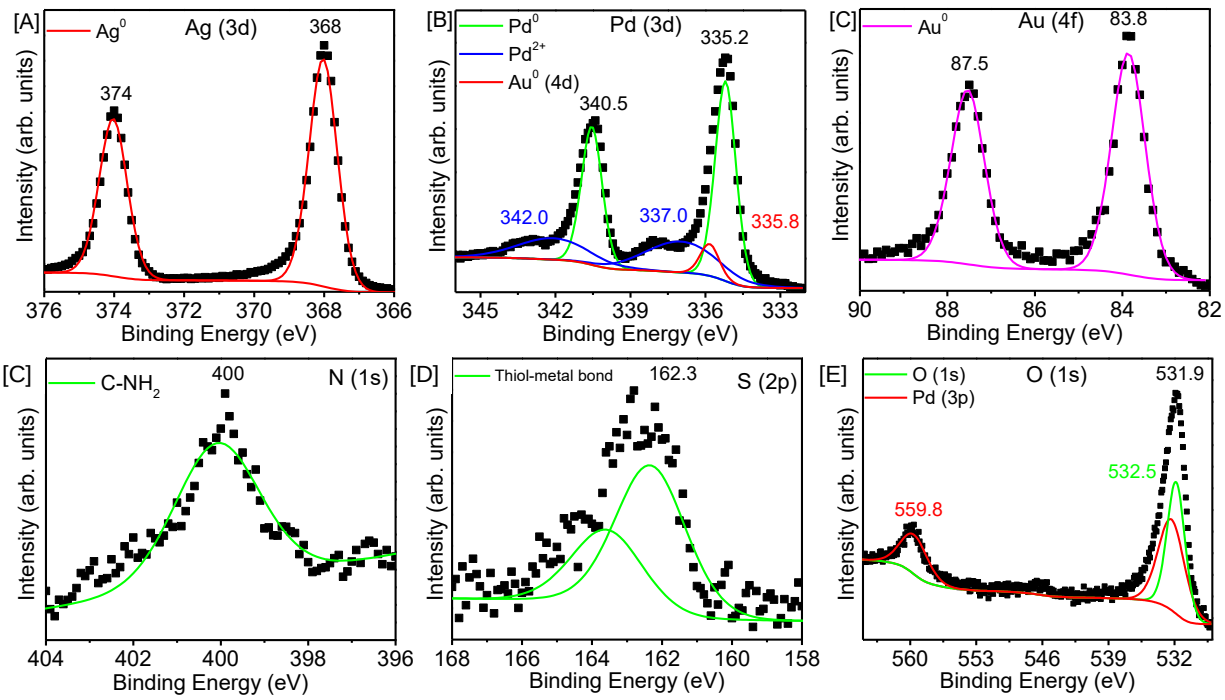

Figure 4.9 XPS spectra of Au/Ag/Pd alloy aerogel (A) Ag (3d), (B) Pd (3d) and (C) Au (4f) along with (D) N (1s), (E) S (2p) and (F) O (1s). The dotted symbols indicate the raw spectral data and the color lines are fitted deconvolutions.

Elemental composition of the precursor NPs and aerogels were investigated by EDS and ICP-OES. The close energy range of Ag (2.98 keV) and Pd (2.84 keV) causes a major overlap of the characteristic X-rays. Thus, ICP-OES was employed to probe the elemental composition of all samples. Two different sets were studied where set I consists of nominal Au:Ag:Pd molar ratio of 1:3:1 and set II with 0.5:3:2. In general, composition of the alloy NPs are in agreement with the initial concentrations of metal precursors employed in the synthesis. For both sets, different amounts of oxidant were introduced to facilitate the gelation and investigate the dealloying effects. Since the reaction of $C(NO_2)_4$ with GSH produces HNO_3, the amount of $C(NO_2)_4$ governs the

dealloying of Ag from ternary NPs. Thus, a quantitative measure of the *in-situ* generated HNO_3 was carried out by measuring the pH of the supernatant solution. For set I aerogel, where the initial concentration of Ag is higher, a linear decrease in the Ag content was noted with increasing $C(NO_2)_4$ while the Pd content is increased from 9.3 to 21.6 % (Figure 4.10 A). In contrast, for set II aerogels, where the initial Pd content is higher, the concentration of Ag remained almost constant, regardless of dealloying (Figure 4.10 B). To further investigate the dealloying effects, an excess amount of oxidant was introduced (X = 7.34, pH = 2.1) to set II alloy NPs, yet no significant changes were observed in the Ag composition. At higher Pd concentrations, GRR had already removed large amount of Ag to accommodate the Pd adatoms. Afterward, even though higher amount of HNO_3 was produced no substantial dealloying of Ag is noted. This behavior suggests that certain Ag amount cannot be removed from alloy NPs regardless of the concentration of HNO_3 (up to pH ≥ 2.1). However, Lu et al.[135] reported the complete dealloying of Ag from Au/Ag alloy nanocubes using an external wet-chemical etchant ($Fe(NO_3)_3$). It has been reported that the use of high concentrations of $Fe(NO_3)_3$ results in broken nanocubes with deformed shapes. This phenomenon further proves that certain concentration of Ag is necessary to maintain the original morphology of alloy NPs and complete dealloying of Ag may not be feasible with such low concentrations of HNO_3. Similar results were obtained in the synthesis of nanoporous Au electrodes, where 70% HNO_3 has been employed to partially dealloy bulk Au/Ag.[61, 143]

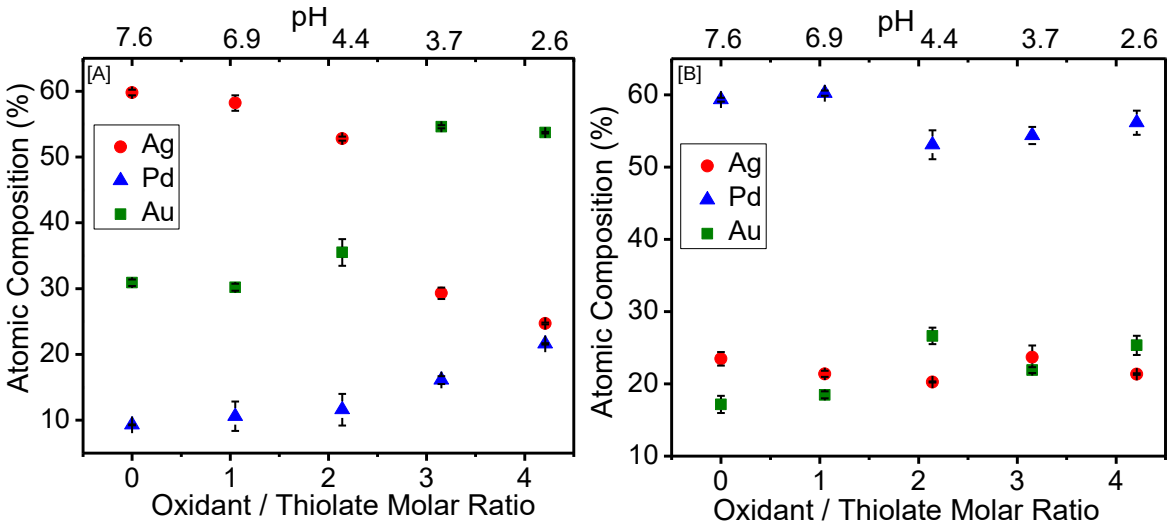

Figure 4.10 Elemental compositions of the alloy aerogels produced from (A) set I and (B) set II Au/Ag/Pd alloy NPs along with the oxidant/thiolate molar ratio and pH of the supernatant solution of corresponding hydrogels. The error bars indicate the variation in atomic composition for 3 individual prepared aerogel samples.

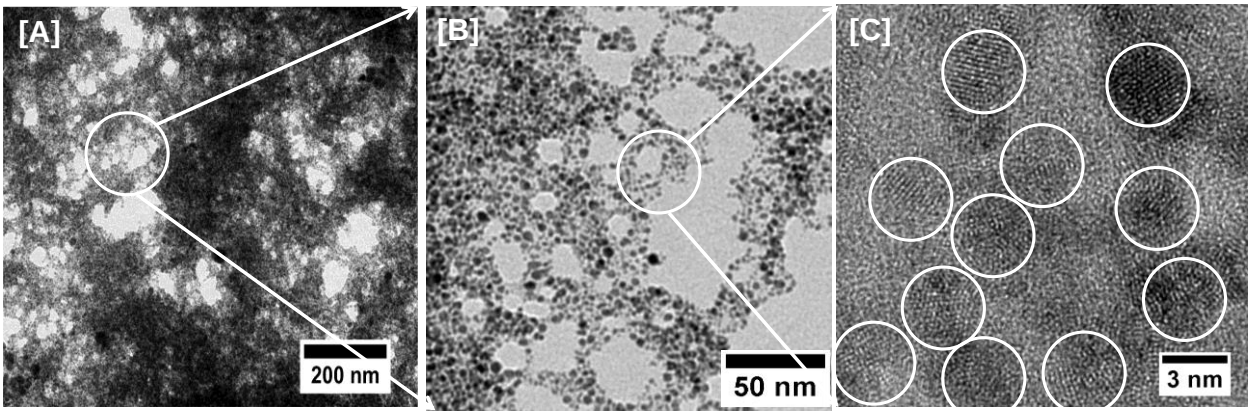

Figure 4.11 (A, B) Low and (C) high resolution TEM images of Au/Ag/Pd aerogels exhibiting porous morphology, where individual NP are directly interconnected to give rise a pearl necklace structure.

Low resolution TEM was employed to investigate the morphology of the ternary NPs and aerogels. As evident in Figure 4.3 A, set I alloy NPs exhibit spherical morphology and narrow size dispersity, which when assembled together, show meso- to macro-porous superstructure, consistent with prior reports of metal aerogels (Figure 4.11). The gel structure is composed of an interconnected network of ternary NPs that underwent direct cross-linking to produce pearl necklace array of particles. Furthermore, the multi-metallic nature of the aerogel has been proved through STEM-EDS elemental maps (Figure 4.12). For set I alloy aerogels, primary particle size shows a systematic decrease with increasing $C(NO_2)_4$, consistent with the results obtained from PXRD. However, the particle size in the gel framework is larger than the crystallite size calculated from Scherrer equation, which we attributed to crystallite growth during supper critical drying (SCD) drying. On the contrary, primary particles in the set II alloy aerogels produced a highly-branched wire-like network with a typical thickness of 4.1 ±

0.74 nm (Figure 4.13). This aerogel superstructure did not exhibit individual NPs separated from each other but rather a fused, wire-like morphology. To further investigate the growth of wires, morphological changes of precursor NPs were investigated at the initial stage of gelation (Figure 4.13). From HRTEM and HAADF images (Figure 4.14), the fusion of anisotropic NPs into chain-like, polymeric superstructure is noted. Furthermore, the average chain diameter (4.1 ± 0.74 nm) is similar to the size of primary NPs (4.8 ± 1.3 nm), suggesting the fusion of alloy NPs. It is anticipated that during gelation, Au/Ag/Pd adatoms undergo cohesive attraction with other surface atoms and can be fused together to produce a wire like morphology.[144] This polymeric morphology is believed to generate a number of grain boundaries, which is of great interest for catalysis. A similar morphology has been reported with other multi-metallic (Au/Ag and Ag/Pt) alloy aerogels produced *via* oxidative self-assmbly.[1d, 38b] Comparable results were also reported for CdSe/CdS nanorods, where tip to tip interactions of the precursor nanorods were evident upon direct cross-linking.[1d, 47e, 144] Despite significant differences in gel morphology, both nanostructures indicate the highly porous nature of the material consisting of a large number of mesopores and macroporous throughout the superstructure.

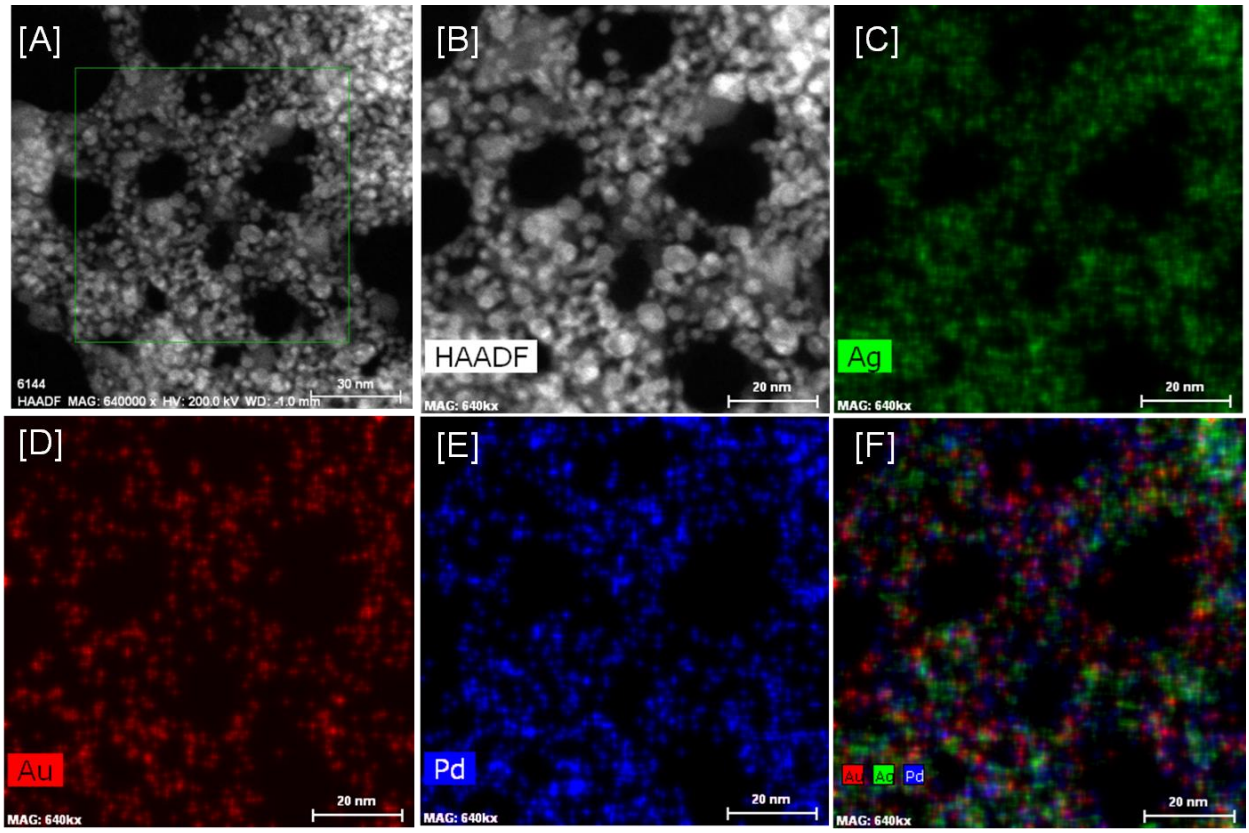

Figure 4.12 [A-B] High resolution STEM images of Au/Ag/Pd aerogels produced from set I alloy NPs along with elemental maps of [C] Ag, [D] Au, [E] Pd and overlay of [F] Ag, Au and Pd indicating the homogeneous distribution of elemental components throughout the superstructure. The elemental compositions (Ag = 58.2, Pd = 10.6, and Au = 31.2 %) were obtained through ICP-OES analysis.

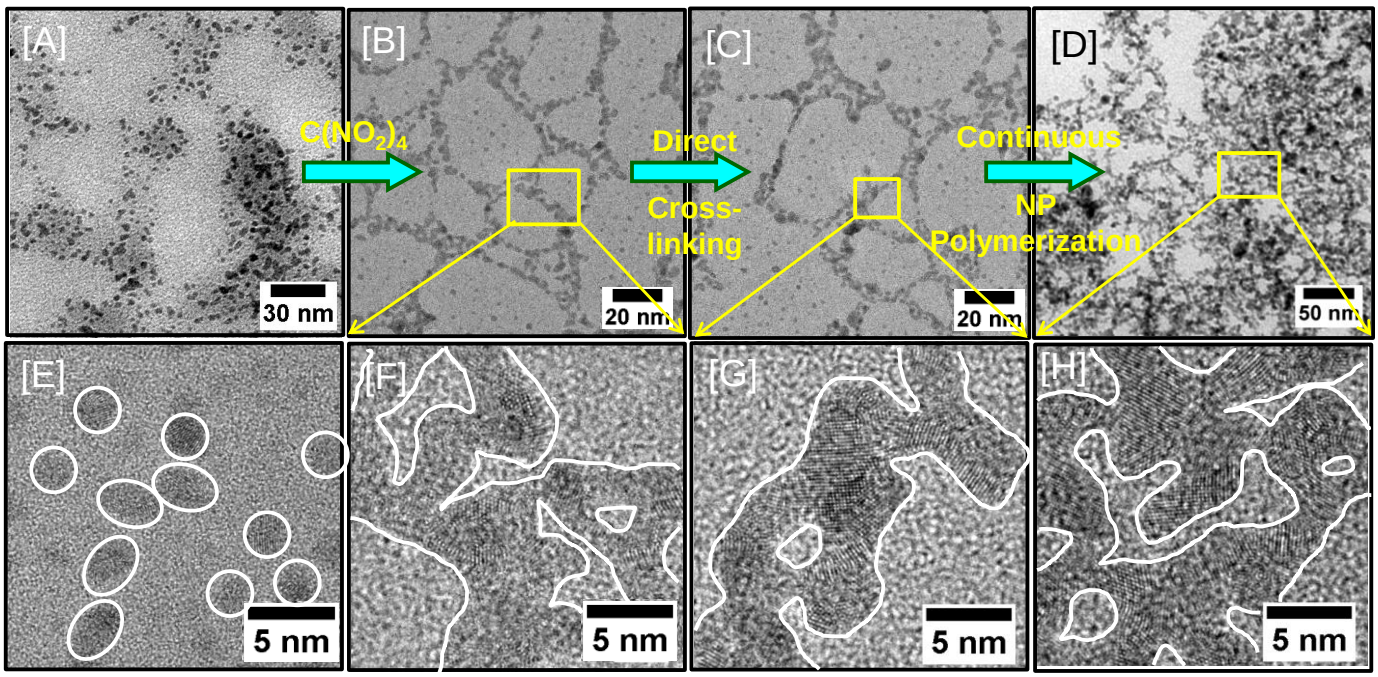

Figure 4.13 TEM images illustrating the morphological changes of set II alloy NPs upon oxidation-induced self-assembly. [A-E] GSH-stabilized Au/Ag/Pd alloy NPs, viscous NP sol produced after [B-F] 60 min and [C-D] 120 min addition of $C(NO_2)_4$ along with [D-H] Au/Ag/Pd alloy aerogels obtained after supercritical drying.

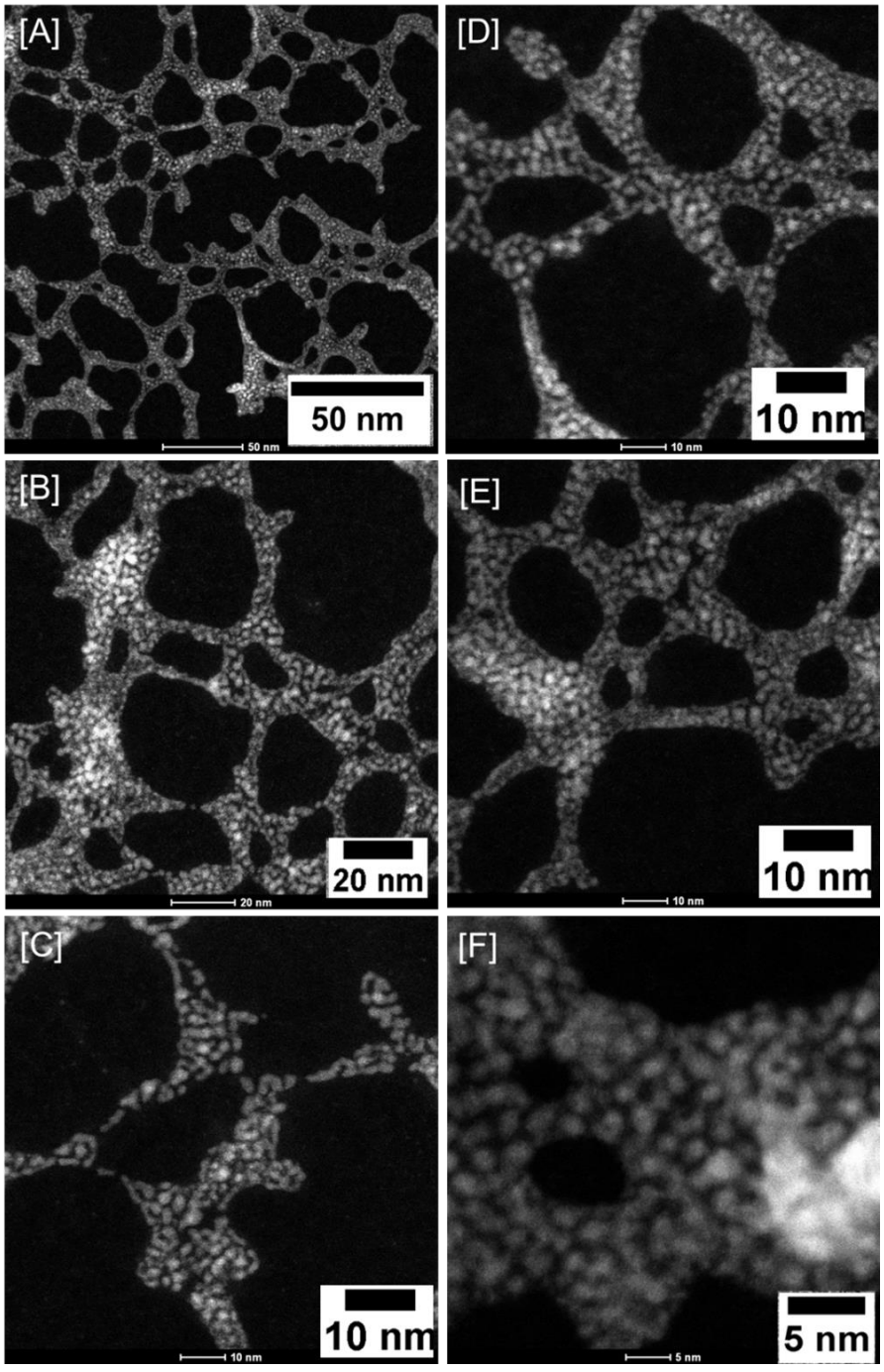

Figure 4.14 High angle annular dark field images of pre-oxidized sol of set II alloy NPs illustrating direct interparticle interactions and crosslinking during gelation. The elemental compositions (Ag = 23.5, Pd = 59.3, and Au = 17.2 %) were obtained through ICP-OES analysis.

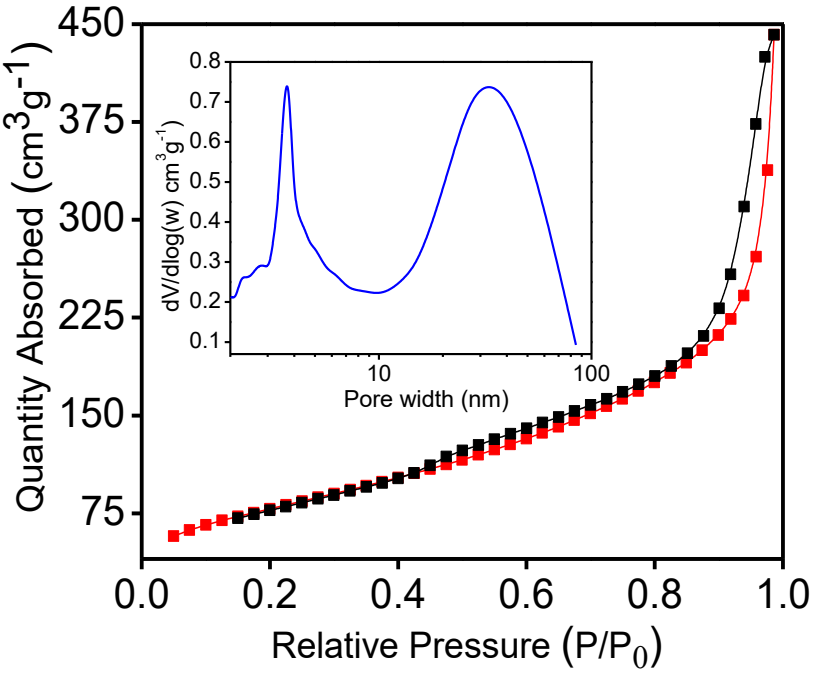

Figure 4.15 Representative nitrogen adsorption (red) desorption (black) isotherm of Au/Ag/Pd aerogels. The corresponding BJH model pore distribution plots is shown as an inset.

The low density and highly porous nanostructure of the alloy aerogels has been further confirmed by nitrogen adsorption/desorption isotherms (Figure 4.15). A typical isotherm of Au/Ag/Pd aerogels represents a combination of type IV and II curves, consistent with the formation of a meso-to-macroporous superstructure.[56] The hysteresis loops of all isotherms indicate a combination of H1 and H3 character, suggesting the presence of cylindrical and slit-shaped pore geometries.[56] The BET modeled surface areas of alloy aerogels are 282 – 80 m^2/g for X= 1.05 – 4.21. A significant decrease in surface area is noted with increasing concentration of $C(NO_2)_4$ owing to increased condensation of alloy NPs. The surface area obtained for Au/Ag/Pd

aerogels are much larger than those of the previously reported metal aerogels, suggesting significant potential in catalyst and sensor development.[1d, 47b, 145]

The pore size distributions of alloy aerogels were computed by applying the BJH model to desorption branches of nitrogen adsorption/desorption isotherms. Au/Ag/Pd aerogels exhibit a wide range of pores from meso- to macro-porous region, yielding average pore diameters of 9.3 – 16.1 nm and cumulative pore volume of 0.25 – 0.7 cm^3/g. Interestingly, two distinct pore distributions were noted in the ternary aerogels: one sharp feature centered around 3 – 5 nm and a broad distribution from 10 – 100 nm (Figure 4.15 inset). It is anticipated that during gelation, NP aggregates can be produced with smaller cavities with the simultaneous growth of larger pores (Figure 4.11, 4.13). Thus, the narrow pore distribution at ~3-5 nm likely represents the interparticle cavities, whereas the larger pore distribution likely corresponds to meso- to macro-pore network created by the 3-dimensional assembly of alloy NPs.

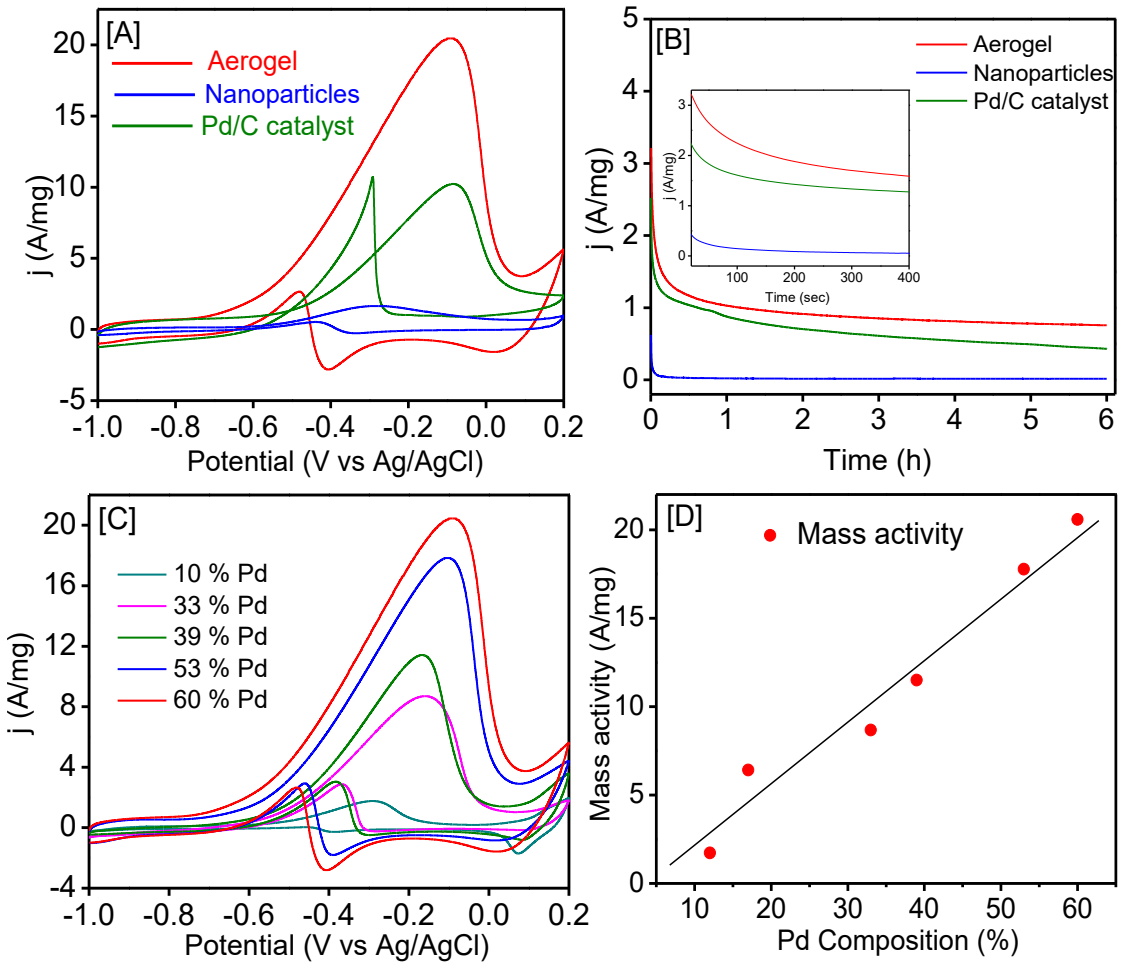

Figure 4.16 (A) Mass normalized cyclic voltammograms (CVs) for electroxidation of ethanol and (B) i-t curves (at constant potential of 0.3 V) of Au/Ag/Pd alloy NPs, corresponding aerogels, and commercial Pd/C catalyst. [C] Comparative CV (mass normalized) study of Au/Ag/Pd aerogels as a function of Pd content along with [D] corresponding mass activity plot. All measurements were carried out in 1 M KOH + 1 M ethanol solution at a 50 mVs^{-1} scan rate.

Au/Ag/Pd aerogels exhibit high electrochemical performance for electro-oxidation of ethanol in alkaline medium in comparison to commercial Pd/C (10 wt%). The CVs for

the electro-oxidation of ethanol at a scan rate of 50 mVs^{-1} are depicted in Figure 4.16 A. Two current peaks characteristic of ethanol oxidation can be identified in all voltammograms. The quasi-symmetric anodic peak around -0.1 V observed in the forward scan can be assigned to the oxidation of freshly adsorbed ethanol.[57, 146] A crucial parameter that determines the activity of the catalyst is the forward current density (I_f).[147] The low surface area and nonporous nature of precursor NPs accounts for the poor catalytic activity with I_f value ~one tenth of commercial Pd/C. On the other hand, ternary alloy aerogels exhibit ~ 20-30 times increase in current density compared to precursor NPs. The electro-oxidation of ethanol with ternary alloy aerogels is characterized by comparatively higher I_f value of 20.55 A/mg, which is twice that of the commercial Pd/C and almost similar to prior report on Pd aerogels.[57] A closer examination of the CV segments obtained in the forward scan shows that the accompanied peak potential (E_f) for the aerogel (onset potential of aerogel -0.56 V and Pd/C -0.43 V) is more negative than that of commercial Pd/C. The observed negative shift (~130 mV) in the onset potential reflects enhanced kinetics of ethanol electro-oxidation. During the reverse scan, similar trend (negative shift in the peak potential) was noted where anodic oxidation current peaks were recorded at -0.48 and -0.29 V for the ternary alloy aerogel and commercial Pd/C, respectively. This peak can be attributed to sweeping of the incompletely oxidized carbonaceous intermediates produced on the electrode surface during the forward potential sweep.[57, 146] The efficient oxidation of ethanol during anodic sweep and high tolerance of alloy aerogel for carbonaceous organic residues is reflected in the higher I_f/I_b ratio, which is ~ 8 times higher than the commercial Pd/C.[57] The observed high I_f/I_b ratio could be attributed to

the alloying effect with Au, which increases the stability of aerogels against poisoning effects.[146-147]

To monitor the effect of palladium content on the catalytic activity, a series of alloy aerogels were studied in the electro-oxidation of ethanol (Figure 4.16 C-D). With increasing palladium content (10 - 60 %) almost a linear increase in the forward current density, I_f/I_b ratio, and mass activity were noted. As indicated from the TEM study, aerogels with higher Pd content exhibit a wire-like (polymeric) morphology. This unique microstructure having pristine active surface and high energy crystal facets is believed to enhance the catalytic performance. To explore the mechanism of ethanol electro-oxidation, the relation of current density *vs* square root of the scan rate was constructed. The ethanol electro-oxidation by the ternary alloy aerogels is controlled by mass transport[57] at relatively fast scan rates (≥ 50 mV s^{-1}) where a linear relationship is observed as depicted in Figure 4.17.

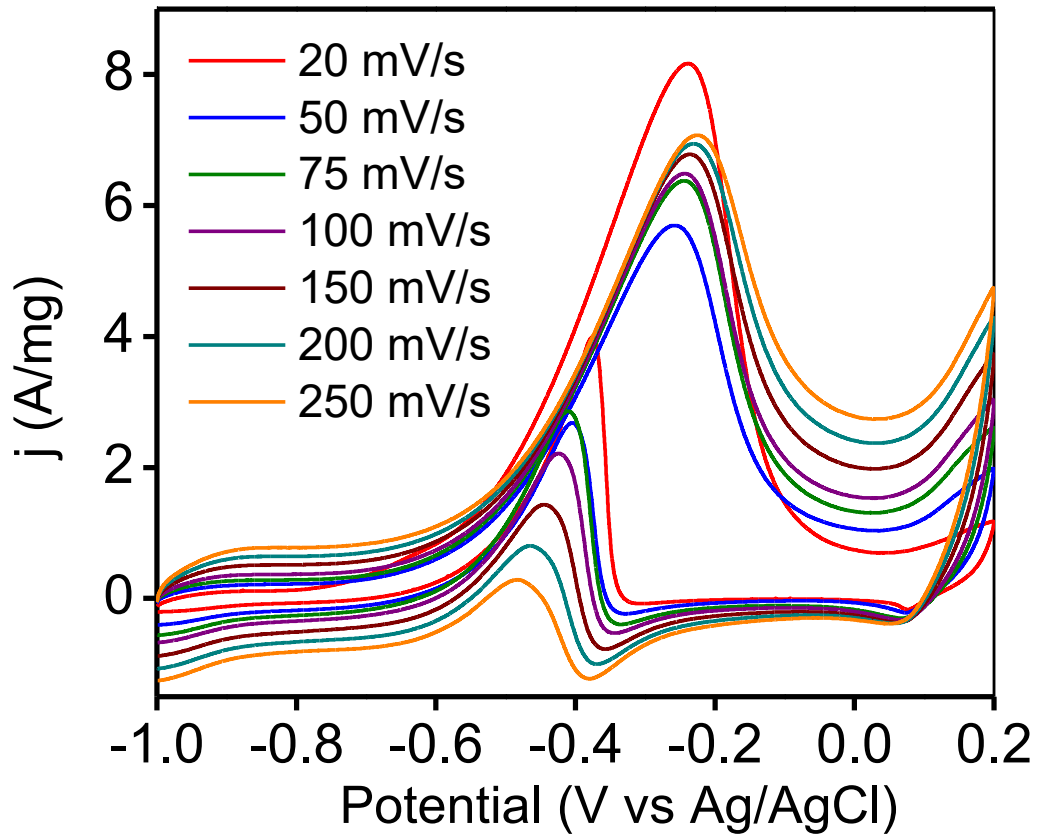

Figure 4.17 CV of electro-oxidation of ethanol by Au/Ag/Pd alloy aerogel (Ag = 20.3, Pd = 53.1, and Au = 26.6 %) in 1.0 M KOH solution. The mass activities of ethanol (1.0 M) oxidation were recorded at different scan rate to elucidate the reaction mechanism (1.0 M KOH + 1.0 M ethanol solution).

The stability of alloy NPs, aerogels, and commercial Pd/C catalyst towards electro-oxidation of ethanol was evaluated by current vs time measurements at a constant potential of 0.3 V for 6 h (Figure 4.16 B). The current density of the aerogel decayed rapidly at the beginning then reached a steady state (plateau) value at ~1.5 h, which is significantly higher than that of the commercial Pd/C. The initial decrease in the current density can be attributed to the blockage/poisoning of the surface sites by adsorbed organic intermediates (e.g. COads, CH_3OHads, and CHO species).[57, 146-147] Once the

aerogel electrode reached the steady state, no obvious decay in the current density is noted (up to 6 h.), reflecting the high catalytic activity, long-term stability and durability of alloy aerogels. Further studies, which are beyond the scope of this work are currently underway to investigate the effects of microstructure and morphology on electrocatalytic performance.

4.4 Conclusions

We have successfully produced Au/Ag/Pd alloy NPs with two distinct morphologies *via* stepwise GRR using Ag NP as a template. The as synthesized ternary alloy NPs were transformed into high surface area, mesoporous, conducting aerogels *via* controlled oxidation of the surfactant ligands. Selective de-alloying of Ag has been achieved by fine tuning of oxidant/thiolate molar ratio. Among two different sets of aerogel, set I aerogels exhibit significant dealloying effects with increasing concertation of the *in-situ* generated HNO_3, whereas set II aerogels showed no significant change in the elemental compositions. A systematic TEM study was carried out on sol-gel transformation of alloy NPs, which revealed direct attachment and alloying of NPs to generate a wire-like gel morphology. The resultant nanostructures exhibit extremely low density, high surface area and mesoporosity and high electrocatalytic activity for oxidation of ethanol in comparison to precursor NPs and commercial Pd/C catalyst. The synergistic effect of three different elements, self-supported nature, and high electrical conductivity of ternary aerogels mitigate the catalyst poisoning and exhibits better chemical and structural stability.

Chapter 5

Assembly of Au/Ag/Pt Ternary Alloy Nanoparticles into Monolithic Aerogels in the Application of Methanol Oxidation

5.1 Introduction

Pt-based catalysts exhibit highest catalytic activity due to their higher chemical stability and selectivity. The existence of the partially-filled d orbital in the outer layer of Pt accounts for easy complexation and result in intermediates, which are highly active in catalytic reactions.[164] Extremely low reactivity towards air and moisture as well as rapid intermediate formation during any chemical reactions enhance the catalytic activity of Pt compared to other noble metals. Many organic reactions such as hydrogenation of alkene, oxidation of alcohols, and reduction of p-nitrophenol are highly dependent on the high reactivity of Pt catalyst.[166] However, due to the higher cost and scarcity of Pt, alloys with other noble/non-noble metals have received noteworthy interest in recent years. Synthesis of multi-metallic noble metal alloys with tunable morphology and composition has attracted increasing attention because of their significant potential in several technologies such as catalysis, sensing, and surface enhance Raman scattering. Accordingly, numerous synthetic methods have been developed to produce Pt based multimetallic NPs with high catalytic activity and physiochemical stability.[22]

In addition to organic catalysis, electrocatalysis is another focus of contemporary catalytic reactions. A direct methanol fuel cell (DMFC) is one of the most ideal mobile energy forms, which is a proton exchange membrane fuel cell with high energy

conversion efficiency. Despite enhanced catalytic property, generation of poisonous species on the Pt NPs surface (CO_{ads} and CHO_{ads}), as well as severe degradation during alcohol oxidation results in poor catalytic activity of Pt based electrocatalyst.[23] Recent literature work showed that Au modified Pt exhibits enhanced electrocatalytic activity, as the organic constituents are (carbonaceous species) preferably oxidized by the Au and as a consequence enhances the durability and electrocatalytic activity.

This inspires us to build the ternary alloy NPs and aerogels consisting of Au, Ag, and Pt via proposed sol-gel chemistry. The alloying effect of the NPs will generate a promising electrocatalyst with low poisoning and their self-supported porous nanostructure will provide a facile pathway for both molecular and electronic transport further enhancing the catalytic activity of discrete Au/Ag/Pt alloy NPs. Thus, in this chapter, we report the synthesis and characterization of Au/Ag/Pt alloy aerogels and its potential in methanol electro-oxidation reactions.

5.2 Experimental Section

Synthesis of GSH Functionalized Ag NP Templates

Silver nanoparticles were produced by employing a literature method with significant modification to scale up the synthesis.[76] In a typical reaction, 3 mL of 10 mM $AgNO_3$ and 300 µL of 10 mM glutathione were added to 50 mL of ice cold milli-Q water. Then, 10 mL of 0.1 M NaOH was added to adjust the pH ~12 that resulted in a color change from colorless to pale yellow suggesting the formation of Ag_2O NPs. Finally, 3.6 mL of 10 mM $NaBH_4$ was slowly added at a rate of 0.5 mL/min to produce a yellow-brown solution of Ag NPs.

Synthesis of Au/Ag/Pt Ternary Alloy NPs Sol

After successful preparation of Ag NPs, 10 mL of 2.0 mM H_2PtCl_6 and 10 mL of 12 mM AA were simultaneously injected at a rate of 1 mL min^{-1} via a syringe pump. The color of the reaction solution changed to dark brown, suggesting the formation of Ag/Pt NPs. To the above reaction mixture, 10 mL of $HAuCl_4$ (0.25 mM) was added at a rate of 1 mL min^{-1} to produce ternary Au/Ag/Pt alloy NPs. As-prepared Au/Ag/Pt NPs were purified and concentrated using centrifuge filtration to produce 3 mM Au/Ag/Pt sol. The centrifuge filters (Sartorius, Vivaspin 20 mL MWCO 30000) filled with Au/Ag/Pt NP sol was centrifuged at 3500g for 7–8 min to reduce the volume to 2–3 mL. The concentrated sols were then mixed with 5–10 mL of mili-Q water and centrifuged to remove the residual byproducts (Na, NO_3^-, OH^-, and unreacted thiolates). This step has been performed multiple times to reduce the volume of the Au/Ag/Pt sol, while retaining the colloidal stability of ternary NPs.

Synthesis of Au/Ag/Pt Alloy Hydrogels and Aerogels

The Au/Ag/Pt sol (3 mM) was divided into 2 mL aliquots and placed in glass vials. Gelation was induced by the introduction oxidizing agent (1% $C(NO_2)_4$) ranging from 100 to 400 µL to 2 mL of 3 mM NP sol. The gradual condensation of the sol into opaque hydrogel was noted within 8-10 h. Varying amounts of oxidant (1% $C(NO_2)_4$, 100–400 µL) were added to study the dealloying effect.

The resulting hydrogels were aged for 2–3 days and the byproducts of the oxidation were removed by exchanging with acetone 4–6 times over 3–5 days. The aerogels of the hydrogel were produced by CO_2 supercritical drying (SCD). Porous microcapsules (SPI Supplies Inc.) filled with acetone exchanged hydrogels were loaded into the SCD

dryer and filled with liquid CO_2 at 15 °C. The acetone treated gels were then exchanged with liquid CO_2 5–6 times over 1–2 days. Finally, the gels were dried at 40 °C for 18 min to produce monolithic Au/Ag/Pt alloy aerogels.

Electrochemical measurement

The Au/Ag/Pt aerogel ink was prepared by mixing ~4 mg of the aerogels with 25 µL of nafion and 400 µL of iso-propanol followed by sonication for 30-60 seconds. The modified working electrodes were produced by drop casting the aerogel ink on the clean surface on a glassy carbon electrode (GCE, 5 mm in diameter, or 0.196 cm^2 in area). After each loading (20 µL) of the ink, it was allowed to dry at room temperature. A desired loading of the aerogels was achieved via several coating. After drying the electrodes in ambient air, it was further dried at 50 °C for 12 h in an oven and stored in a desiccator prior to electrochemical measurements.

The electrochemical performance of ternary alloy aerogels for electro-oxidation of methanol was investigated using cyclic voltammetry (CV) and chronoamperometry using a CHI-401 electrochemical workstation (CH Instruments Inc.). The aqueous electrolyte solution (KOH, 1 M) was prepared with ultrapure water and prior to any electrochemical measurement; all the tested solutions were de-aerated using high purity nitrogen for 1 h. All the electrochemical measurements were conducted in 1.0 M KOH aqueous solution containing ethanol in a conventional three-electrode test cell at room temperature. Potentials of the working electrode were recorded against Ag/AgCl (1.0 M) (CH Instruments Inc.) reference electrode and Pt wire was used as the counter electrode. Activation of the ternary alloy aerogel modified GCE was carried out by conducting CV for 100 cycles at 50 mVs^{-1} (1 M KOH) with a potential range -1.0 to 0.2 V

(vs. Ag/AgCl). Stability and tolerance of the as-prepared ternary alloy aerogel catalysts were evaluated by chronoamperometry (1.0 M KOH + 1.0 M ethanol).

5.3 Results and Discussion

Galvanic replacement reaction (GRR) provides a versatile approach for the transformation of monometallic solid NPs into more complex multimetallic nanostructures with varying size and shapes. Although several complications are known with the GRR reactions due to the simultaneous co-reduction of different metallic precursors, a number of synthetic efforts are being developed due to the interesting physical properties and applicability of these more complex nanostructures.[166] Despite significant advances in the field of bimetallic and core-shell NPs, ternary and quaternary noble metal NPs with precisely controlled size and shape are relatively unexplored. Thus, the initial focus of this work was centered on the synthesis of size and shape controlled Au/Ag/Pt NPs followed by sol-gel assembly into functional superstructures (aerogels) for application in electro-catalytic oxidation of methanol.

For the synthesis of tri-metallic alloy NPs, preformed Ag NPs were used as the template where step-wise galvanic replacement reactions were carried out first with H_2PtCl_6 and finally with $HAuCl_4$ to synthesize Ag/Pt and Au/Ag/Pt NPs, respectively. Precursor Ag NPs were produced by following a literature procedure with significant modification to scale up the reaction. In a basic media, $AgNO_3$ and glutathione produces Ag_2O NPs, which then undergo slow chemical reduction with $NaBH_4$ to produce precursor Ag NPs (5.1 ± 1.1 nm).[76] A visible color change of the reaction from pale yellow to yellow-brown with the evolution of surface plasmon resonance (SPR) peak

around 400-410 nm suggests the formation of Ag NPs. Depending on the reduction potential (Scheme 5.1), H_2PtCl_6 was introduced first along with ascorbic acid (AA). The presence of AA has been found to have a significant effect in the formation of Ag/Pt alloy, as it facilitates the diffusion of Ag and Pt atom due to the minor difference in reduction potential (Scheme 5.1). Red shifting of surface Plasmon to 421 nm indicates the formation of Ag/Pt alloy NPs. Finally, introduction $HAuCl_4$ to Ag/Pt sol further red shifts the Ag Plasmon to 430 nm suggesting the production of Au/Ag/Pt alloy NPs (Figure 5.1).

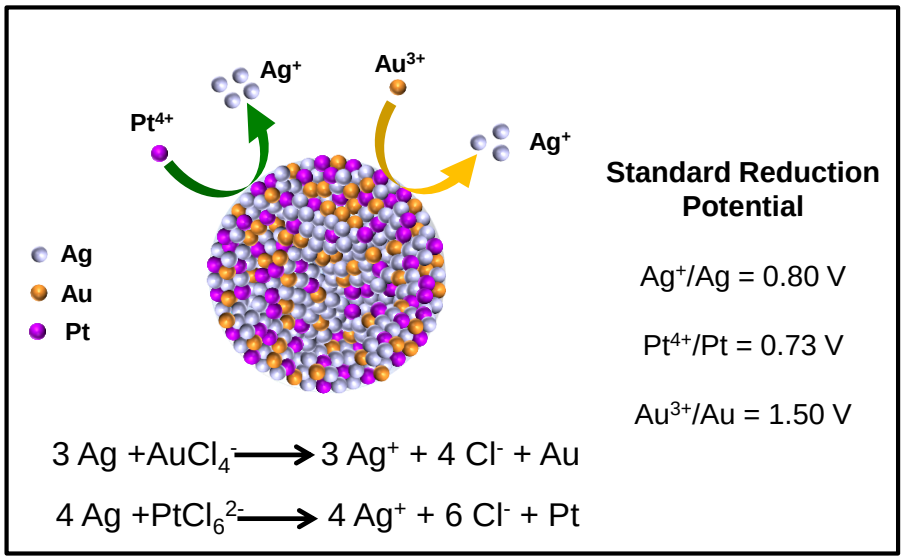

Scheme 5.1 Schematic illustration of the synthesis of Au/Ag/Pt alloy NPs via stepwise galvanic replacement reaction.

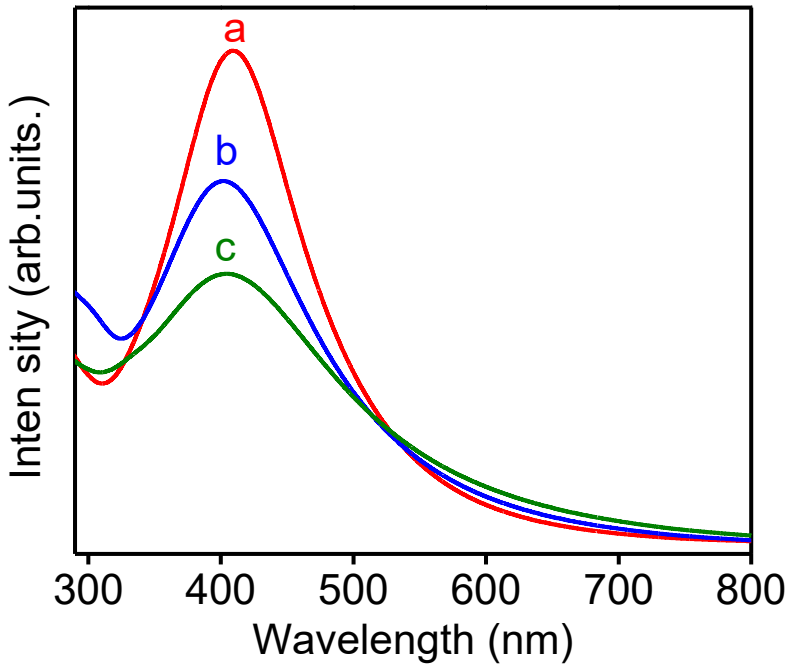

Figure 5.1 Normalized UV-visible absorption spectra of (a) Ag NPs along with (b) Ag/Pt and (c) Au/Ag/Pt produced by galvanic replacement of glutathione coated Ag NPs.

Low resolution TEM images of the as-synthesized Au/Ag/Pt ternary NPs exhibit nearly spherical morphology with an average diameter of 3.7 ± 0.9 nm (Figure 5.2 A). Although the spherical morphology of the NPs was prominent, a small fraction of NPs also resulted in with anisotropic shapes. It is anticipated that during GRR, inter-diffusion of the surface atoms are vary spontaneous and consequentially results in spherical to anisotropic particles. HRTEM images of the individual particles exhibit a lattice constants of 2.2 – 2.3 Å, which appears to be smaller than the Ag crystallite (2.4 Å), indicating the lattice contraction with incorporation of Au and Pt. Similar phenomena have also been observed through PXRD study where shifting of the Bragg's diffractions (characteristics to face centered cubic Ag) towards higher 2 theta was observed for Au/Ag/Pt ternary NPs. To obtain a detailed knowledge about the atomic scale structure

of the ternary alloy NPs, STEM-EDS elemental maps were employed (Figure 5.2). Overlay of the Au, Ag, and Pt maps indicates alloying, suggesting the homogeneous solid solution behavior of as-synthesized ternary NPs.

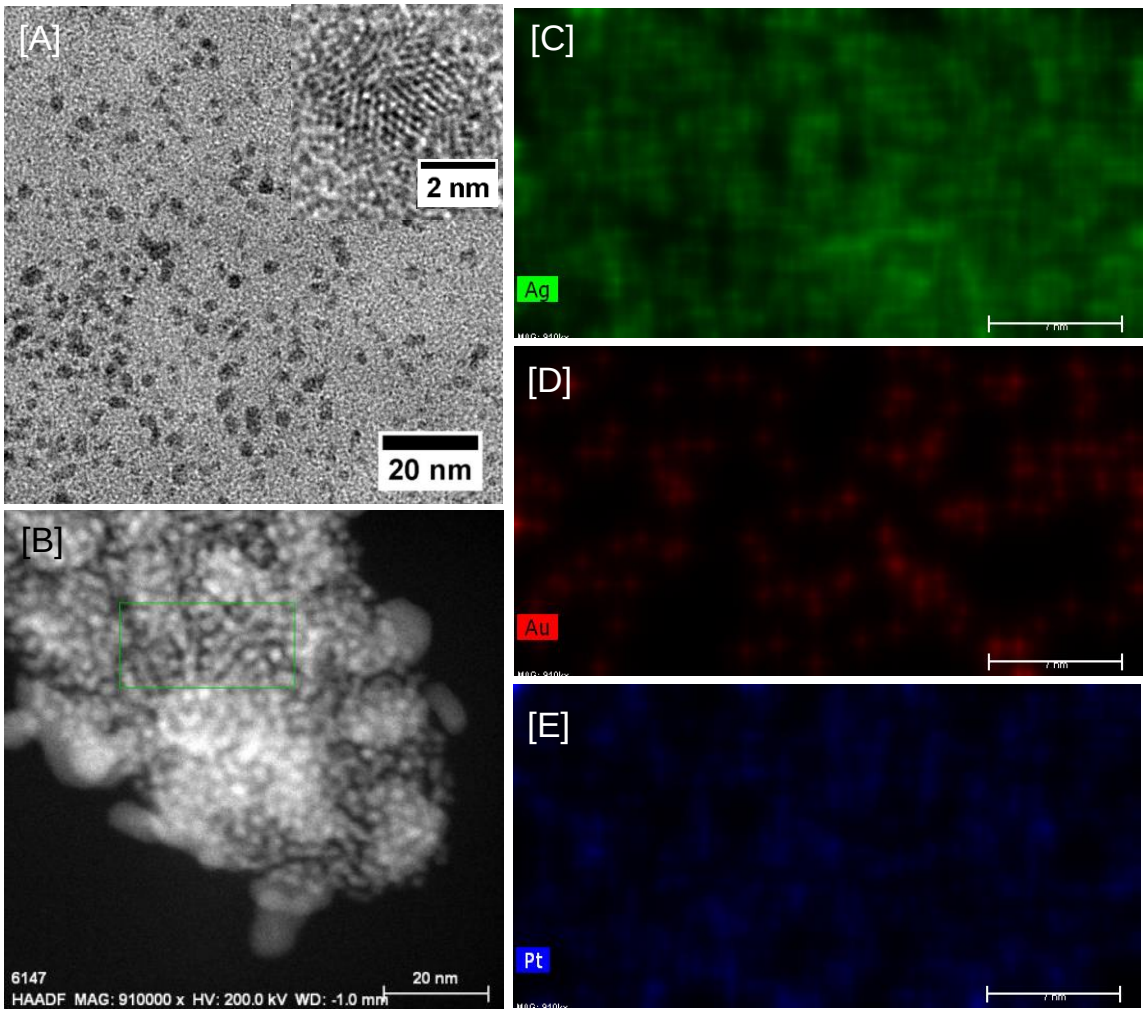

Figure 5.2 [A] Low resolution TEM and [B] STEM images of Au/Ag/Pt alloy NPs along with elemental maps of [C] Ag, [D] Au, [E] Pt, indicating the growth of homogeneous alloys.

As-prepared Au/Ag/Pt alloy NPs were concentrated via centrifuge filtration to obtain a concentrated sol (0.3 M), which was washed several times with milli-pure water to remove the ionic byproducts ((Na^+, Cl^-, and BO^{2-}).[1] Introduction of $C(NO_2)_4$ into the concentrated and purified sol initiates the condensation of NPs into hydrogel material. $C(NO_2)_4$ oxidizes the GSH ligands from the NPs surface to sulfenyl nitrates, which then undergo reaction with another GSH moiety to produce glutathione disulfide (GS-SG) as shown in equation 5.1, and 5.2.

$$GSH + C(NO_2)_4 \rightarrow GSNO_2 + C(NO_2)_3^- + H^+ \ldots\ldots\ldots (5.1)$$

$$GSH + GSNO_2 \rightarrow GS - SG + NO_2^- + H^+ \ldots\ldots\ldots\ldots\ldots (5.2)$$

During the oxidation, low coordinated active sites are generated on the NP surface, which can connect with similar active site on another NP to produce inter-facially connected NP frameworks (Figure 5.3), which are morphologically similar to metal oxide gels. The hydrogels were aged for 6-12 h under ambient condition and exchanged with acetone over a time period of 2 -3 days to remove byproducts (GS-SG and RSO_3). Finally, the acetone exchanged wet gels were dried using supercritical CO_2 to produce monolithic Au/Ag/Pt aerogels. Ternary alloy aerogels are black color and show ~5-10% of volume loss compared to corresponding hydrogels.

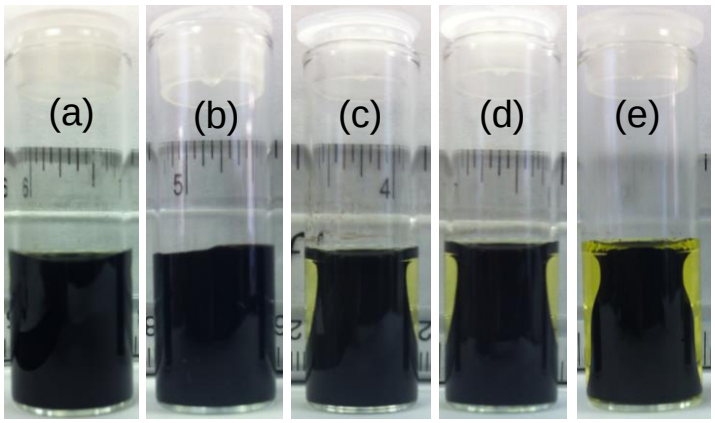

Figure 5.3 Photographic images of Au/Ag/Pt hydrogels as a function of time: (a) concentrated sol of Au/Ag/Pt NPs, (b) condensation of NPs to hydrogels produced after 1 h via oxidation of surface thiolate ligands, including aging time of (c) 4 h, (d) 6 h, and (e) 8 h, respectively.

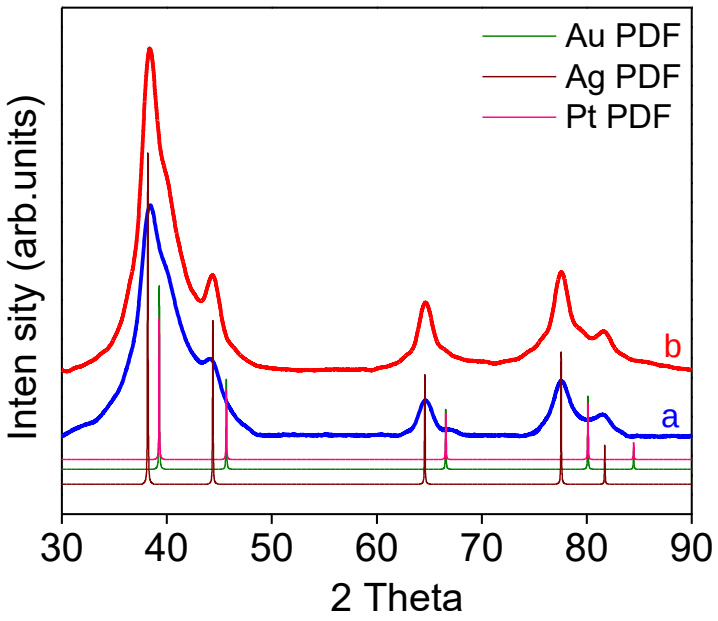

Figure 5.4 Powder X-ray diffraction patterns of (a) Au/Ag/Pt NPs along with (b) Au/Ag/Pt alloy aerogels. The ICDD-PDF overlays of cubic Ag (wine, 01-0870719), Pt (pink, 00-0040802) and Au (olive, 03-0658601) are shown as vertical lines.

The powder X-ray diffraction pattern of Au/Ag/Pt alloy NPs and corresponding aerogels were studied to investigate the structure and crystallinity of the materials upon GRR and oxidative gelation (Figure 5.4). The absence of AgCl or any other impurity peaks suggests the high-purity of as synthesized material. The diffraction pattern of the ternary alloy NPs and aerogels displayed characteristic face centered cubic Ag phase (JCPDS # Ag 01-0807-7191) with minor shifting towards the larger 2θ angles due to lattice contraction with the incorporation of Au and Pt in the structure, during GRR. This observation further confirms the successful growth of homogeneous, ternary alloys. The average crystallite size of the ternary NPs and aerogels were calculated by applying Scherrer formula to the (111) and (220) planes, which reveals values of 3.4 ± 0.2 nm and 3.6 ± 0.2 nm (Table 5.1) for the NPs and aerogels, respectively. The average diameter of the NPs within the aerogel framework appears to be slightly larger than the precursor NPs, which can be attributed to crystallite growth during supercritical drying of the hydrogels.[2]

Table 5.1 Comparative Results of Crystallite and Average Particles Sizes, Elemental Compositions, and SPR Maxima Wavelength of as Prepared Au/Ag/Pt NPs and Corresponding Aerogels along with Surface area, Average Pore Diameters, and Cumulative Pore Volumes of Ternary Aerogels.

Sample		**Au/Ag/Pt NPs**	**Au/Ag/Pt aerogels**
Crystallite size (nm)[a]		3.4 ± 0.2	3.6 ± 0.2
Average particles size		3.7 ± 0.9	3.8 ± 1.2
Elemental composition (ICP-OES)[b]	Ag	37.4	31.0
	Pt	50.9	54.4
	Au	11.7	14.6
SPR maxima (nm)	Ag	410	N/A
	Ag/Pt	421	
	Au/Ag/Pt	430	
Surface area (m^2/g)[c]		3.94	230
Average pore width (nm)[c]		5.27	16.3
Average pore volume (cm^3/g)[c]		0.003	1.08

[a] Crystallite sizes were calculated by applying Scherrer formula for all diffraction peaks in PXRD pattern.
[b] Weight % of Ag, Pd, and Au were calculated based on ICP-OES analysis averaging 3 individual samples.
[c] BET and BJH models were applied to the nitrogen adsorption/desorption isotherms to investigate the surface area and pore characteristics, respectively.

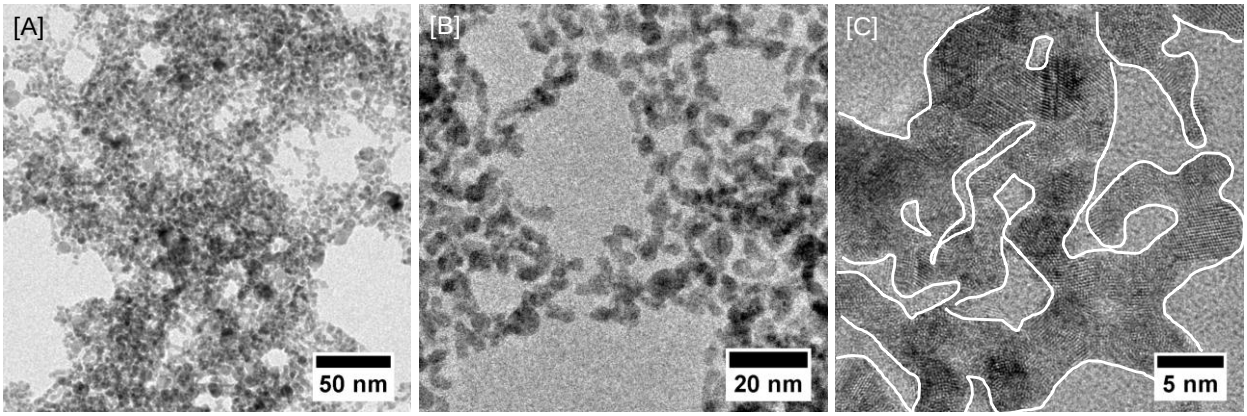

Figure 5.5 [A-B] Low and [C] high resolution TEM images of Au/Ag/Pt aerogels exhibiting wire like morphology where the NPs are directly interconnected to give rise a porous nanostructure.

The low resolution TEM images of the aerogels were studied to investigate the morphology and porosity of the aerogels. Interestingly, it has been observed that the ternary metal aerogels produced via oxidative assembly of precursor NPs (Figure 5.5) grew into a wire-like morphology. The interconnection between the NPs appears to be highly crystalline as evident from the HRTEM in Figure 5.5 C, suggesting direct alloying of ternary NPs. This can be accountable for the spontaneous growth of the ternary NPs during GRR, which when assembled together undergoes fusion into a wire like morphology, similar to Ag/Au/Pd aerogels (chapter 4). The average diameter of the wire in the aerogel structure is 3.8 ± 1.2 nm, which are in close match with the typical dimension of ternary NPs. This suggest that the aerogel superstructures are produced through the direct cross linking of the individual NPs without the formation of secondary or tertiary aggregates.[3] Regardless of the NP morphology, aerogels exhibits highly

porous nature of the materials, consisting of a large number of mesopores (2–50 nm) and macropores (> 50 nm) throughout the gel framework.

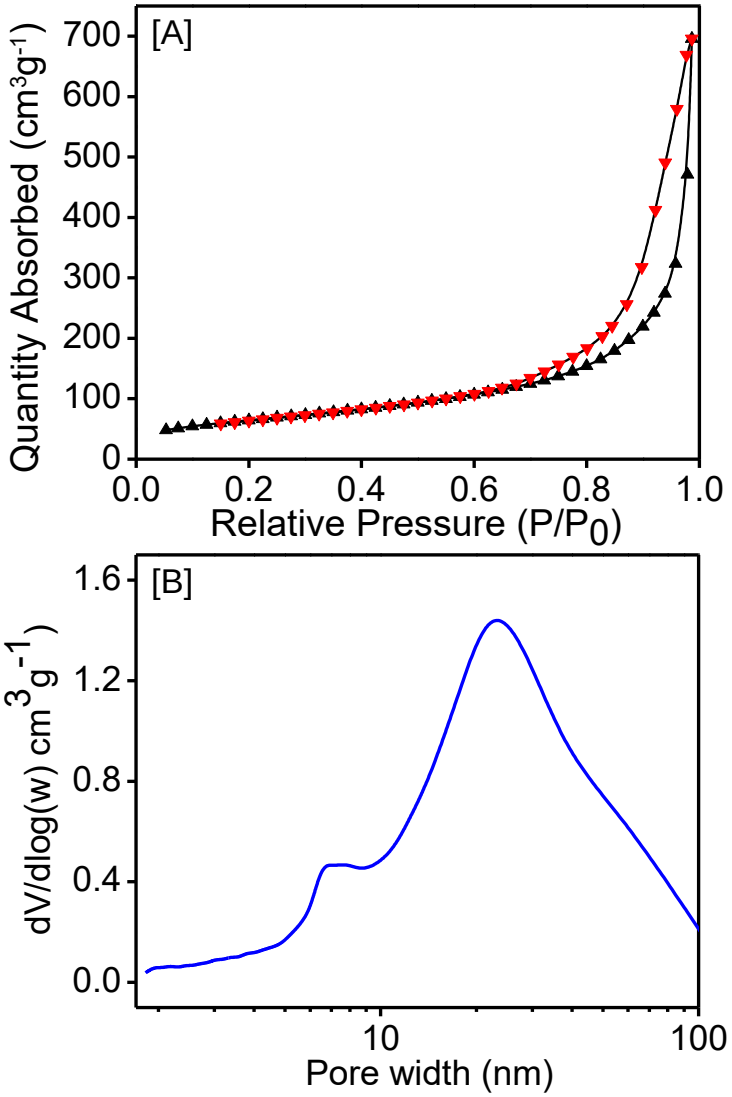

Figure 5.6 [A] Representative nitrogen adsorption (black) desorption (red) isotherm of Au/Ag/Pt aerogels along with [B] the corresponding BJH model pore distribution plot.

Porous morphology of the Au/Ag/Pt ternary alloy aerogels were further investigated via surface area and porosity measurement from the nitrogen adsorption-desorption isotherms. The typical isotherm showed in Figure 5.6 A, corresponds to type IV curves implying the meso (2–50 nm) porous structure of the aerogel consistent with the TEM analysis. The hysteresis loop of the isotherm have a combination of H1 and H3 character that represents the slit and cylindrical shape pores in the ternary alloy aerogel structure. The surface area for the aerogel obtained from the BET modeled nitrogen adsorption isotherm is 230 m^2/g, which is significantly higher than the corresponding NPs (3.94 m^2/g), implying highly porous nature of the superstructure.

The average pore diameters and cumulative pore volumes of the aerogels were computed from the desorption branches of the nitrogen adsorption/desorption isotherms (Figure 5.6 B). The pore distribution analysis of the ternary alloy aerogels exhibits two distinct peaks, one is ~ 6 nm and the other centered at ~16 nm and extended till 100 nm. The pore distribution at ~6 nm is most likely due to the smaller cluster formation during NP condensation, whereas the large pores extending from 16-100 nm represents meso-to-macro pores resulting from the 3-dimensional gel network. Such distinctive pore size distribution provides a unique opportunity for small molecules to have a facile accessibility to the gel framework which, can potentially makes the aerogel, a better catalyst.

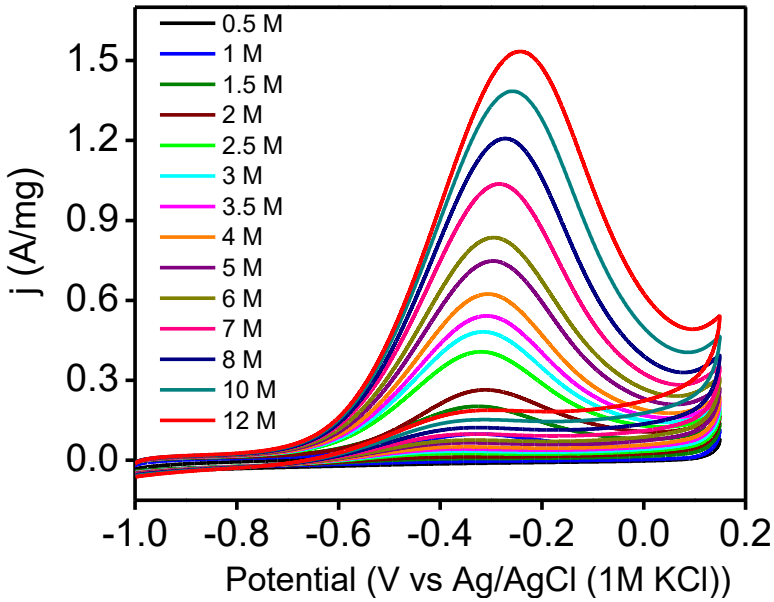

Figure 5.7 Mass normalized CV for electroxidation of methanol on Au/Ag/Pt aerogels exhibits linear increase in current density with increasing concentration of MeOH indicating higher stability (12 M MeOH) of the aerogels. All measurements were carried out in 1 M KOH + 1 M ethanol solution at a 50 mVs^{-1} scan rate.

The catalytic property of Au/Ag/Pt alloy aerogels was investigated for the electro-oxidation of methanol. As depicted in Figure 5.7, all the CVs consist of two peak currents, characteristics of methanol oxidation. The symmetric anodic peak around -0.3 V observed in anodic sweep can be assigned to oxidation of freshly adsorbed methanol species on the aerogels. Interestingly, it has been observed that the anodic peak current density for electro-oxidation of MeOH linearly increases with the concentration of alcohol (up to 12 M). However, at this significantly high concentration of alcohol, shifting of the oxidation peak potential to less negative values were also observed. In addition, the oxidation peak became less symmetric, which represents the irreversibility of the system at higher alcohol concentration. The higher alcohol up take of the

aerogels (12 M) indicates promising catalytic activity of the aerogels in electro-oxidation of MeOH. In the reverse scan, an anodic oxidation peak current around -0.4 V was observed, which is attributed to the sweeping of the incompletely oxidized carbonaceous organic intermediates generated in the electrode surface during the forward potential sweep. The ability of handling this higher MeOH concentration suggests the superior catalytic activity of the self-supported ternary aerogels for electrocatalytic reactions.

5.4 Conclusions

We have successfully produced Au/Ag/Pt ternary NPs via GRR on the preformed Ag NPs template. During the formation of ternary NPs, a number of faceted structure was generated which has the potential for promising electro-catalyst. As prepared Au/Ag/Pt NPs were successfully transformed into high surface area, self-supported, aerogel superstructures via controlled oxidation of the surfactant ligands. The resultant aerogels exhibit extremely low density, direct NP connectivity, high surface area (230 m^2/g) and porosity (2-50 nm), making them promising for catalysis. Low and high resolution TEM images reveal the establishment of direct interfacial interactions between colloidal NPs, which led to growth into a wire like morphology. A linear increase in the oxidation current density was observed with increasing concentration of MeOH (up to 12 M), indicating better stability of the ternary aerogels at higher MeOH concentration. The alloying property combined with unique porous architecture of Au/Ag/Pt aerogels suffers less poisoning during electro-oxidation of MeOH and provides better opportunity for the smaller molecules to channel through the aerogel superstructure.

Chapter 6

Conclusions and Prospectus

In this following dissertation, we have successfully developed a new strategy for the self-assembly of inherently similar and dissimilar nanomaterials into self-supported nanostructures with no use of intervening ligands and substrate supports. Direct interfacial interactions between nanosized constituents were achieved by progressive removal of thiolate ligands from colloidal NPs upon introduction of oxidative reagents ($C(NO_2)_4$), H_2O_2, or benzoyl peroxide). Chemical oxidation of the surfactant ligands has been assumed to produce low coordinated active sites on the NP surface, which then undergo cohesive attraction and polymerization to results in a wet “jello-like” hydrogels. Finally, the hydrogels were dried under supercritical conditions to produce mesoporous aerogels. Resultant NP monoliths (aerogels) can retain the unique physical properties of primary NPs. Thus, the gelation phenomena can be used to effectively integrate inherently similar or dissimilar nanomaterials with the potential to achieve enhanced optical and catalytic properties.

In chapter 3, we developed a strategy for efficient coupling of metal (Ag, Au) and semiconductor (CdSe) via co-gelation of precursor particles. Oxidative removal of surfactant ligands provides the opportunity for semiconductor and metal NPs to interact at the interface that can led to enhance or novel photophysical properties that are distinct from individual components. To study the structure and surface of the CdSe/Ag hybrids, PXRD and XPS was performed. The presence of characteristic Bragg’s diffraction peaks of both hexagonal CdSe and face center cubic Ag in the same aerogel

structure indicates heterogeneous mixture of both semiconductor and metal NPs. Consistent with previous literature, XPS results showed Cd^{2+}, and Ag^{0} on the aerogel surface. In addition, the presence of reduced Se_n^{n-} species was also observed along with Se^{2-} from the core of the nanocrystal, which is assumed to make Ag-Se_n^{n-} direct interfacial bonds, effectively coupling the chemically dissimilar constituents. The resulting surface bond is expected to enhance the overlapping of electronic wave functions of CdSe and Ag facilitating the direct electron tunneling between metal and the semiconductor. This direct coupling of NPs has minimum effect on CdSe absorption onsets at low Ag content whereas a systematic red shift and band tailing effects were observed at high Ag content, possibly due to excessive overlap of metal-semiconductor electronic wave functions. In contrast, PL and TRPL analyses of CdSe/Ag hybrids (0.27 % and 0.53 % Ag) revealed the emergence of a new emission energy at ~640 nm with a decay time of ~600 ns, which is significantly different from those of the band-edge (1.83 ± 0.03 ns) and trap state (1190 ± 120 ns) emission of CdSe aerogels, suggesting the generation of an alternate radiative decay pathway. Introduction of the co-gelation phenomena optimizes the interfacial interactions of NP constituents to a moderate extent via the formation of fractal aggregates. This approach of coupling metal-semiconductor energies has the potential to impact on a number of optical technologies including but not limited to biomedical, solar energy harvesting, and photocatalysis.

An added benefit of the newly developed sol-gel chemistry is the potential to produce porous, conducting nanoarchitectures composed entirely of metal NPs. This provides a facile pathway for tunneling of both charge carriers and small molecules potentially producing high performance electrocatalyst. In chapter 4, we have successfully

produced significantly smaller (3-5 nm) Au/Ag/Pd alloy NPs with control over morphology and composition via GRR of thiol-coated Ag NPs. Two distinct morphologies of ternary alloy NPs were transformed into high surface area, mesoporous, conducting aerogels via controlled oxidation of the surfactant ligands. The selective de-alloying of Ag from ternary nanostructures was achieved by tuning the oxidant/thiolate molar ratio, which governs the condensation of NPs and crystallinity of the alloy aerogels. Set I aerogels, where Ag composition is higher (Au: Ag: Pd = 31.2: 58.2: 10.6), exhibit significant dealloying effects with increasing concentration of the in-situ generated HNO_3. Thus, a significant decrease in the crystallite size was noted through PXRD and TEM analyses. In contrast, the Ag content remains essentially unchanged in set II alloy aerogels, where initial concentration of Au, Ag, and Pd are 17.2, 23.5, and 59.3 %, respectively. This discrepancy has been attributed to substantial Ag amount (~20 %) needed to maintain the monolithic gel structure. The surface analysis by XPS indicates a reduction in surface states of all elements, consistent with the oxidative gelation and formation of direct interparticle bonds. A systematic TEM study on sol-gel transformation of set II alloy NPs revealed direct attachment and alloying of anisotropic NPs to produce a wire-like (polymeric) gel morphology. In contrast, the aerogels produced from nearly spherical, set I alloy NPs exhibit colloidal gel morphology. The resultant nanostructures exhibit extremely low density (0.02 – 0.06 g/cm^3), high surface area (282 – 80 m^2/g) and mesoporosity (9 – 16 nm), offering prospectives for number of new technologies. As synthesized Au/Ag/Pd NPs, corresponding aerogels, and commercial Pd/C catalyst were studied in the electro-oxidation of ethanol. The alloy aerogels exhibit electro-catalytic activity that is ~20-30

times higher than those of the precursor NPs and excellent chemical and structural durability compared to commercial Pd/C catalyst. The alloying effect, self-supported nature, and high electrical conductivity of ternary aerogels mitigate the catalyst poisoning effects and enhance the chemical and structural stability. These unique features make the Au/Ag/Pd alloy aerogels a promising catalyst or electrocatalyst for a number of new technologies.

As a natural extension of Au/Ag/Pd aerogel project, thiolate-stabilized Au/Ag/Pt alloy NPs were also produced and assembled into conductive, porous gel frameworks via controlled oxidation of the surface ligands. In chapter 5, Au/Ag/Pt ternary NPs were synthesized via GRR on the preformed Ag NP templates. The stepwise GRR was carried out where depending on the reduction potential, first Ag/Pt and finally Au/Ag/Pt ternary alloy NPs were successfully produced. Random deposition of Pt and Au during GRR resulted in spherical to anisotropic morphologies of ternary alloy NPs. As-prepared Au/Ag/Pt NPs were successfully transformed into high surface area, self-supported, aerogel superstructures via controlled oxidation of the surfactant ligands. The resultant aerogels exhibit extremely low density, direct NP connectivity, high surface area (230 m^2/g) and mesoporosity (2-50 nm), making them promising for electrocatalysis. Low and high resolution TEM images revealed the establishment of direct interfacial linkages of colloidal NPs, which led to growth into a wire like hydro-/aero-gels. The ternary aerogels were studied for the electro-oxidation of methanol. A linear increase in the oxidation current density was observed with increasing concentration of MeOH (up to 12 M), indicating better stability of the ternary aerogels at higher MeOH concentration. The alloying property combined with unique porous architecture of Au/Ag/Pt aerogels offer

less poisoning during electro-oxidation and provides better opportunity for the smaller molecules to channel through the aerogel superstructure.

The sol-gel chemistry for the assembly of inherently similar or dissimilar nano-entities provides a powerful yet effective method for addressing a number of pressing problems in the applications of NPs. The direct interfacial linkages between the metal and semiconductor NPs in a purely inorganic 3D macrostructures holds out the future for optoelectronic devices where direct bonding between NPs can facilitate electron tunneling leading to new or enhance optical property. Preserving the quantum confine effect of CdSe, the emission energy boundary can be extended only by the incorporation of significantly lower amount of Ag that eventually can open up a new window for the LED applications. In addition, the combined feature of porosity with the interconnected NP network comprised of solely metal NPs has the potentials for developing better catalyst/electro-catalysts. The directly hardwired network of metallic NPs gives a facile conduit for diffusion of small molecules whereas the oxidative removal of surfactant ligands produces gel materials with pristine active catalytic surfaces. As the effect of size and morphology of the nanoparticulate constituents in the gel framework has been found to have critical control over the gel morphology and consequently their optoelectronic and electro-catalytic properties, an investigation on this mechanism is currently underway.

References

1. (a) Arachchige, I. U.; Brock, S. L., Sol−Gel Methods for the Assembly of Metal Chalcogenide Quantum Dots. *Acc. Chem. Res.* **2007,** *40*, 801−809; (b) Arachchige, I. U.; Mohanan, J. L.; Brock, S. L., Sol-Gel Processing of Semiconducting Metal Chalcogenide Xerogels: Influence of Dimensionality on Quantum Confinement Effects in a Nanoparticle Network. *Chem. Mater.* **2005,** *17*, 6644−6650; (c) Brock, S. L.; Arachchige, I. U.; Kalebaila, K. K., Metal Chalcogenide Gels, Xerogels and Aerogels. *Comments Inorg. Chem.* **2006,** *27*, 103-126; (d) Bigall, N. C.; Herrmann, A.-K.; Vogel, M.; Rose, M.; Simon, P.; Carrillo-Cabrera, W.; Dorfs, D.; Kaskel, S.; Gaponik, N.; Eychmüller, A., Hydorgels and Aerogels from Noble Metal Nanoparticles. *Angew. Chem. Int. Ed.* **2009,** *48*, 9731−9734; (e) Gaponik, N.; Wolf, A.; Marx, R.; Lesnyak, V.; Schilling, K.; Eychmuller, A., Three-Dimensional Self-Assembly of Thiol-Capped CdTe Nanocrystals: Gels and Aerogels as Building Blocks for Nanotechnology. *Adv. Mater.* **2008,** *20*, 4257–4262.

2. Quinten, M., *Optical Properties of Nanoparticle Systems*. Wiley-VCH Verlag & Co.: Germany, 2011.

3. Keating, C. D.; Musick, M. D.; Keefe, M. H.; Natan, M. J., Kinetics and Thermodynamics of Au Colloid Monolayer Self-Assembly: Undergraduate Experiments in Surface and Nanomaterials Chemistry. *J. Chem. Educ.* **1999,** *76*, 949–955.

4. Trindade, T.; O'Brien, P.; Pickett, N. L., Nanocrystalline Semiconductors: Synthesis, Properties, and Perspectives. *Chem. Mater.* **2001,** *13*, 3843–3858.

5. Smith, A. M.; Nie, S., Semiconductor Nanocrystals: Structure, Properties, and Band Gap Engineering. *Acc. Chem. Res.* **2010,** *43*, 190-200.

6. Elliott, R. Intensity of Optical Absorption by Excitons. *J. Phys. Rev.* **1957,** *108*, 1384–1389.

7. Nirmal, M.; Brus, L. Luminescence Photophysics in Semiconductor Nanocrystals. *Acc. Chem. Res.* **1999,** *32*, 407-414.

8. Alivisatos, A. P., Semiconductor Clusters, Nanocrystals, and Quantum Dots. *Science* **1996,** *271*, 933-937.

9. Lu, X.; Rycenga, M.; Skrabalak, S. E.; Wiley, B.; Xia, Y., Chemical Synthesis of Novel Plasmonic Nanoparticles. *Annu. Rev. Phys. Chem.* **2009,** *60*, 167-192.

10. Rycenga, M.; Cobley, C. M.; Zeng, J.; Li, W.; Moran, C. H.; Zhang, Q.; Qin, D.; Xia, Y., Controlling the Synthesis and Assembly of Silver Nanostructures for Plasmonic Applications. *Chem. Rev.* **2011**, 3669-3712.

11. Sun, Y.; Jiang, L.; Zhong, L.; Jiang, Y.; Chen, X., Towards Active Pasmonic Response Devices. *Nano Res.* **2015,** *8*, 406-417.

12. Halas, N. J.; Lal, S.; Chang, W.-S.; Link, S.; Nordlander, P., Plasmons in Strongly Coupled Metallic Nanostructures. *Chem. Rev.* **2011,** *111*, 3913–3961.

13. Odom, T. W.; Schatz, G. C., Introduction to Plasmonics. *Chem. Rev.* **2011,** *111*, 3667-3668.

14. Yang, P.; Xu, Y.; Chen, L.; Wang, X.; Mao, B.; Xie, Z.; Wang, S.-D.; Bao, F.; Zhang, Q., Encapsulated Silver Nanoparticles Can be Directly Converted to Silver Nanoshell in the Gas Phase. *Nano Lett.* **2015,** *15*, 8397–8401.

15. W. Niu; Y. A. A. Chua; W. Zhang; H. Huang; X. Lu, Highly Symmetric Gold Nanostars: Crystallographic Control and Surface-Enhanced Raman Scattering Property. *J. Am. Chem. Soc.* **2015,** *137*, 10460-10463.

16. (a) Linic, S.; Christopher, P.; Ingram, D. B., Plasmonic-Metal Nanostructures for Efficient Conversion of Solar to Chemical Energy. *Nature Mater.* **2011,** *10*, 911-921; (b) Huang, X.; Zeng, Z.; Bao, S.; Wang, M.; Qi, X.; Fan, Z.; Zhang, H., Solution-Phase Epitaxial Growth of Noble Metal Nanostructures on Dispersible Single-Layer Molybdenum Disulfide Nanosheets. *Nature Commun.* **2013,** *4*, 1-8.

17. (a) Ongartkit, A.; Ananta, S.; Srisombat, L., Preparation of Ag/Au/Pt Nanoparticles and their Catalytic Properties. *Chem. Phys. Lett.* **2014,** *605*, 85-88; (b) Guo, S.; Zhang, X.; Zhu, W.; He, K.; Su, D.; Mendoza-Garcia, A.; Ho, S. F.; Lu, G.; Sun, S., Nanocatalyst Superior to Pt for Oxygen Reduction Reactions: The Case of Core/Shell Ag(Au)/CuPd Nanoparticles. *J. Am. Chem. Soc.* **2014,** *136*, 15026-15033.

18. (a) Antolini, E., Formation of Carbon-Supported PtM Alloys for Low Temperature Fuel Cells: a Review. *Mater. Chem. Phys.* **2003,** *78*, 563-573; (b) Liu, R.; Smotkin, E. S., Array Membrane Electrode Assemblies for High throughput Screening of Direct Methanol Fuel Cell Anode Catalysts. *J. Electroanal. Chem.* **2002,** *535*, 49-55; (c) Paulus, U. A.; Endruschat, U.; Feldmeyer, G. J.; Schmidt, T. J.; Bonnemann, H.; Behm, R. J., New PtRu Alloy Colloids as Precursors for Fuel Cell Catalysts. *J. Catal.* **2000,** *195* 383-393; (d) Long, J. W.; Stroud, R. M.; Swider-Lyons, K. E.; Rolison, D. R., How To Make Electrocatalysts More Active for Direct Methanol Oxidation Avoid PtRu Bimetallic Alloys! *J. Phys. Chem. B* **2000,** *104*, 9772-9776; (e) Zhou, W.; Zhou, Z.; Song, S.; Li, W.; Sun, G.; Tsiakaras, P.; Xin, Q., Pt Based Anode Catalysts for Direct Ethanol Fuel Cells. *Appl. Catal. B* **2003,** *46*, 273-285.

19. Lee, D.; Jang, H. Y.; Hong, S.; Park, S., Synthesis of Hollow and Nanoporous Gold/Platinum Alloy Nanoparticles and their Electrocatalytic Activity for Formic Acid Oxidation. *J. Coll. Int. Sci.* **2012,** *388*, 74- 79.

20. (a) Monyoncho, E. A.; Steinmann, S. N.; Michel, C.; Baranova, E. A.; Woo, T. K.; Sautet, P., Ethanol Electro-oxidation on Palladium Revisited Using Polarization Modulation Infrared Reflection Absorption Spectroscopy (PM-IRRAS) and Density Functional Theory (DFT): Why Is It Difficult to Break the C-C Bond? *ACS Catal.* **2016,** *6*, 4894−4906; (b) Yin, J.; Shan, S.; Ng, M. S.; Mott, D.; Gang, W.; Kang, N.; Luo, J.; Zhong, C.-J., Catalytic and Electrocatalytic Oxidation of Ethanol over Palladium-Based Nanoalloy Catalysts. *Langmuir* **2013,** *29*, 9249-9258.

21. Li, J.; Zhang, J. Z., Optical Properties and Applications of Hybrid Semiconductor Nanomaterials. *Coord. Chem. Rev.* **2009,** *253*, 3015-3041.

22. Costi, R.; Saunders, A. E.; Banin, U., Colloidal Hybrid Nanostructures: A New Type of Functional Materials. *Angew. Chem. Int. Ed.* **2010,** *49*, 4878- 4897.

23. Zhao, S.; Chen, S.; Wang, S.; Li, D.; Ma, H., Preparation, Phase Transfer, and Self-Assembled Monolayers of Cubic Pt Nanoparticles. *Langmuir* **2002,** *18*, 3315–3318.

24. Schmid, G.; Baumle, M.; Geerkens, M.; Heim, I.; Osemann, C.; Sawitowski, T., Current and Future Applications of Nanoclusters. *Chem. Soc. Rev.* **1999,** *28*, 179-185.

25. Suh, W. H.; Jang, A. R.; Suh, Y.; Suslick, K. S., Porous, Hollow, and Ball-in-Ball Metal Oxide Microspheres: Preparation, Endocytosis, and Cytotoxicity. *Adv. Mater.* **2006,** *18*, 1832-183.

26. Turkevich, J.; Stevenson, P. C.; Hillier, J., A Study of the Nucleation and Growth Processes in the Synthesis of Colloidal Gold. *Discuss. Faraday Soc.* **1951,** *11*, 55-75.

27. Duan, J.; Liu, J.; Yao, H.; Mo, D.; Hou, M.; Sun, Y.; Chen, Y.; Zhang, L., Controlled Synthesis and Diameter-Dependent Optical Properties of Cu Nanowire Arrays. *Mater. Sci. Eng. B* **2008,** *147*, 57-62.

28. Yu, X.; Cao, C.; An, X., Facile Conversion of Fe Nanotube Arrays to Novel α-Fe_2O_3 Nanoparticle Nanotube Arrays and Their Magnetic Properties. *Chem. Mater.* **2008,** *20*, 1936-1940.

29. Huang, C. J.; Chiu, P. H.; Wang, Y. H.; Meen, T. H.; Yang, C. F., Synthesis and Characterization of Gold Nanodogbones by the Seeded Mediated Growth Method. *Nanotechnology* **2007,** *18*, 395603/1-395603/6.

30. Robinson, R. D.; Sadtler, B.; Demchenko, D. O.; Erdonmez, C. K.; Wang, L. W.; Alivisatos, A. P., Spontaneous Superlattice Formation in Nanorods through Partial Cation Exchange. *Science* **2007,** *317*, 355-358.

31. Kundu, S.; Panigrahi, S.; Praharaj, S.; Basu, S.; Ghosh, S. K.; Pal, A.; Pal, T., Anisotropic Growth of Gold Clusters to Gold Nanocubes under UV Irradiation. *Nanotechnology* **2007,** *18*, 075712/1-075712/7.

32. Sun, Y.; Xia, Y., Shape-Controlled Synthesis of Gold and Silver Nanoparticles. *Science* **2002,** *298*, 2176-2179.

33. Sherry, L. J.; Jin, R.; Mirkin, C. A.; Schatz, G. C.; Van Duyne, R. P., Localized Surface Plasmon Resonance Spectroscopy of Single Silver Triangular Nanoprisms. *Nano Lett.* **2006,** *6,* 2060-2065.

34. La Mer, V. K.; Dinegar, R. H., Theory, Production and Mechanism of Formation of Monodispersed Hydrosols. *J. Am. Chem. Soc.* **1950,** *72*, 4847–4854.

35. Zhuang, Z.; Peng, Q.; Li, Y. Controlled Synthesis of Semiconductor Nanostructures in the Liquid Phase. *Chem. Soc. Rev.* **2011,** *40*, 5492–5513.

36. Thanh, N. T. K.; Maclean, N.; Mahiddine, S. Mechanisms of Nucleation and Growth of Nanoparticles in Solution. *Chem. Rev.* **2014,** *114*, 7610-7630.

37. (a) Guo, S. J.; Wang, E. K., Noble Metal Nanomaterials: Controllable synthesis and Application in Fuel Cells and Analytical Sensors. *Nano Today* **2011,** *6*, 240-264; (b) Banadaki, A. D.; Kajbafvala, A., Recent Advances in Facile Synthesis of Bimetallic Nanostructures: An Overview. *J. Nanomat* **2014,** *2014*, 1-28; (c) Zhu, C. Z.; Du, D.; Eychmuller, A.; Lin, Y. H., Engineering Ordered and Nonordered Porous Noble Metal Nanostructures: Synthesis, Assembly, and Their Applications in Electrochemistry. *Chem. Rev.* **2015,** *115*, 8896-8943.

38. (a) Weiner, R. G.; Smith, A. F.; Skrabalak, S. E., Synthesis of Hollow and Trimetallic Nanostructures by Seed- Mediated Co-reduction. *Chem. Commun.* **2015,** *51*, 8872-8875; (b) Gao, X.; Esteves, R. J. A.; Nahar, L.; Nowaczyk, J.; Arachchige, I. U., Direct Cross-Linking of Au/Ag Alloy Nanoparticles into Monolithic Aerogels for Application in Surface Enhanced Raman Scattering. *ACS Appl. Mater. Interfaces* **2016,** *8*, 13076-13085; (c) Jing, H.; Wang, H., Structural Evolution of Ag-Pd Bimetallic Nanoparticles through Controlled Galvanic Replacement: Effects of Mild Reducing Agents. *Chem. Mater* **2015,** *27* 2172- 2180.

39. (a) Ratchford, D.; Shafiei, F.; Kim, S.; Gray, S. K.; Li, X., Manipulating Coupling between a Single Semiconductor Quantum Dot and Single Gold Nanoparticle. *Nano Lett.* **2011,** *11*, 1049−1054; (b) Shevchenko, E. V.; Talapin, D. V.; Murray, C. B.; O'Brien, S., Structural Characterization of Self-Assembled Multifunctional Binary

Nanoparticle Superlattices. *J. Am. Chem. Soc.* **2006,** *128*, 3620−3637; (c) Sreeprasad, T. S.; Samal, A. K.; Pradeep, T., One, Two, and Three-Dimensional Superstructures of Gold Nanorods Induced by Dimercaptosuccinic Acid. *Langmuir* **2008,** *24*, 4589−4599; (d) Urban, J. J.; Talapin, D. V.; Shevchenko, E. V.; Murray, C. B., Self- Assembly of PbTe Quantum Dots into Nanocrystal Superlattices and Galssy Films. *J. Am. Chem. Soc.* **2006,** *128*, 3248−3255.

40. Shevchenko, E. V.; Talapin, D. V.; Kotov, N. A.; O'Brien, S.; Murray, C. B., Structural Diversity in Binary Nanoparticle Superlattices. *Nature* **2006,** *439*, 55-59.

41. Rolison, D. R.; Dunn, B., Electrically Conductive Oxide Aerogels: New Materials in Electrochemistry. *J. Mater. Chem.* **2001,** *11*, 963-980.

42. (a) Pierre, A. C.; Pajonk, G. M., Chemistry of Aerogels and Their Applications. *Chem. Rev.* **2002,** *102*, 4243-4265; (b) Hüsing, N.; Schubert, U., Aerogels-Airy Materials: Chemistry, Structure, and Properties. *Angew. Chem. Int. Ed.* **1998,** *37*, 22-45.

43. Pekala, R. W.; Mayer, S. T.; Poco, J. F.; Kaschmitter, J. L. *Mat. Res. Soc. Symp. Proc.* **1994,** *349*, 79-84.

44. (a) Feng, J.; Feng, J.; Zhang, C., Shrinkage and Pore Structure in Preparation of Carbon Aerogels. *J. Sol-Gel Sci. Technol.* **2011,** *59*, 371-380; (b) Mulik, S.; Sotiriou-Leventis, C.; Leventis, N., Macroporous Electrically Conducting Carbon Networks by Pyrolysis of Isocyanate-Cross-Linked Resorcinol-Formaldehyde Aerogels. *Chem. Mater.* **2008,** *20*, 6985-6997.

45. (a) Gacoin, T.; Lahlil, K.; Larregaray, P.; Boilot, J.-P., Transformation of CdS Colloids: Sols, Gels, and Precipitates. *J. Phys. Chem. B* **2001,** *105*, 10228-10235; (b)

Gacoin, T.; Malier, L.; Boilot, J.-P. Sol–Gel Transition in CdS Colloids. *J. Mater. Chem.* **1997,** *7*, 859-860; (c) Gacoin, T.; Malier, L.; Boilot, J.-P. New Transparent Chalcogenide Materials Using a Sol-Gel Process. *Chem. Mater.* **1997,** *9*, 1502-1504.

46. Mohanan, J. L.; Brock, S. L. A New Addition to the Aerogel Community: Unsupported CdS Aerogels with Tunable Optical Properties. *J. Non-Cryst. Solids* **2004,** *350*, 1-8.

47. (a) Mohanan, J. L.; Arachchige, I. U.; Brock, S. L. Porous Semiconductor Chalcogenide Aerogels. *Science* **2005,** *307*, 397-400; (b) Arachchige, I. U.; Brock, S. L. Sol-Gel Assembly of CdSe Nanoparticles to form Porous Aerogel Networks. *J. Am. Chem. Soc.* **2006,** *128*, 7964-7971; (c) Yu, H.; Liu, Y.; Brock, S. L. Tuning the Optical Bandgap of Quantum Dot Assemblies by Varying the Network Density *ACS Nano* **2009,** *3*, 2000-2006; (d) Yu, H.; Bellair, R.; Kannan, R. M.; Brock, S. L. Engineering Strength, Porosity, and Emission Intensity of Nanostructured CdSe Networks by Altering the Building-Block Shape. *J. Am. Chem. Soc.* **2008,** *130*, 5054–5055; (e) Yu, H.; Brock, S. L. Effects of Nanoparticle Shape on the Morphology and Properties of Porous CdSe Assemblies (Aerogels). *ACS Nano* **2008,** *2*, 1563-1570.

48. (a) Jeong, S. H.; Lee, J. W.; Ge, D.; Sun, K.; Nakashima, T.; Yoo, S. I.; Agarwal, A.; Li, Y.; Kotov, N. A. Reversible Nanoparticle Gels With Colour Switching. *J. Mater. Chem.* **2011,** *21*, 11639-11643; (b) Yao, Q.; Brock, S. L. Porous CdTe Nanocrystal Assemblies: Ligation Effects on the Gelation Process and the Properties of Resultant Aerogels. *Inorg. Chem.* **2011,** *50*, 9985−9992.

49. Pala, I. R.; Brock, S. L. ZnS Nanoparticle Gels for Remediation of Pb^{2+} and Hg^{2+} Polluted Water. *ACS Appl. Mater. Interfaces* **2012,** *4*, 2160-2167.

50. Ganguly, S.; Brock, S. L. Toward Nanostructured Thermoelectrics: Synthesis and Characterization of Lead Telluride Gels and Aerogels. *J. Mater. Chem.* **2011,** *21*, 8800-8806.

51. Hitihami-Mudiyanselage, A.; Senevirathne, K.; Brock, S. L. Assembly of Phosphide Nanocrystals into Porous Networks: Formation of InP Gels and Aerogels. *ACS Nano* **2013,** *7*, 1163−1170.

52. Ganguly, S.; Zhou, C.; Morelli, D.; Sakamoto, J.; Brock, S. L. Synthesis and Characterization of Telluride Aerogels: Effect of Gelation on Thermoelectric Performance of Bi_2Te_3 and $Bi_{2-x}Sb_xTe_3$ Nanostructures. *J. Phys. Chem. C* **2012,** *116*, 17431–17439.

53. Nahar, L.; Esteves, R. J. A.; Hafiz, S.; Özgür, U.; Arachchige, I. U. Metal-Semiconductor Hybrid Aerogels: Evolution of Optoelectronic Properties in a Low Dimensional CdSe/Ag Nanoparticle Assembly. *ACS Nano* **2015,** *9*, 9810−9821.

54. Gill, S. K.; Hope-Weeks, L. J. Monolithic Aerogels of Silver Modified Cadmium Sulfide Colloids. *Chem. Commun.* **2009,** *29*, 4384-4386.

55. Gill, S. K.; Brown, P.; Hope-Weeks, L. J. Gold Modified Cadmium Sulfide Aerogels. *J. Sol-Gel Sci. Technol.* **2011,** *57*, 68-75.

56. Gao, X.; Esteves, R. J.; Luong, T. T. H.; Jaini, R.; Arachchige, I. U. Oxidation-Induced Self-Assembly of Ag Nanoshells into Transparent and Opaque Ag Hydrogels and Aerogels. *J. Am. Chem. Soc.* **2014,** *136*, 7993−8002

57. Liu, W.; Herrmann, A. K.; Geiger, D.; Borchardt, L.; Simon, F.; Kaskel, S.; Gaponik, N.; Eychmuller, A. High-Performance Electrocatalysis on Palladium Aerogels. *Angew. Chem. Int. Ed.* **2012,** *51*, 5743-5747.

58. (a) Bond, G. C. T., D. T. Catalysis by Gold. *Catal. ReV.* **1999,** *41*, 319-388; (b) You, T.; Niwa, O.; Tomita, M.; Hirono, S. Characterization of Platinum Nanoparticle-Embedded Carbon Film Electrode and its Detection of Hydrogen Peroxide. *Anal. Chem.* **2003,** *75*, 2080-2085; (c) Joo, S. H.; Choi, S. J.; Kwa, K. J.; Liu, Z. Ordered Nanoporous Arrays of Carbon Supporting High Dispersions of Platinum Nanoparticles. *Nature* **2001,** *412*, 169-172; (d) Rintoul, M. D.; Torquato, S.; Yeong, C.; Keane, D. T.; Erramilli, S.; Jun, Y. N.; Dabbs, D. M.; Aksay, I. A. Structure and Transport Properties of a Porous Magnetic Gel via X-ray Microtomography. *Phys. Rev.* **1996,** *54*, 2663-2669.

59. Sing, K. S. W. Reporting Physisorption Data for Gas/Solid Systems with Special Reference to the Determination of Surface Area and Porosity. *Pure Appl. Chem.* **1985,** *57*, 603-619.

60. (a) Chen, A.; Wang, J.; Wang, Y.; Jia, Y.; Gu, J.; Xie, X.; Pan, D. Effects of Pore Size and Residual Ag on Electrocatalytic Properties of Nanoporous Gold Films Prepared by Pulse Electrochemical Dealloying. *Electrochim. Acta* **2015,** *153*, 552–558; (b) Patel, J.; Radhakrishnan, L.; Zhao, B.; Uppalapati, B.; Daniels, R. C.; Ward, K. R.; Collinson, M. M. Electrochemical Properties of Nanostructured Porous Gold Electrodes in Biofouling Solutions. *Analyt. Chem.* **2013,** *85*, 11610–11618; (c) Fritz, J. D.; Pickering, H. W. J. Selective Anodic Dissolution of Cu-Au Alloys: TEM and Current Transient Study. *J. Electrochem. Soc.* **1991,** *138*, 3209-3218; (d) Freeman, C. J.; Farghaly, A. A.; Choudhary, H.; Chavis, A. E.; Brady, K. T.; Reiner, J. E.; Collinson, M. M. Microdroplet-Based Potentiometric Redox Measurements on Gold Nanoporous Electrodes. *Analyt. Chem.* **2016,** *88*, 3768–3774.

61. Collinson, M. M. Nanoporous Gold Electrodes and Their Applications in Analytical Chemistry. *ISRN Anal. Chem.* **2013,** *2013*, 1-21.

62. Huang, J. F.; Sun, I. W. Fabrication and Surface Functionalization of Nanoporous Gold by Electrochemical Alloying/Dealloying of Au–Zn in an Ionic Liquid, and the Self-Assembly of L-Cysteine Monolayers. *AdV. Funct. Mater.* **2005,** *15*, 989-994.

63. Pugh, D. V.; Dursun, A.; Corcoran, S. G. Electrochemical and Morphological Characterization of Pt–Cu Dealloying. *J. Electrochem. Soc.* **2005,** *152*, 455-459.

64. Thorp, J. C.; Sieradzki, K.; Tang, L.; Crozier, P. A.; Misra, A.; Nastasi, M.; Mitlin, D.; Picraux, S. T. Formation of Nanoporous Noble Metal Thin Films by Electrochemical Dealloying of Pt_xSi_{1-x}. *Appl. Phys. Lett.* **2006,** *88*, 1-3

65. Xu, C. X.; Su, J. X.; Xu, X. H.; Liu, P. P.; Zhao, H. J.; Tian, F.; Ding, Y. Low Temperature CO Oxidation over Unsupported Nanoporous Gold. *J. Am. Chem. Soc.* **2007,** *129*, 42-43.

66. Qian, L. H.; Yan, X. Q.; Fujita, T.; Inoue, A.; Chen, M. W. Surface enhanced Raman Scattering of Nanoporous Gold: Smaller Pore Sizes Stronger Enhancements. *Appl. Phys. Lett.* **2007,** *90*, 153120-153122.

67. Guo, X.; Han, J.; Liu, P.; Chen, L.; Ito, Y.; Jian, Z.; Jin, T.; Hirata, A.; Li, F.; Fujita, T.; Asao, N.; Zhou, H.; Chen, M. W. Hierarchical Nanoprorosity Enhaced Reversible Capacity of Bicontinuous Nanoporous Metal Based Li-O_2 Battery. *Sci. Rep.* **2016,** *6*, 1-8.

68. Tappan, B.; Steiner, S. A.; Luther, E. R. Nanoporous Metal Foams. *Angew. Chem. Int. Ed.* **2010,** *49*, 4544–4565.

69. West, A. R. *Basic Solid State Chemistry* 2nd ed.; John Wiley & Suns Ltd.: New York, 1999.

70. Borchert, H.; Shevehenko, E. V.; Robert, A.; Mekis, I.; Kornowski, A.; Grubel, G.; Weller, H. Determination of Nanocrystal Sizes: A Comparison of TEM, SAXS, and XRD Studies of Highly Monodisperse $CoPt_3$ Particles. *Langmuir* **2005** *21*, 1931–1936.

71. Flewitt, P. E. J.; Wild, R. K. *Physical Methods for Materials Characterization*. Institute of Physics Publishing :Philadelphia, 1994.

72. Reimer, L., *Scanning Electron Microscopy*. Springer-Verlag Berlin Heidelberg: New York, 1998.

73. Williams, D. B.; Carter, C. B. *Transmission Electron Microscopy A Textbook for Materials Science*. Plenum Press : New York: New York, 1969.

74. Van Der Heide, P. *X-ray Photoelectron Spectroscopy An Introduction to Principles and Practices*. John Wiley & Sons, Inc.: Hoboken: Newjersy, 2012.

75. Wendlandt, W. W.; Helcht, H. G. *Chemical Analysis: Reflectance Spectroscopy*. Interscience: New York: New York, 1966.

76. (a) Tsuge, A.; Uwamino, Y.; Ishizuka, T.; Suzuki, K. Quantitative-Analysis of Powdery Sample by Diffuse Reflectance Infrared Fourier-Transform Spectrometry - Determination of the a-Component in Silicon-Nitride. *Appl. Spectrosc.* **1991,** *45* 1377-1380; (b) Nowak, M.; Kauch, B.; Szperlich, P. Determination of Energy Band Gap of Nanocrystalline SbSI Using Diffuse Reflectance Spectroscopy. *Rev. Sci. Instrum.* **2009,** *80, 1-3*.

77. Tandon, S. P.; Gupta, J. P. Measurement of Forbidden Energy gap of Semiconductors by Diffuse Reflectance Technique. *Phys. Stat. Sol.* **1970,** *38*, 363-367.

78. Lumb, M. D. *Luminescence Spectroscopy*. Academic Press: New York, 1978.

79. Chen, X.; Samia, A. C. S.; Lou, Y.; Burda, C., *J. Am. Chem. Soc.* **2005,** *127*, 4372-4375.

80. (a) Hafiz, S. A.; Esteves, R. J.; Demchenko, D. O.; Arachchige, I. U.; Özgür, Ü. Energy Gap Tuning and Carrier Dynamics in Colloidal $Ge_{1-x}Sn_x$ Quantum Dots. *J. Phys. Chem. Lett.* **2016,** *7*, 3295−3301; (b) Crooker, S. A.; Barrick, T.; Hollingsworth, J. A.; Klimov, V. I. Multiple Temperature Regimes of Radiative Decay in CdSe Nanocrystal Quantum Dots: Intrinsic Limits to the Dark-Exciton Lifetime. *Appl. Phys. Lett.* **2003,** *82*, 2793-2795.

81. Hou, X.; Jones, B. T. Field Instrumentation in Atomic Spectroscopy. *Microchem. J.* **2000,** *66*, 115-145.

82. Webb, P. A.; Orr, C. *Analytical Methods in Fine Particle Technology*. Micromeritics: Norcross, Georgia, 1997.

83. Gregg, S. J.; Sing, K. S. W. *Adsorption, Surface Area and Porosity*. 2nd ed.; Academic Press: New York, 1982.

84. Evans, D. H.; O'Connel, K. M.; Petersen, R. A.; Kelly, M. J. Cyclic Voltammetry. *J. Chem. Edu.* **1983,** *60*, 290-293.

85. Bard, A. J.; Faulkner, L. R. *Electrochemical Methods: Fundamentals and Applications*. 2nd ed.; John Willey & Sons, INC.: New York, 2001.

86. (a) Liang, Z. X.; Zhao, T. S.; Xu, J. B.; Zhu, L. D. Mechanism study of the Ethanol Oxidation Reaction on Palladium in Alkaline Media. *Electrochim. Acta* **2009,** *54*, 2203-2208; (b) Chung, D. Y.; Lee, K. J.; Sung, Y. E. J. Methanol Electro-Oxidation on the Pt

Surface: Revisiting the Cyclic Voltammetry Interpretation. *Phys. Chem. C* **2016,** *120*, 9028-9035.

87. Esteves, R. J.; Ho, M. Q.; Arachchige. I. U. Nanocrystalline Group IV Alloy Semiconductors: Synthesis and Characterization of $Ge_{1-x}Sn_x$ Quantum Dots for Tunable Bandgaps. *Chem. Mater.* **2015,** *27***,** 1559–1568.

88. Yu, J.; Xiang, Q.; Zhou, M. Preparation, Characterization and Visible-Light-Driven Photocatalytic Activity of Fe-Doped Titania Nanorods and First-Principles Study for Electronic Structures. *Appl. Catal. B-Environ.* **2009,** *90*, 595-602.

89. (a) Xiang, Q.; Yu, J.; Wang, W.; Jaroniec, M. Nitrogen self-doped nanosized TiO_2 sheets with exposed {001} facets for enhanced visible-light photocatalytic activity. *Chem. Commun.* **2011,** *47*, 6906-6908. (b) Park, J. H.; Kim, S.; Bard, A. J. Novel Carbon-Doped TiO_2 Nanotube Arrays with High Aspect Ratios for Efficient Solar Water Splitting. *Nano Lett.* **2006,** *6*, 24-28. (c) Xiang, Q. J.; Yu, J. G.; Jaroniec, M. Nitrogen and Sulfur Co-Doped TiO2 Nanosheets with Exposed {001} Facets: Synthesis, Characterization and Visible-Light Photocatalytic Activity. *Phys. Chem. Chem. Phys.* **2011,** *13*, 4853-4861.

90. Rajeshwar, K.; de Tacconi, N. R. Solution Combustion Synthesis of Oxide Semiconductors for Solar Energy Conversion and Environmental Remediation. *Chem. Soc. Rev.* **2009,** *38*, 1984-1998.

91. Dai, G.; Yu, J.; Liu, G. Synthesis and Enhanced Visible-Light Photoelectrocatalytic Activity of p-n Junction BiOI/TiO_2 Nanotube Arrays. *J. Phy. Chem. C* **2011,** *115*, 7339-7346.

92. (a) Hou, W.; Cronin, S. B. A Review of Surface Plasmon Resonance-Enhanced Photocatalysis. *Adv. Funct. Mater.* **2013,** *23*, 1612-1619. (b) Xiao, M.; Jiang, R.; Wang, F.; Fang, C.; Wang, J.; Yu, J. C. Plasmon-Enhanced Chemical Reactions. *J. Mater. Chem. A* **2013,** *1*, 5790-5805. (c) Wang, P.; Huang, B.; Dai, Y.; Whangbo, M. H. Plasmonic Photocatalysts: Harvesting Visible Light With Noble Metal Nanoparticles. *Phys. Chem. Chem. Phys.* **2012,** *14*, 9813-9825. (d) Zhou, X.; Liu, G.; Yu, J.; Fan, W. Surface Plasmon Resonance-Mediated Photocatalysis by Noble Metal-Based Composites Under Visible Light. *J. Mater. Chem.* **2012,** *22*, 21337- 21354.

93. (a) Costi, R.; Saunders, A. E.; Banin, U. Colloidal Hybrid Nanostructures: A New Type of Functional Materials. *Angew. Chem. Int. Ed.* **2010,** *49*, 4878- 4897. (b) Li, J.; Zhang, J. Z. Optical Properties and Applications of Hybrid Semiconductor Nanomaterials. *Coord. Chem. Rev.* **2009,** *253*, 3015-3041.

94. Jiang, R. B.; Li, B. X.; Fang, C. H.; Wang, J. F. Metal/Semiconductor Hybrid Nanostructures for Plasmon-Enhanced Applications. *Adv. Mater.* **2014,** *26*, 5274-5309.

95. (a) Zhang, W.; Govorov, A. O.; Bryant, G. W. Semiconductor-Metal Nanoparticle Molecules: Hybrid Excitons and the Nonlinear Fano Effect. *Phys. Rev. Lett.* **2006,** *97*, 1-4. (b) Zhang, J. T.; Tang, Y.; Lee, K.; Ouyang, M. Tailoring Light-Matter-Spin Interactions In Colloidal Hetero-Nanostructures. *Nature* **2010,** *466*, 91-95.

96. (a) Samanta, A.; Zhou, Y. D.; Zou, S. L.; Yan, H.; Liu, Y. Fluorescence Quenching of Quantum Dots by Gold Nanoparticles: A Potential Long Range Spectroscopic Ruler. *Nano Lett.* **2014,** *14*, 5052-5057. (b) Kumar, A.; Chaudhary, V., Optical and Photophysical Properties of Ag/CdS Nanocomposites - An Analysis of Relaxation Kinetics of the Charge Carriers. *J.Photochem. Photobiol.* **2007,** *189*, 272-279.

97. Hendel, T.; Lesnyak, V.; Kuehn, L.; Herrmann, A.; Bigall, N. C.; Borchardt, L.; Kaskel, S.; Gaponik, N.; Eychmueller, A. Mixed Aerogels from Au and CdTe Nanoparticles. *Adv. Funct. Mater.* **2013,** *23*, 1903-1911.

98. Lesnyak, V.; Wolf, A.; Dubavik, A.; Borchardt, L.; Voitekhovich, S. V.; Gaponik, N.; Kaskel, S.; Eychmueller, A. 3D Assembly of Semiconductor and Metal Nanocrystals: Hybrid CdTe/Au Structures with Controlled Content. *J. Am. Chem. Soc.* **2011,** *133*, 13413-13420.

99. Zhang, X.; Marocico, C. A.; Lunz, M.; Gerard, V. A.; Gun'ko, Y. K.; Lesnyak, V.; Gaponik, N.; Susha, A. S.; Rogach, A. L.; Bradley, A. L. Wavelength, Concentration, and Distance Dependence of Nonradiative Energy Transfer to a Plane of Gold Nanoparticles. *ACSNano* **2012,** *6*, 9283-9290.

100. Ben Moshe, A.; Markovich, G., Synthesis of Single Crystal Hollow Silver Nanoparticles in a Fast Reaction-Diffusion Process. *Chem. Mater.* **2011,** *23*, 1239-1245.

101. Brinas, R. P.; Hu, M.; Qian, L.; Lymar, E. S.; Hainfeld, J. F. Gold Nanoparticle Size Controlled By Polymeric Au(I) Thiolate Precursor Size. *J. Am. Chem. Soc.***2008,** *130*, 975-982.

102. Detty, M. R.; Friedman, A. E.; Oseroff, A. R. A Mechanism for the Oxidation of Glutathione to Glutathione Disulfide with Organotellurium (IV) and Organoselenium (TV) Compounds - A Stepwise Process with Implications for Photodynamic Therapy and Other Oxidative Chemotherapy. *J. Org. Chem.* **1994,** *59*, 8245-8250.

103. Borchert, H.; Shevehenko, E. V.; Robert, A.; Mekis, I.; Kornowski, A.; Grubel, G.; Weller, H. Determination of Nanocrystal Sizes: A Comparison of TEM, SAXS, and XRD Studies of Highly Monodisperse COPt3 Particles. *Langmuir* **2005,** *21*, 1931-1936.

104. Pala, I. R.; Arachchige, I. U.; Georgiev, D. G.; Brock, S. L., Reversible Gelation of II-VI Nanocrystals: The Nature of Interparticle Bonding and the Origin of Nanocrystal Photochemical Instability. *Angew. Chem. Int. Ed.* **2010,** *49*, 3661-3665.

105. (a) Katari, J. E. B.; Colvin, V. L.; Alivisatos, A. P. X-Ray Photoelectron-Spectroscopy of CdSe Nanocrystals with Applications to Studies of the Nanocrystals Surface. *J. Phys. Chem.* **1994,** *98*, 4109-4117. (b) Vargas-Hernandez, C.; Lara, V. C.; Vallejo, J. E.; Jurado, J. F.; Giraldo, O. XPS, SEM and XRD investigations of CdSe films prepared by chemical bath deposition. *Phys. Stat. Sol. B* **2005,** *242*, 1897-1901.

106. (a) Chen, R. Z.; Xu, D. S.; Guo, G. L.; Tang, Y. Q. Electrodeposition of Silver Selenide Thin Films From Aqueous Solutions. *J. Mater. Chem.* **2002,** *12*, 1437-1441. (b) Jia, J.; Bendounan, A.; Kotresh, H. M.; Chaouchi, K.; Sirotti, F.; Sampath, S.; Esaulov, V. A. Selenium Adsorption on Au(111) and Ag(111) Surfaces: Adsorbed Selenium and Selenide Films. *J. Phys. Chem. C* **2013,** *117*, 9835-9842. (c) Yao, Q.; Arachchige, I. U.; Brock, S. L. Expanding the Repertoire of Chalcogenide Nanocrystal Networks: Ag_2Se Gels and Aerogels by Cation Exchange Reactions. *J. Am. Chem. Soc.* **2009,** *131*, 2800-2801.

107. Brillson, L. J. Transition in Schottky-Barrier Formation with Chemical Reactivity. *Phys. Rev. Lett.***1978,** *40*, 260-263.

108. Okasha, A.; Mohamed, M. B.; Negm, S.; Talaat, H. Weak Exciton-Plasmon and Exciton-Phonon Coupling in Chemically Synthesized Ag/CdSe Metal/Semiconductor Hybrid Nanocomposite. *Phys. E.* **2012,** *44*, 2094-2098.

109. (a) Pankove, I. J. *Optical Processes in Semiconductor.* Dover Publications, Inc.: New York, 1971; pp 8-10. (b) Lesnyak, V.; Wolf, A.; Dubavik, A.; Borchardt, L.;

Voitekhovich, S. V.; Gaponik, N.; Kaskel, S.; Eychmueller, A. 3D Assembly of Semiconductor and Metal Nanocrystals: Hybrid CdTe/Au Structures with Controlled Content. *J. Am. Chem. Soc.* **2011,** *133*, 13413-13420.

110. Arachchige, I. U.; Brock, S. L. Sol–Gel Methods for the Assembly of Metal Chalcogenide Quantum Dots. *Acc. Chem. Res.* **2007,** *40*, 801-809.

111. Nirmal, M.; Murray, C. B.; Bawendi, M. G. Fluorescence-Line Narrowing in CdSe Quantum Dots-Surface Localization of the Photogenerated Exciton *Phys. Rev. B* **1994,** *50*, 2293-2300.

112. (a) Bawendi, M. G.; Carroll, P. J.; Wilson, W. L.; Brus, L. E. Luminescence Properties of CdSe Quantum Crystallites-Resonance Between Interior and Surface Localized States. *J. Chem. Phys.* **1992,** *96*, 946-954. (b) Donega, C. d. M.; Bode, M.; Meijerink, A. Size- and Temperature-Dependence of Exciton Lifetimes in CdSe Quantum Dots. *Phys. Rev. B* **2006,** *74*, 1-20. (c) Abdellah, M.; Karki, K. J.; Lenngren, N.; Zheng, K. B.; Pascher, T.; Yartsev, A.; Pullerits, T. Ultra Long-Lived Radiative Trap States in CdSe Quantum Dots. *J. Phys. Chem. C* **2014,** *118*, 21682-21686. (d) Jones, M.; Lo, S. S.; Scholes, G. D. Quantitative Modeling of the Role of Surface Traps in CdSe/CdS/ZnS Nanocrystal Photoluminescence Decay Dynamics. *Proc. Natl. Acad. Sci. U.S.A.,* **2009**, *106*, 3011-3016.

113. Leventis, N.; Chandrasekaran, N.; Sadekar, A. G.; Mulik, S.; Sotiriou-Leventis, C. The Effect of Compactness on the Carbothermal Conversion of Interpenetrating Metal Oxide/Resorcinol-Formaldehyde Nanoparticle Networks to Porous Metals and Carbides. *J. Mater. Chem.* **2010**, *20*, 7456-7471.

114. Kagan, C. R.; Murray, C. B.; Bawendi, M. G. Long-Range Resonance Transfer of Electronic Excitations in Close-Packed CdSe Quantum-dot Solids. *Phys.Rev. B* **1996**, *54*, 8633-8639.

115. (a) Johnson, P. B.; Christy, R. W. Optical Constants of the Noble Metals. *Phys. Rev. B* **1972,** *6*, 4370−4379; (b) Xu, Y.; Dong, Y.; Shi, J.; Xu, M.; Zhang, Z.; Yang, X. Au@Pt Core-Shell Nanoparticles Supported on Multiwalled Carbon Nanotubes for Methanol Oxidation. *Catal. Commun.* **2011,** *13*, 54−58; (c) Bigall, N. C.; Reitzig, M.; Naumann, W.; Simon, P.; Van Pée, K.-H.; Eychmüller, A., Fungal Templates for Noble-Metal Nanoparticles and Their Application in Catalysis. *Angew. Chem. Int. Ed.* **2008,** *47*, 7876−7879.

116. Wright, A.; Gabaldon, J.; Burckel, D. B.; Jiang, Y.-B.; Tian, Z. R.; Liu, J.; Brinker, J.; Fan, H. Hierachically Organized Nanoparticle Mesostructure Arrays Formed through Hydrothermal Self-Assembly. *Chem. Mater.* **2006,** *18*, 3034−3038.

117. (a) Wessels, J. M.; Nothofer, H.-G.; Ford, W. E.; von Wrochem, F.; Scholz, F.; Vossmeyer, T.; Schroedter, A.; Weller, H.; Yasuda, A. Optical and Electrical Properties of Three-Dimensional Interlinked Gold Nanoparticle Assemblies. *J. Am. Chem. Soc.* **2004,** *126*, 3349 − 3356; (b) Shavel, A.; Gaponik, N.; Eychmüller, A. The Assembly of Semiconductor Nanocrystals. *Eur. J. Inorg. Chem.* **2005,** *2005,* 3613–3623.

118. (a) Luther, J. M.; Law, M.; Song, Q.; Perkins, C. L.; Beard, M. C.; Nozik, A. J. Structural, Optical and Electrical Properties of Self-Assembled Films of PbSe Nanocrystals Treated with 1,2 Ethanedithiol. *ACS Nano* **2008,** *2*, 271-280; (b) Talapin, D. V.; Murray, C. B. PbSe Nanocrystal Solids for n- and p-Channel Thin Film Field-Effect Transistors. *Science* **2005,** *310*, 86-89.

119. Crooks, R. M.; Zhao, M.; Sun, L.; Chechik, V.; Yeung, L. K. Dendrimer-Encapsulated Metal Nanoparticles: Synthesis, Characterization, and Applications to Catalysis. *Acc. Chem. Res.* **2001,** *34*, 181–190.

120. Ahn, H.; Chandekar, A.; Kang, B.; Sung, C.; Whitten, J. E. Electrical Conductivity and Vapor-Sensing Properties of w-(3-Thienyl)alkanethiol-Protected Gold Nanoparticle Films. *Chem. Mater.* **2004,** *16*, 3274-3278.

121. Urban, J. J.; Talapin, D. V.; Shevchenko, E. V.; Kagan, C. R.; Murray, C. B. Synergism in Binary Nanocrystal Superlattices Leads to Enhanced p-Type Conductivity in Self-Assembled PbTe/Ag_2Te Thin Films. *Nat. Mater.* **2007,** *6*, 115-121.

122. (a) Korala, L.; Li, L.; Brock, S. L. Transparent Conducting Films of CdSe(ZnS) Core(Shell) Quantum Dot Xerogels. *Chem. Commun.* **2012,** *48*, 8523-8525; (b) Korala, L.; Wang, Z.; Liu, Y.; Maldonado, S.; Brock, S. L. Uniform Thin Films of CdSe and CdSe(ZnS) Core(shell) Quantum Dots by Sol-Gel Assembly: Enabling Photoelectrochemical Characterization and Electronic Applications. *ACS Nano* **2013,** *7*, 1215–1223

123. Wang, R.; Li, G.; Dong, Y.; Chi, Y.; Chen, G. Carbon Quantum Dot-Functionalized Aerogels for NO_2 Gas Sensing. *Anal. Chem.* **2013,** *85*, 8065−8065.

124. Yao, Q.; Brock, S. L. Porous CdTe Nanocrystal Assemblies: Ligation Effects on the Gelation Process and the Properties of Resultant Aerogels. *Inorg. Chem.* **2011,** *50*, 9985-9992.

125. (a) Herrmann, A.-K.; Formanek, P.; Borchardt, L.; Klose, M.; Giebeler, L.; Eckert, J.; Kaskel, S.; Gaponik, N.; Eychmueller, A. Multimetallic Aerogels by Template-Free Self-Assembly of Au, Ag, Pt, and Pd Nanoparticles. *Chem. Mater.* **2014,** *26*, 1074-1083;

(b) Liu, W.; Haubold, D.; Rutkowski, B.; Oschatz, M.; Hübner, R.; Werheid, M.; Ziegler, C.; Sonntag, L.; Liu, S.; Zheng, Z.; Herrmann, A.-K.; Geiger, D.; Terlan, B.; Gemming, T.; Borchardt, L.; Kaskel, S.; Czyrska, A.-F.; Eychmüller, A. Self-Supporting Hierarchical Porous PtAg Alloy Nanotubular Aerogels as Highly Active and Durable Electrocatalysts. *Chem. Mater.* **2016** *28*, 6477–6483.

126. (a) Shin, W. K.; Lee, Y. W.; Park, Y.; Choi, B.-S.; Hong, J. W.; Park, K.-H.; Hand, S. W., One-Pot Synthesis of Trimetallic Au@PdPt Core-Shell Nanoparticles with High Catalytic Performance. *ACS Nano* **2013,** *9*, 7945- 7955; (b) Liu, X.-J.; Cui, C.-H.; Li, H.-H.; Lei, Y.; Zhuang, T.-T.; Sun, M.; Arshad, M. N.; Albar, H. A.; Sobahi, T. R.; Yu, S.-H. Hollow Ternary PtPdCu Nanoparticles: A Superior and Durable Cathodic Electrocatalyst. *Chem. Sci.* **2015,** *6*, 3038-3043; (c) Li, F.-M.; Kang, Y.-Q.; Peng, R.-L.; Li, S.-N.; Xia, B.-Y.; Liu, Z.-H.; Chen, Y. Sandwich-Structured Au@Polyallylamine@Pd Nanostructures: Tuning the Electronic Properties of the Pd Shell for Electrocatalysis. *J. Mater. Chem. A* **2016,** *4*, 1020-1024; (d) Dimitratos, N.; Lopez-Sanchez, J. A.; Anthonykutty, M.; Brett, G.; Carley, A. F.; Tiruvalam, R. C.; Herzing, A. A.; Kiely, C. J.; Knight, D. W.; Hutchings, G. J. Oxidation of Glycerol Using Gold-Palladium Alloy-Supported Nanocrystals. *Phys. Chem. Chem. Phys.* **2009,** *11*, 4952-4961; (e) Lee, D.; Jang, H. Y.; Hong, S.; Park, S. Synthesis of Hollow and Nanoporous Gold/Platinum Alloy Nanoparticles and Their Electrocatalytic Activity for Formic Acid Oxidation. *J. Colloid Interf. Sci.* **2012,** *388*, 74-79.

127. Yin, A.-X.; Min, X.-Q.; Zhang, Y.-W.; Yan, C.-H. Shape-Selective Synthesis and Facet-Dependent Enhanced Electrocatalytic Activity and Durability of Monodisperse Sub-10 nm Pt-Pd Tetrahedrons and Cubes. *J. Am. Chem. Soc.* **2011,** *133*, 3816–3819.

128. Chen, Y.; Lai, S.; Jiang, S.; Fu, C.; Li, A.; Chen, Y.; Lai, X.; Hu, J. Synthesis and Enhanced Electrocatalytic Properties of Au/Pd/Pt Nanohollows. *Mat. Lett.* **2015,** *157*, 15-18.

129. Zhang, P.; Dai, X.; Zhang, X.; Chen, Z.; Yang, Y.; Sun, H.; Wang, X.; Wang, H.; Wang, M.; Su, H.; Li, D.; Li, X.; Qin, Y. One-Pot Synthesis of Ternary Pt-Ni-Cu Nanocrystals with High Catalytic Performance. *Chem. Mater.* **2015,** *27*, 6402-6410.

130. Sneed, B. T.; Young, A. P.; Jalalpoor, D.; Golden, M. C.; Mao, S.; Jiang, Y.; Wang, Y.; Tsung, C.-K., Shaped Pd-Ni-Pt Core-Sandwich-Shell Nanoparticles: Influence of Ni Sandwich Layer on Catalytic Electrooxidations. *ACS Nano* **2014,** *8*, 7239-7250.

131. (a) Herbani, Y.; Nakamura, T.; Sato, S. Synthesis of Platinum-Based Binary and Ternary Alloy Nanoparticles in an Intense Laser Field. *J. Colloid Interface Sci.* **2012,** *375*, 78-87; (b) Zhang, H.; Okumura, M.; Toshima, N. Stable Dispersions of PVP-Protected Au/Pt/Ag Trimetallic Nanoparticles as Highly Active Colloidal Catalysts for Aerobic Glucose Oxidation. *J. Phys. Chem. C* **2011,** *115*, 14883-14891.

132. Venkatesan, P.; Santhanalakshmi, J. Designed Synthesis of Au/Ag/Pd Trimetallic Nanoparticle-Based Catalysts for Sonogashira Coupling Reactions. *Langmuir* **2010,** *26*, 12225-12229.

133. Niu, K.-Y.; Kuliich, S. A.; Yang, J.; Zhu, A. L.; Du, X.-W. Galvanic Replacement Reactions of Active-Metal Nanoparticles. *Chem. Eur. J.* **2012,** *18*, 4234-4241.

134. Yin, Z.; Zhang, Y.; Chen, K.; Li, J.; Li, W.; Tang, P.; Zhao, H.; Zhu, Q.; Bao, X.; Ma, D. Monodispersed Bimetallic PdAg Nanoparticles With Twinned Structures: Formation and Enhancement for the Methanol Oxidation. *Sci. Rep.* **2014,** *4288*, 1-9.

135. Lu, X.; Au, L.; Mclellan, J.; Li, Z.-Y.; Marquez, M.; Xia, Y. Fabrication of Cubic Nanocages and Nanoframes by Dealloying Au/Ag Alloy Nanoboxes with an Aqueous Etchant Based on $Fe(NO_3)_3$ or NH_4OH. *Nano Lett.* **2007,** *7*, 1764-1769.

136. (a) Toyoshima, R.; Hiramatsu, N.; Yoshida, M.; Amemiya, K.; Mase, K.; Mun, B. S.; Kondoh, H., CO Adsorption on Pd–Au Alloy Surface: Reversible Adsorption Site Switching Induced by High-Pressure CO. *J. Phys. Chem. C* **2016,** *120*, 416–421; (b) Yang, L.; Liub, X.; Lua, Q.; Huanga, N.; Liua, M.; Zhanga, Y.; Yaoa, S. Catalytic and Peroxidase-Like Activity of Carbon Based-AuPd Bimetallic Nanocomposite Produced Using Carbon Dots as the Reductant. *Anal. Chim. Acta.* **2016,** *930*, 23–30.

137. Ho, M. Q.; Esteves, R. J. A.; Kerdarnath, G.; Arachchige, I. U. Size-Dependent Optical Properties of Luminescent Zn_3P_2 Quantum Dots *J. Phys. Chem. C* **2015,** *119*, 10576-10584.

138. Castner, D. G. X-ray Photoelectron Spectroscopy Sulfur 2p Study of Organic Thiol and Disulfide Binding Interactions with Gold Surfaces. *Langmuir* **1996,** *12*, 5083–5086.

139. Acharyya, D.; Huang, K. Y.; Chattopadhyay, P. P.; Ho, M. S.; Fechte, H.-J.; Bhattacharyya, P. Hybrid 3D Structures of ZnO Nanoflowers and PdO Nanoparticles as a Highly Selective Methanol Sensor. *Analyst* **2016,** *141*, 2977-2989.

140. Sipra, C.; Betty, C. A.; Bhattacharyya, K.; Saxena, V.; Bhattacharya, D., Nanostructured PdO Thin Film from Langmuir-Blodgett Precursor for Room-Temperature H_2 Gas Sensing. *ACS Appl. Mater. Interfaces.* **2016,** *8*, 16997-7003.

141. Thotaab, R.; Ganesh, V. Simple and Facile Preparation of Silver–Polydopamine (Ag–PDA) Core–Shell Nanoparticles for Selective Electrochemical Detection of Cysteine. *RSC Adv.* **2016,** *6*, 49578-49587.

142. Brown, N. M. D.; Hewitt, J. A.; Meenan, B. J. X-ray Photoelectron Spectroscopy Studies of Fired Palladium Electrode Ink Materials. *Surf. Interface Anal.* **1993,** *20*, 215–22.

143. Farghaly, A. A.; Lam, M.; Freeman, C. J.; Uppalapati, B.; Collinson, M. M. Potentiometric Measurements in Biofouling Solutions: Comparison of Nanoporous Gold to Planar Gold. *J. Electrochem. Soc.* **2016,** *163*, 3083-3087.

144. Paradinal, S. S.; Dorfs, D.; Friebe, S.; Freytag, F.; Wolf, A.; Bigall, N. C. Aerogels from CdSe/CdS Nanorods with Ultra-long Exciton Lifeimes and High Fluorescence Quantum Yields. *Adv. Mater.* **2015,** *27*, 6152-6156.

145. Ranmohotti, K. G. S.; Gao, X.; Arachchige, I. U. Salt-Mediated Self-Assembly of Metal Nanoshells into Monolithic Aerogel Frameworks. *Chem. Mater.* **2013,** *25*, 3528−3534.

146. Cai, B.; Wen, D.; Liu, W.; Herrmann, A. K.; Benad, A.; Eychmüller, A., Function-Led Design of Aerogels: Self-Assembly of Alloyed PdNi Hollow Nanospheres for Efficient Electrocatalysis. *Angew. Chem. Int. Ed.* **2015,** *54*, 13101-13105.

147. Hu, C.; Zhai, X.; Zhao, Y.; Bian, K.; Zhang, J.; Qu, L.; Zhang, H.; Luo, H., Small-Sized PdCu Nanocapsules on 3D Graphene for Highperformance Ethanol Oxidation. *Nanoscale* **2014,** *6*, 2768−2775.

LAMIA NAHAR

Phone: 804-588-8484 | Email: naharl@vcu.edu
300 West Franklin Street, Apt: 701W, Richmond, VA 23220

EDUCATION

- Ph. D. Inorganic and Materials Chemistry (GPA 3.42/4.0), May 2017 (Expected)
  Virginia Commonwealth University, Richmond, Virginia.
  Dissertation: Self-supported Assembly of Metal and Semiconductor Nanostructures for Enhanced Optoelectronic and Electrocatalytic Properties.
  Advisor: Prof. Indika U. Arachchige.

- M. S. Inorganic and Analytical Chemistry (GPA 4.0/4.0), 2009, University of Dhaka, Bangladesh.
  Thesis: Investigation on Mixed Ligand Complexes of Metal-Adenine (Metal = Co(II), Cu(II) and Zn(II)) with 2,2'–Bipyridine, 1, 10-Phenanthroline and Oxalic Acid.
  Advisor: Prof. Pradip Kumar Bakshi.

- B. Sc. (Honors) in Chemistry (GPA 4.0/4.0), 2007, University of Dhaka, Bangladesh.

RESEARCH EXPERIENCE

2012 – 2017 Graduate Research Assistant, Department of Chemistry, Virginia Commonwealth University

- Designed and developed a methodology for the synthesis of Au/Ag/Pd and Au/Ag/Pt alloy nanoparticles (NPs).
- Investigated the oxidation-induced self-assembly of metal NPs into high surface area, mesoporous nanostructures (aerogels) and studied their application in electrocatalytic oxidation of alcohols.
- Investigated the colloidal aggregation of metal NPs via in-situ NMR to probe the gelation mechanism.
- Fabricated Au/Ag alloy aerogels for application in surface enhance Raman scattering (SERS) and detection of chronic biological molecules (e.g. Isoprostanes, antioxidants).
- Developed a new general methodology for the efficient integration of plasmonic and excitonic properties of Ag and CdSe NPs to produce metal-semiconductor hybrid nanostructures.
- Collaborated with a research group from Department of Chemistry to investigate the optical properties of highly porous pyrene-quinoxaline-derived benzimidazole-linked polymers with increasing conjugation in the polymer structure.

2008 – 2009 Graduate Assistant, Department of Chemistry, University of Dhaka, Bangladesh.

- Synthesized the mixed ligand complexes of metal-adenine (Metal = Co(II), Cu(I I) and Zn(II)) with 2,2'-bipyridine, 1,10-phenanthroline and oxalic acid ligands to investigate the effect of secondary ligands.

2006 – 2007 Undergraduate research studies for the partial fulfillment of B. Sc. (Honors) degree
Department of Chemistry, University of Dhaka, Bangladesh.

- Developed a synthetic route for adenine complexes of cobalt (II), copper (II) and zinc (II) to investigated their physicochemical properties by UV-visible, infrared spectroscopy, cyclic voltammetry, and magnetic susceptibility measurements.

TECHNICAL EXPERTIES

Spectroscopy and Microscopy

- Powder X-ray diffraction (PXRD)
- Energy dispersive spectroscopy (EDS)
- Diffuse reflectance spectroscopy (DRA)
- Inductively coupled plasma optical emission spectroscopy (ICP-OES)
- Nuclear magnetic resonance spectroscopy (NMR),
- Surface enhance Raman scattering, Raman spectroscopy
- Fourier transform IR (FTIR), UV-vis-near IR absorption and emission spectroscopy
- Transmission electron microscopy (TEM)
- Scanning electron microscopy (SEM)

Instruments

- Cyclic voltammetry (CV)
- BET surface area analyzer
- Super critical dryer, Spin coater

Data Analysis

- Origin, Sigma plot, Excel, MS office, Chem draw

TEACHING AND MANAGING EXPERIENCE

2012 – 2015 Graduate Teaching Assistant**,** Virginia Commonwealth University

- Held weekly review sessions, recitations, and performed laboratory sessions for Inorganic, Organic, and General Chemistry classes.
- Graded weekly reports, quizzes, and exams.
- Held office hours to help undergraduate students with their weekly assignments.

2010 – 2011 Lecturer, American International University Bangladesh, Dhaka, Bangladesh

- Delivered lectures to undergraduate students on topics relating to Organic and Analytical Chemistry and Separation Science.
- Coordinated and set up relevant laboratory experiments with other teaching assistants.
- Assigned and graded exams, quizzes, and exams.
- Held office hours to advise and assist undergraduate students with their assignments.

2012 – Present Graduate Lab and Training Responsibilities, Virginia Commonwealth University

- Lab manager and Hygiene officer (2015 – present).
- Trained users in transmission electron microscopy (TEM), Raman spectrophotometer, scanning electron microscopy (SEM), and energy dispersive spectroscopy (EDS).
- Managed and maintained the florescence spectrophotometer, supercritical dryer, surface area and porosimetry analyzer and cyclic voltammeter.
- Maintained a full and up-to-date chemical inventory for the lab.

2013 – 2016 Graduate Supervisor for Undergraduate Students, Virginia Commonwealth University

- Trained junior graduate and undergraduate students on Schlenk line and air sensitive chemistry.
- Helped them on the operation of powder X-ray diffractometer, scanning electron microscopy, transmission electron microscopy, energy dispersive spectroscopy.

- Assigned and supervised day to day experiments.
- Encouraged and assisted undergraduate students to write research reports and helped them with preparing oral/poster presentations.

AWARDS AND FELLOWSHIPS

- Dissertation Research Fellowship, VCU Graduate School (2016-2017).
- Distinguished Chemist Fund Award, VCU Department of Chemistry (2016-2017).
- Altria Graduate Research Fellowship, VCU Department of Chemistry (2015-2016).
- Fred M. Hawkridge Summer Research Fellowship, VCU Department of Chemistry (2015).
- University Merit scholarship, University of Dhaka (2006-2007).

PEER-REVIEWED JOURNAL ARTICLES

1. Nahar, L.; Farghaly, A. A.; Esteves, R. J. A.; Arachchige, I. U. "Nanostructured Au/Ag/Pd Alloy Aerogels as High Efficiency Alcohol Oxidation Electrocatalysts" ***J. Am. Chem. Soc.*** Submitted.

2. Tallapally, V.; Esteves, R. J. A.; Nahar, L.; Arachchige, I. U. "Multivariate Synthesis of Tin Phosphide Nanoparticles: Temperature, Time, and Ligand Control of Size, Shape, and Crystal Structure" ***Chem. Mater.*** **2016,** *28*, 5406−5414.

3. Gao, X.; Esteves, R. J. A.; Nahar, L.; Nowaczyk, J.; Arachchige, I. U. "Direct Cross-Linking of Au/Ag Alloy Nanoparticles into Monolithic Aerogels for Application in Surface Enhanced Raman Scattering" ***ACS Appl. Mater. Interfaces*** **2016,** *8*, 13076-13085.

4. Nahar, L.; Esteves, R. J. A.; Hafiz, S.; Özgür, Ü.; Arachchige, I. U. "Metal-Semiconductor Hybrid Aerogels: Evolution of Optoelectronic Properties in a Low-Dimensional CdSe/Ag Nanoparticle Assembly" ***ACS Nano*** **2015**, *9*, 9810-9821.

5. Altarawneh, S.; Nahar, L.; Arachchige, I. U.; El-Ballouli, A. O.; Hallal, K. M.; Kaafarani, B. R.; Rabbani, M. G.; Arvapallya, R. K.; El-Kaderi, H. M. "Highly Porous and Photoluminescent Pyrenequinoxaline-Derived Benzimidazole-Linked Polymers" ***J. Mater. Chem. A*** **2015**, *3*, 3006-3010.

6. Nahar, L.; Arachchige, I. U. "Sol-Gel Methods for the Assembly of Metal and Semiconductor Nanoparticles" ***JSM Nanotechnol. Nanomed.*** **2013**, *1*, 1004/1-1004/6.

7. Nahar, L.; Shaikh, A. A.; and Bakshi, P. K. "Preparation and Characterization of Adenine Complexes of Co(II), Cu(II), and Zn(II)" ***Dhaka Univ. J. Sci.*** **2011**, *59*, 223-227.

CONFERENCE PAPERS

1. Nahar, L.; Farghaly, A. A.; Arachchige, I. U. "Porous Metal Aerogels as High Efficiency Alcohol Oxidation Electrocatalysts." Poster presentation, ***252nd ACS National Meeting***, Philadelphia, PA, United States, August 21-25, 2016.

2. Nahar, L.; Gao, X.; Esteves, R. J. A.; Arachchige, I. U. "Sol-Gel Assembly of Au/Ag alloy Nanoparticles into Aerogels for Application in Surface Enhanced Raman Scattering" Poster presentation, ***252nd ACS National Meeting***, Philadelphia, PA, United States, August 21-25, 2016.

3. Nahar, L.; Arachchige, I. U. "Sol-Gel Method: An Advanced Technique to Obtain a 3D Superstructure of Metal-Semiconductor Hybrid Nanoparticles." Oral presentation, ***250th ACS National Meeting***, Boston, MA, United States, August 16-20, 2015.

REFERENCES

1. Dr. Indika U. Arachchige (Ph. D. Advisor)
   Assistant Professor
   Department of Chemistry
   Virginia Commonwealth University
   Richmond, VA 23284
   Tel. (804) 828-6855
   Email: iuarachchige@vcu.edu

2. Dr. Maryanne Collinson
   Professor
   Department of Chemistry
   Virginia Commonwealth University
   Richmond, VA- 23220
   Tel. (804) 828-7509
   E-mail: mmcollinson@vcu.edu

3. Dr. Hani El-Kaderi
   Associate Professor
   Department of Chemistry
   Virginia Commonwealth University
   Richmond, VA- 23284
   Tel. (804) 828-7505
   E-mail: helkaderi@vcu.edu